
ON IN-SITU METHODOLOGIES FOR THE
CHARACTERISATION AND SIMULATION OF
VIBRO-ACOUSTIC ASSEMBLIES

PH.D. THESIS
ACOUSTICS RESEARCH CENTRE, UNIVERSITY OF SALFORD
GREATER MANCHESTER

AUTHOR
JOSHUA W R MEGGITT

SUPERVISOR
PROF. ANDY T MOORHOUSE

*A thesis submitted in partial fulfilment of the requirements
for the degree of Doctor of Philosophy*

JUNE 2017

DECLARATION OF AUTHORSHIP

I, Joshua W R Meggitt, declare that this Thesis titled, 'On In-situ Methodologies for the Characterisation and Simulation of Vibro-Acoustic Assemblies' and the work presented in it are my own. I confirm that:

- This work was done wholly or mainly while in candidature for a research degree at this University.
- Where any part of this thesis has previously been submitted for a degree or any other qualification at this University or any other institution, this has been clearly stated.
- Where I have consulted the published work of others, this is always clearly attributed.
- Where I have quoted from the work of others, the source is always given. With the exception of such quotations, this thesis is entirely my own work.
- I have acknowledged all main sources of help.
- Where the thesis is based on work done by myself jointly with others, I have made clear exactly what was done by others and what I have contributed myself.

Signed:

Date:

"Be excellent to each other, and party on dudes"

Abraham Lincoln

ABSTRACT

A drive towards leaner engineering has seen the use of physical prototypes become a limiting factor in the development of new products. Consequently, alternative prototyping methods are of interest. With their ability to reduce cost, accelerate time to market, and optimize products to higher levels of performance and reliability, virtual methods offer an attractive alternative. Methods for virtual prototyping with respect to visual design and engineering (i.e CAD and CAE) are particularly well developed. Unfortunately, the same cannot be said in the realm of acoustics. Although numerical methods, such as finite and boundary element analysis, are able to predict, with some accuracy, the passive properties of simple assembly components, they currently lack the ability to accurately model more complex vibro-acoustic components, for example vibration sources and their associated vibratory mechanisms. Consequently, the adoption of any virtual acoustic prototyping (VAP) methodology will require some element of experimental work. As such, this Thesis concerns the development and implementation of experimental methods for the independent characterisation of assembly components, with particular emphasis on in-situ approaches. The methods discussed in this work will focus on the determination of active and passive sub-structure properties that may be recombined virtually within a dynamic sub-structuring framework so as to construct a VAP. A well constructed VAP will allow for an engineer to ‘listen’ to a product without it having to physically exist. With the growing importance of product sound quality, this offers a considerable advantage, particularly in the early stages of product development.

Work begins by developing an in-situ method for the independent characterisation of resilient coupling elements. The approach holds a number of advantages over current methods as it may be applied to arbitrary structures and over a wide frequency range. In order to provide a flexible and workable method that may be used in a practical scenario three experimental extensions are provided. These extensions concern; the finite difference approximation for rotational degrees of freedom, the round trip identity for remote measurement positions, and generalised transmissibility for the use of operationally determinable quantities. Experimental studies show that the proposed method, and its extensions, are capable of determining the independent

passive properties of coupling elements from a range of different assembly types with good accuracy.

The in-situ characterisation approach goes on to form the basis of a novel in-situ decoupling procedure which is shown to accurately determine the independent free interface frequency response functions (FRFs) of resiliently coupled source and receiver sub-structures. The decoupling procedure provides a convenient alternative to the free suspension of a sub-structure whilst providing a number of potential benefits, for example, characterisation whilst under representative mounting conditions. The approach is validated experimentally and used to decouple both single and multi-contact resonant assemblies with great success.

The in-situ blocked force approach is re-introduced to the reader as a method for independently characterising the active component of a source sub-structure. Methods for assessing uncertainties involved are also discussed. The blocked force method is subsequently extended so as to allow for an estimate of uncertainties to be made. The concept of error propagation is investigated and an experimental study presented. This study is aimed at providing an example of the in-situ blocked forces application, whilst validating the proposed measure of uncertainty.

The Thesis concludes with an experimental case study utilizing the methods proposed throughout. This case study concerns the construction of a VAP whereby an electric pump is resiliently coupled to a cavity backed plate. It is shown that, together, the proposed methods allow for the construction of a VAP capable of predicting, with reasonable accuracy, the operational pressure and velocity response of an assembly.

ACKNOWLEDGEMENTS

Firstly, I would like to express my immeasurable gratitude towards my supervisor Prof. Andy Moorhouse for his continuous support, patience and motivation. It would be by no means an understatement to say that I could not have asked for a better supervisor and mentor for my PhD studies. I am also especially indebted to Dr. Andy Elliot whose guidance, encouragement, and insightful comments have been indispensable.

Also in need of special thanks are the remaining members of staff at the Acoustic Research Center. Furthermore, I would also like to acknowledge with much appreciation the role of all those involved in the Research projects I was employed on throughout my PhD studies, notably those residing at Dyson UK, The Boeing Company and The University of Liverpool.

A special thanks must also be paid to my fellow G10/G11 post-graduates. The past 3/4 years has been awash with enjoyable conversations, snacks, boardgames and beers, and it goes without saying that my time as a post-graduate would certainly have been a lot less enjoyable without you all.

Beyond the realms of the Newton Building there are a few people whose support and friendship I would like to acknowledge; Tim, Kate, Phil, and all my friends back home. I must also pay a special thanks to John Saxton, for it was he who first introduced me to acoustics and unknowingly set me on this delightful path.

On a more personal note I would like to thank my love, Rosie, for her endless support and patience. It is safe to say that forgetting to wear shoes that night was the best mistake I ever made. Last but not the least, I must thank my family; Mum, Dad and Jack. Without their love and encouragement I would certainly not be in the position I am today, and for that I am eternally grateful.

CONTENTS

Abstract	iii
Contents	v
List of Figures	vii
List of Tables	viii
Author Publications	ix
Symbols	x
Foreword	xii
I Introduction and Literature Review	1
1 Introduction	2
1.1 Research Context and the VAP Approach	2
1.2 Thesis Topics, Aims and Objectives	7
1.3 Thesis Outline	8
2 Literature	9
2.1 Definitions	9
2.1.1 Mobility	9
2.1.2 Impedance	10
2.1.3 Degrees of Freedom & LTI Systems	11
2.2 Source Characterisation	13
2.3 Dynamic Sub-structuring	19
2.3.1 Sub-structure Decoupling	22
2.4 Isolator Characterisation	22
II Coupling Elements	28
3 Characterisation of Resilient Elements	29
3.1 In-situ Characterisation of Coupling Elements	29
3.2 Theoretical Development	30
3.3 Numerical Validation	37

3.4	Experimental Application	42
3.4.1	Single Contact	43
	Mass-Isolator-Mass	43
	Transmissibility Validation	49
	Mass-Isolator-Plate	50
	Beam-Isolator-Plate	53
3.4.2	Multiple Contact	58
	Beam-Isolator(2)-Plate	58
3.5	Concluding Remarks	63
4	Experimental Extensions	64
4.1	Rotational Degrees of Freedom	64
4.1.1	Finite Difference Approach	66
4.1.2	Numerical Validation	69
4.1.3	Experimental Validation	71
	4.1.3.1 Single Contact	71
	Mass-Isolator-Mass	71
4.2	Extension to Remote Measurement Positions	73
4.2.1	Dual Interface Round Trip	75
4.2.2	Remote In-situ Characterisation	76
	4.2.2.1 Remote Partial Interface Method	76
	4.2.2.2 Remote Full Interface Method	78
4.2.3	Experimental Validation	79
	4.2.3.1 Single Contact	79
	Beam-Isolator-Plate	79
	4.2.3.2 Multiple Contact	84
	Beam-Isolator(2)-Plate	84
4.3	Operational Characterisation via the Generalised Transmissibility	88
	4.3.1 Generalised Transmissibility Concept	89
	4.3.2 Operational Dynamic Transfer Stiffness	92
	4.3.3 Experimental Validation	94
	4.3.3.1 Single Contact	94
	Beam-Isolator-Plate	94
	4.3.3.2 Multiple Contact	97
	Beam-Isolator(2)-Plate	97
4.4	Concluding Remarks	100
III	Source and Receivers	102
5	In-Situ Sub-structure Decoupling	103
5.1	Sub-structure Decoupling	103
5.2	In-situ Decoupling Theory	106
5.3	Experimental Investigation	112
	5.3.1 Single Contact	113

5.3.1.1	Mass-Isolator-Plate	113
5.3.1.2	Beam-Isolator-Plate	116
5.3.2	Multiple Contact	121
5.3.2.1	Beam-Isolator(2)-Plate	121
5.4	Concluding Remarks	125
6	Blocked Force Characterisation	126
6.1	Independent Source Characterisation	126
6.2	Blocked Force Theory	128
6.2.1	Impedance Formulation	129
6.2.2	Mobility Formulation	132
6.2.3	Blocked Force Determination	134
6.2.3.1	Experimental Considerations	136
6.2.3.2	Post Processing for Auralisation	138
6.3	Accounting for Uncertainty	140
6.3.1	On-board and Transferability Validation	140
6.3.1.1	Artificial Excitation	142
6.3.2	Sample Space Approach - Expected Value and Standard De- viation	142
6.3.2.1	Nature of the Sample Space Uncertainty	145
6.3.2.2	Alternative Uncertainty Approach	147
6.3.2.3	Propagation of Uncertainty	150
6.4	Experimental Validation	153
6.4.1	Resiliently Coupled Source and Receiver	154
6.4.1.1	Artificial Excitation	155
	Blocked Forces and Standard Deviations	156
	On-board Validation	163
6.4.1.2	Operational Excitation	167
	Blocked Forces and Standard Deviations	168
	On-board Validation	171
	Transferability Validation	174
6.5	Concluding Remarks	177
IV	Experimental Case Study and Conclusions	178
7	Case Study	179
7.1	Building Blocks	179
7.2	Dynamic Sub-Structuring	180
7.2.1	Numerical Example: Beam-Beam	182
7.3	Experimental Case Study	187
	1a) Passive Source Characterisation	189
	1b) Active Source Characterisation	192
	2) Resilient Coupling Element Characterisation	192
	3) Receiver Characterisation	193

4) Dynamic Sub-Structuring	194
5) Operational Prediction	201
7.4 Concluding Remarks	209
8 Conclusion	210
V Appendices and Bibliography	215
Appendices	216
A Regularisation	216
B Matrix Identities	219
C Summary of Assembly Details	220
D Matrix Reduction	221
E Experimental Case Study - IOA Conference Proceeding Manuscript	222
E.1 Introduction	222
E.2 Source Characterisation: Blocked Force Method	223
E.3 Dynamic Sub-structuring: Impedance Approach	226
E.4 In-Situ Isolator Characterisation	228
E.5 Case-Study	229
E.6 Conclusion	232
Bibliography	233

LIST OF FIGURES

1.1	Diagrammatic representation of a general VAP problem.	6
2.1	Cartesian co-ordinate system and notation of forces and velocities. . .	12
3.1	Schematic of an arbitrary source-isolator-receiver system.	31
3.2	Forces contributing to the velocity of interface c_1 (as in Equation 3.6).	32
3.3	Graphical depiction of the numerical simulation carried out.	37
3.4	The upper and lower bounds of the artificial noise matrix \mathbf{N} corresponding to SNRs of 60dB and 40dB, compared against the upper and lower bounds of the mobility matrix \mathbf{Y}	40
3.5	Translational transfer impedance obtained via numerical simulation. Solid blue line is the exact transfer impedance obtained from I whilst uncoupled.	41
3.6	Diagrammatic representation of the mass-isolator-mass test rig. Red arrows correspond to the direction and position of the applied forces, whilst blue arrows indicate the positive direction of the measured accelerations.	45
3.7	Dynamic transfer stiffness and transfer mobility measurements made on assemblies A and B (see Table 3.2).	46
3.8	Dynamic transfer stiffness and transfer mobility measurements made on assemblies C and D (see Table 3.2). Low level excitation at c_2 was used to avoid introducing non-linearities.	47
3.9	Dynamic transfer stiffness and transfer mobility measurements made on assemblies C and D (see Table 3.2). High level excitation at c_2 was used to exaggerate non-linearities resulting from large difference in mass behaviours.	48
3.10	Measured and predicted transmissibilities of assembly B obtained using a dynamic stiffness determined from assembly A	50
3.11	Diagrammatic representation of the mass-isolator-plate test rig, E . Red arrows correspond to the direction and position of the applied forces, whilst blue arrows indicate the positive direction of the measured accelerations.	51
3.12	Dynamic transfer stiffness and transfer mobility measurements made on assemblies C and E (see tables 3.2 and 3.3).	52
3.13	Diagrammatic representation of the beam-isolator-plate test rig, F , showing both full and partial interface measurement set-ups. Red arrows correspond to the direction and position of the applied forces, whilst blue arrows indicate the positive direction of the measured accelerations.	54

3.14	Dynamic transfer stiffness and transfer mobility measurements made on assemblies C and F using partial interface approach.	55
3.14	(Continued) Dynamic transfer stiffness and transfer mobility measurements made on assemblies C and F using partial interface approach.	56
3.15	Diagrammatic representation of the beam-isolator(2)-plate test rig, G , for full and partial interface measurements. Red arrows correspond to the direction and position of the applied forces, whilst blue arrows indicate the positive direction of the measured accelerations.	60
3.16	Dynamic transfer stiffness and transfer mobility measurements made on assemblies C and G (see tables 3.2 and 3.5) using full and partial interface approach.	61
3.16	(Continued) Dynamic transfer stiffness and transfer mobility measurements made on assemblies C and G (see tables 3.2 and 3.5) using full and partial interface approach.	62
4.1	Force and velocity positions for finite difference approximation.	66
4.2	Rotational transfer impedance $\tilde{\mathbf{Z}}_{\mathbf{I}\psi 2\tau_1}$ obtained via numerical simulation using finite difference approach. Solid blue line is the exact transfer impedance obtained from beam I whilst decoupled.	70
4.3	Dynamic transfer stiffness and transfer mobility measurements made on assemblies.	72
4.4	Mobility paths for the round trip and ‘broken’ round trip terms of Equation 4.24.	77
4.5	Diagrammatic representation of the beam-isolator(2)-plate test rig, G . Red arrows correspond to the direction and position of the applied forces, whilst blue arrows indicate the positive direction of the measured accelerations.	80
4.6	Contact interface mobility matrix determined from assembly F (see tables 3.4) using direct and round trip methods. For the round trip case both determined and over-determined results are presented.	81
4.7	Dynamic transfer stiffness’ $K_{I_{c1c2}}$ determined from assemblies C and F (see tables 3.2 and 3.4) using direct and remote method (see Sections 3.2 and 4.2.2). For remote cases both determined and over-determined results are presented.	83
4.8	Diagrammatic representation of the beam-isolator(2)-plate test rig, H . Red arrows correspond to the direction and position of the applied forces, whilst blue arrows indicate the positive direction of the measured accelerations.	84
4.9	Point mobilities from full mobility matrix determine via round trip.	85
4.10	Dynamic transfer stiffnesses $K_{I_{c11c21}}$ and $K_{I_{c12c22}}$ determined from assembly F using direct and remote methods (see Sections 3.2 and 4.2.2). For remote cases both determined and over-determined results are presented.	86

4.10	(Continued) Dynamic transfer stiffnesses $K_{I_{c11c21}}$ and $K_{I_{c12c22}}$ determined from assembly F using direct and remote methods (see Sections 3.2 and 4.2.2). For remote cases both determined and over-determined results are presented.	87
4.11	Mobility paths for the round trip and ‘broken’ round trip terms of remote partial interface impedance relation of Equation 4.24. Highlighted paths are to be replaced by generalised transmissibility terms.	88
4.12	Diagrammatic representation of the beam-isolator(2)-plate test rig, G . Red arrows correspond to the direction and position of the applied forces, whilst blue arrows indicate the positive direction of the measured accelerations.	95
4.13	Transmissibility based predictions determined from assembly F using mobility and velocity based approaches.	96
4.14	Diagrammatic representation of the beam-isolator(2)-plate test rig, H . Red arrows correspond to the direction and position of the applied forces, whilst blue arrows indicate the positive direction of the measured accelerations.	97
4.15	Elements of the transmissibility matrix $\mathbf{T}_{C_{c2b}}$ determined via time averaged velocity and standard mobility measurements on assembly G	98
4.16	Elements of the transmissibility matrix $\mathbf{T}_{C_{c1b}}$ determined via time averaged external velocity and standard mobility measurements on assembly G	99
4.17	Dynamic transfer stiffness predictions for the two resilient elements of assembly G using the time averaged velocity based transmissibility approach (over-determined).	100
5.1	Diagrammatic representation of the general multi-contact assembly considered in the in-situ decoupling procedure.	107
5.2	Coupled and in-situ decoupled effective mass (a) and acceleration (b) of the source sub-structure of assembly E . A diagrammatic representation of the assembly shown in the inset of b (a full size diagram can be found in Figure 3.11).	114
5.2	(Continued) Coupled, in-situ decoupled and physically uncoupled impedance (c) and mobility (d) of the receiver sub-structure of assembly E	116
5.3	Coupled and in-situ decoupled impedance (a) and mobility (b) of the source sub-structure of assembly F . A diagrammatic representation of the assembly is shown in the inset of b (a full size diagram can be found in Figure 3.13a).	118
5.3	Continued: Coupled, in-situ decoupled and physically uncoupled impedance (d) and mobility (e) of the receiver sub-structure of assembly F	119
5.4	Coupled and in-situ decoupled mobilities of the source sub-structure of assembly G . A diagrammatic representation of the assembly is shown in the inset of d (a full size diagram can be found in Figure 3.15a).	122

5.4	Continued: Coupled and in-situ decoupled mobilities of the receiver sub-structure of assembly G	123
6.1	Diagrammatic representation of independent source quantities.	127
6.2	General source-receiver system.	130
6.3	Source-receiver assembly highlighting the DoF subsets S and R . Symbols \times represent response DoFs, whilst \otimes represent solution DoFs at the source-receiver interface. In this rigid case $S \subset R$	143
6.4	Photos of source and sensor positioning used throughout Chapter 6.	155
6.5	Determined, over-determined and expected blocked forces for feet 1-4 of assembly K	157
6.6	Spread in blocked force sample space for one foot of the pump using artificial excitation. Also shown, the expected, over-determined and determined blocked force.	158
6.7	Determined forces from assembly H for each DoF combination used in the sample space approach, where the frequencies shown are $f_1 \approx 144\text{Hz}$, $f_2 \approx 365\text{Hz}$, and $f_3 \approx 2191\text{Hz}$	159
6.8	Determined, over-determined and trimmed expected blocked forces for feet 1-4 of assembly H	160
6.9	Trimmed expected blocked force at foot 1 with \pm the trimmed standard error of the mean. The $\pm\text{SEM}$ plot has been passed through a 3 point moving average filter so as to improve clarity.	161
6.10	Coefficient of variation for the blocked force at foot 1 determined using the trimmed standard deviation and mean.	162
6.11	On-board validation on assembly H using an artificial excitation, using over-determined and expected blocked forces.	164
6.12	Transfer mobilities and corresponding coherences between the remote reference point and each foot of the source.	165
6.13	On-board validation using expected blocked force with propagated SEM. The $\pm\text{SEM}$ plot has been passed through a 5 point moving average filter so as to improve clarity.	166
6.14	Coefficient of variation for each blocked force (grey) used in the on-board validation, and the predicted operational velocity of assembly K (orange).	167
6.15	Over-determined and trimmed expected operational blocked forces for feet 1-4 of assembly K	169
6.16	Spread in blocked force sample space for one foot of the pump using operational excitation. Also shown, the expected, over-determined and determined blocked force.	170
6.17	Over-determined and trimmed expected operational blocked forces for feet 1-4 of assembly H in 3rd octave-bands.	171
6.18	On-board validation on assembly H for over-determined and expected blocked forces.	172
6.19	On-board validation on assembly H for over-determined and expected blocked forces in 3rd octave bands.	173

6.20	Coefficient of variation for each blocked force (grey) and the resultant prediction on assembly H (orange), in 3rd octave bands.	174
6.21	Transferability validation using an artificial excitation, using over-determined and expected blocked forces.	175
6.22	Transferability validation using an artificial excitation, using over-determined and expected blocked forces.	176
6.23	Coefficient of variation for each blocked force (grey) and the resultant prediction on assembly I (orange), in 3rd octave bands.	176
7.1	Diagrammatic representation of numerical study coupling two beams end-to-end.	183
7.2	Results of a numerically simulated dynamic sub-structuring problem. Point mobility matrix of the sub-structured SR assembly. Also shown are the mobilities determined directly for assembly C	186
7.3	Diagrammatic representation of the experimental case study (assembly N). Electric pump (<i>S</i>) mounted via 4 resilient elements (<i>I</i>) to a cavity backed plate (<i>R</i>). Two remote sensors (r_1, r_2) are located on the housing, with a measurement microphone (p_1) in the cavity.	187
7.4	Coupled point mobilities of the source sub-structure determined using full remote contact interface relation (see Equation 4.29) and the collocated remote relation (see Equation 7.18).	190
7.5	Coupled, in-situ decoupled and physically uncoupled point mobilities of the source sub-structure.	191
7.6	Dynamic transfer stiffness obtained from MIM assembly for use in experimental case study.	193
7.7	Coupled transfer mobilities between the source and the top face determined via dynamic sub-structuring and direct measurement.	198
7.8	Coupled transfer mobilities between the source and side face determined via dynamic sub-structuring and direct measurement.	199
7.9	Coupled and uncoupled vibro-acoustic transfer functions determined via dynamic sub-structuring and direct measurement.	200
7.10	Operational velocity prediction at r_1 using transferred blocked forces (over-determined and expected) and directly measured transfer mobilities. Also shown is the directly measured velocity on the coupled assembly.	202
7.11	Operational velocity prediction at r_1 in 3rd octave bands using transferred blocked forces (over-determined and expected) and directly measured transfer mobilities. Also shown is the directly measured velocity on the coupled assembly and the 95% confidence intervals obtained from the propagated blocked force covariance matrix.	203
7.12	Coefficient of variation for each blocked force and the predicted operational velocity (using directly measured transfer mobilities) in 3rd octave bands.	203

7.13	Operational velocity prediction at r_1 using transferred blocked forces (over-determined and expected) and sub-structured transfer mobilities. Also shown is the directly measured velocity on the coupled assembly.	204
7.14	Operational velocity prediction at r_1 in 3rd octave bands using transferred blocked forces (over-determined and expected) and sub-structured transfer mobilities. Also shown is the directly measured velocity on the coupled assembly and the 95% confidence intervals obtained from the propagated blocked force covariance matrix.	205
7.15	Coefficient of variation for each blocked force and the predicted operational velocity (using sub-structured transfer mobilities) in 3rd octave bands.	206
7.16	Operational cavity pressure prediction at p_1 using transferred blocked forces (over-determined and expected) and sub-structured vibro-acoustic transfer function. Also shown is the directly measured pressure in the coupled assembly.	207
7.17	Operational cavity pressure prediction at p_1 using transferred blocked forces (over-determined and expected) and sub-structured vibro-acoustic transfer function. Also shown is the directly measured pressure in the coupled assembly and the 95% confidence intervals obtained from the propagated blocked force covariance matrix.	208
7.18	Coefficient of variation for each blocked force and the predicted operational cavity pressure in 3rd octave bands.	208
8.1	Source-receiver diagrams for operational and blocked forces.	224
8.2	General source-isolator-receiver system.	228
8.3	Diagrammatic illustration of case study.	229
8.4	Sub-structured and directly measured transfer mobilities between each foot of the source to the remote receiver point.	230
8.5	Operational response of assembly at remote measurement point. Responses measured directly and predicted (using sub-structured and directly measured transfer mobilities) using blocked forces determined from another assembly. Lower plot shows the above in one third octave bands with ± 5 dB for greater clarity.	231

LIST OF TABLES

2.1	A list of commonly used frequency response functions along with their relations. E.g. $K = i\omega Z = -\omega^2 \hat{M}$ or $i\omega C = Y = A/i\omega$	11
2.2	Dynamic sub-structuring domains and their use in theoretical and experimental studies.	20
3.1	Geometry, material properties and excitation/response positions for free-free beam simulations, where; L - length, W - width, H - height, E - Young's modulus, ρ - density, and x_{ij} - excitation/response position. Highlighted x_{ij} correspond to those of the coupling interfaces, c_1 and c_2	38
3.2	Details on the construction of Mass-Isolator-Mass (MIM) assemblies.	44
3.3	Details on the construction of the Mass-Isolator-Plate assembly. . . .	51
3.4	Details on the construction of the Beam-Isolator-Plate assembly. . . .	53
3.5	Details on the constructions of the Beam-Isolator(2)-Plate assembly. .	59
4.1	Details on the construction of Mass-Isolator-Mass assemblies used in the determination of rotational dynamic transfer stiffness.	71
6.1	Details on the construction of experimental assemblies.	154
7.1	Independent sub-structure quantities used in the construction of a VAP.	180
7.2	Geometry, material properties and excitation/response positions for free-free beam simulations, where; L - length, W - width, H - height, E - Young's modulus, ρ - density, and x_{ij} - excitation/response position. Highlighted x_{ij} correspond to those of the coupling interfaces, c_1 and c_2	182
7.3	Assembly details for experimental case study.	188
8.1	Summary of details on the construction of experimental assemblies. .	220

AUTHOR PUBLICATIONS

First Author

- Meggitt, J. W. R., Moorhouse, A. T. (2017). The in-situ decoupling of resiliently coupled sub-structures. In ICSV 2017. London.
- Meggitt, J. W. R., Elliott, A. S., Moorhouse, A. T., Banwell, G., Hopper, H., & Lamb, J. (2016). In-situ characterisation of ducted sources of airborne sound. In Internoise 2016. Hamburg.
- Meggitt, J. W. R., Elliott, A. S., & Moorhouse, A. T. (2016). Virtual assemblies and their use in the prediction of vibro-acoustic responses. In Proceedings of the Institute of Acoustics. Warwickshire.
- Meggitt, J. W. R., Elliott, A. S., & Moorhouse, A. T. (2015). In-situ determination of dynamic stiffness for resilient elements. In NOVEM: Noise and Vibration - Emerging Methods. Dubrovnik.
- Meggitt, J. W. R., Elliott, A. S., & Moorhouse, A. T. (2015). In-situ determination of dynamic stiffness for resilient elements. *Journal of Mechanical Engineering Science*, 0(0), 1-8.

Second Author

- Banwell, G., Hopper, H., Moorhouse, A. T., Elliott, A. S., & Meggitt, J. W. R. (2015). Methods for auralising sound with tonal components. In ICSV 2016.
- Elliott, A. S., Meggitt, J. W. R., & Moorhouse, A. T. (2015). Blocked forces for the characterisation of structure borne noise. In Internoise 2015 (pp. 5798-5805). San Fransisco.

SYMBOLS

General remarks: Symbols and formulations are by the most part given in the frequency domain, unless otherwise specified. For clarity, explicit frequency dependence notations has been omitted, except where confusion may arise.

Matrix quantities are indicated by bold upper-case font whilst vector quantities are shown in bold lower-case. Individual matrix and vector elements are shown in standard typeface and their position indicated by subscripts ij and i , respectively.

Symbol definitions are tabulated below. Symbols used only in passing are not included.

Roman Capitals:

Y	Mobility
Y_{ij}	Mobility element
Z	Impedance
K	Dynamic stiffness
T	Generalised transmissibility
H	Vibro-acoustic transfer function
B	Finite difference transformation
L	Boolean localisation

Greek Capitals

Δ	Finite difference spacing
----------	---------------------------

Lower-case Greek letters

ω	Angular frequency
α, β, γ	Rotational Cartesian coordinates
\angle	Phase angle
τ	Torque

Lower-case Roman letters

v	Velocity
v_i	Velocity element
x	Displacement
f	Force
$\bar{\mathbf{f}}$	Blocked force
p	Sound pressure
x, y, z	Cartesian coordinates
i	Imaginary unit

Accents and other symbols

$ x $	Magnitude
$x(t)$	Time domain signals
\tilde{x}	Finite difference approximation
\acute{x}	Operational quantity
\dot{x}	Derivative
\hat{x}	Time averaged

FOREWORD

A large proportion of the work presented in this Thesis was inspired by the research undertaken as part of an externally funded project I was lucky enough to work on. This project, entitled 'Characterisation of vibration sources and isolators for structure-borne noise', ran in collaboration with the University of Liverpool, The Boeing Company, LORD and ITT Enidine.

As this project came to an end, so did my Masters by research programme. It was only with securing additional funding through the Innovate UK funded project 'Towards zero prototyping' that I was able to transfer onto the PhD programme that has resulted in this Thesis. The 'Towards zero prototyping' project ran in collaboration with the high technology company Dyson and, although none of the work carried out has made it directly into this Thesis, it was an incredibly rewarding project and has certainly helped shape this piece of work.

For Dot.

**PART I. INTRODUCTION AND
LITERATURE REVIEW**

INTRODUCTION

This introductory Chapter will outline the context behind the work presented in this Thesis and introduce the ‘Virtual Acoustic Prototype’ (VAP) concept. Following this the topics, aims and objectives of this Thesis will be discussed, and lastly, its structure outlined.

CONTENTS

1.1	Research Context and the VAP Approach	2
1.2	Thesis Topics, Aims and Objectives	7
1.3	Thesis Outline	8

1.1 RESEARCH CONTEXT AND THE VAP APPROACH

A drive towards leaner engineering has seen the use of physical prototypes become a limiting factor in both new product development (NPD) and the continual development of existing products. Consequently, alternative prototyping methods are of interest. With their ability to reduce cost, accelerate time to market, and optimize products to higher levels of performance and reliability, virtual prototyping methods are considered the most suitable alternative, particularly with regards to the assessment of vibro-acoustic performance. Garcia et al.[1] define a *virtual prototype* as “A computer-based simulation of a system or subsystem with a degree of functional realism comparable to a physical prototype” and furthermore the process of *virtual prototyping* as “The process of using a virtual prototype, in lieu of a physical prototype, for test and evaluation of CE specific characteristics of a candidate design”. It

has been shown that the use of virtual prototyping not only encourages communication between different engineering disciplines during early design stages, but can be used to provide an impressive demonstration that may help ‘sell’ a design or product to higher management [2]. Furthermore, with previous research showing that 70% - 80% of a final product’s quality and 70+% of its entire life-cycle cost are determined in the product design phase, an efficient design process can offer one of the single greatest opportunities for cost reduction [3, 4]. Providing such an efficiency may be considered the primary advantage of any virtual prototyping method.

Methods for virtual prototyping with respect to visual design and engineering (i.e. CAD and CAE) have been around for many decades and as such are particularly well developed, as demonstrated by the plethora of available 3D drawing packages, etc. Extending the virtual prototype concept to the realms of acoustics one arrives at the aptly named *virtual acoustic prototype* (VAP), defined by Moorhouse [5] as “...a computer representation of a machine, e.g. a washing machine, fridge, lawnmower etc., such that its sound can be heard without it necessarily having to exist as a physical machine”. Outlined more explicitly, the VAP concept involves the construction of a virtual assembly from the properties of its constituent components in such a way that best represents the physical workings and/or acoustic ‘appearance’ of the real machine and, furthermore, can be used to produce auralisations of said machine. Here, the term ‘auralisation’ may be defined as, “the creation and subsequent presentation of audible sound files generated from numerical (simulated, measured, or synthesized) data”. With the ever growing importance of product sound quality [6], methods for accurately assessing the subjective response to a design change is of particular interest and is the perfect example of a VAP application. Unfortunately, the field of virtual acoustic prototyping is far less advanced than its visual counterparts, owed in part to the often complex nature of vibro-acoustic problems, not to mention the remarkable sophistication of the human ear.

With regards to their vibro-acoustic properties, the components of an assembly may be described as either ‘active’, or ‘passive’, depending upon their behaviour. An active component is one that generates vibro-acoustic disturbances, e.g. pumps, motors, and other sources, whilst a passive component simply transmits or radiates said disturbances (and in doing so affect their frequency content) e.g. resilient elements, housings, etc. Both active and passive components may be described in

part by their appropriate frequency response functions (FRFs).¹ However, an active component requires a secondary descriptor in order to account for its operational activity. For now, this may be referred to generally as a source strength (SS). Depending upon the nature of the source mechanism (i.e. air-borne, structure-borne, etc.) and the medium of the target response (i.e. pressure at listening position, structural velocity at remote assembly position, etc...), the FRFs and SSs may be based on different physical quantities (i.e force, pressure, velocity, etc.).

The successful implementation of a VAP requires the properties of both component types to be determined and handled correctly. This statement leads onto one of the most important concepts in virtual acoustic prototyping, that of *independent characterisation*. In order to allow for the coupling and exchange of both active and passive components within a general VAP framework, the individual components must be characterised independently from the remainder of the assembly, i.e. in such a way that is invariant of any acoustic or structural loading, and thus provides an intrinsic property of that component.

Although numerical methods such as finite element analysis (FEA) are able to predict, with some accuracy, the independent passive properties of a simple assembly components, the reality is somewhat more complicated. State-of-the-art FEA methods, although powerful, currently lack the ability to reliably model the complex behaviour of source activity, i.e. the noise generating mechanisms within an active component. Consequently, the adoption of any VAP methodology will require some element of experimental work, at least for the foreseeable future.

Whilst attempts have been made at establishing an experimentally based VAP framework [7], a lack of measurement protocols and clear guidelines has seen its adoption within industry hindered. Similar approaches have however been adopted within the automotive industry under a variety of names [8–11]. These methods tend to be based on some variant of the well established diagnostic method, transfer path analysis (TPA) [12]. However, with a lack of independent component characterisation (discussed further in Section 2.2) the resulting models are generally limited in application, often requiring assembly modifications (i.e. interchange or installation of additional components) to be handled in an artificial way that bears limited resemblance to the physics involved.

¹An FRF is a frequency domain representation of the input/output relation for a given system (see Section 2.1). Alternative methods are available in the modal, state-space, and physical domain, although experimentally, these are seldom used.

A simplistic representation of a general VAP framework is given by Equation 1.1, where having successfully characterised each component independently, the total sound pressure level, p , at a given receiver point, r , is determined from the sum of N source strengths (SS) weighted by their appropriate FRFs.

$$p_r(\omega) = \sum_{i=1}^N \text{FRF}_{ri}(\omega) \text{SS}_i(\omega) \quad (1.1)$$

Here, the FRF relating an operational source strength (SS_i) to the target quantity (p_r), may itself be some combination of ‘sub-FRFs’, each of which describes the behaviour of a sub-component in the transfer path. Consider the automotive example of an engine mounted in a car. The engine is supported by a number of resilient mounts, these are in turn coupled to the sub-frame, which is in turn coupled to the coachwork, which radiates into the cabin. The assembly FRF is a combination of the sub-component FRFs of the engine, resilient supports, sub-frame, coachwork, and lastly the vibro-acoustic FRF into the cabin. This concept can be visualised more generally in Figure 1.1 where a source sub-component (**S**) containing some operational activity (**O**), is coupled by some resilient support (**I**) to a receiver sub-component (**R**), which is itself coupled to a compartment (**C**), in which the target position (**r**) is located.

Whilst the prediction of an operational response, as in Equation 1.1, is based on the classic forward problem, whereby one has knowledge of an initial condition or ‘cause’ (e.g. a source strength), alongside some propagation model (e.g. an FRF), this Thesis is largely concerned with the reverse procedure, namely, the inverse problem. Inverse problems typically concern the determination of some quantity that may not be observed directly, from some other observable quantity (i.e. determining a cause from an observed effect). Such approaches are often applied in the determination of both active and passive component properties, that is, for determining the unknown cause of a given disturbance, or the properties of the propagating medium. Unfortunately, inverse problems are typically ill-posed and highly sensitive to experimental error. A process referred to as regularisation is often employed as a means of compensating for this. With the methods introduced though this Thesis being largely based on inverse procedures, for completeness, a more thorough discussion on the concept of regularisation is presented in Appendix A.

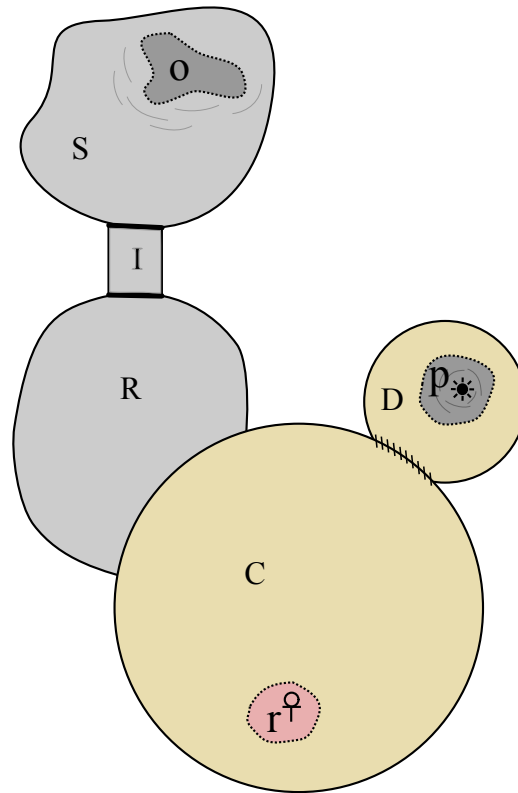


Figure 1.1: Diagrammatic representation of a general VAP problem.

The main challenge in the construction of a VAP may be outlined as; the independent characterisation of both the appropriate FRFs (or sub-FRFs) and source strengths that make up a given assembly. Once the pressure level at a given receiver location is determined, as per Equation 1.1, an auralisation may be produced and presented to a listener for subjective evaluation, or as part of some objective assessment, i.e. sound quality metrics [8].

To summarise, the construction of a VAP requires the completion of the following:

- 1 Independent characterisation of the sub-components, including both active and passive properties.
- 2 Measurement and/or prediction of the coupled assembly's passive properties.
- 3 Prediction of the coupled assembly's operational response.
- 4 Auralisation of the operational response.

1.2 THESIS TOPICS, AIMS AND OBJECTIVES

Over the last four decades considerable work has been undertaken in the field of vibro-acoustic characterisation, however, there still exist significant gaps in the literature that impede the further development of VAPs, among other experimentally based prediction methodologies. Of these gaps, it is arguably the independent characterisation of assembly sub-structures that presents the largest hurdle. Although promising steps have been taken with regards to the determination of a suitable source strength quantity, i.e. via the in-situ blocked force approach [13] (see discussion in Section 2.2), methods for determining the appropriate passive properties of source, receiver and coupling sub-structures are less well developed. One of the largest hurdles faced is the characterisation of such quantities whilst the components are under representative loading and mounting conditions. The sensitivity of structural components to such conditions may lead to erroneous VAP predictions if the intended installation conditions differ from those of the characterisation. Such discrepancies may be avoided by use of in-situ measurement methods. That is, characterisation methods that do not require the structural components to be removed from their intended installation. That said, there exists very little literature concerning the in-situ passive characterisation of source, receiver or coupling sub-structures. It is only with reliable methods for the characterisation of such components that we can begin to construct VAPs in such a way that their true capabilities may be exploited.

With the above in mind, the primary aim of this Thesis may be stated as follows; *to provide a comprehensive set of methods that allow for the construction of a virtual acoustic prototype (VAP) from measurements made in-situ.* This aim will be achieved through the completion of the following objectives:

- 1** Develop a general method for the in-situ characterisation of resilient coupling elements.
 - The method will be extended via a number of state-of-the-art experimental methods so as to provide greater flexibility.
 - Validations will be provided through experimental and numerical studies.
- 2** Develop an in-situ method for independently characterising the passive properties of resiliently coupled source and receiver sub-structures.

- The method will make use of the in-situ characterisation approach and its associated extensions.
 - The decoupling procedure will be validated through a number of experimental studies.
- 3** Introduce the in-situ blocked force approach as an independent characterisation for the active component of a source sub-structure.
- Discuss methods for assessing the uncertainties involved in the blocked force characterisation and subsequent prediction.
 - Provide an experimental demonstration of the above uncertainty measures.
- 4** Bring together the above methodologies and construct a VAP.
- Outline an experimental dynamic sub-structuring procedure.
 - Carry out an experimental case study.

1.3 THESIS OUTLINE

Following the introductory discussion that is **Chapter 1**, the remainder of this Thesis will be structured as follows. In **Chapter 2** we will begin with an overview of the literature pertinent to the aims of this Thesis. In doing so the current state-of-art in the fields of source characterisation, isolator characterisation and dynamic sub-structuring will be outlined. Following this, **Chapter 3** will cover the development of an in-situ characterisation method for resilient elements. In **Chapter 4** the in-situ method is extended via a number of state-of-the-art experimental methods, allowing for increased flexibility with regards to its application. In **Chapter 5** the in-situ characterisation approach will be used to mathematically de-couple resiliently coupled source and receiver sub-structures, so as to determine their independent passive properties. **Chapter 6** will introduce the blocked force as a method for independently characterising the activity of structural sources. In **Chapter 7**, the methods presented through Chapters 3-6 are applied in the characterisation and prediction of an experimental case study. Lastly, in **Chapter 8** we will draw some concluding remarks and discuss suitable areas for future work.

LITERATURE

In this Chapter a brief overview is given of the literature pertinent to the context and aims of this Thesis. Topics of particular relevance are those of; independent source characterisation, dynamic sub-structuring and isolator characterisation. The following sections will aim to; introduce the reader to these concepts, outline their development and ultimately detail their current state-of-art.

CONTENTS

2.1	Definitions	9
2.2	Source Characterisation	13
2.3	Dynamic Sub-structuring	19
2.4	Isolator Characterisation	22

2.1 DEFINITIONS

Before reviewing the literature, the important concepts of mobility and impedance are defined. (The reader is referred to [14] for a more detailed discussion.)

2.1.1 MOBILITY

Mobility is defined by,

$$\mathbf{v} = \mathbf{Y}\mathbf{f} \tag{2.1}$$

where $\mathbf{v} \in \mathbb{C}^n$ is an n dimensional vector of resultant velocities, $\mathbf{f} \in \mathbb{C}^m$ is an m dimensional vector of applied forces, and $\mathbf{Y} \in \mathbb{C}^{n \times m}$ is the $n \times m$ dimensional mobility matrix that relates the two. For collocated excitation and response degrees

of freedom (DoFs)¹ ($n = m$), \mathbf{Y} is a square symmetric matrix that satisfies the principle of reciprocity, i.e. $\mathbf{Y} = \mathbf{Y}^T$. The measurement of this matrix is done in such a way that (1) forces are applied one at a time to each point of interest; (2) the forces at all other points are constrained to zero (the structure is allowed to respond freely); (3) the individual elements of the matrix are measured as the complex ratio of velocity response to the single excitation force, as shown in Equation 2.2.

$$Y_{i,j} = \left. \frac{v_i}{f_j} \right|_{f_{i \neq j} = 0} \quad (2.2)$$

In experimental vibro-acoustics mechanical systems are more than often represented by their mobility matrices. The lack of physical constraints (i.e. forces are constrained to zero) makes it is straightforward to achieve the unconstrained conditions required as per their definition. To this end, internationally recognised standard measurement procedures have been made available [15–17] for their measurement.

2.1.2 IMPEDANCE

Impedance is defined by,

$$\mathbf{f} = \mathbf{Z}\mathbf{v} \quad (2.3)$$

where $\mathbf{f} \in \mathbb{C}^n$ is an n dimensional vector of resultant forces, $\mathbf{v} \in \mathbb{C}^m$ is an m dimensional vector of applied velocities and $\mathbf{Z} \in \mathbb{C}^{n \times m}$ is the $n \times m$ dimensional impedance matrix that relates the two. For collocated excitation and response DoFs ($n = m$), \mathbf{Z} is a square symmetric matrix that satisfies the principle of reciprocity, i.e. $\mathbf{Z} = \mathbf{Z}^T$. The measurement of this matrix is done in such a way that (1) the velocities are applied one at a time to each point of interest; (2) the velocities at all other points are constrained to zero (the structure is *not* allowed to respond freely); (3) the individual elements of the matrix are measured as the complex ratio of force response to the single excitation velocity, as shown in Equation 2.4.

$$Z_{i,j} = \left. \frac{f_i}{v_j} \right|_{v_{i \neq j} = 0} \quad (2.4)$$

It is perhaps useful to note that due to the physically constrained nature of impedance, the force at all positional-DoFs (see Section 2.1.3) other than that of the velocity excitation, f_i where $i \neq j$, is the blocked force, \bar{f} , required to constrain the velocity

¹See Section 2.1.3 for a more details discussion on DoFs.

at these points to zero.

$$\bar{f}_i = Z_{i,j} v_j |_{i \neq j} \quad (2.5)$$

The concepts of mobility and impedance may readily be extended to other commonly used kinematic variables, including displacement x and acceleration a . Shown in Table 2.1 are the definitions and relations for a number of commonly used FRF types.

	Name	Symbol	Definition	C	Y	A
	Compliance	C_{ij}	$x_i/f_j _{f_{j \neq i}=0}$	1	$1/i\omega$	$-1/\omega^2$
	Mobility	Y_{ij}	$v_i/f_j _{f_{j \neq i}=0}$	$i\omega$	1	$1/i\omega$
	Accelerance	A_{ij}	$a_i/f_j _{f_{j \neq i}=0}$	$-\omega^2$	$i\omega$	1
	Name	Symbol	Definition	K	Z	M_{eff}
<i>Inverse</i>	Dynamic stiffness	K_{ij}	$f_i/x_j _{x_{j \neq i}=0}$	1	$i\omega$	$-\omega^2$
	Mechanical impedance	Z_{ij}	$f_i/v_j _{v_{j \neq i}=0}$	$1/i\omega$	1	$i\omega$
	Effective mass	\hat{M}_{ij}	$f_i/a_j _{a_{j \neq i}=0}$	$-1/\omega^2$	$1/i\omega$	1

Table 2.1: A list of commonly used frequency response functions along with their relations. E.g. $K = i\omega Z = -\omega^2 \hat{M}$ or $i\omega C = Y = A/i\omega$

2.1.3 DEGREES OF FREEDOM & LTI SYSTEMS

Further to the concepts of mobility and impedance, the notion of degrees-of-freedom (DoFs) requires acknowledged. The DoF of a system describes the number of independent parameters required to uniquely determine its dynamics.

A rigid body permitted to move in 3 dimensions has 6 DoF. In a Cartesian coordinate system these correspond to translations in x , y , and z along with their axial rotations, α , β , and γ , respectively. For mechanical systems translational DoFs are often represented in terms of force, f , and velocity, v , whilst rotational DoFs are described in terms of moment (or torque), τ , and angular velocity, ψ , as shown in Figure 2.1.²

For a rigid body the resultant velocity (or angular velocity) in any given DoF may be represented as a linear combination of all applied forces (and moments), weighted

²The conventional notation for angular velocity, ω , has been replaced with ψ so as to avoid confusion with the angular frequency $\omega = 2\pi f$.

by their appropriate mobilities. That is,

$$v_i = \sum_{j=1}^3 Y_{i,j} f_j + \sum_{k=4}^6 Y_{i,k} \tau_{k-3}. \quad (2.6)$$

The above may be expressed in a matrix notation as,

$$\begin{pmatrix} v_x \\ v_y \\ v_z \\ \psi_\alpha \\ \psi_\beta \\ \psi_\gamma \end{pmatrix} = \begin{bmatrix} Y_{xx} & Y_{xy} & Y_{xz} & Y_{x\alpha} & Y_{x\beta} & Y_{x\gamma} \\ Y_{yx} & Y_{yy} & Y_{yz} & Y_{y\alpha} & Y_{y\beta} & Y_{y\gamma} \\ Y_{zx} & Y_{zy} & Y_{zz} & Y_{z\alpha} & Y_{z\beta} & Y_{z\gamma} \\ Y_{\alpha x} & Y_{\alpha y} & Y_{\alpha z} & Y_{\alpha\alpha} & Y_{\alpha\beta} & Y_{\alpha\gamma} \\ Y_{\beta x} & Y_{\beta y} & Y_{\beta z} & Y_{\beta\alpha} & Y_{\beta\beta} & Y_{\beta\gamma} \\ Y_{\gamma x} & Y_{\gamma y} & Y_{\gamma z} & Y_{\gamma\alpha} & Y_{\gamma\beta} & Y_{\gamma\gamma} \end{bmatrix} \begin{pmatrix} f_x \\ f_y \\ f_z \\ \tau_\alpha \\ \tau_\beta \\ \tau_\gamma \end{pmatrix} \quad (2.7)$$

the compact form of which is given in Equation 2.1, where $\mathbf{v} = [v_x, v_y, v_z, \psi_\alpha, \psi_\beta, \psi_\gamma]^T$ is the resultant velocity vector, and $\mathbf{f} = [f_x, f_y, f_z, \tau_\alpha, \tau_\beta, \tau_\gamma]^T$ is the applied force vector, each containing both translational and rotational DoFs.

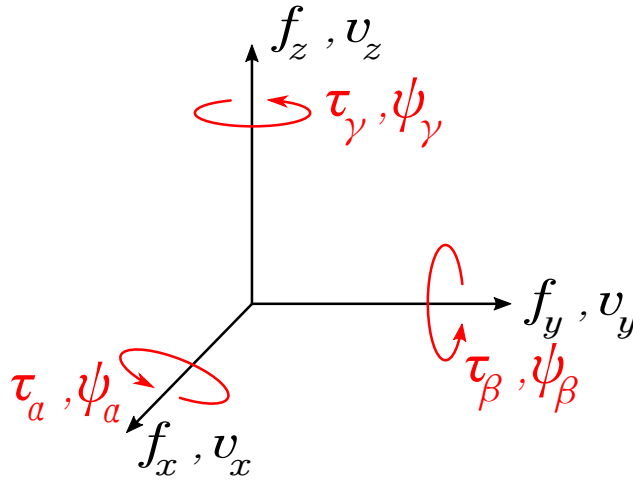


Figure 2.1: Cartesian co-ordinate system and notation of forces and velocities.

A structure permitting deformation has in theory an infinite number of DoFs. An approximation of the dynamics of a continuous structure may, however, be realised by limiting interest to a finite number of N points. The number of DoFs required to completely determine this reduced dynamic system is $6N$. The resulting matrix

equation may be written in block form as,

$$\begin{pmatrix} \mathbf{v}_1 \\ \mathbf{v}_2 \\ \vdots \\ \mathbf{v}_N \end{pmatrix} = \begin{bmatrix} \mathbf{Y}_{11} & \mathbf{Y}_{12} & \cdots & \mathbf{Y}_{1N} \\ \mathbf{Y}_{21} & \mathbf{Y}_{22} & \cdots & \mathbf{Y}_{2N} \\ \vdots & \vdots & \ddots & \vdots \\ \mathbf{Y}_{N1} & \mathbf{Y}_{N2} & \cdots & \mathbf{Y}_{NN} \end{bmatrix} \begin{pmatrix} \mathbf{f}_1 \\ \mathbf{f}_2 \\ \vdots \\ \mathbf{f}_N \end{pmatrix} \quad (2.8)$$

where entries \mathbf{v}_N , \mathbf{f}_N and \mathbf{Y}_{NN} are themselves block vectors and matrices.

At this point it is perhaps useful to make the distinction between positional and coordinate based DoFs. The former refers to the spatial position on a given structure, whilst the latter refers to the coordinate in which a given variable is acting, i.e. translational or rotational. As such, each positional-DoF is made up of 6 coordinate-DoFs. In Equation 2.8 \mathbf{Y}_{NN} may be considered the point mobility of the N th positional-DoF, whilst its constituent elements, shown in Equation 2.7, correspond to coordinate-DoFs at N . The number of individual mobilities required to determine the state of a multi-DoF structure is consequently proportional to the square of the number of DoFs considered. For a linear time invariant (LTI) system the principle of reciprocity may be used to further reduce the number of measurements required [18]. The principle of reciprocity states that the input-output relation between any two DoFs remains unchanged if their force/response roles are interchanged, i.e. $Y_{i,j} = Y_{j,i}^T$. As such, the number of individually required mobilities is only linearly proportional to the number of points. Under certain circumstances further reductions may be made by considering geometric and coupling effects whilst neglecting non-contributing DoFs.

It is important to state that the work considered in this Thesis concerns only linear and time invariant systems, that is, those systems whose outputs may be regarded as weighted linear combinations of their inputs, and furthermore, those whose outputs do not depend upon the time at which the inputs are applied.

2.2 SOURCE CHARACTERISATION

With the continued introduction of stringent noise abatement polices [19–22], alongside the growing importance of product sound quality [23], the ability to accurately predict the acoustic behaviour of an assembly (be-it a vehicle, a washing machine or a

desktop fan) is of interest. Key in the development of such prediction methodology is the successful characterisation of the contributing noise sources (for example; gearboxes, motors, compressors, etc.).

In the characterisation of an acoustic source (air-borne or structure-borne) the fundamental aim may be stated as follows; to determine a physical set of quantities that describe both the active and passive behaviour of the source in such a way that they may later be used to predict an operational response in some other scenario.

To aid the development of an appropriate method the International Organization for Standardization (ISO), Technical Committee on Acoustics TC43, Working Group outlined the following set of requirements that a suitable characterisation method should allow [24]:

- 1) Comparison of one source with another.
- 2) Comparison of sources with set limits.
- 3) Prediction of sound levels when installed.
- 4) Quantification of improvement in new low noise designs.

For many years the general consensus had been that the above were best achieved through a single valued frequency dependent quantity [25], for example sound power. However, as will be discussed shortly, such methods are generally unsuitable for the characterisation of structure-borne sources.

Depending upon the characterisation method employed, determined quantities may, or may not, be independent properties of the source. An independent quantity may be defined as one whose behaviour is an intrinsic property of the sub-structure under investigation, and therefore unaffected by any modifications made to its surroundings. An independent characterisation is generally preferable in that it not only fulfils above objectives, but satisfies the transferability requirements of dynamic sub-structuring (and therefore facilitates the construction of VAPs).

Broadly speaking, characterisation methods may be categorized as either direct, or indirect. Direct methods concern the direct measurement of desired quantities, whilst indirect methods infer the sought after quantities from others that are more easily, or accurately, measured (often using inverse methods).

An acoustic source may be considered either air-borne (or more generally fluid-borne) or structure-borne depending upon the nature of the noise generating mechanisms, or the level at which the practitioner considers the problem. The characterisation of an air-borne source is more than often a simple procedure, owed in part to the weak coupling between the source and receiver sub-structures (i.e. the surrounding environment).³ As such, a number of well established sound power based measurement procedures have been developed, standardised and subsequently adopted with industry [26–28]. Unfortunately, procedures for the characterisation of structural sources are less well developed, not because they are of less significance, but due to their greater complexity. The strong mechanical coupling between source and receiver sub-structures results in the contamination of any directly measurable source quantity by the coupled receiver sub-structure. As such, the adoption of standard air-borne measurement procedures for structural source characterisation is inappropriate. Consequently, the characterisation of structural sources has been a topic of great interest for many decades and a number of alternative methods have been proposed, including; the free velocity [29], operational force [30], blocked force [13], the source descriptor [31], the characteristic power, mirror power and maximum available power [32] and pseudo forces [33], to name but a few.

Further clarifying its requirement, Mondot and Peterson [31] proposed a potential independent source characterisation, the source descriptor and coupling function. It was shown that an expression for complex power between source and receiver sub-structures could be manipulated in such a way that yields two coefficients; a source descriptor and a coupling function. The source descriptor is an independent source property that is proportional to power and involves both its active and passive properties. The source descriptor may be interpreted as the source’s ability to deliver power, whilst its product with the coupling function, a term proportional to the ratio of the source and receiver mobilities, determines the active power transmitted from the source to receiver. The original single contact point formulation was extended to multiple-contacts through the application of both ‘effective mobilities’ [34–36] and ‘interface mobilities’ [37]. In the former, the resulting multi-point source descriptor became a function of force distribution and therefore dependent upon the receiver and no longer an independent property of the source. An independence retaining generalization of the source descriptor to multi-point connected systems was later presented by Moorhouse [32] and termed the ‘characteristic power’. Defined as the dot product of the blocked force and free velocity vectors, the characteristic

³In highly resonant environments more sophisticated methods may be required.

power provides an equivalent single point model for multi-point connected structures. Unlike its single case counterpart, the determination of characteristic power requires the inversion of a measured source mobility matrix and is therefore susceptible to inversion error and ill-conditioning. Also presented by Moorhouse [32] were the concepts of mirror power and maximum available power, describing the power delivered by a vibrating source into a passive receiver structure whose properties are the mirror and complex conjugate of the source, respectively. With both the source descriptor and its generalization, the characteristic power, being defined on a power basis, translational and rotational contributions are dimensionally compatible and can therefore be collapsed into a single value. The characteristic power has since been introduced as part of the European standard EN 12354-5 for the *prediction of structure-borne sound levels from building equipment* [38].

Alternative power based methods, where the source is coupled to a standardized receiver structure have also been investigated, most notably the reception plate method [25, 39, 40]. Analogous to the reverberation method for the measurement of air-borne sound power, the reception plate method determines the power transmitted into a plate from the plate's loss factor, averaged velocity, mass per unit area, and surface area. Idealizations such as velocity and force sources hold for light (source mobility much less than plate mobility) and heavy structures, respectively. However, the characterisation is not independent and does not usually allow for the transfer of data, other than for approximate predictions in specific environments. Regardless of its limitations, the reception plate has been introduced as part of the European standard EN 15657-1 for the *characterisation of structure-borne sound sources under laboratory conditions* [41].

Currently, the only *internationally* recognised standard measurement method for structural source characterisation is ISO 9611 [29], where a direct procedure for measuring the velocity of resiliently mounted machinery is described, from which a free velocity may be approximated. The free velocity describes the active component of a source in terms of the motion of its contact interface whilst uncoupled and freely suspended. The free velocity is therefore an independent property of the source. To provide a complete source characterisation the free velocity must be accompanied by some measure of the source's passive properties, i.e. its free mobility. Although the standard provides a simple measurement procedure it is seldom used in practise. Its lack of uptake may be put down to the practicality of achieving the 'freely suspended' mounting condition. Additionally, the potential variation in mounting conditions

between characterisation and installation may well pose problems. Furthermore, unlike power based methods, the dimensions of translational and rotational components are not compatible and therefore the free velocity can not be collapsed to a single frequency dependent variable. A practical application of the free velocity in the prediction of structure-borne noise emission from resiliently mounted machinery was demonstrated by Moorhouse and Gibbs [42, 43]. Assumptions based on the coupling and phase between contact DoFs allowed for a multi-contact theory to be established. Unfortunately the simplifying assumptions led to a reduction in applicability to a narrow range of cases. Recent work by Moorhouse et al. [44] has shown that the free velocity may be determined from in-situ operational measurements via the application of the round trip [45] and in-situ blocked force [13] relations. In doing so the free velocity may be determined from measurements conducted under representative mounting conditions, partly avoiding the need to freely suspend the source. Through a similar application of the round trip and in-situ blocked force relations it was also shown that the aforementioned characteristic power [32] may also be determined partly through in-situ operational measurements.

Perhaps the most common approach to source characterisation, particularly within the automotive and aerospace sector [30, 46] is the operational force method, also referred to as indirect force determination [47]. The operational force method determines the forces acting on a receiver structure through an inverse approach whereby a measured receiver mobility matrix is inverted and subsequently multiplied by an operational velocity vector. Unfortunately, this does require the source and receiver sub-structures to be decoupled for the FRF measurement. In contrast to the direct measurement of free velocity, the operation force method does allow for operational measurements to be made in-situ, and thus avoids discrepancies between mounting conditions. Sadly, as with the characteristic power, the inverse approach is susceptible to ill conditioning. Fortunately, however, with the operational force method forming the basis of the well established diagnostic method ‘transfer path analysis’ (TPA) [12], much work has been focused on the minimization of this error, with particular emphasis on regularisation techniques, see [48, 49].⁴ Although well adopted within industry and having become more or less standard practice, the operational forces obtained are not independent properties of the source and can not transferred between assemblies.

⁴An overview of the general concept of regularisation with regards to force identification may be found in Appendix A.

Janssens and Verheij proposed an alternative in-situ approach, referred to as the pseudo-force method, whereby the internal excitation of a source is reproduced by a set of fictitious forces on its outer surface [33]. Unlike the operational force method, pseudo forces may be determined using entirely in-situ measurements, thus allowing for diagnostic methods (similar to TPA) to be carried out without having to dismantle the assembly. The pseudo force method has since been used to compare source strengths of different machines [50], and conduct diagnostic tests on ships [51, 52]. A similar method was presented by Ohlrich, instead termed the equivalent force method [53, 54]. Unfortunately, the forces determined using these methods have little physical meaning, and their transferability is limited. Furthermore, although they may produce equivalent response fields, it is difficult to directly compare the pseudo-forces of two different sources due to their dependence upon measurement position.

In stark contrast to the free velocity, the blocked force offers an alternative independent source characterisation [55]. Defined as the force required to completely restrain a contact interface, the blocked force, like the free velocity, suffers from practicality issues. Unlike the free velocity, where the source is required to be freely suspended, the blocked force requires the source to be coupled to an immovable object. This is clearly not achievable, however, an approximation may be obtained over a limited frequency range, at the cost of a large, impractical test rig. Ignoring the practical limitations, the blocked force does, in theory, like the free velocity, provide an independent measure of a sources activity. Recent work by Moorhouse et al. [13] has shown that blocked force may be determined in-situ using an inverse method similar to that the operational force method. A similar conclusion was arrived at independently by D’Klerk [56]. The blocked force approach of Moorhouse and De’Klerk [13, 56] allows for a structural source to be independently characterised whilst *in-situ*, and therefore under representative mounting conditions, thus combining the advantages of both the free velocity and operational force methodologies. Furthermore, unlike the pseudo-force approach of Janssens and Verheij [33], blocked forces have significant physical meaning, and moreover, being defined at the source-receiver interface, they may be readily used in the comparison of different sources. Since its realisation, the in-situ blocked force approach has received much attention, leading to a number of publications [57–59], particularly within the automotive [60], aerospace [61, 62] and domestic product [63] sectors. Its popularity has since led to the development of a blocked force based TPA procedure, referred to in the literature as ‘in-situ TPA’ [12, 64, 65]. In-situ TPA allows for an entirely in-situ measurement

based diagnostic procedure which, unlike the pseudo force methodology, pertains to quantities of physical meaning. It is perhaps of interest to note that pseudo forces, when determined at a source-receiver contact interface, are in fact identical to the blocked forces, unfortunately however, Jannsens and Verheij do not appear to have been aware of this at the time. The in-situ blocked force approach may additionally be considered a generalization of the single point synthesised force presented by Lai [66], and further realised as a consequence of an equivalent field representation as shown by Bobrovnikskii [67].

As the field currently stands, the in-situ blocked force method appears to offer the most suitable approach to independently characterising the activity of structural sources. To this end, the method is currently in the process of standardisation by the International Organisation for Standardisation, Technical Committee ISO TC43/ SC1/ WG57.

2.3 DYNAMIC SUB-STRUCTURING

Often when predicting structure-borne sound and vibration it is convenient to model an assembly in such a way that the FRFs of the individual sub-structures are obtained independently, then coupled together mathematically. This method will be referred to here as ‘dynamic sub-structuring’ (DSS), although may be found in the literature under a number of names, including; sub-structure synthesis, structural synthesis, sub-structure coupling, among others. The DSS concept offers two distinct advantages over the direct measurement of FRFs. Firstly, it enables components to be interchanged with ease and their influence upon the global dynamic behaviour of an assembly assessed quantitatively. Secondly, the integration of analytical and/or numerical data with experimentally determined FRFs becomes feasible. Both of these offer clear advantages, particularly within the field of virtual acoustic prototyping. The general concept of DSS may be formulated in any of the 4 domains one typically encounters in structural dynamics and vibration; physical (where systems are characterised by their mass, stiffness and damping matrices), state-space (where systems are described in terms of their state-variables), modal (where systems are characterised by their eigenvalue/vector and modal damping matrices) or FRF (where systems are characterised by their frequency response function matrices). The application of a given domain formulation is generally dependent upon

whether the work undertaken is of a theoretical or experimental nature. Outlined in Table 2.2 are the relative occurrences of domain types for theoretical and experimental work. With the work of this Thesis concerned with the development of experimental methodologies, it is the FRF based formulations that are of particular interest here.

	Physical	State-space	Modal	FRF
Theoretical	Always	Often	Typical	Unusual
Experimental	Never	Unusual	Typical	Always

Table 2.2: Dynamic sub-structuring domains and their use in theoretical and experimental studies. Table adapted from [68].

Historically, the roots of DSS may be traced to the field of domain decomposition, where the desire to analyse complex problems was addressed by first considering the solutions to the simpler problems of its constituent components, and then determining an interface solution [69]. Perhaps the earliest example of domain decomposition was the iterative process proposed by Schwarz [70] in 1890, whereby the existence of a solution to a domain consisting of a coupled circle and square was proven. Fast forward 70 years and the concepts of domain decomposition had begun to make their way into the field of structural dynamics. These early DSS ideas, largely known as ‘component-mode synthesis’, were mostly developed as reduction techniques and likely fuelled by the papers of Hurty [71, 72]. It wasn’t until the 1980’s however, with advancements in multi-channel data acquisition, that these methods became attractive tools to the experimental structural dynamic community. Perhaps the first step towards an FRF based DSS procedure was made by Crowley et al. [73], who proposed the structural modification method ‘SMURF’ (structural modification using experimental frequency response function). However, it was not until a few years later, when Jetmundsen [74] formulated the now classic FRF based sub-structuring method, that experimental DSS began to gain popularity. Since Jetmundsen, a number of alternative approaches have been proposed. Although, with the physics of the problem remaining unchanged these simply go about applying compatibility and equilibrium conditions in a different manner. However, an essential requirement common to all DSS approaches is the independence of the sub-structure FRFs. That is, the FRFs of each sub-structure must be obtained in a transferable manner, an example being their free-interface mobilities.

Generally speaking, a DSS approach may be considered a member of one of two families, depending on whether its formulation considers interface displacements or forces as unknowns. These are referred to as the primal and dual formulations, respectively [75].

Of the DSS methods available, the ‘classical impedance coupling’ approach (also referred to as the basic impedance coupling process [76] or primal impedance formulation [75]) is arguably the most straightforward, both conceptually and in terms of its implementation. The method itself exists within the primal family and can be realised in a number of ways. It is well known that the enforcement of compatibility and equilibrium between single DoF mechanical sub-structures results in a coupled structure whose impedance is equal to the sum of the individual sub-structure impedances. The extension of this concept to multi-DoF systems forms the basis of the classical impedance approach. Its implementation requires the free-interface mobility of each sub-structure to be measured and subsequently inverted. The resulting impedance matrices are then summed accordingly before being inverted back to mobility form (usually required). It is this approach that is most often used in the assembly of finite element models. The classical approach requires all DoFs to be included in the inversion process, including those remote from the coupling interface. As such, ill-conditioning is a serious concern, particularly when dealing with large DoF assemblies.. Furthermore, matrix inversions are computationally expensive procedures. The multiple inversions required at each frequency, along with the limited computational power and precision of early computers, meant that more computationally efficient algorithms were required.

Jetmundsen developed [77] and subsequently proposed [74] a generalized DSS methodology that not only provided an efficient synthesis of the coupled assemblies dynamic behaviour from experimental data, but was particularly well-suited for combining experimental and numerical data. The proposed method required only a single matrix inversion, whilst employing graph theory to form the required connections. Unlike the classical approach the single inversion is performed on a matrix containing *only* the coupling DoFs, thus offering the potential for improved conditioning and efficiency. The approach proposed by Jetmundsen has since been reformulated according to the dual domain decomposition method to form what is referred to as the Lagrange Multiplier Frequency Based Sub-structuring (LM FBS) method [78]. The LM FBS approach offers a number advantages over its predecessor; not only

may it be expressed more simply, but only single coupling matrix is required to coupled N sub-structures, unlike Jetmundsen's approach which required $N + 1$.

2.3.1 SUB-STRUCTURE DECOUPLING

In more recent years the DSS concept has been reversed, and instead used in the *de-coupling* of assemblies [79–83]. Referred to here as dynamic sub-structure decoupling (DSSD), the procedure may be used to extract the independent passive property of a given sub-structure (i.e. the target sub-structure) from the measured properties of the coupled assembly and that of the remaining uncoupled sub-structure (i.e the residual sub-structure). Such a procedure offers the distinct advantage that the independent passive property of a given sub-structure may be determined without the need for free suspension, as would normally be required. This is of particular interest in cases where free suspension is simply not possible, for example; in cases where sub-structures are very large and heavy, and resilient mounting becomes impractical (for example the decoupling of train carriages from their bogies [84]), or in cases where sub-structures are very small and lightweight, and resilient mounting does not sufficiently represent a free suspension.

Like DSS, the concept of DSSD is also of relevance to the field of virtual acoustic prototyping. As previously stated, a fundamental requirement of a general VAP framework is that each sub-structure is characterised independently. This includes their passive properties. DSSD potentially offers an alternative means to characterise the passive properties of both source and receiver sub-structures.

2.4 ISOLATOR CHARACTERISATION

The use of resilient elements, i.e. vibration isolators, for the abatement of structure-borne noise and vibration is wide spread throughout many engineering disciplines and their general application well understood. Notable examples include; automobile engine mounts, resilient supports for buildings, resilient mounts/flexible couplings for shipboard machinery and small isolators for domestic products.

A practising engineer is often concerned with assessing, characterising, or predicting the performance of a resilient element. As such, a number of methods have been made available. Perhaps the most well established is that of the transmissibility

ratio. Defined for a single DoF system as the ratio of forces (or velocities) above and below the resilient element, the transmissibility offers an intuitive picture of the problem, providing a clear identification of the regions of amplification and attenuation [55]. Unfortunately, the transmissibility describes the performance of an assembly, not the resilient element itself. As such, it does not provide a transferable quantity, thus limiting its use to assemblies of similar dynamic behaviour. Alternative approaches based on insertion loss [85–87] and transmitted power [88, 89] have also been investigated yet, like the transmissibility, neither provide an independent characterisation of the resilient element. As with the characterisation of structural sources, a preferred quantity should be independent of the assembly in which the element is installed, and by virtue an intrinsic property of the resilient element. Such an independence ensures the transferability of data between assemblies and thus its compatibility with DSS procedures and, consequently, the general VAP framework outlined in Chapter 1.

The preferred quantity, for which the transmission of vibrational energy through a resilient element is described, is the dynamic transfer stiffness [85]. The dynamic transfer stiffness, denoted $\mathbf{K}_{\mathbf{I}_{ij}}$ (or reciprocally by $\mathbf{K}_{\mathbf{I}_{ji}}$), is a frequency dependent quantity that describes the relation between an applied displacement at one side of a mount to the resultant blocked force at the other,

$$\bar{\mathbf{f}}_i = \mathbf{K}_{\mathbf{I}_{ij}} \mathbf{x}_j \Big|_{i \neq j}. \quad (2.9)$$

Determined by the elastic, inertial and damping properties of the element⁵, the dynamic transfer stiffness and can be related to other commonly used FRFs via Table 2.1. Much like a static measure of stiffness, dynamic measures (i.e frequency dependent) often exhibit a sensitivity to static pre-load, dynamic excitation level, temperature and relative humidity [91]. The nature of these non-linearities make the complete characterisation of the resilient element a complicated and involved task. That said, accounting for the effects of temperature and relative humidity are merely experimental hurdles, albeit awkward ones to negotiate.

With each side of an element able to move in 6 coordinate DoFs, the dynamic transfer stiffness is completely (neglecting any non-linearities) described by the 6×6 transfer

⁵At low frequencies only the elastic and damping properties contribute to the global behaviour of the mount. At higher frequencies the inertia of the distributed mass becomes significant and second order resonances occur [90].

stiffness matrix,

$$\mathbf{K}_{\mathbf{I}_{c1c2}} = \begin{bmatrix} K_{I_{x1x2}} & K_{I_{x1y2}} & K_{I_{x1z2}} & K_{I_{x1\alpha2}} & K_{I_{x1\beta2}} & K_{I_{x1\gamma2}} \\ K_{I_{y1x2}} & K_{I_{y1y2}} & K_{I_{y1z2}} & K_{I_{y1\alpha2}} & K_{I_{y1\beta2}} & K_{I_{y1\gamma2}} \\ K_{I_{z1x2}} & K_{I_{z1y2}} & K_{I_{z1z2}} & K_{I_{z1\alpha2}} & K_{I_{z1\beta2}} & K_{I_{z1\gamma2}} \\ K_{I_{\alpha1x2}} & K_{I_{\alpha1y2}} & K_{I_{\alpha1z2}} & K_{I_{\alpha1\alpha2}} & K_{I_{\alpha1\beta2}} & K_{I_{\alpha1\gamma2}} \\ K_{I_{\beta1x2}} & K_{I_{\beta1y2}} & K_{I_{\beta1z2}} & K_{I_{\beta1\alpha2}} & K_{I_{\beta1\beta2}} & K_{I_{\beta1\gamma2}} \\ K_{I_{\gamma1x2}} & K_{I_{\gamma1y2}} & K_{I_{\gamma1z2}} & K_{I_{\gamma1\alpha2}} & K_{I_{\gamma1\beta2}} & K_{I_{\gamma1\gamma2}} \end{bmatrix}, \quad (2.10)$$

where, for example, $K_{I_{z1\beta2}}$ represents the dynamic transfer stiffness relating an angular displacement about the y axes at interface 2, to the resultant translational blocked force in the z direction at interface 1. Subscript I indicates that the marked quantity is a property of the resilient element, not the assembly.

A complete description of the resilient element must also include the dynamic point stiffness matrices, $\mathbf{K}_{\mathbf{I}_{c1c1}}$ and $\mathbf{K}_{\mathbf{I}_{c2c2}}$. Such matrices describe the relationship between applied displacements and resultant forces upon the same side of the mount. The complete dynamic stiffness matrix $\mathbf{K}_{\mathbf{I}}$ is thus given by the 12×12 partitioned matrix,

$$\mathbf{K}_{\mathbf{I}} = \left[\begin{array}{c|c} \mathbf{K}_{\mathbf{I}_{c1c1}} & \mathbf{K}_{\mathbf{I}_{c1c2}} \\ \hline \mathbf{K}_{\mathbf{I}_{c2c1}} & \mathbf{K}_{\mathbf{I}_{c2c2}} \end{array} \right]. \quad (2.11)$$

The dynamic transfer stiffness appears as an integral part of a number of well established experimental methodologies, including; stiffness based TPA [12], the standardised prediction of transmitted structure-borne power [92], among others. Unfortunately however, successful implementation of these methods rely heavily upon the successful determination of an elements dynamic transfer stiffness.

Having established the concept of the dynamic transfer stiffness, let us turn attention to the literature pertinent to its determination.

With their widespread application it is no surprise that a number of methods have been developed for the characterisation of resilient elements. Broadly speaking, these methods may be categorised as either experimental or model based, with the former being further categorised as either direct or indirect. Model based methods, including both analytical and numerical approaches, although offering valuable insight into physical mechanisms, are generally limited in their application due to the highly non-linear nature of resilient elements. A selection of model based approaches may be found in [93–98]. However, with the work of this Thesis concerned with the

development of experimental methodologies, the remainder of this Section will focus on experimental methods only. Like the characterisation of structural sources, experimentally based direct methods are concerned with the *direct* measurement of sought after quantities (i.e. force and displacement), whilst *indirect* methods infer these quantities from those more easily measured.

The classic direct method [99] determines the dynamic transfer stiffness from the *direct* measurement of a receiver side force (by installing load cells between the mount and a rigid blocking foundation) and source side displacement, due to an applied harmonic excitation. More recent adaptations of the method have included the measurement of a receiver side acceleration so as to account for the bias error introduced as a result of the required force distribution plate (to provide a uniform force distribution). Once measured, the dynamic transfer stiffness is simply determined from the ratio of source side displacement to the corrected receiver side force. Similar interpretations of this method have been used by many [43, 88, 100], however, its application is typically limited to low frequencies as a result of assembly resonances [101]. Furthermore, the direct method is typically limited to translational DoFs due to the complications involved in the direct determination of moment forces.

As part of an investigation into the high frequency dynamics of rail fasteners, Thompson and Verheij proposed an indirect method [102], originally developed in the work of Verheij [85], for determining the dynamic transfer stiffness of resilient elements. The method itself requires the resilient mount to be placed between two large blocking masses, the upper of which is excited harmonically whilst the accelerations of both are measured. Knowing the mass of the lower block allows the force to be determined indirectly via Newtons 2nd law, thus providing the required inputs to a dynamic transfer stiffness calculation. With an upper frequency limit determined by the rigid behaviour of the lower mass, Thompson and Verheij were able to determine stiffness values up to 1000Hz (using a lower mass of 1600kg) under a number of pre-loads. These stiffnesses were shown to agree well with comparisons derived from field measurements. Shortly afterwards, Thompson et al. proposed a number of refinements to the method [103]. Taking the dynamic behaviour of the measurement assembly into account by considering the difference in acceleration above and below the mount, whilst accounting for the frequency dependence of the blocking mass, the upper and lower frequency limits of the method were extended. Also presented in [103] was a procedure allowing for separation of in-plane and rotational DoFs. Similar indirect approaches, whereby a blocking mass is used to indirectly determine the

receiver side force, may be found in [104–107], although with the general concept remaining unchanged, these will not be discussed in any further detail.

The direct and indirect methods described above have gone on to form parts 2 and 3 of the International Standard series ISO 10846 for the characterisation of resilient elements [108, 109]. Part 4 of the aforementioned standard demonstrates the application of both the direct and indirect approaches to the characterisation of resilient elements that are not simple resilient supports, i.e. flexible hoses, pipe hangers, etc. Last in the series, part 5 [110] outlines a method for determining the low frequency dynamic point stiffness using a rigid blocking mass with source side force and displacement measurements. Throughout the ISO series a number of test rig designs are given so as to apply the above methods to in-plane DoFs (i.e. x and y), although, with its focus largely on translational stiffness determination, only limited guidelines are given with regards to rotational stiffness components.

In [111] Kari further develops the indirect method of Thompson and Verheij [103] by adopting an improved excitation and termination arrangement (to suppress unwanted cross coupling between DoF) whilst using an over-determined system of equations. This over-determination is made possible by using multiple blocking masses and repeating the measurement procedure. Kari also employs a source correlation technique and stepped sine excitation to increase signal-to-noise ratio, thus extending the working frequency range. Also given are a number of test rig arrangements for both translation and rotational stiffness determination. The results presented appear to have smooth magnitude and phase curves, displaying the anti-resonances, resonances and pre-load dependence expected from a resilient element.

An impact based method was proposed by Lin et al. [112], and further developed by Ooi and Ripin [113], whereby the point and transfer stiffness properties of a resilient element are determined from a simplified single DoF mass on a spring model, assuming a blocked foundation. Although presented up to 800Hz, results were generally poor with considerable noise contamination, requiring a piecewise polynomial curve fitting to extract a useful stiffness value. Furthermore, the point stiffness values determined were only valid for very low frequencies, where the contribution of the mass may be considered negligible in comparison to that of the resilient element.

An alternative method was presented by Kim and Singh [101] where both translational and rotational dynamic transfer stiffnesses are extracted from a theoretical

model using experimental data. The proposed approach requires a number of measured mobilities which, in conjunction with rigid body theory, allow for a set of dynamic stiffness values to be extracted from a mass-isolator-mass model. The properties of the inertial elements are assumed known, and as such their free translational and rotational behaviour is readily calculable. From this the translational, rotational and cross stiffness terms may be determined from measurements made on an equivalent physical assembly. However, the simplified nature of the model has meant that only linear time-invariant structures may be considered, and furthermore the effects of pre-load, temperature, etc. could not be accounted for. Regardless of these limitations the authors were able to determine stiffness values in fair agreement with results obtained from an MTS Test Star 2 dynamic characterisation machine.

Of the established methods, Kari's modified indirect method [111] appears to provide the most promising approach for determining reliable dynamic transfer stiffness values. However, a fundamental assumption underpins all indirect approaches whereby a blocking mass is used. Theoretically any blocking mass should be perfectly rigid if its acceleration is to be truly constrained. Since the indirect method relies upon a measurable acceleration on the blocking mass to infer a receiver side force, this cannot truly be the blocking force. Although likely a reasonable approximation at most frequencies, a method whereby such an assumption is not required would be beneficial.

PART II. COUPLING ELEMENTS

CHARACTERISATION OF RESILIENT ELEMENTS

In this Chapter an in-situ method for determining the dynamic transfer stiffness of resilient coupling elements is proposed. The in-situ approach allows for multiple coupling elements to be characterised simultaneously in assemblies consisting of arbitrary source and receiver sub-structures. Following its theoretical development, the in-situ approach is validated first numerically, and then experimentally.

CONTENTS

3.1	In-situ Characterisation of Coupling Elements	29
3.2	Theoretical Development	30
3.3	Numerical Validation	37
3.4	Experimental Application	42
3.5	Concluding Remarks	63

3.1 IN-SITU CHARACTERISATION OF COUPLING ELEMENTS

The methods currently used to determine the dynamic transfer properties of coupling elements rely heavily upon the experimental and theoretical assumptions of an ideal blocking mass and/or rigid body theory. Although these assumption hold to some degree in most cases, they often impose strict limitations with regards to the method's application. Furthermore, although catering for rotational DoFs, these

methods tend to require multiple test rigs. These are not only large, inconvenient, and expensive to manufacture but, arguably, place coupling elements under non-representative mounting conditions. The sensitivity of elastic materials with regards to temperature, humidity and pre-load is well acknowledged [114]. It is therefore not unreasonable to expect the mounting condition of a coupling element to influence its dynamics. With this under consideration, it is clear that there exists a need for a characterisation method that is not only based on minimal assumptions, but may be applied with relative ease and without the need for any specially designed test rigs. It is the aim of this Chapter to accomplish the above through the development of an in-situ characterisation approach. The in-situ approach (as it will be referred to hereafter) allows for resilient coupling elements to be characterised whilst installed within an assembly consisting of arbitrary source and receiver sub-structures (providing that they are linear and time invariant).

The remainder of this Chapter will see the theoretical development behind the in-situ approach followed by its validation, both numerically and experimentally.

3.2 THEORETICAL DEVELOPMENT

Let us consider the general source-isolator-receiver (**SIR**) system depicted in Figure 3.1, where two sub-structures (denoted **S** and **R**) are coupled via some element **I**, which may or may not be made up of multiple individual coupling elements. The coupling DoFs at the **SI** and **IR** interfaces will be referred to as c_1 and c_2 , respectively. Furthermore, for generality, a set of remote positional DoFs are included on both **S** and **R**. These will be referred to as a and b , respectively. For completeness, the above system may be fully described by the following system of equations, in conjunction with the force equilibrium and compatibility conditions given in Equation 3.2.

$$\begin{aligned}
 \mathbf{v}_{\mathbf{S}_a} &= \mathbf{Y}_{\mathbf{S}_{aa}} \mathbf{f}_{\mathbf{S}_a} + \mathbf{Y}_{\mathbf{S}_{ac1}} \mathbf{f}_{\mathbf{S}_{c1}} & , & & \mathbf{v}_{\mathbf{S}_{c1}} &= \mathbf{Y}_{\mathbf{S}_{c1a}} \mathbf{f}_{\mathbf{S}_a} + \mathbf{Y}_{\mathbf{S}_{c1c1}} \mathbf{f}_{\mathbf{S}_{c1}} \\
 \mathbf{v}_{\mathbf{I}_{c1}} &= \mathbf{Y}_{\mathbf{I}_{c1c1}} \mathbf{f}_{\mathbf{I}_{c1}} + \mathbf{Y}_{\mathbf{I}_{c1c2}} \mathbf{f}_{\mathbf{I}_{c2}} & , & & \mathbf{v}_{\mathbf{I}_{c2}} &= \mathbf{Y}_{\mathbf{I}_{c2c1}} \mathbf{f}_{\mathbf{I}_{c1}} + \mathbf{Y}_{\mathbf{I}_{c2c2}} \mathbf{f}_{\mathbf{I}_{c2}} \\
 \mathbf{v}_{\mathbf{R}_{c2}} &= \mathbf{Y}_{\mathbf{R}_{c2b}} \mathbf{f}_{\mathbf{R}_b} + \mathbf{Y}_{\mathbf{R}_{c2c2}} \mathbf{f}_{\mathbf{R}_{c2}} & , & & \mathbf{v}_{\mathbf{R}_b} &= \mathbf{Y}_{\mathbf{R}_{bb}} \mathbf{f}_{\mathbf{R}_b} + \mathbf{Y}_{\mathbf{R}_{bc2}} \mathbf{f}_{\mathbf{R}_{c2}}
 \end{aligned} \tag{3.1}$$

$$\begin{aligned} \mathbf{v}_{\mathbf{S}c_1} = \mathbf{v}_{\mathbf{I}c_1} = \mathbf{v}_{\mathbf{C}c_1} \quad , \quad \mathbf{v}_{\mathbf{I}c_2} = \mathbf{v}_{\mathbf{R}c_2} = \mathbf{v}_{\mathbf{C}c_2} \\ \mathbf{f}_{\mathbf{S}c_1} + \mathbf{f}_{\mathbf{I}c_1} = 0 \quad , \quad \mathbf{f}_{\mathbf{I}c_2} + \mathbf{f}_{\mathbf{R}c_2} = 0 \end{aligned} \quad (3.2)$$

In the above, and throughout the remainder of this Thesis, capitalised subscripts are used to denote the sub-structure to which a quantity belongs, whilst lower case subscripts denote the position on said sub-structure. For example, $\mathbf{f}_{\mathbf{I}c_1}$ refers to the force applied to the uncoupled element \mathbf{I} at the position c_1 , whilst $\mathbf{Y}_{\mathbf{S}ac_1}$ refers to the uncoupled mobility of \mathbf{S} relating an excitation at c_1 to a response at a . Quantities belonging to coupled structures are denoted by the capitalised subscript \mathbf{C} , for example, $\mathbf{Y}_{\mathbf{C}ab}$ refers to the coupled mobility of the assembly, relating an excitation at b to a response at a . Equations 3.1 and 3.2 are considered in their most general form such that force and velocity vectors, \mathbf{v} and \mathbf{f} , may include both translational and rotational DoFs, as in Equation 2.7.

With the above in mind, the property of the coupling element we wish to determine, namely the dynamic transfer impedance (of which dynamic transfer stiffness is readily calculable, see Table 2.1), is defined as,

$$\bar{\mathbf{f}}_{\mathbf{C}c_2} = \mathbf{Z}_{\mathbf{I}c_2c_1} \mathbf{v}_{\mathbf{C}c_1} \quad (3.3)$$

where, $\mathbf{v}_{\mathbf{C}c_1}$ is a vector of applied velocities at the interface c_1 , and $\bar{\mathbf{f}}_{\mathbf{C}c_2}$ is the vector of resultant blocked forces required to restrain the velocity of interface c_2 .

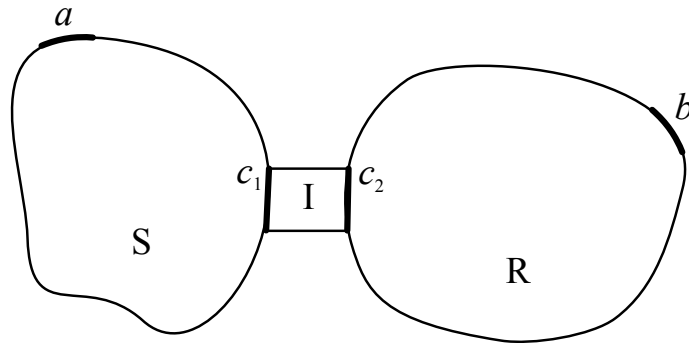


Figure 3.1: Schematic of an arbitrary source-isolator-receiver system.

Let us consider, at first, the above definition from a purely qualitative point of view. The $\mathbf{v}_{\mathbf{C}c_2} = 0$ constraint imposed by the blocked condition at c_2 can be thought to effectively remove the influence of the receiver sub-structure, \mathbf{R} , from the transfer impedance. Similarly, an applied velocity at c_1 is applied irrespective of the passive properties of the source sub-structure, \mathbf{S} . We can therefore reassure

ourselves that the dynamic transfer impedance is an independent property of the isolator, a fact well known. Current methods for determining this dynamic transfer impedance (discussed in Section 2.4) place considerable restrictions on the behaviour of the source and receiver sub-structures depicted in Figure 3.1, i.e. rigid body behaviour, blocked termination, etc. In what follows we establish an alternative approach capable of determining the dynamic transfer impedance from an assembly consisting of arbitrary source and receiver sub-structures.

Let us first consider the blocked force term on the left hand side of Equation 3.3, $\bar{\mathbf{f}}_{C_{c_2}}$. It was shown by Bobrovnikskii [67] that for a coupled assembly the resultant velocity field in a receiver sub-structure, due to an applied force on a source sub-structure, may be reproduced identically by the application of the negative blocked force vector at the coupling interface. Now suppose we *artificially* excite the **SIR** assembly by some external force vector, \mathbf{f} , at the remote DoF a . Using Bobrovnikskii's equivalent field representation, the following equality may be established,

$$\mathbf{v}_{C_b} = \mathbf{Y}_{C_{ba}} \mathbf{f}_a = -\mathbf{Y}_{C_{bc_2}} \bar{\mathbf{f}}_{C_{c_2}} \quad (3.4)$$

where $\bar{\mathbf{f}}_{C_{c_2}}$ is the resultant blocked force at c_2 due to the externally applied force at a . Rearrangement of Equation 3.4 yields the relationship between an arbitrarily applied force at a , and the resultant blocked force at c_2 ,

$$\bar{\mathbf{f}}_{c_2} = -\mathbf{Y}_{C_{bc_2}}^{-1} \mathbf{Y}_{C_{ba}} \mathbf{f}_a. \quad (3.5)$$

Let us now consider the velocity term on the right hand side of Equation 3.3, $\mathbf{v}_{C_{c_1}}$, resulting from the same remotely applied force, \mathbf{f}_a .

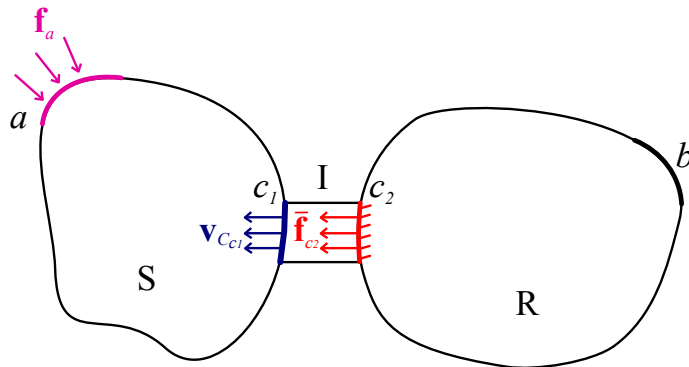


Figure 3.2: Forces contributing to the velocity of interface c_1 (as in Equation 3.6).

This velocity results from the superposition of the velocities due to the two forces acting on the assembly, \mathbf{f}_a and $\bar{\mathbf{f}}_{c_2}$ (as shown in Figure 3.2), and as such may be written as,

$$\mathbf{v}_{C_{c_1}} = \mathbf{Y}_{C_{c_1a}} \mathbf{f}_a + \mathbf{Y}_{C_{c_1c_2}} \bar{\mathbf{f}}_{c_2}. \quad (3.6)$$

Substitution of Equation 3.5 into Equation 3.6 allows us to describe the velocity at c_1 in terms of the externally applied force at a only.

$$\mathbf{v}_{C_{c_1}} = [\mathbf{Y}_{C_{c_1a}} - \mathbf{Y}_{C_{c_1c_2}} \mathbf{Y}_{C_{bc_2}}^{-1} \mathbf{Y}_{C_{ba}}] \mathbf{f}_a \quad (3.7)$$

Equations 3.5 and 3.7 may now be substituted into Equation 3.3, i.e. the definition of dynamic transfer impedance,

$$-\mathbf{Y}_{C_{bc_2}}^{-1} \mathbf{Y}_{C_{ba}} \mathbf{f}_a = \mathbf{Z}_{I_{c_2c_1}} [\mathbf{Y}_{C_{c_1a}} - \mathbf{Y}_{C_{c_1c_2}} \mathbf{Y}_{C_{bc_2}}^{-1} \mathbf{Y}_{C_{ba}}] \mathbf{f}_a. \quad (3.8)$$

Suppose we now apply a number of external force excitations at a , and arrange the corresponding force vectors, \mathbf{f}_{a_i} , as columns of a force matrix \mathbf{F}_a . With free reign over the nature of each applied force, we are able to ensure the invertability of the force matrix \mathbf{F}_a .

$$-\mathbf{Y}_{C_{bc_2}}^{-1} \mathbf{Y}_{C_{ba}} \mathbf{F}_a = \mathbf{Z}_{I_{c_2c_1}} [\mathbf{Y}_{C_{c_1a}} - \mathbf{Y}_{C_{c_1c_2}} \mathbf{Y}_{C_{bc_2}}^{-1} \mathbf{Y}_{C_{ba}}] \mathbf{F}_a \quad (3.9)$$

By post-multiplying both sides of Equation 3.9 by the inverse force matrix, \mathbf{F}_a^{-1} , we are able to cancel the force terms and, following some simple rearrangement, arrive at a formulation for the dynamic transfer impedance in terms of the passive properties of the coupled assembly only.

$$\mathbf{Z}_{I_{c_2c_1}} = -\mathbf{Y}_{C_{bc_2}}^{-1} \mathbf{Y}_{C_{ba}} [\mathbf{Y}_{C_{c_1a}} - \mathbf{Y}_{C_{c_1c_2}} \mathbf{Y}_{C_{bc_2}}^{-1} \mathbf{Y}_{C_{ba}}]^{-1} \quad (3.10)$$

Making use of the matrix inversion lemma identity [115], as shown in Equation B.11, the above formulation may be rewritten in a more convenient and final form.¹

Partial interface impedance relation:

$$\mathbf{Z}_{I_{c_2c_1}} = -[\mathbf{Y}_{C_{c_1a}} \mathbf{Y}_{C_{ba}}^{-1} \mathbf{Y}_{C_{bc_2}} - \mathbf{Y}_{C_{c_1c_2}}]^{-1} \quad (3.11)$$

¹The name ‘partial interface’ refers to the fact that Equation 3.11 requires only a single contact interface, c_2 , to be excited. All other excitations are remote to the coupling interface.

Equation 3.11 states that the independent dynamic transfer impedance matrix of a coupling element may be determined from the coupled mobility matrices; $\mathbf{Y}_{C_{c1a}}$, $\mathbf{Y}_{C_{ba}}$, $\mathbf{Y}_{C_{bc2}}$ and $\mathbf{Y}_{C_{c1c2}}$, measured on an assembly consisting of arbitrary source and receiver sub-structures. No assumptions have been made with regards to the behaviour of the source and receiver sub-structures, other than that they are linear and time invariant. Furthermore, no assumptions have been made with regards to the properties of the coupling element. The in-situ approach may therefore, in theory, be applied to both resilient and rigid coupling elements.

The experimental implementation of Equation 3.11 requires measurements to be made at the coupling interfaces, c_1 and c_2 , and the remote DoFs, a and b . The number of remote DoFs required to successfully determine the transfer impedance of \mathbf{I} will depend upon the number of elements under investigation. For a single element in a single coordinate-DoF, a single remote a and b DoF is sufficient. For each additional element or coordinate-DoF, included in the characterisation, an additional DoF must be included at either a or b , thus avoiding under-determination. Equation 3.11 does, however, facilitate the over-determination of the problem. Unlike the over-determination method used by Kari [111], Equation 3.11 requires no additional sub-structures to be attached to the assembly. Over-determination of Equation 3.11 may be achieved by including additional DoFs at either a or b . In both cases the least squares solution is acquired, as suggested by the pseudo inverse matrix identity presented in Equation B.12.

It is perhaps worth noting that the partial interface nature of Equation 3.11 offers the potential characterisation of elements whose interfaces are only partially accessible. Here, a partly accessible interface refers to one that is accessible enough for vibration sensors to be fitted, whilst insufficiently accessible to allow for an excitation to be applied.

Although Equation 3.11 may be simpler in form, Equation 3.10 provides a valuable insight which would perhaps otherwise be overlooked. Consider the general solution to the inverse of a block matrix [116],

$$\begin{bmatrix} \mathbf{A} & \mathbf{B} \\ \mathbf{C} & \mathbf{D} \end{bmatrix}^{-1} = \begin{bmatrix} (\mathbf{A} - \mathbf{B}\mathbf{D}^{-1}\mathbf{C})^{-1} & -\mathbf{A}^{-1}\mathbf{B}(\mathbf{D} - \mathbf{C}\mathbf{A}^{-1}\mathbf{B})^{-1} \\ -\mathbf{D}^{-1}\mathbf{C}(\mathbf{A} - \mathbf{B}\mathbf{D}^{-1}\mathbf{C})^{-1} & (\mathbf{D} - \mathbf{C}\mathbf{A}^{-1}\mathbf{B})^{-1} \end{bmatrix}. \quad (3.12)$$

The off-diagonal entries given in Equation 3.12 are identical in form to that of Equation 3.10. If we consider the following substitutions; $\mathbf{A} = \mathbf{Y}_{C_{c1a}}$, $\mathbf{B} = \mathbf{Y}_{C_{c1c2}}$,

$\mathbf{C} = \mathbf{Y}_{\mathbf{C}_{ba}}$ and $\mathbf{D} = \mathbf{Y}_{\mathbf{C}_{bc2}}$, the dynamic transfer impedance matrix $\mathbf{Z}_{\mathbf{I}_{c2c1}}$ is given by the lower diagonal entry of the following matrix inverse,

$$\begin{bmatrix} (\mathbf{Y}_{\mathbf{C}_{c1a}} - \mathbf{Y}_{\mathbf{C}_{c1c2}} \mathbf{Y}_{\mathbf{C}_{bc2}}^{-1} \mathbf{Y}_{\mathbf{C}_{ba}})^{-1} & -\mathbf{Y}_{\mathbf{C}_{c1a}}^{-1} \mathbf{Y}_{\mathbf{C}_{c1c2}} (\mathbf{Y}_{\mathbf{C}_{bc2}} - \mathbf{Y}_{\mathbf{C}_{ba}} \mathbf{Y}_{\mathbf{C}_{c1a}}^{-1} \mathbf{Y}_{\mathbf{C}_{c1c2}})^{-1} \\ \mathbf{Z}_{\mathbf{I}_{c2c1}} & (\mathbf{Y}_{\mathbf{C}_{bc2}} - \mathbf{Y}_{\mathbf{C}_{ba}} \mathbf{Y}_{\mathbf{C}_{c1a}}^{-1} \mathbf{Y}_{\mathbf{C}_{c1c2}})^{-1} \end{bmatrix} = \dots$$

$$\dots = \begin{bmatrix} \mathbf{Y}_{\mathbf{C}_{c1a}} & \mathbf{Y}_{\mathbf{C}_{c1c2}} \\ \mathbf{Y}_{\mathbf{C}_{ba}} & \mathbf{Y}_{\mathbf{C}_{bc2}} \end{bmatrix}^{-1}. \quad (3.13)$$

Although this mobility matrix may not appear particularly interesting, if we consider the remote excitation points, a and b , to lie at the coupling interfaces, c_1 and c_2 , Equation 3.13 reduces to that of the coupled interface mobility matrix.²

Full interface impedance relation:

$$\begin{bmatrix} \mathbf{Z}_{\mathbf{C}_{c1c1}} & \mathbf{Z}_{\mathbf{I}_{c1c2}} \\ \mathbf{Z}_{\mathbf{I}_{c1c2}} & \mathbf{Z}_{\mathbf{C}_{c2c2}} \end{bmatrix} = \begin{bmatrix} \mathbf{Y}_{\mathbf{C}_{c1c1}} & \mathbf{Y}_{\mathbf{C}_{c1c2}} \\ \mathbf{Y}_{\mathbf{C}_{c2c1}} & \mathbf{Y}_{\mathbf{C}_{c2c2}} \end{bmatrix}^{-1} \quad (3.14)$$

The focus of the remainder of this Chapter will be to investigate the practical application of this Equation, together with the partial interface variant given by Equation 3.11.

Equation 3.14 states that the independent dynamic transfer impedance of an arbitrary coupling element may be determined from the inverse of its coupled contact interface mobility matrix.

In this full interface form the ability to over-determine the problem is no longer available, as the remote DoFs, a and b , are collocated to those of c_1 and c_2 , respectively. It should be noted that resultant diagonal elements are the point impedances of the coupled assembly which, unlike the transfer impedances, are not independent properties of the coupling element.

Equation 3.14 may be realised via an alternative approach based on a simple dynamic sub-structuring problem. Consider the coupling of three sub-structures, as in Figure 3.1, via the classical impedance approach [76]. It can be seen from Equation 3.15 that the coupling of source and receiver sub-structures does not effect the transfer

²The name ‘full interface’ refers to the fact that Equation 3.14 requires the *full* coupling interface matrix to be measured, i.e. excitations at both c_1 and c_2 .

component of the coupling element impedance matrix.

$$\begin{bmatrix} \mathbf{Z}_{S_{c1c1}} & 0 \\ 0 & 0 \end{bmatrix} + \begin{bmatrix} \mathbf{Z}_{I_{c1c1}} & \mathbf{Z}_{I_{c1c2}} \\ \mathbf{Z}_{I_{c2c1}} & \mathbf{Z}_{I_{c2c2}} \end{bmatrix} + \begin{bmatrix} 0 & 0 \\ 0 & \mathbf{Z}_{R_{c2c2}} \end{bmatrix} = \begin{bmatrix} \mathbf{Z}_{S_{c1c1}} + \mathbf{Z}_{I_{c1c1}} & \mathbf{Z}_{I_{c1c2}} \\ \mathbf{Z}_{I_{c1c2}} & \mathbf{Z}_{I_{c2c2}} + \mathbf{Z}_{R_{c2c2}} \end{bmatrix}. \quad (3.15)$$

The right hand side of Equation 3.15 represents the coupled impedance matrix \mathbf{Z}_C and can clearly be obtained from the inverse of the coupled mobility matrix, $\mathbf{Z}_C = \mathbf{Y}_C^{-1}$.

Unlike the partial interface approach, which only requires the excitation of a single contact interface, the full interface approach requires the excitation of both source and receiver contact interfaces. As such, its application would likely be limited to instances where access is unrestricted.

The in-situ approaches presented above offer a number of potential benefits over alternative methods. To begin with, no assumptions are made with regards to the properties of source and receiver sub-structures (other than that they are linear and time invariant), as such, measurements may be conducted in-situ on an arbitrary assembly. This not only negates the need for any large and inconvenient test rigs, but offers the potential to characterise coupling elements whilst installed in their intended environment and, therefore, under representative mounting conditions. Secondly, the general form of Equation 3.11, in theory, allows for multiple coupling elements to be characterised in multiple coordinate-DoFs simultaneously, therefore negating the need for multiple test rigs. Lastly, with no assumptions having been made with regards to the properties of the coupling element, the method may be applied to rigid as well as resilient coupling elements.

In general, a resilient element will display some degree of non-linear behaviour, the extent of which will vary between element types. In such cases the in-situ approach may still be considered valid providing that, further to linearity and time invariance, the transfer properties may be assumed to be locally linear. Local linearity here refers to the condition whereby the forces applied to a coupling element, due to the operational activity of an active source sub-structure, result in displacements that remain within the linear range of the element under its given pre-load. This amounts to the assumption that the properties of the coupling element are unaffected by the operation of the source. The region over which this assumption is met will depend on the dynamic behaviour of the source sub-structure, the pre-load applied over the

coupling element, and its dynamic properties. However, it is believed that in most practical scenarios this assumption would hold true. In cases where the operational source exerts a large enough force, the external forces applied in the determination of the transfer impedance may no longer be representative of the intended operational state, and the resulting transfer impedance may no longer be appropriate. The notion of local linearity in fact highlights one of the main advantages of the in-situ approach, that is its ability to characterise elements whilst under a realistic loading.

The remainder of this Chapter will focus on the numerical and experimental validation of the above theoretical developments, to see if they can be realised in practice.

3.3 NUMERICAL VALIDATION

In order to provide an initial validation, and further investigate the theoretical developments of Section 3.2, a numerical study has been carried out. In this study, the transfer impedance of an interior portion of free-free beam is determined from simulated mobilities on a full length beam. Such a simulation allows for both the partial and full interface approaches, presented in Equations 3.11 and 3.14, respectively, to be validated and, furthermore, their sensitivity to noise investigated.

A free-free beam model was chosen for this study as it provides a relatively general case and, furthermore, allows for the in-situ approach to be demonstrated (albeit numerically) on a non-resilient and strongly coupled assembly.

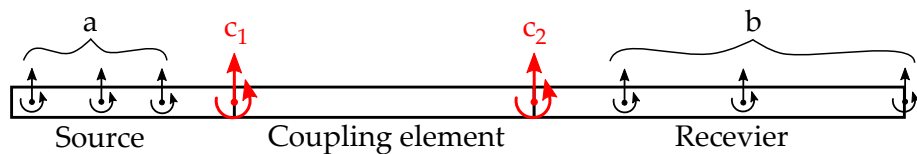


Figure 3.3: Graphical depiction of the numerical simulation carried out.

The interior portion of a free-free beam may be considered the coupling element, **I**, between two outer portions, **S** and **R**. Together the **SIR** beam represents the coupled assembly from which we are aiming to determine the transfer impedance of **I**. In keeping with the notation of Section 3.2, the coupling interfaces are referred to as c_1 and c_2 , as shown in Figure 3.3. Due to their strong coupling, both translational and rotational DoFs have been included in the simulations. The translational mobility of

a free-free beam excited at an arbitrary point, x_j , for an arbitrary receiver position, x_i , is given by [117] as,

$$Y_{ij} = \frac{i\omega}{2\bar{B}k^3} (f_1(x_j)g_1(x_i) + f_2(x_j)g_2(x_i)) \quad 0 \leq x_i \leq x_j \quad (3.16)$$

$$Y_{ij} = \frac{i\omega}{2\bar{B}k^3} (f_1(x_i)g_1(x_j) + f_2(x_i)g_2(x_j)) \quad x_j \leq x_i \leq l \quad (3.17)$$

where, $i = \sqrt{-1}$ is the imaginary unit, \bar{B} is the beam bending stiffness, k is the bending wave number, l is the beam length and;

$$f_1(x) = \cosh kx - \cosh k(l-x) \cos kl - \sinh k(l-x) \sin kl \\ - \cos kx + \cos k(l-x) \cosh kl - \sinh kl \sin k(l-x) \quad (3.18)$$

$$f_2(x) = \sinh kx - \sinh k(l-x) \cos kl - \sin kl \cosh k(l-x) \\ - \sin kx + \sinh kl \cos k(l-x) - \cosh kl \sin k(l-x) \quad (3.19)$$

$$g_1(x) = -\frac{(\sin kx + \sinh kx)}{2(1 - \cosh kl \cos kl)} \quad (3.20)$$

$$g_2(x) = \frac{(\cos kx + \cosh kx)}{2(1 - \cosh kl \cos kl)}. \quad (3.21)$$

The angular velocity and moment mobilities are obtained by differentiating Equations 3.16-3.17 with respect to x_i and x_j , respectively. The transfer impedance of the coupling element, \mathbf{I} , may be determined exactly by simulating an uncoupled free-free beam of equal length. The uncoupled impedance matrix is given by the inverse of the uncoupled mobility matrix, $\mathbf{Z}_{\mathbf{I}} = \mathbf{Y}_{\mathbf{I}}^{-1}$. The transfer element of this matrix will be referred to as the ‘exact’ transfer impedance, and used as a comparison against those determined from the coupled **SIR** assembly.

Beam	$L(m)$	$W(m)$	$H(m)$	$E(N/m^2)$	$\rho(kg/m^3)$	$x_{ij}(m)$
SIR	1.2	0.1	0.01	200×10^9	7000	{0.05, 0.13, 0.22, 0.3 , 0.7 , 0.87, 1.06, 1.14}
I	0.4	0.1	0.01	200×10^9	7000	{ 0 , 0.4 }

Table 3.1: Geometry, material properties and excitation/response positions for free-free beam simulations, where; L - length, W - width, H - height, E - Young’s modulus, ρ - density, and x_{ij} - excitation/response position. Highlighted x_{ij} correspond to those of the coupling interfaces, c_1 and c_2 .

The geometric and material properties of the coupled assembly, **SIR**, and the uncoupled coupling element, **I**, along with the excitation/response positions used in the simulations, are given in Table 3.1.

Further to an initial validation of Equations 3.11 and 3.14, it is of interest to assess the stability of each approach when subjected to varying amounts of artificial noise. The aim of this noise is to simulate, in a somewhat appropriate way, the noise one may encounter in practice. In reality, such noise consists of both correlated and uncorrelated sources. The former being comprised of errors arising from signal conditioning, transduction, signal processing and user measurement, with the latter being composed of errors resulting from thermal noise and other external disturbances [118].

In the absence of a more realistic model, the artificial noise introduced here is done so via a time domain random noise model with a Gaussian amplitude distribution,

$$p(x) = \frac{1}{\sigma\sqrt{2\pi}} e^{-\frac{(x-\mu)^2}{2\sigma^2}} \quad (3.22)$$

with zero mean ($\mu = 0$) and standard deviation $\sigma = 5 \times 10^{-7}$. It should be noted that this method of introducing artificial noise is not intended to simulate the error resulting from user measurement error, i.e. inaccuracy with a force hammer. Instead, it is the aim of this study to reveal the sensitivity of each approach whilst subjected to an error of uncorrelated nature.

For each simulated mobility, $Y_{i,j}$, an independent time domain noise vector is generated, thus allowing for the inclusion of both excitation and response noise independently. Each time domain noise vector, $n_{i,j}(t)$, is Fourier transformed and scaled such that the contaminated mobilities have a signal-to-noise ratio (SNR) of L dB. A suitable scaling is achieved via an energy normalisation and may be formulated as,

$$N_{i,j}(\omega) = 10^{-L/10} \sum_{\omega} Y_{i,j}(\omega)^2 \frac{\mathcal{F}\{n_{i,j}(t)\}}{\sum_{\omega} \mathcal{F}\{n_{i,j}(t)\}^2} \quad (3.23)$$

where, $10^{-L/10}$ is a linear measure of the SNR, $\sum_{\omega} Y_{i,j}^2$ is the total energy in the noise free signal, $\sum_{\omega} \mathcal{F}\{n(t)\}^2$ is the total energy in the noise signal. Each $N_{i,j}$ is assembled to construct the noise matrix, **N**. The noise contaminated mobility matrix, $\hat{\mathbf{Y}}_{\mathbf{C}}$, is subsequently given by,

$$\hat{\mathbf{Y}}_{\mathbf{C}} = \mathbf{Y}_{\mathbf{C}} + \mathbf{N}. \quad (3.24)$$

The inclusion of noise in such a way is akin to introducing an artificial noise floor for each element of the mobility matrix, \mathbf{Y}_C , such that it has an SNR of L dB. For illustrative purposes, shown in Figure 3.4 are the upper and lower bounds of the two levels of artificial noise used in this study. Also shown, for a sense of scale, are the upper and lower bounds of the mobility matrix \mathbf{Y}_C .

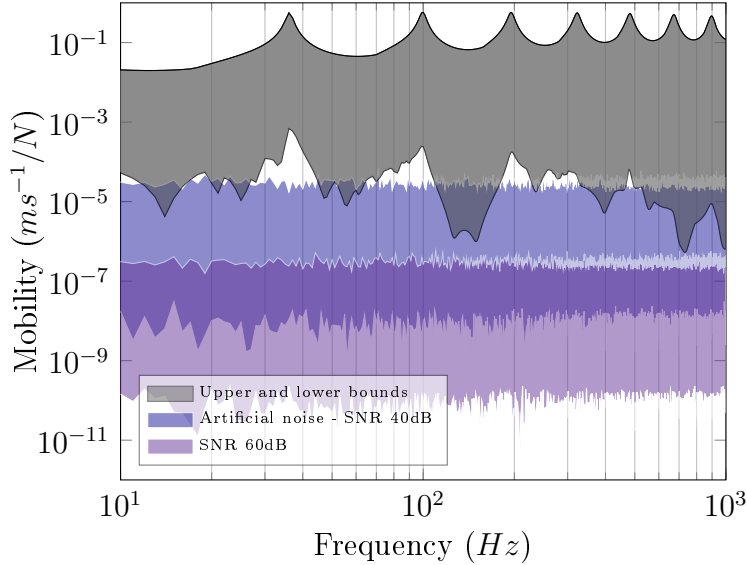


Figure 3.4: The upper and lower bounds of the artificial noise matrix \mathbf{N} corresponding to SNRs of 60dB and 40dB, compared against the upper and lower bounds of the mobility matrix \mathbf{Y} .

Shown in Figure 3.5a are the translational transfer impedances of $\mathbf{Z}_{\mathbf{I}_{c1c2}}$, determined from the coupled assembly via the partial (dot-dashed orange) and full (dashed yellow) interface approaches, without the inclusion of artificial noise. It can be seen that both the partial and full interface approaches are in near perfect agreement with the exact transfer impedance determined from the uncoupled element, \mathbf{I} (differences are on the scale of numerical error). This may in itself be considered a partial validation of the in-situ approach. A full validation will require further experimental verification and will be covered later (see Section 3.4). It should be noted that due to the inclusion of rotational DoFs, the transfer impedance of the coupling element is given by the 2×2 matrix,

$$\mathbf{Z}_{\mathbf{I}_{c1c2}} = \begin{bmatrix} Z_{I_{x1x2}} & Z_{I_{\alpha1x2}} \\ Z_{I_{x1\alpha2}} & Z_{I_{\alpha1\alpha2}} \end{bmatrix}. \quad (3.25)$$

However, for clarity, only the translational $Z_{I_{x1x2}}$ component results are presented here. The additional transfer impedances, not shown for brevity, are also in near perfect agreement with the exact impedances.

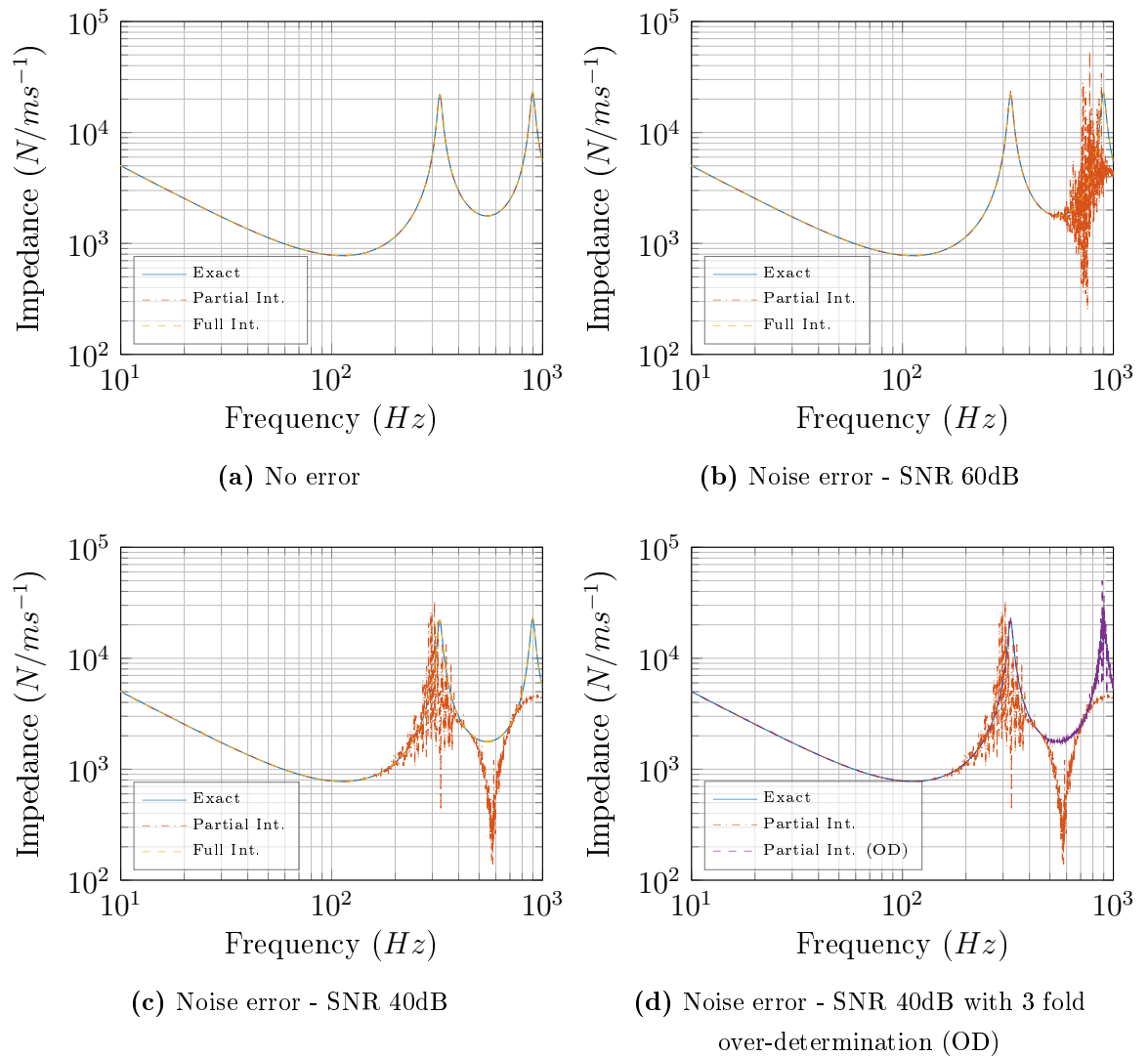


Figure 3.5: Translational transfer impedance obtained via numerical simulation. Solid blue line is the exact transfer impedance obtained from I whilst uncoupled.

Figures 3.5b-3.5c demonstrate the effect of introducing artificial noise, as set out through Equations 3.22-3.24. Two levels of noise have been considered here, corresponding to an SNR of 60dB and 40dB, respectively. It can be seen that the partial interface approach (dot-dashed orange) appears far more sensitive to the effects of noise than the full interface approach (dashed yellow). This may be justified in part due to the two matrix inversions required by the partial interface approach (Equation 3.11) as opposed to the single inversion by the full interface approach. It is well known that matrix inversions are particularly sensitive to noise and that small errors may easily be amplified and dominate the resulting inverse. Under the influence of both levels of noise, the full interface approach yields a transfer impedance in excellent agreement with that of the exact impedance. A further increase in the level

of noise can be shown to introduce a noticeable error. However, this error remains considerably less than that of the partial approach.

Unlike the full interface approach, where the number of mobilities used to determine the transfer impedance is limited by the number of interface DoFs, the partial interface approach allows for over-determination through the use of additional remote DoFs. Shown in Figure 3.5d are the determined (dot-dashed orange) and over-determined (dashed purple) transfer impedances obtained via the partial interface approach. This was achieved by including two further remote points at b . It can be seen that the over-determination has greatly reduced the effect of noise. Although some error still remains, this may be reduced further by increasing the level of over-determination, or by taking multiple averages for each mobility, thus diminishing the influence of noise.

3.4 EXPERIMENTAL APPLICATION

In order to further validate and assess the practical application of the in-situ method, a number of experimental studies have been conducted. The dynamic transfer stiffness of two different resilient elements are determined via the partial and full interface approaches. At this point only the translational coordinate-DoF z is considered. For completeness, and to highlight the experimental challenges associated with the in-situ approach, the characterisation procedure has been undertaken on a variety of assembly types, including; non-resonant, resonant, single and multi-contact assemblies. At first we will consider only single contact assemblies, beginning with the simplest case of a non-resonant mass-isolator-mass assembly. Resonant source and receiver sub-structures, along with multi-contact assemblies, will be introduced with increasing complexity as the Section progresses.

In these experimental studies, and throughout the remainder of this Thesis, unless otherwise stated, mobilities are measured using an impact excitation (with a B&K instrumented force hammer, Type 8206-001, with a hard plastic tip) as per BS 6897 Part 5 [17]. Accelerations are measured using single axis accelerometers (B&K Type 4507 B 004 or Type 4507 B 006). Data capture and mobility calculations are performed using a 01dB multi-channel analyser (AREVA NetdB DAQ-12/DAQ-32), along with its associated software package (dBFA Suite). With the exception of mobility calculations all further post-processing is done using MATLAB [119].

Assuming the input excitation to be comparatively free from noise, all mobilities are calculated using the H_1 transfer function formulation [120],

$$H_1(\omega) = \frac{S_{ab}(\omega)}{S_{aa}(\omega)} \quad (3.26)$$

where, S_{ab} is the input/output (force/acceleration) cross-spectrum, and S_{aa} is the input auto-spectrum. A frequency resolution of 0.390625Hz and FFT length of 65536 is used throughout. Lastly, each mobility is determined from the linear average of 3 independent excitation and response measurements.

3.4.1 SINGLE CONTACT

Although unlikely to be encountered in reality, a single contact assembly offers the simplest case in which the in-situ approach may be applied. A number of assembly types are considered here; firstly, a non resonant mass-isolator-mass (**MIM**) assembly; secondly, a partially resonant mass-isolator-plate (**MIP**) assembly; and lastly, a highly resonant beam-isolator-plate (**BIP**) assembly. Further assembly details will be presented as and when required.

MASS-ISOLATOR-MASS - The dynamic transfer stiffness of two different resilient elements have been determined using the full interface approach.³ The experimental set-up for this is shown diagrammatically in Figure 3.6, where a spaced accelerometer pair is adhered above and below the coupling mount. The assemblies used here, and throughout the remainder of this Chapter, are coupled using an industrial strength adhesive, rested on foam pads, and elevated using a number of bricks, so as to provide access to both contact interfaces.

Each resilient element has been characterised in two different **MIM** assemblies, details of which are presented in Table 3.2. It is important to note that the resilient element used in assemblies **A** and **B** was a large and relatively stiff isolator. It was therefore assumed that a small change in the source mass would be unlikely to introduce any significant non-linearities with regards to its pre-load. The resilient element used in assemblies **C** and **D** was a small and relatively soft isolator. To avoid the introduction of any pre-load based non-linearities, the source mass was kept constant between these two assemblies. For the **MIM** assemblies considered

³The mass-like nature of the source and receiver sub-structures used here meant that the partial interface approach would be of little benefit.

Tag	Type	Assembly Details
A	MIM	Source mass 0.86kg, receiver mass 0.68kg, resilient element: Continental CONTITECH 27 796 25-29
B	MIM	Source mass 1.8kg, receiver mass 0.86kg, resilient element: Continental CONTITECH 27 796 25-29
C	MIM	Source mass 0.68kg, receiver mass 0.86kg, resilient element: Fibet 2525vv18 60 IRHD
D	MIM	Source mass 0.68kg, receiver mass 3.25kg, resilient element: Fibet 2525vv18 60 IRHD

Table 3.2: Details on the construction of Mass-Isolator-Mass (**MIM**) assemblies.

here, only the full interface approach is investigated, as it made little sense to include remote measurement positions when the assembly is simply composed of mass like elements.

The full interface measurement procedure, applied to assemblies **A-D**, may be outlined as follows,

- 1 Forces are applied at each of the accelerometer positions at interface c_1 , and the mobilities $\mathbf{Y}_{\mathbf{C}_{c_1c_1}}$ and $\mathbf{Y}_{\mathbf{C}_{c_2c_1}}$ are measured.
- 2 Forces are applied at each of the accelerometer positions at interface c_2 , and the mobilities $\mathbf{Y}_{\mathbf{C}_{c_1c_2}}$ and $\mathbf{Y}_{\mathbf{C}_{c_2c_2}}$ are measured.

Following this, the 4×4 spaced mobility matrix was constructed and an appropriate sign convention applied so as to account for the direction of measured quantities. The rows and columns corresponding to the spaced pairs are averaged to provide the central point and transfer mobilities. The resulting 2×2 contact interface mobility matrix was inverted and the dynamic transfer impedance extracted from the off-diagonal elements, as per Equation 3.6. Multiplication by $i\omega$ yields the dynamic transfer stiffness. The above procedure was performed on assemblies **A-D**, the results of which are presented in Figures 3.7 - 3.9.

Let us first consider assemblies **A** and **B**. Shown in Figure 3.7a are the transfer mobilities, $\mathbf{Y}_{\mathbf{C}_{c_1c_2}}$, measured across the two assemblies. As expected, the two differ, confirming that the transfer mobility is a property of the assembly, not the mount. Shown in Figure 3.7b are the dynamic transfer stiffnesses, $\mathbf{K}_{\mathbf{I}_{c_1c_2}}$, determined from assemblies **A** (blue) and **B** (orange). As one would expect from an independent quantity, the two are in excellent agreement. The determined stiffnesses display the

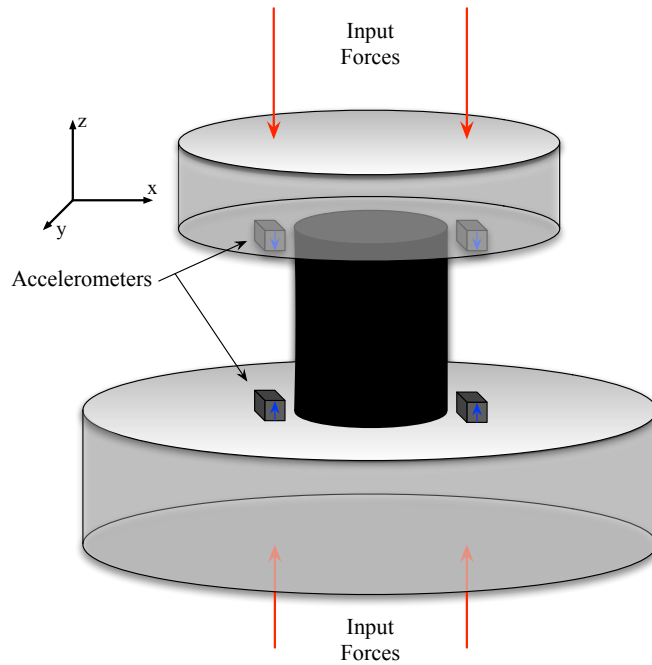
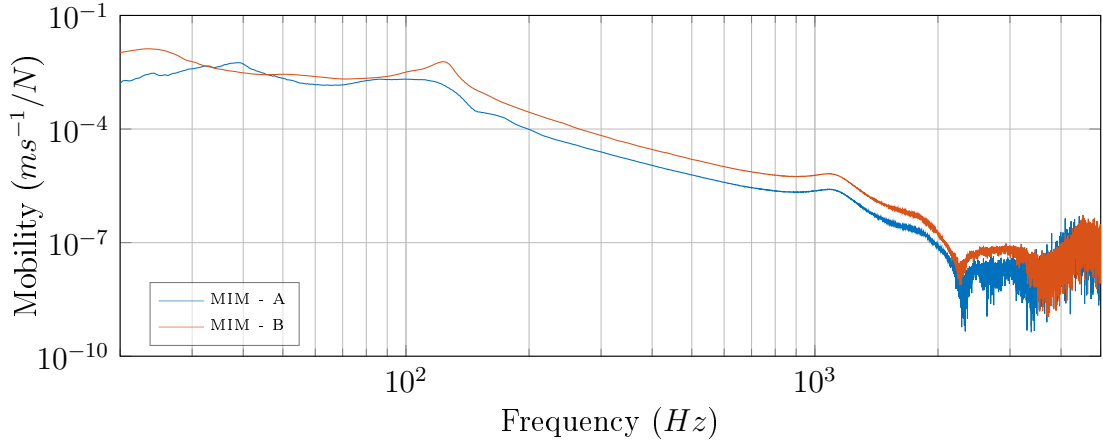
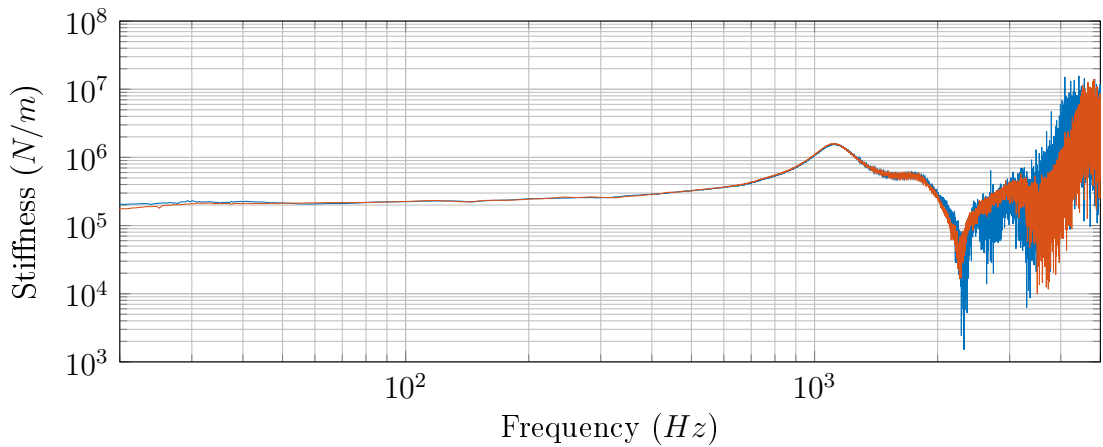


Figure 3.6: Diagrammatic representation of the mass-isolator-mass test rig. Red arrows correspond to the direction and position of the applied forces, whilst blue arrows indicate the positive direction of the measured accelerations.

phenomena expected from a resilient element, i.e. a near linear stiffness with a well damped internal resonance, occurring in this particular isolator at approximately 1kHz. Beyond this internal resonance, an increasing amount of noise is observed. This is a result of the resiliently attenuated vibration falling below the sensitivity threshold of the measurement equipment. The frequency at which this noise is introduced is dependent upon the stiffness of mount and the inertia of the assembly, with a larger masses requiring a larger vibration amplitude in order to exceed the sensitivity threshold. It is of interest to note that the resilient mount used here, a ‘SCHWINGMETALL Compression Mount, C Type, Mould Number 27796/C’, is supplied with a static spring stiffness of $16,800\text{N/m}$. Comparing this to the measured value at 20Hz of approx $20,000\text{N/m}$, it is not unreasonable to put the 19% increase in stiffness down to differences in pre-load, not to mention the frequency dependent nature of rubber-like materials.

Let us now consider assemblies **C** and **D**. Shown in Figure 3.8a are the transfer mobilities measured across the two assemblies. As in assemblies **A** and **B**, these transfer mobilities differ considerably. The dynamic transfer stiffnesses determined from assemblies **C** (blue) and **D** (orange) are shown in Figure 3.8c. Again, these stiffnesses are in excellent agreement with one another. Although as before, the high frequency stiffness is heavily contaminated by noise resulting from the limited dynamic range of the measurement equipment. Like the Continental mount (used in assemblies **A** and **B**), the stiffnesses determined for the Fibet mount display a near

(a) Transfer mobility $Y_{C_{1e2}}$ of assembly **A** and **B**(b) Dynamic transfer stiffness $K_{I_{e1e2}}$ of assembly **A** and **B****Figure 3.7:** Dynamic transfer stiffness and transfer mobility measurements made on assemblies **A** and **B** (see Table 3.2).

linear stiffness response, as expected. Unlike the Continental mount however, no internal resonance is observed. This is likely due to the isolator's smaller size pushing the first internal resonance into the noise contaminated region. A small amount of disagreement between the two stiffnesses can be observed particularly in the lower frequency range, between roughly 20-40Hz. A potential cause for this disagreement is highlighted in Figure 3.8c. Shown in Figure 3.8c are the reciprocal transfer mobilities measured across assembly **D**. Although in agreement across the majority of their frequency range, below approximately 50Hz this agreement worsens. A likely reason for this breakdown in reciprocity is a non-linearity introduced by the excitation of the source and receiver masses. If the forces used to excite the assembly above and below the mount result in sufficiently different mount displacements, the two transfer mobilities may end up representing the mount whilst under different 'conditions'. Additionally, the compact nature of the Fibet mount made for a less stable **MIM**

assembly and was therefore more likely to be effected by non-linearities due to impact excitation level.

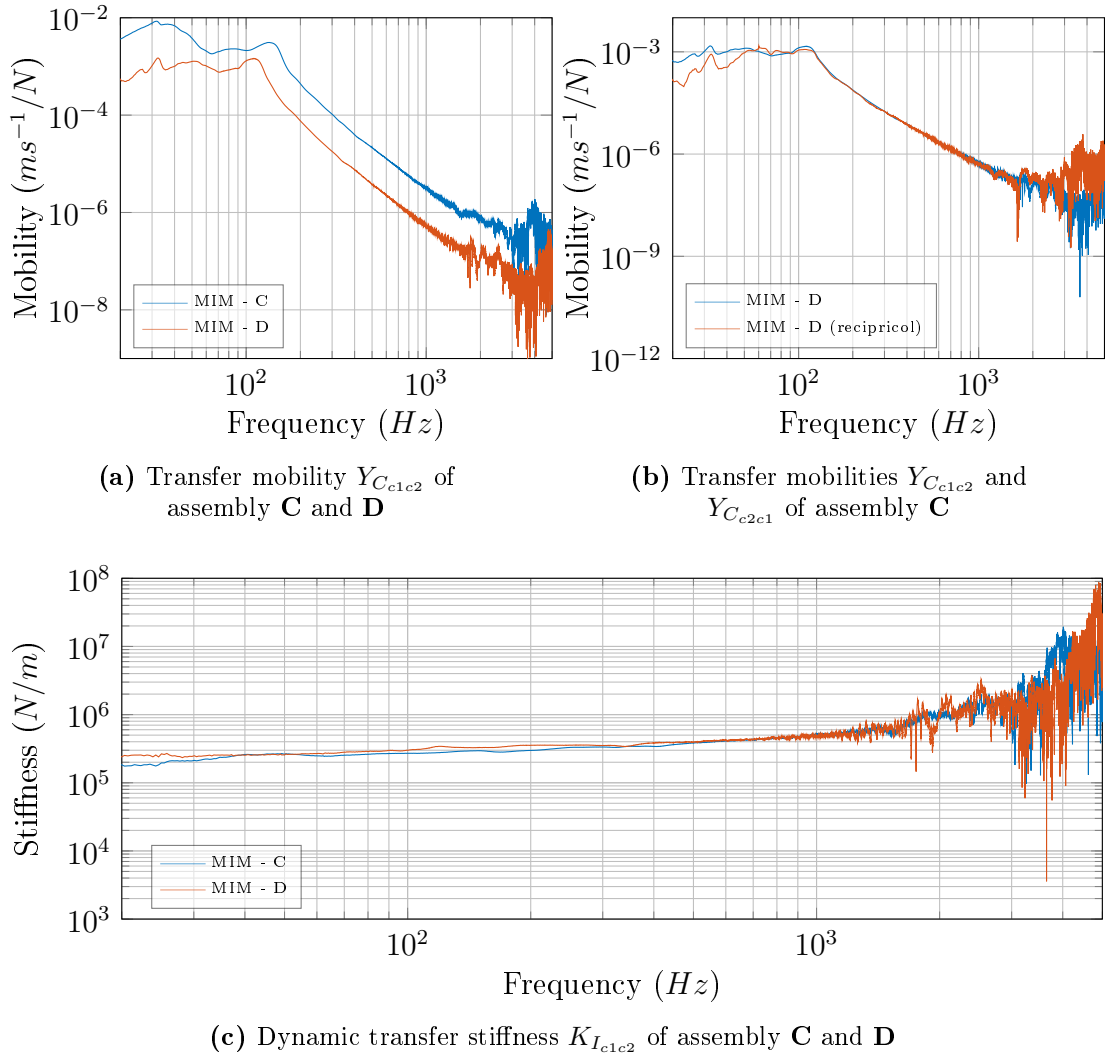


Figure 3.8: Dynamic transfer stiffness and transfer mobility measurements made on assemblies **C** and **D** (see Table 3.2). Low level excitation at c_2 was used to avoid introducing non-linearities.

In order to further investigate the effect of poor reciprocity, assembly **D** was re-tested using a higher level of excitation, the results of which are presented in Figure 3.9. Shown in Figure 3.9a are the transfer mobilities measured across assemblies **C** (blue) and **D** (orange). Comparison against Figure 3.8a shows that the higher level excitation has led to a slight reduction in the effect of high frequency noise, as one would expect. The resulting reciprocal agreement between the transfer mobilities of assembly **D** is shown in Figure 3.9b. It can be seen that the higher level excitation has benefited the low frequency reciprocity, whilst worsening the agreement about the primary resonance. This result is reflected in the resulting dynamic transfer

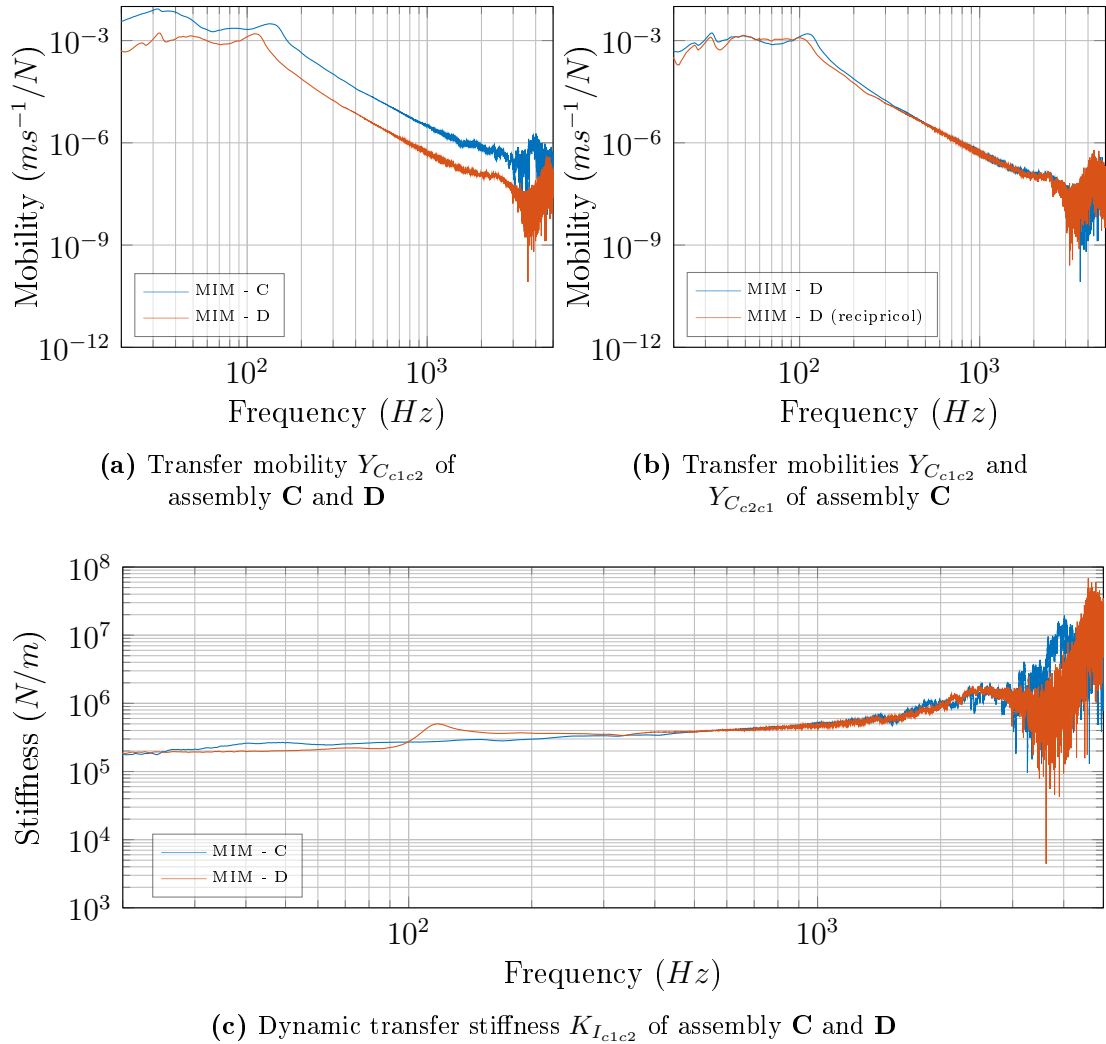


Figure 3.9: Dynamic transfer stiffness and transfer mobility measurements made on assemblies **C** and **D** (see Table 3.2). High level excitation at c_2 was used to exaggerate non-linearities resulting from large difference in mass behaviours.

stiffness, shown in Figure 3.9c. An unexpected resonance at approximately 130Hz has appeared in the dynamic transfer stiffness of assembly **D** (orange). This is clearly an artefact resulting from the poor reciprocity about the transfer mobility's primary resonance. However, the improved low frequency reciprocity can be seen to benefit the low frequency stiffness agreement between the two assemblies.

Although by no means an exhaustive study, this result highlights the importance of self consistency. Although each mobility is correct in its own right, the 'effective conditions' under which they were determined may differ due to the difference in excitation level. As such, although likely correct for their corresponding conditions, they are not representative of the same assembly. This lack of self consistency is likely

caused by the susceptibility of resilient elements to non-linearities, not to mention experimental error, and is perhaps the main limitation of the in-situ approach.

TRANSMISSIBILITY VALIDATION - It has so far been shown that the dynamic transfer stiffness of a resilient element, determined via the full interface approach, is an independent quantity. However, the validity of the resulting stiffness has only been partially verified from the knowledge of a static stiffness. A further validation is provided here by means of a transmissibility prediction. The transmissibility of a single DoF system may be obtained either experimentally, through the ratio of operational velocities, as in Equation 3.27,

$$T_{\text{meas}} = \frac{v_{C_{c2}}}{v_{C_{c1}}} = \frac{Y_{C_{c2c1}}}{Y_{C_{c1c1}}} \quad (3.27)$$

or theoretically, using a simplified model, i.e. mass on a spring, as in Equation 3.28,

$$T_{\text{pred}} = \frac{Z_s}{Z_m + Z_s} \quad (3.28)$$

where, Z_s and Z_m are the spring and supported mass impedances, respectively. Assuming the **MIM** assemblies investigated above behave similarly to that of a mass on a spring, it is possible to use measured and predicted transmissibilities as a means of validating the dynamic stiffnesses obtained via the in-situ approach. The validation process undertaken may be outlined as follows:

- 1 The dynamic transfer impedance of the Continental mount is determined from the **MIM** assembly, **A**.
- 2 A second **MIM** assembly, **B**, is constructed and its transmissibility measured directly via Equation 3.27.
- 3 Using the theoretical source mass impedance of assembly **B**, ($Z_m = i\omega M^{(B)}$), along with the mount impedance determined from assembly **A**, ($Z_s = Z_{I_{c1c2}}^{(A)}$), the transmissibility of **B** is predicted via Equation 3.28. A comparison against the measured transmissibility is given in Figure 3.10a.
- 4 Assembly **B** is inverted such that the receiver mass becomes the source mass and step 3 is repeated. A comparison for this second configuration is given in Figure 3.10b.

- * It is assumed that the inversion of assembly **B** does not introduce any non-linearities due to the slight change in pre-load.

It can be seen that in both cases the frequencies at which the transmissibility peaks are predicted with considerable accuracy. The difference in amplitude between the measured and predicted transmissibilities may be put down to the simplified nature of the mass on a spring model. In reality the **MIM** assembly was suspended on a foam matting, the compliance and damping of which has been neglected. Also neglected were the contributions of any rotational or in-plane DoFs. However, regardless of the difference in amplitude, Figure 3.10 clearly shows that the dynamic transfer impedance obtained from one assembly may be used to predict the response of another with good accuracy. This not only confirms the transferability of the dynamic transfer impedance/stiffness, but also that it is in fact the true impedance/stiffness of the mount.

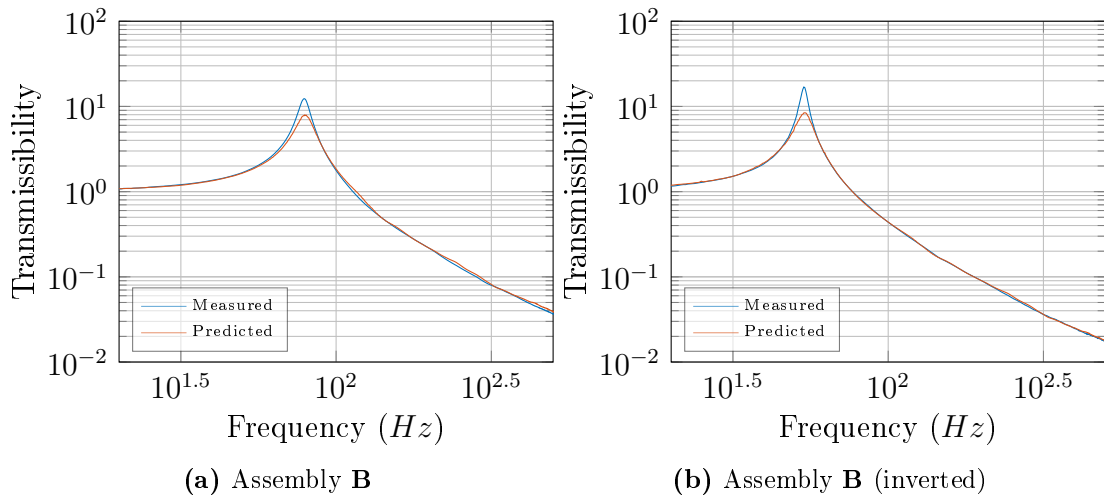


Figure 3.10: Measured and predicted transmissibilities of assembly **B** obtained using a dynamic stiffness determined from assembly **A**.

MASS-ISOLATOR-PLATE - In reality, it is unlikely that either the source or receiver sub-structure will behave like an ideal mass. It is therefore of interest to assess the performance of the in-situ approach on resonant assemblies. We will first consider a partly resonant mass-isolator-plate (**MIP**) assembly. Further details on the construction of this assembly are presented in Table 3.3. Again, with the mass-like nature of the source sub-structure, only the full interface approach is considered here. The partial interface approach will be considered in the next study.

Tag	Type	Assembly Details ($h \times w \times l$)
E	MIP	Source mass 0.86kg, receiver plate $50\text{cm} \times 75\text{cm} \times 0.7\text{cm}$, resilient element: Fibet 2525vv18 60 IRHD

Table 3.3: Details on the construction of the Mass-Isolator-Plate assembly.

The experimental set-up for the **MIP** assembly is shown diagrammatically in Figure 3.11, where two spaced accelerometer pairs are adhered above and below the isolator. The measurement procedure here follows that of assemblies **A-D**, where forces were applied at each accelerometer position. The resulting mobility matrix was averaged, and inverted, as per Equation 3.14. Stiffness values were subsequently determined from the off diagonal elements.

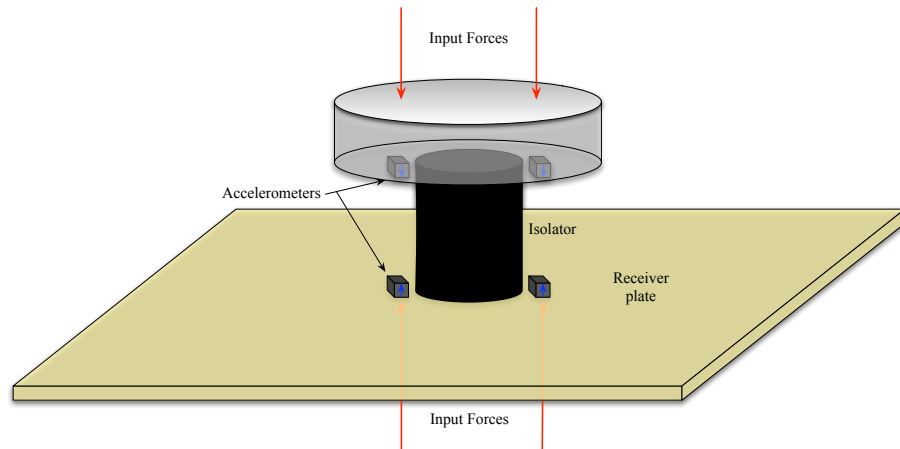
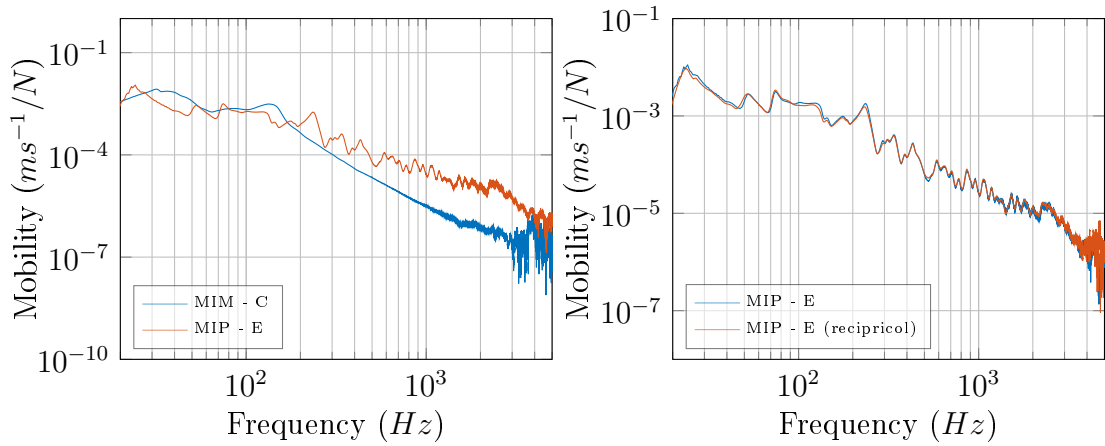


Figure 3.11: Diagrammatic representation of the mass-isolator-plate test rig, **E**. Red arrows correspond to the direction and position of the applied forces, whilst blue arrows indicate the positive direction of the measured accelerations.

Shown in Figure 3.12 are the results obtained from assembly **E**, compared against those from assembly **C**.⁴ Shown in Figure 3.12a are the transfer mobilities measured across the isolator in assemblies **E** (orange) and **C** (black). As one would expect with the introduction of a resonant substructure, the transfer mobility of assembly **E** is made up of multiple resonances, differing significantly from that of assembly **C**. Shown in Figure 3.12c are the dynamic transfer stiffnesses determined from the two assemblies. Also shown is the reciprocal dynamic transfer stiffness obtained from assembly **E**. It can be seen that, regardless of the huge between their transfer mobilities, their dynamic transfer stiffnesses are in good agreement. The stiffness

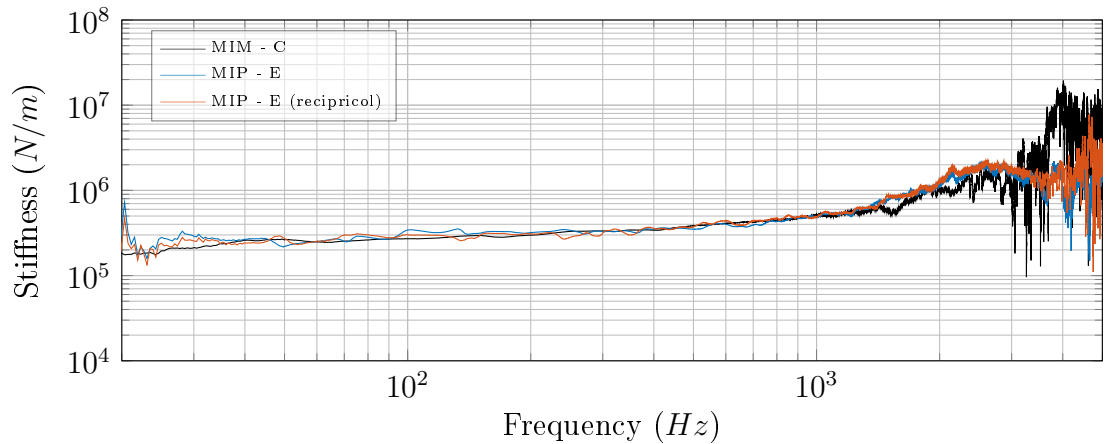
⁴Through the remainder of this Chapter we will consider the stiffness determined from assembly **C** as the ‘true’ stiffness, and use it for comparative purposes.

values determined from assembly **E** can be seen to vary slightly above and below that of assembly **C**, whilst clearly displaying the correct overall characteristics. As demonstrated previously, these variations, about what we will consider the ‘target’ stiffness, are likely due to discrepancies in the mobility matrices’ reciprocal agreement. Additionally, it can be seen that due to the lower inertia of the plate-like receiver sub-structure, a more defined high frequency stiffness is obtained, from which the first internal isolator resonance can be observed. The transfer mobilities



(a) Transfer mobility $Y_{C_{c1c2}}$ of assembly **C** and **E**

(b) Transfer mobilities $Y_{C_{c1c2}}$ and $Y_{C_{c2c1}}$ of assembly **E** showing reciprocity



(c) Dynamic transfer stiffness $K_{I_{c1c2}}$ of assembly **C** and **E**

Figure 3.12: Dynamic transfer stiffness and transfer mobility measurements made on assemblies **C** and **E** (see tables 3.2 and 3.3).

of assembly **E** are shown in Figure 3.12b. The reciprocal agreement is good across the entire frequency range. Some small deviations can be seen, particularly at lower frequencies, where the largest deviations in the stiffness are found. However, regardless of these small deviations, Figure 3.12 clearly shows that the in-situ method,

implemented via the full interface approach, is capable of determining a dynamic transfer stiffness, and thus independently characterising a resilient element whilst installed within a partly resonant assembly.

BEAM-ISOLATOR-PLATE - The last single contact case considered here is the beam-isolator-plate (**BIP**) assembly, **F**. Assembly **F** follows on from the partly resonant **MIP** assembly, where both source and receiver sub-structures now exhibit resonant behaviour. Further details on the construction of assembly **F** may be found in Table 3.4. A steel beam was chosen so as to introduce sharp, minimally damped resonances, representative of what may be encountered in a worst case practical scenario. A diagrammatic representation of this assembly is shown in Figure 3.13. With both source and receiver sub-structures now of a continuous nature, full *and* partial interface approaches are investigated.⁵

Tag	Type	Assembly Details
F	BIP	Source beam ($5cm \times 25cm \times 0.9cm$), receiver plate ($50cm \times 75cm \times 0.7cm$), resilient element: Fibet 2525vv18 60 IRHD

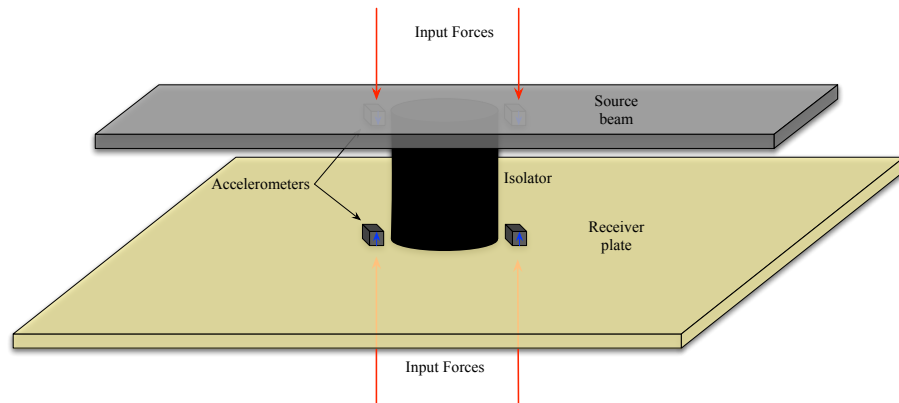
Table 3.4: Details on the construction of the Beam-Isolator-Plate assembly.

Let us first consider the full interface approach. The experimental set-up for this is shown diagrammatically Figure 3.13a, where two spaced accelerometer pairs are adhered above and below the mount. The measurement procedure here follows that of assemblies **A-E**, where forces are applied at each accelerometer position. The resulting mobility matrix was averaged, and inverted, as per Equation 3.14. Stiffness values were subsequently determined from the off diagonal transfer elements.

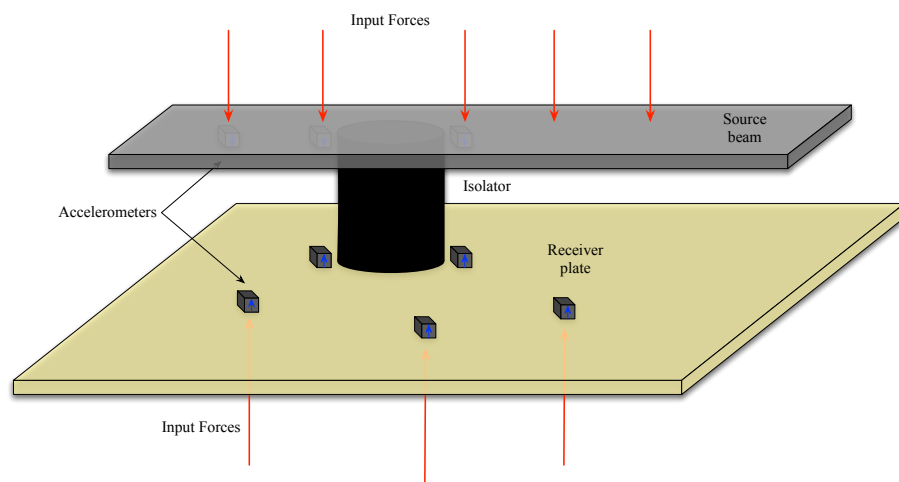
Shown in Figure 3.14b are the transfer mobilities measured across assemblies **C** (black) and **F** (orange). As we have come to expect, the two transfer mobilities differ considerably, with the mobility of assembly **F** now containing both damped and undamped resonances from the receiver and source sub-structures, respectively. Shown in Figure 3.14a are the dynamic transfer stiffness (and its reciprocal) determined from assembly **F** (blue and orange). Also shown is the stiffness obtained from the **MIM** assembly **C** (black). On inspection it can be seen that a large resonant artefact

⁵It is worth noting that although the partial interface approach appears simpler with regards to the experimental set-up, Figure 3.13b represents the experimental set-up required to over-determine the problem in multiple ways. In practise the partial interface approach arguably provides a simpler experimental procedure as only a single interface excitation is required.

occurs at approximately 500Hz. Further investigation reveals that this is the same frequency at which the transfer mobility's primary anti-resonance occurs.



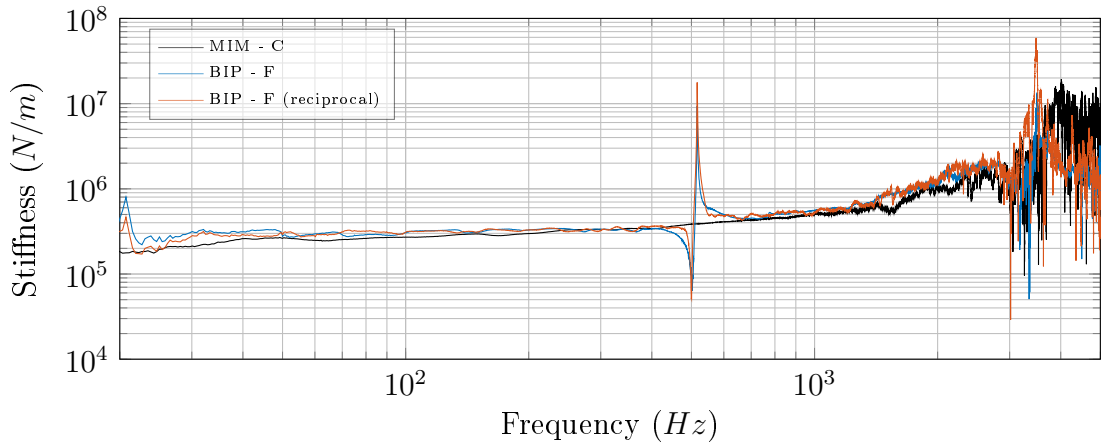
(a) Full interface set-up



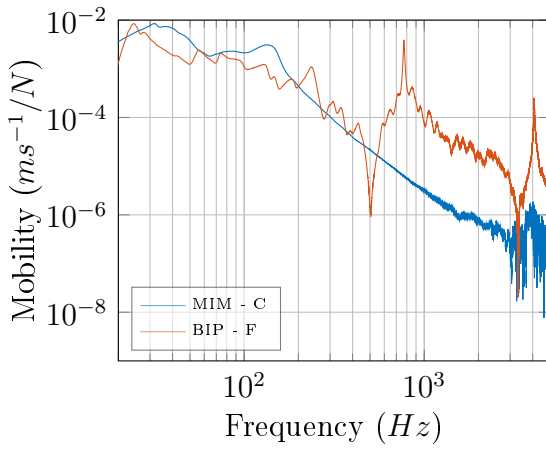
(b) Partial interface set-up

Figure 3.13: Diagrammatic representation of the beam-isolator-plate test rig, \mathbf{F} , showing both full and partial interface measurement set-ups. Red arrows correspond to the direction and position of the applied forces, whilst blue arrows indicate the positive direction of the measured accelerations.

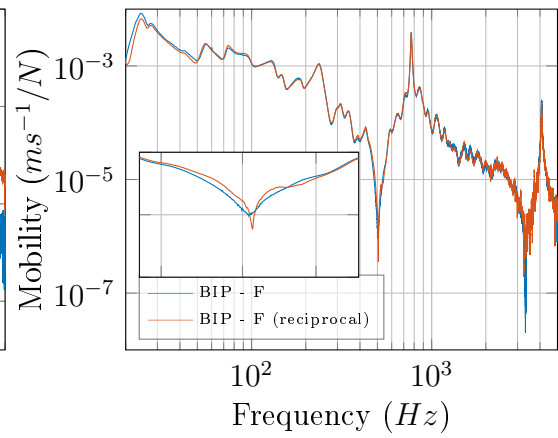
The disagreement between reciprocal transfer mobilities, about this anti-resonance, is shown more clearly in the in-set of Figure 3.14c. This discrepancy is likely caused by an inaccuracy in the excitation at the contact interfaces. With anti-resonances being dependent upon excitation and response position, they are particularly sensitive to experimental error, i.e. hammer inaccuracy. Interestingly, the stiffness in the region of the transfer mobility's primary resonance (approx 800Hz) is free from any such artefacts. This is because resonances are determined by the geometrical and material properties of the sub-structure/assembly.



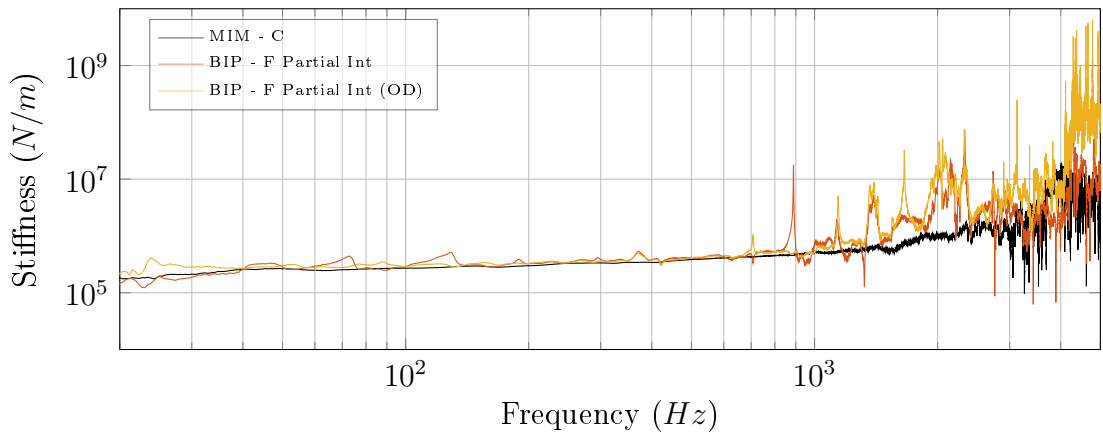
(a) Dynamic transfer stiffness $K_{I_{c1c2}}$ of assembly **F** and **C** (see tables 3.2 and 3.4) using the full interface approach.



(b) Transfer mobility $Y_{C_{c1c2}}$ of assembly **C** and **F**

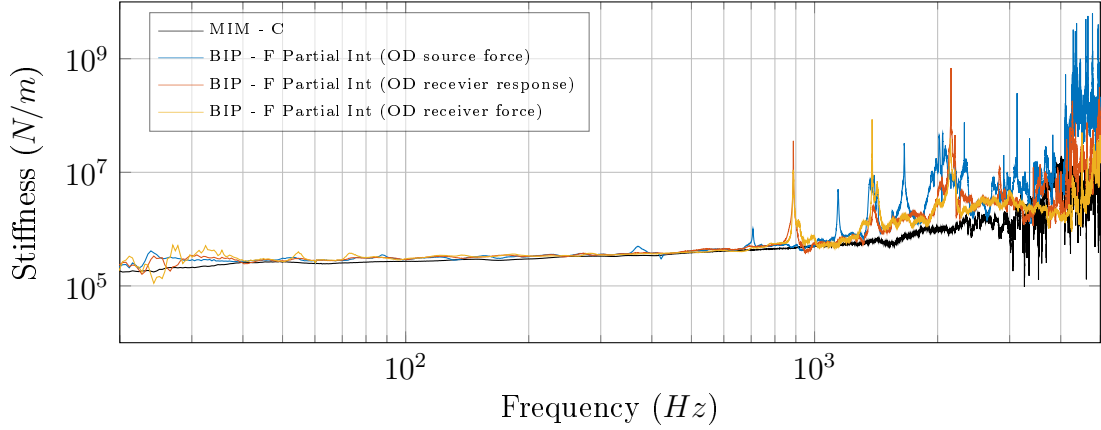


(c) Transfer mobilities $Y_{C_{c1c2}}$ and $Y_{C_{c2c1}}$ of assembly **F**. (Inset covers frequency range 438-581Hz)



(d) Dynamic transfer stiffness $K_{I_{c1c2}}$ of assembly **F** and **C** determined via partial and full interface approaches.

Figure 3.14: Dynamic transfer stiffness and transfer mobility measurements made on assemblies **C** and **F** using partial interface approach.



(e) Dynamic transfer stiffness $K_{I_{c1c2}}$ of assembly **C** and **F**.

Figure 3.14: (Continued) Dynamic transfer stiffness and transfer mobility measurements made on assemblies **C** and **F** using partial interface approach.

The resonances are therefore invariant to excitation or response position and do not vary between impacts.

With the exception of this anti-resonance error, the stiffnesses determined from assembly **F** are in good agreement with that of assembly **C**, with some small deviations occurring below approximately 40Hz.

Let us now consider the partial interface approach. Unlike the full interface, the partial approach requires remote measurement positions on both source and receiver sub-structures. Referring back to Equation 3.11,

$$\mathbf{Z}_{I_{c2c1}} = [\mathbf{Y}_{C_{c1a}} \mathbf{Y}_{C_{ba}}^{-1} \mathbf{Y}_{C_{bc2}} - \mathbf{Y}_{C_{c1c2}}]^{-1}$$

the mobilities required are; $\mathbf{Y}_{C_{c1a}}$, $\mathbf{Y}_{C_{ba}}$, $\mathbf{Y}_{C_{bc2}}$, and $\mathbf{Y}_{C_{c1c2}}$. At this point it is worth noting that the principle of reciprocity may be used to manipulate Equation 3.11 in a number of ways. In its standard form, over-determination can be achieved through the use of additional applied forces at a , or additional responses at b . Although, since it is generally more convenient to over-determine a problem by use of additional forces, as it requires no additional measurement equipment, we may use the reciprocal relations; $\mathbf{Y}_{C_{ba}}^{-1} = \mathbf{Y}_{C_{ab}}^{-T}$ and $\mathbf{Y}_{C_{bc2}} = \mathbf{Y}_{C_{c2b}}^T$, to manipulate Equation 3.11 such that it allows for the over-determination at b via additional applied forces, as opposed to responses.

$$\mathbf{Z}_{I_{c2c1}} = [\mathbf{Y}_{C_{c1a}} \mathbf{Y}_{C_{ab}}^{-T} \mathbf{Y}_{C_{c2b}}^T - \mathbf{Y}_{C_{c1c2}}]^{-1} \quad (3.29)$$

In order to implement these over-determination approaches, multiple remote measurement positions have been included on both source and receiver sub-structures. The experimental set-up for this is shown diagrammatically in Figure 3.13b where, in addition to the two spaced accelerometer pairs, a single remote accelerometer is placed on the source sub-structure, with a further 3 placed on the receiver sub-structure. Here we are not considering the over-determination at a via responses, therefore only a single remote source side accelerometer was required. The measurement procedure may be outlined as follows:

- 1 Forces are applied at each of the three remote source positions, a , and the transfer mobilities $\mathbf{Y}_{\mathbf{C}_{c1a}}$ and $\mathbf{Y}_{\mathbf{C}_{ba}}^{-1}$ are measured.
 - 2 Forces are applied at the interface, c_2 , and the transfer mobilities $\mathbf{Y}_{\mathbf{C}_{bc2}}$ and $\mathbf{Y}_{\mathbf{C}_{c1c2}}$ are measured.
 - 3 Forces are applied at the three remote receiver positions, b , and the transfer mobilities $\mathbf{Y}_{\mathbf{C}_{ab}}^{-1}$ and $\mathbf{Y}_{\mathbf{C}_{c2b}}$ are measured. (This step is only required if a force over-determination at b is sought)
- * Spaced forces and responses at interfaces c_1 and c_2 are averaged such that they provide the central force and response.

The advantage of the partial interface approach is evident here in that it requires only a single mount transfer mobility to be measured, allowing the practitioner to avoid an ‘inaccessible’ contact interface or, in our case, interface c_1 . Furthermore, the partial approach may be over-determined through the use of additional excitation or response measurements at the remote DoFs, a or b .

Shown in Figure 3.14d are the dynamic transfer stiffnesses obtained from assembly \mathbf{F} via the determined (orange) and over-determined (yellow) partial interface approach. Here the over-determined stiffness is achieved through additional forces applied remotely on the source. A comparison against the full interface stiffness, presented in Figure 3.14a, clearly shows that the reciprocity-related artefact at $500Hz$ has been avoided. This is likely due to the partial interface approach only requiring a single mount transfer mobility, with reciprocity implicitly assumed. Beyond this resonant artefact, relatively good agreement is achieved when compared against the **MIM** stiffness of assembly \mathbf{C} (black). Through the use of over-determination it can be seen that a number of the artefacts observed in the determined case are avoided,

including those at 70, 130 and 900Hz, albeit at the expense of slightly worse agreement below 40Hz. Above approximately 1000Hz a number of resonant artefacts are observed. In this region the over-determined prediction appears to offer little improvement.

Lastly, shown in Figure 3.14e are the over-determined stiffnesses resulting from; additional source excitations (blue), receiver excitations (yellow) and receiver responses (orange). It can be seen that in the region 40-900Hz the three over-determined stiffness are in good agreement. Beyond this the three approaches differ slightly, with the introduction of different resonant artefacts. Regardless of this disagreement, Figure 3.14e clearly shows that over-determination via additional forces or responses, on either sub-structure, can be used to provide reasonable stiffness values.

3.4.2 MULTIPLE CONTACT

An advantage of the in-situ approach over other currently available methods is its ability to determine the dynamic transfer stiffness in multiple DoFs simultaneously. These DoFs may be either coordinate based (i.e. rotational and in-plane DoF) or positional (i.e multiple isolators). In this Section the application of the in-situ approach to the simultaneous characterisation of multiple resilient elements within a multi-contact resonant assembly is investigated. The beam-isolator(2)-plate (**BI(2)P**) assembly considered here consists of a steel beam resiliently mounted to a perspex plate via two resilient elements. It is believed that the highly resonant and multi-contact nature of this assembly is likely more challenging than what would often be encountered in a practical scenario.

BEAM-ISOLATOR(2)-PLATE - For the beam-isolator(2)-plate assembly a steel beam is resiliently mounted to a perspex plate via two mounts, as shown diagrammatically in Figure 3.15. For consistency, the same mount type has been used as in assemblies **C-F**. Further assembly details are given in Table 3.5.

Let us consider first the full interface approach. The experimental set-up for this is shown diagrammatically in Figure 3.15a, where a spaced accelerometer pair is adhered above and below *each* mount. The measurement procedure here follows that of the single contact case, where forces are applied at each accelerometer position, except now, an 8×8 mobility matrix is constructed. The spaced forces and responses are averaged to give the 4×4 contact interface mobility matrix. Inversion

and extraction of the off diagonals, as per Equation 3.14, yields dynamic transfer impedance, from which the transfer stiffnesses are calculated.

Tag	Type	Assembly Details
G	BI(2)P	Source beam ($3.7\text{cm} \times 45\text{cm} \times 0.9\text{cm}$), receiver plate ($50\text{cm} \times 75\text{cm} \times 0.7\text{cm}$), resilient element: Fibet 2525vv18 60 IRHD

Table 3.5: Details on the constructions of the Beam-Isolator(2)-Plate assembly.

With the contact interface matrix of dimension 4×4 the resultant off-diagonal transfer impedance element is a 2×2 sub-matrix containing the transfer impedance of each isolator,

$$\left[\begin{array}{cc|cc} \mathbf{Z}_{C_{c11c11}} & \mathbf{Z}_{C_{c11c12}} & \mathbf{Z}_{I_{c11c21}} & \mathbf{Z}_{I_{c11c22}} \\ \mathbf{Z}_{C_{c12c11}} & \mathbf{Z}_{C_{c12c12}} & \mathbf{Z}_{I_{c12c21}} & \mathbf{Z}_{I_{c12c22}} \\ \hline \mathbf{Z}_{I_{c21c11}} & \mathbf{Z}_{I_{c21c12}} & \mathbf{Z}_{C_{c21c21}} & \mathbf{Z}_{C_{c21c22}} \\ \mathbf{Z}_{I_{c22c11}} & \mathbf{Z}_{I_{c22c12}} & \mathbf{Z}_{C_{c22c21}} & \mathbf{Z}_{C_{c22c22}} \end{array} \right] = \left[\begin{array}{cc|cc} \mathbf{Y}_{C_{c11c11}} & \mathbf{Y}_{C_{c11c12}} & \mathbf{Y}_{C_{c11c21}} & \mathbf{Y}_{C_{c11c22}} \\ \mathbf{Y}_{C_{c12c11}} & \mathbf{Y}_{C_{c12c12}} & \mathbf{Y}_{C_{c12c21}} & \mathbf{Y}_{C_{c12c22}} \\ \hline \mathbf{Y}_{C_{c21c11}} & \mathbf{Y}_{C_{c21c12}} & \mathbf{Y}_{C_{c21c21}} & \mathbf{Y}_{C_{c21c22}} \\ \mathbf{Y}_{C_{c22c11}} & \mathbf{Y}_{C_{c22c12}} & \mathbf{Y}_{C_{c22c21}} & \mathbf{Y}_{C_{c22c22}} \end{array} \right]^{-1} \quad (3.30)$$

where c_{11} and c_{12} are the source-isolator interfaces at first and second mount, respectively. Similarly, c_{21} and c_{22} are the isolator-receiver interfaces for the first and second mount, respectively. The transfer impedances of interest here are $\mathbf{Z}_{I_{c11c21}}$ and $\mathbf{Z}_{I_{c12c22}}$, and their reciprocal values $\mathbf{Z}_{I_{c21c11}}$ and $\mathbf{Z}_{I_{c22c12}}$, respectively.

Shown in Figures 3.16a and 3.16b are the dynamic transfer stiffnesses obtained for each mount (orange), including their reciprocal values (yellow). Also shown is the stiffness obtained from the **MIM** assembly, **C** (black). It should be noted that although the mounts used in assembly **G** were of the same type, neither were the actual mount used in assembly **C**. As such, their stiffnesses may differ slightly due to manufacturing tolerances. That said, the stiffnesses determined from assembly **G** are in fair agreement with those from assembly **C**, and certainly display the overall expected characteristics. A slight over-prediction of the stiffness can be seen in both cases when compared against that of assembly **C**. These deviations are likely due to the small differences between individual isolators, and the slight change in their mounting conditions resulting from the assembly's multi-contact nature.

Like the stiffnesses observed in the **BIP** case of Figure 3.14a, the stiffnesses here can be seen to exhibit a number of resonant artefacts. The first two of these can

clearly be attributed to assembly anti-resonances occurring at approximately 250Hz and 500Hz. These anti-resonances can be observed in the transfer mobilities $\mathbf{Y}_{C_{c11c21}}$ and $\mathbf{Y}_{C_{c12c22}}$, presented in Figures 3.16c and 3.16d, respectively. The remaining artefacts are likely caused by other assembly anti-resonances, or combinations thereof, that are not so clearly identified within the assemblies mobility matrix. Regardless, Figures 3.16a and 3.16b clearly demonstrate that the full interface approach is capable of characterising multiple elements simultaneously, albeit with some degree of contamination about assembly anti-resonances.

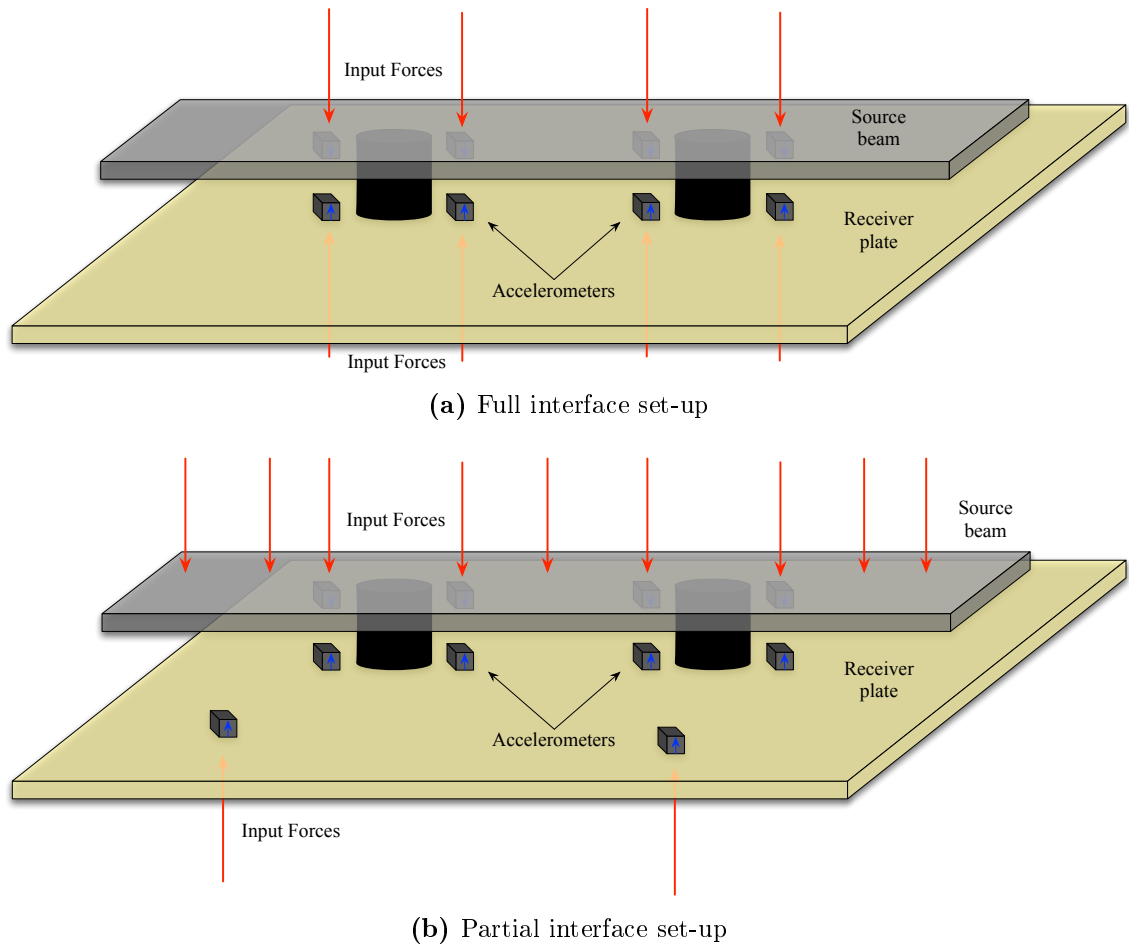
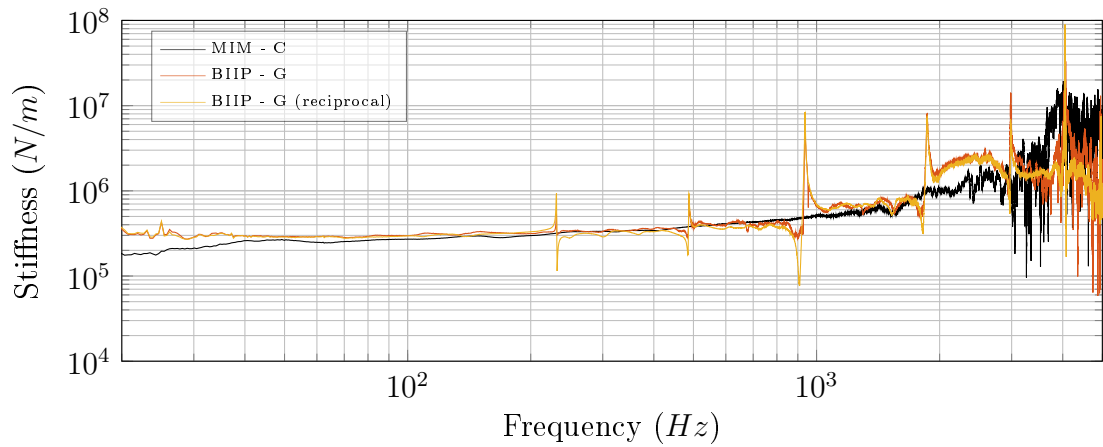
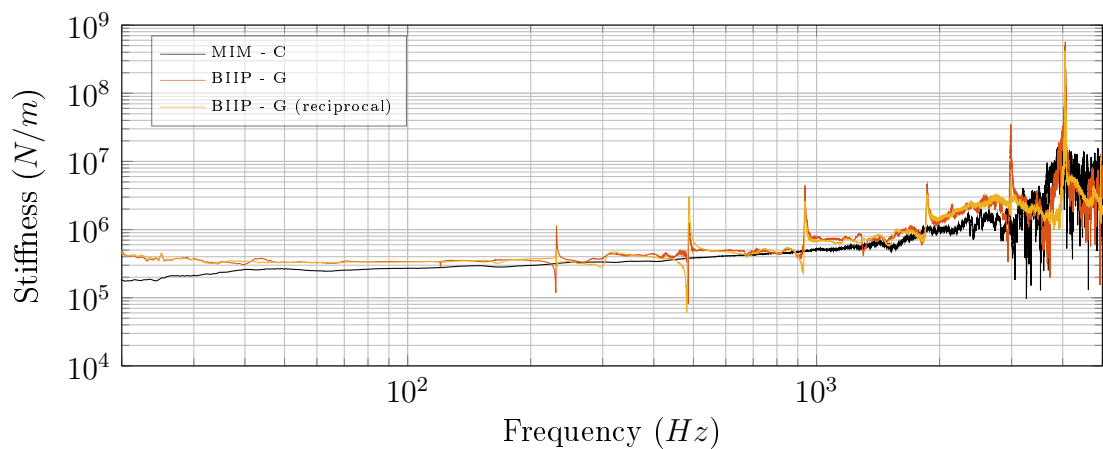


Figure 3.15: Diagrammatic representation of the beam-isolator(2)-plate test rig, \mathbf{G} , for full and partial interface measurements. Red arrows correspond to the direction and position of the applied forces, whilst blue arrows indicate the positive direction of the measured accelerations.

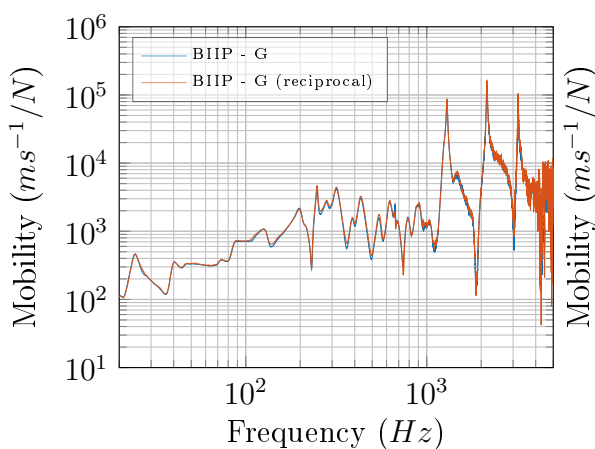
Let us now consider the partial interface approach. As in the single contact case, the partial interface approach requires the mobilities; $\mathbf{Y}_{C_{c1a}}$, $\mathbf{Y}_{C_{ba}}$, $\mathbf{Y}_{C_{bc2}}$, and $\mathbf{Y}_{C_{c1c2}}$, or some reciprocal variation thereof, depending upon the over-determination approach implemented.



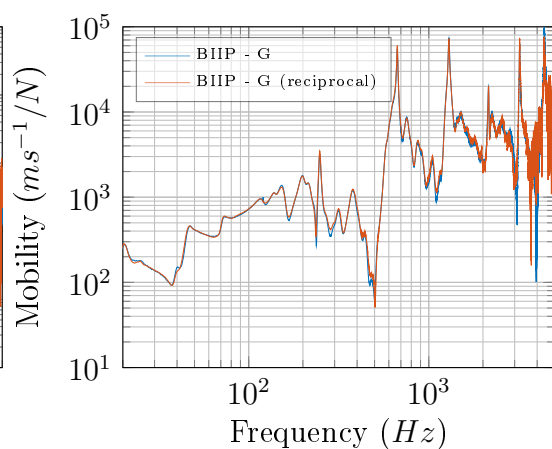
(a) Dynamic transfer stiffnesses $K_{I_{c11c21}}$ and $K_{I_{c21c11}}$ of isolator 1 in assembly **G**, and $K_{I_{c1c2}}$ of assembly **C**, determined using full interface approach.



(b) Dynamic transfer stiffnesses $K_{I_{c12c21}}$ and $K_{I_{c22c12}}$ of isolator 2 in assembly **G**, and $K_{I_{c1c2}}$ of assembly **C**, determined using full interface approach.

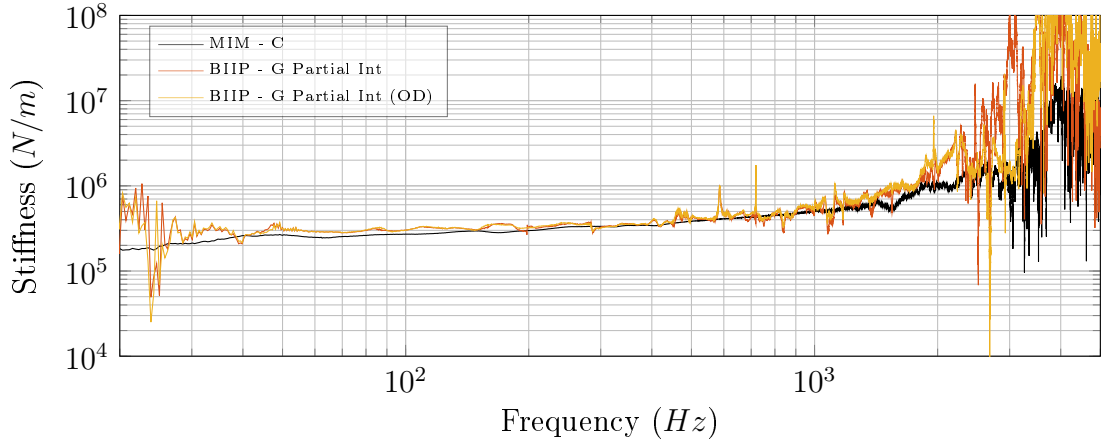


(c) Transfer mobilities $Y_{C_{c11c21}}$ and $Y_{C_{c21c11}}$ of assembly **G**.

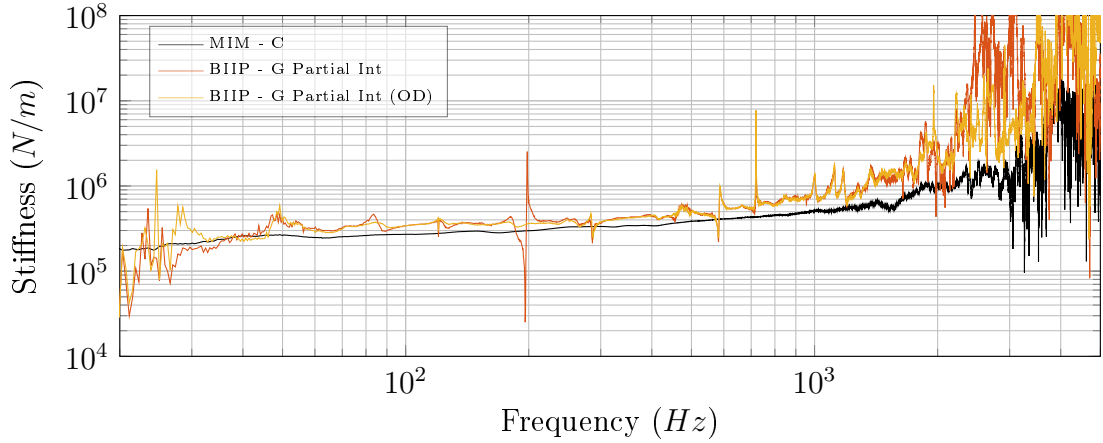


(d) Transfer mobility $Y_{C_{c12c22}}$ and $Y_{C_{c22c12}}$ of assembly **G**.

Figure 3.16: Dynamic transfer stiffness and transfer mobility measurements made on assemblies **C** and **G** (see tables 3.2 and 3.5) using full and partial interface approach.



(e) Dynamic transfer stiffnesses $K_{I_{c11c21}}$ and $K_{I_{c21c11}}$ of isolator 1 in assembly **G**, and $K_{I_{c1c2}}$ of assembly **C**, determined using partial and full interface approaches, respectively.



(f) Dynamic transfer stiffnesses $K_{I_{c12c22}}$ and $K_{I_{c22c12}}$ of isolator 2 in assembly **G**, and $K_{I_{c1c2}}$ of assembly **C**, determined using partial and full interface approaches, respectively.

Figure 3.16: (Continued) Dynamic transfer stiffness and transfer mobility measurements made on assemblies **C** and **G** (see tables 3.2 and 3.5) using full and partial interface approach.

Here we will consider only the source side over-determination via additional forces. As such, we avoid any reciprocal substitutions. The experimental set-up for this is shown diagrammatically in Figure 3.15b where, in addition to the spaced accelerometer pairs, 2 remote accelerometers are included on the receiver sub-structure.

The measurement procedure follows that of the single contact case (whilst accounting for the two coupling elements and the 5 remote source side excitations). In this case, step 3 may be ignored since only a source side over-determination is considered.

Shown in Figures 3.16e and 3.16f are the stiffnesses obtained via the partial interface approach for both determined (orange) and over-determined (yellow) cases. As observed in assembly **F**, the partial interface approach avoids the resonant artefacts encountered via the full interface approach. However, this is done at the cost of arguably poorer overall performance, particularly at low frequencies, that is, below around 40Hz. Over-determination can be seen to be particularly beneficial in the determination of $K_{I_{c12c22}}$, where it completely avoids the 200Hz artefact observed in the determined stiffness. Regardless, Figures 3.16e and 3.16f clearly demonstrate that the partial interface approach is capable of simultaneously characterising multiple elements whilst installed within a highly resonant assembly.

3.5 CONCLUDING REMARKS

This Chapter has been concerned with the development and validation of an in-situ method for the independent characterisation of resilient coupling elements. Following a theoretical development, two variants of the in-situ approach were presented, namely the ‘partial’ and ‘full’ interface impedance relations. These were validated numerically using a simplified beam model and, later, experimentally using a number of increasingly complex assembly types. Promising results were obtained in all cases, with the partial interface approach appearing to be the more reliable of the two, likely due to the over-determination that it permits.

It is important to reiterate that the proposed approach allows for the in-situ determination of the dynamic *transfer* impedance. The driving point impedances obtained through the full interface approach are properties of the coupled assembly, not the coupling element. Determination of the driving point impedance would require further assumptions, or the implementation of a sub-structure decoupling procedure, neither of which are considered here.

In the next Chapter the in-situ approach is further extended via a number of state-of-the-art experimental methods so as to provide a more robust and flexible characterisation method.

EXPERIMENTAL EXTENSIONS

In this Chapter the in-situ approach presented previously is further extended through the incorporation of advanced experimental techniques, including; the finite difference approximation, the round trip identity and the concept of generalised transmissibility. Together, the in-situ approach, alongside the proposed extensions, aims to provide a powerful characterisation tool that is capable of circumventing many of the experimental hurdles faced in practice.

CONTENTS

4.1	Rotational Degrees of Freedom	64
4.2	Extension to Remote Measurement Positions	73
4.3	Operational Characterisation via the Generalised Transmissibility	88
4.4	Concluding Remarks	100

4.1 ROTATIONAL DEGREES OF FREEDOM

Previous literature has shown that although not always necessary, rotational DoFs can play an important role in the coupling of mechanical sub-structures [57]. As such, an experimentally robust characterisation method must be capable of accounting for rotational DoFs in some way. Although current methods allow for the characterisation of rotational DoFs, they often rely upon either; numerous test rigs, involving multiple excitation and termination arrangements [109, 111], or are based upon assumption that limits their application [101]. In the former, each coordinate-DoF requires a different excitation and termination arrangement and is determined separately. The full characterisation of an element is therefore a laborious and time

intensive procedure. Furthermore, an assumption is made with regards to the behaviour of the terminating condition, which is often only approximately met over a narrow frequency range. The later approach [101], being based on rigid body theory, imposes significant restrictions on the nature of the source and receiver sub-structures and, additionally, does not allow for the effect of pre-load to be accounted for.

The generality of the in-situ method presented in Section 3.2 harbours no limitations with regards to the number of DoFs being solved for, the effect of pre-load, or the nature of the source and receiver sub-structures. That is providing one can accurately excite and measure the DoFs of interest and, furthermore, that the intended application remains locally linear to that of the characterisation.

It is the aim of this Section to further extend the proposed in-situ approach so as to facilitate the simultaneous determination of both translational and rotational dynamic transfer stiffnesses. The main challenge to overcome with such an aim is that of an accurate and convenient moment excitation, a topic that has received much interest over the years. Consequently, a plethora of experimental methods have been proposed, including; twin shaker arrangements [121], blocks [122–124], magnetostrictive exciters [125, 126] and synchronised hammers [127]. A more detailed review these methods may be found in [128].

More recently, an interesting approach was proposed by Moorhouse et al. [44] whereby moment excitation is avoided altogether and instead replaced by a number of translational excitations remote to the point of interest. Coined as the ‘round trip’, this approach, in theory, allows for the determination of a complete mobility matrix, including rotational, in-plane and cross terms, without having to excite any moments or in-plane forces directly. An alternative approach, originally proposed by Sattinger [129] and further developed by Elliott et al [128], is that of the finite difference approximation. Employing a pair of translational excitation and responses, separated by a finite distance, the finite difference approach allows for both moment excitation and angular velocities to be approximated without having to directly apply or measure either. The finite difference approach has the advantage of not requiring any modifications to be made to the structure under investigation and, furthermore, requires only standard measurement equipment. The finite difference approximation therefore offers a convenient way to include rotational DoFs within the in-situ approach. A similar approach, coined the ‘virtual point transformation’,

has been proposed by Van der Seijs et al [130]. The virtual point approach relies on the kinematic relations between a set of locally remote DoFs and the ‘virtual point’ at which the translational and rotational DoFs are required. The virtual point transformation may be considered a generalisation of the finite difference approach, whereby the measurement positions are not restricted to a spaced pair centred about the position of interest. Although promising results have been demonstrated, the approach requires very precise knowledge of each sensor’s position and orientation with respect to the virtual point. As such, its implementation is rather involved.

The remainder of this Section will focus on the incorporation of the finite difference approximation within the in-situ approach.

4.1.1 FINITE DIFFERENCE APPROACH

We will begin by introducing the finite difference approximation for a single positional-DoF on an arbitrary structure C , where the only coordinate-DoFs of interest are those of translation, z , and its axial rotation. For such a structure the point mobility matrix at the positional-DoF 0, is given by,

$$\mathbf{Y}_{\mathbf{C}00} = \begin{bmatrix} Y_{C_{v_0 f_0}} & Y_{C_{v_0 \tau_0}} \\ Y_{C_{\psi_0 f_0}} & Y_{C_{\psi_0 \tau_0}} \end{bmatrix} \quad (4.1)$$

where, τ_0 and α_0 represent the applied moment and resultant angular velocity at position 0, respectively. Each element of Equation 4.1 may be defined explicitly as,

$$Y_{C_{v_0 f_0}} = \frac{v_0}{f_0} \Big|_{\tau_0=0}, \quad Y_{C_{v_0 \tau_0}} = \frac{v_0}{\tau_0} \Big|_{f_0=0}, \quad Y_{C_{\psi_0 f_0}} = \frac{\psi_0}{f_0} \Big|_{\tau_0=0}, \quad Y_{C_{\psi_0 \tau_0}} = \frac{\psi_0}{\tau_0} \Big|_{f_0=0}. \quad (4.2)$$

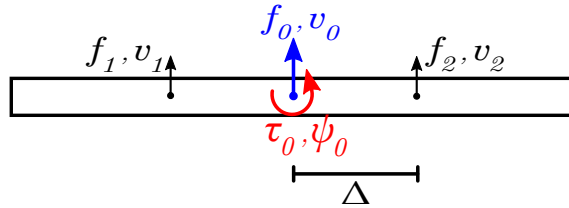


Figure 4.1: Force and velocity positions for finite difference approximation.

Let us now consider the pair of applied forces, f_1 and f_2 , and their resultant velocities, v_1 and v_2 , at two positional-DoFs centred about 0, and separated by a finite distance 2Δ , as shown in Figure 4.1. It was shown by Sattinger [129], and later by

Elliott et al. [128], that the translational, rotational and cross mobilities of Equation 4.2 may be approximated from the translational mobilities measured at 1 and 2 according to,

$$\tilde{Y}_{v_0 f_0} \approx \frac{Y_{v_1 f_1} + Y_{v_2 f_1} + Y_{v_1 f_2} + Y_{v_2 f_2}}{4} \quad (4.3)$$

$$\tilde{Y}_{\psi_0 f_0} \approx \frac{-Y_{v_1 f_1} + Y_{v_2 f_2}}{4\Delta} \quad (4.4)$$

$$\tilde{Y}_{v_0 \tau_0} \approx \frac{-Y_{v_1 f_1} + Y_{v_2 f_2}}{4\Delta} \quad (4.5)$$

$$\tilde{Y}_{\psi_0 \tau_0} \approx \frac{Y_{v_1 f_1} - Y_{v_2 f_1} - Y_{v_1 f_2} + Y_{v_2 f_2}}{4\Delta^2} \quad (4.6)$$

where, $\tilde{}$ represents an approximation via finite difference. A convenient matrix form is given by,

$$\begin{bmatrix} \tilde{Y}_{v_0 f_0} & \tilde{Y}_{v_0 \tau_0} \\ \tilde{Y}_{\psi_0 f_0} & \tilde{Y}_{\psi_0 \tau_0} \end{bmatrix} \approx \begin{bmatrix} \frac{1}{2} & \frac{1}{2} \\ \frac{-1}{2\Delta} & \frac{1}{2\Delta} \end{bmatrix} \begin{bmatrix} Y_{v_1 f_1} & Y_{v_1 f_2} \\ Y_{v_2 f_1} & Y_{v_2 f_2} \end{bmatrix} \begin{bmatrix} \frac{1}{2} & \frac{-1}{2\Delta} \\ \frac{1}{2} & \frac{1}{2\Delta} \end{bmatrix} \quad (4.7)$$

or more compactly as,

$$\tilde{\mathbf{Y}} = \mathbf{B}\mathbf{Y}\mathbf{B}^T \quad (4.8)$$

where \mathbf{B} is a finite difference transformation matrix. The pre-multiplication of \mathbf{Y} by \mathbf{B} may therefore be considered a row based operation that yields the translational and angular responses, whilst post-multiplication may be considered a column based operation that yields the translational force and moment excitations.

With a full derivation of the finite difference equations presented by Elliott et al. [128] alongside an experimental validation and numerical error analysis, neither will be provided here. However, it is worth noting that the error analysis carried out by Elliott et al. showed the resultant error, for an analytical beam, to be inversely proportional to bending stiffness and mobility magnitude, whilst being proportional to separation distance Δ and frequency. This error introduces a bandwidth over which the finite difference approximation valid. Above this, the bending wavelength becomes comparable to the sensor spacing and large deviations arise due to the breakdown of locally rigid behaviour; below, where the bending wavelength is very large compared to that of the sensor spacing, the measured mobilities are similar enough that noise is introduced as a result of the differences required in the approximation. The finite difference method is thus limited to a working frequency range dependent on the sensor spacing and frequency range of interest.

The incorporation of the finite difference approximation within the in-situ approach allows, in theory, for the simultaneous characterisation of both translational and rotational DoFs. Our aim may thus be achieved with the use of minimal additional hardware and experimental effort. However, application of the finite difference approach does require each mount interface to be instrumented with a spaced pair of accelerometers.¹

With the partial interface relation (see Equation 3.11) we are only concerned with determining the rotational DoFs at the coupling interfaces, c_1 and c_2 . Pre-multiplication of $\mathbf{Y}_{C_{c1a}}$ and $\mathbf{Y}_{C_{c1c2}}$, by the finite difference transformation matrix \mathbf{B} , yields a response at c_1 that includes both translation and angular velocities. Similarly, post-multiplication of $\mathbf{Y}_{C_{bc2}}$ and $\mathbf{Y}_{C_{c1c2}}$ by \mathbf{B}^T results in an excitation at c_2 that is a finite difference approximation including both force and moments. Factorising out the \mathbf{B} terms we arrive at the finite difference approximation for the partial interface relation.

Finite difference partial interface impedance relation:

$$\tilde{\mathbf{Z}}_{I_{c2c1}} = [\mathbf{B} (\mathbf{Y}_{C_{c1a}} \mathbf{Y}_{C_{ba}}^{-1} \mathbf{Y}_{C_{bc2}} - \mathbf{Y}_{C_{c1c2}}) \mathbf{B}^T]^{-1} \quad (4.9)$$

The full interface relation (see Equation 3.14) requires a block diagonal transformation matrix to be constructed. Subsequent pre- and post-multiplication of the contact interface mobility matrix by this block matrix yields the finite difference approximation for the full interface relation.

Finite difference full interface impedance relation:

$$\begin{bmatrix} \tilde{\mathbf{Z}}_{C_{c1c1}} & \tilde{\mathbf{Z}}_{I_{c1c2}} \\ \tilde{\mathbf{Z}}_{I_{c1c2}} & \tilde{\mathbf{Z}}_{C_{c2c2}} \end{bmatrix} = \left(\begin{bmatrix} \mathbf{B} & \mathbf{0} \\ \mathbf{0} & \mathbf{B} \end{bmatrix} \begin{bmatrix} \mathbf{Y}_{C_{c1c1}} & \mathbf{Y}_{C_{c1c2}} \\ \mathbf{Y}_{C_{c2c1}} & \mathbf{Y}_{C_{c2c2}} \end{bmatrix} \begin{bmatrix} \mathbf{B} & \mathbf{0} \\ \mathbf{0} & \mathbf{B} \end{bmatrix}^T \right)^{-1} \quad (4.10)$$

Equations 4.9 and 4.10 provide the finite difference approximations to Equations 3.11 and 3.14, respectively, and allow for the simultaneous characterisation in both translational and rotational DoFs.

¹Experimental studies presented thus far have made use of spaced accelerometer pairs. This was not an essential requirement, with numerous alternative approaches having been available, for example, a single centred accelerometer with a pair of spaced forces.

4.1.2 NUMERICAL VALIDATION

In order to validate the incorporation of the finite difference approximation a brief numerical study has been undertaken. Further to its validation, this study will allow for the influence of the error introduced via the finite difference approximation to be investigated. For consistency, a similar simulation is considered here as in Section 3.3, where the transfer impedance of an internal portion of a free-free beam is determined from a number of full length beam mobilities. In the previous numerical study translational, rotational and cross mobilities were calculated exactly according to Equations 3.16 and 3.17. In this study only translational mobilities are simulated. Rotational and cross mobilities are determined via the application of the finite difference approximation, as presented in Section 4.1.1. The excitation and response positions used here are identical to those used in the previous study, and are presented in Table 3.1, with the exception of the interface DoFs which are now located at $\pm\Delta$ those used previously. Simulations have been carried out for two finite difference spacings, 2cm and 3cm. Furthermore, no artificial noise has been included in these simulations.

Shown in Figure 4.2 are the rotational transfer impedances $\tilde{\mathbf{Z}}_{\mathbf{I}_{\psi 2\tau 1}}$, determined via the finite difference approximations of the partial (dot dashed orange and dashed yellow) and full (orange) interface approaches. Shown in Figures 4.2a and 4.2b are the transfer impedances determined for the $\Delta = 2cm$ spacing. Similarly, Figures 4.2c and 4.2d show the transfer impedances determined for $\Delta = 3cm$. It is clear from Figure 4.2 that the full interface approach is far more sensitive to the error introduced via finite difference approximation than that of the partial interface approach. The transfer impedances determined via the full interface approach are heavily contaminated by resonant artefacts and, furthermore, the resonant peaks located at approximately $300Hz$ and $900Hz$ are shifted considerably. In contrast, the transfer impedances determined via the partial interface approach exhibit no resonant artefacts, with only a minimal shift in resonant frequencies, as shown more clearly in the inset of Figures 4.2c and 4.2d. Also shown in Figures 4.2c and 4.2d are the three fold over-determined transfer impedances. The agreement between determined and over-determined predictions suggests that over-determination does not aid in reducing the error introduced via the finite difference approximation.

From further investigation it can be shown that the resonant artefacts observed in Figures 4.2a and 4.2b occur in regions where the mobility amplitude is at a

maximum, i.e. at resonances. For a single contact case the finite difference error in the mobility is inversely proportional to its magnitude, i.e. larger error in regions of low amplitude.

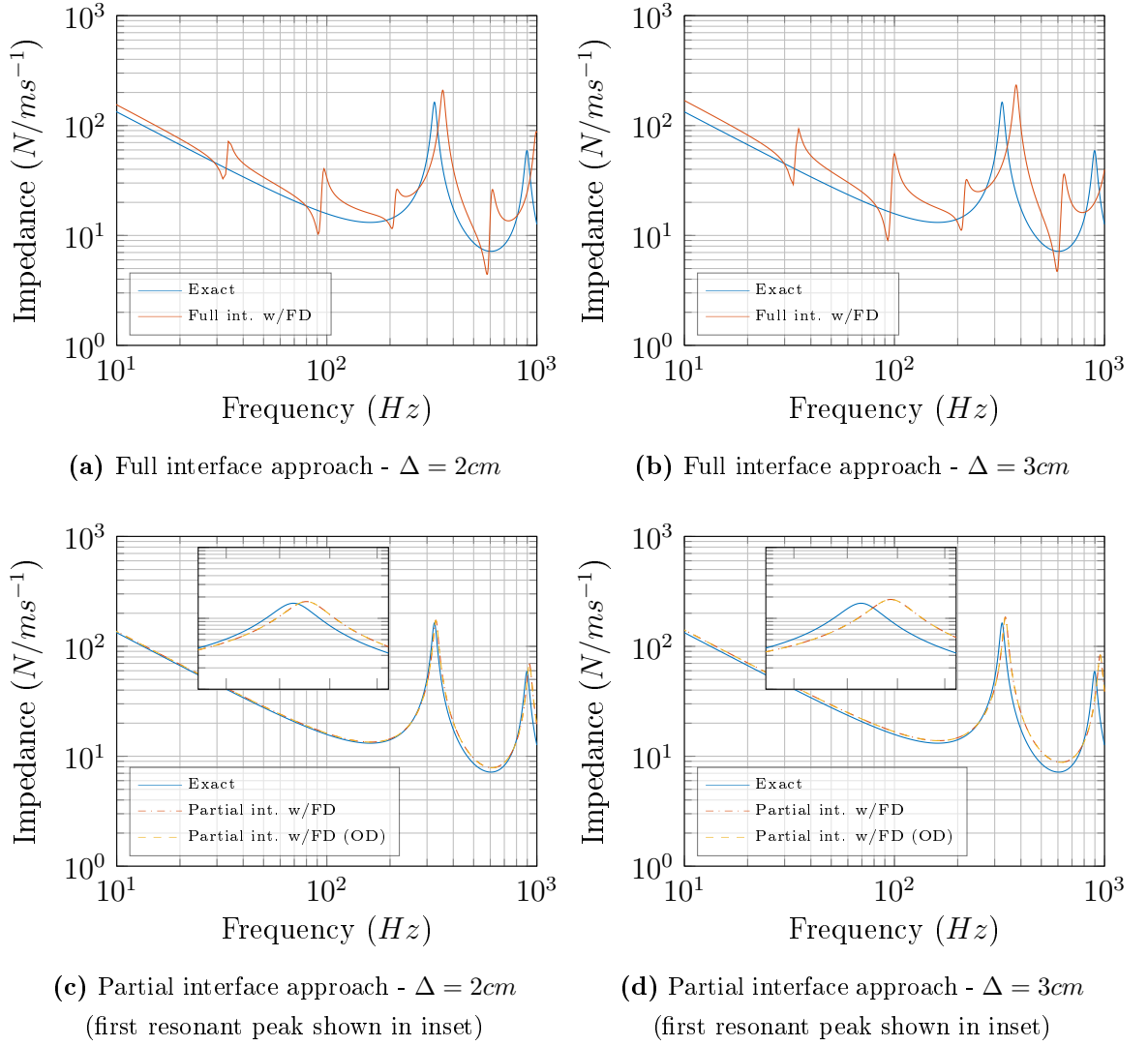


Figure 4.2: Rotational transfer impedance $\tilde{\mathbf{Z}}_{\mathbf{I}\psi_{2\tau 1}}$ obtained via numerical simulation using finite difference approach. Solid blue line is the exact transfer impedance obtained from beam **I** whilst decoupled.

When dealing with impedance we may argue that this error instead becomes *proportional* to the mobility magnitude, due to their inverse relationship. We would thus expect the finite difference error in the impedance to occur in regions where the mobility amplitude is high. Although not so easily extendible to multi-contact cases,

this proportional error is in agreement with those observed in our multi-contact simulations. Also demonstrated is the increase in error with frequency and separation distance, as discussed in [128].

4.1.3 EXPERIMENTAL VALIDATION

With the incorporation of the finite difference approximation having been validated numerically in the above study, and furthermore, with the finite difference approximation itself having already been experimentally validated in [128], the aim here is to simply demonstrate its application in the characterisation of resilient elements. Unfortunately, due to contractual arrangements, project deadlines and other time constraints, this was only achieved via the full interface approach for a single contact mass-isolator-mass assembly type.

4.1.3.1 SINGLE CONTACT

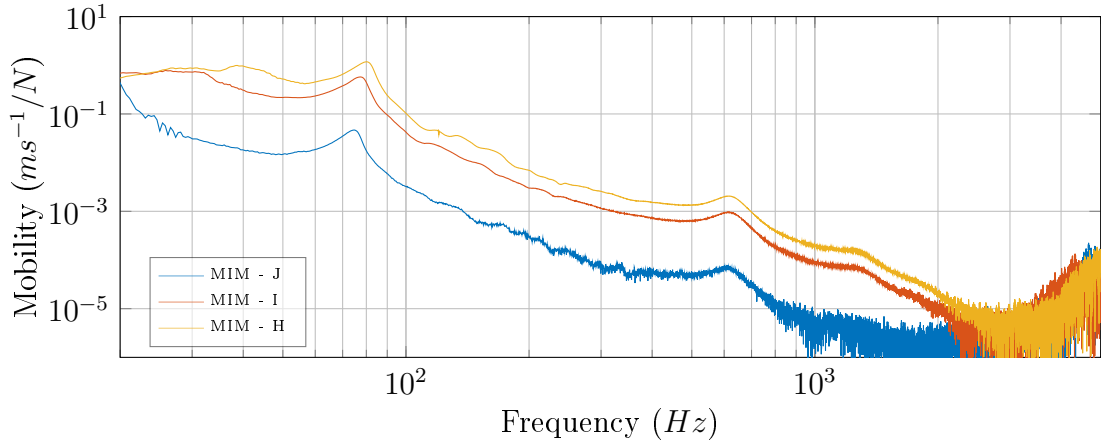
MASS-ISOLATOR-MASS - Unfortunately the M-I-M assemblies used in previous Sections were no longer available at the time of measurement. As such, three additional **MIM** assemblies, **H**, **I**, and **J** are introduced here. Further details of these assemblies are given in Table 4.1.

Tag	Type	Assembly Details
H	MIM	Source mass 0.86kg, receiver mass 3.2kg, resilient element: Continental CONTITECH 27 796 25-29
I	MIM	Source mass 0.86kg, receiver mass 5.1kg, resilient element: Continental CONTITECH 27 796 25-29
J	MIM	Source mass 0.86kg, receiver mass 18.3kg, resilient element: Continental CONTITECH 27 796 25-29

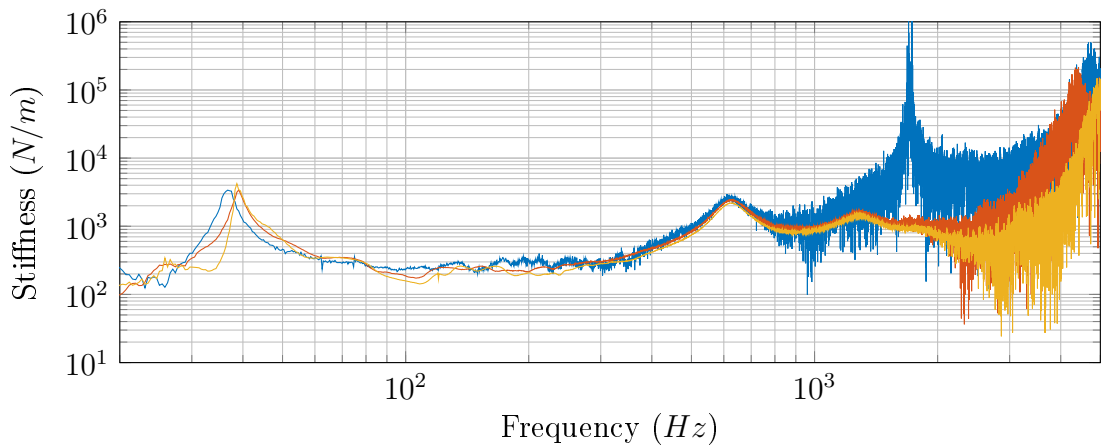
Table 4.1: Details on the construction of Mass-Isolator-Mass assemblies used in the determination of rotational dynamic transfer stiffness.

The measurement procedure for determining the rotational transfer stiffness follows that of the translation stiffness. A spaced pair of accelerometers were adhered above and below the isolator. Forces were applied at each and a 4x4 translational mobility matrix was constructed. This matrix was pre- and post-multiplied by the finite difference transformation matrix, \mathbf{B} and its transpose, \mathbf{B}^T , respectively. The

resulting matrix contained the translation, rotational and cross mobilities. Inversion and subsequent extraction of the off diagonal elements yielded the sought after quantities.



(a) Rotational transfer mobility $Y_{C_{\psi 1 \tau 2}}$



(b) Rotational dynamic transfer stiffness $K_{I_{\tau 1 \psi 2}}$

Figure 4.3: Dynamic transfer stiffness and transfer mobility measurements made on assemblies.

Shown in Figure 4.3 are the results obtained from assemblies **H-J**. Shown in Figure 4.3a are the rotational transfer mobilities, $\tilde{Y}_{C_{\psi 1 \tau 2}}$, for each assembly. As expected, these differ from one another. Again, at high frequencies, the effect of noise becomes severe, particularly in the case of assembly **J**, where a large 18kg receiver mass was used. A primary assembly resonance can be observed at approximately 80Hz, with two further resonances appearing around 600Hz and 1400Hz, although in the case of assembly **J**, this third resonance is masked by the contaminating noise. Shown in Figure 4.3b are the corresponding rotational transfer stiffnesses determined via the

finite difference approximation. It can be seen that the rotational transfer stiffnesses are in good agreement with one another across much of their frequency range. A number of expected phenomena can be observed in the resulting stiffness. The first and second internal resonances can be seen to occur at approximately 600Hz and 1400Hz, coinciding with the mobility of the assembly. This suggests that the corresponding transfer mobility resonances observed in Figure 4.3a are in fact caused by the internal mount resonances. Furthermore, a sharp resonance can be observed in the noise of assembly **J**, appearing at approximately 1800Hz. This is due to a plate-like resonance occurring in the large receiver mass, and is clearly not a property of the mount. An additional low frequency resonance can be observed at approximately 40Hz. This resonance is likely some property of the mount, as it is not visible in the transfer mobility of the assembly. It should also be noted that the primary assembly resonance at approx 80Hz is not seen in the dynamic stiffness, confirming that is a property of the assembly, not the mount.

Although only brief, the experimental investigation carried out above may be considered sufficient in confirming the validity of the finite difference approximation as an extension to the in-situ approach for determining rotational transfer stiffnesses.

4.2 EXTENSION TO REMOTE MEASUREMENT POSITIONS

The in-situ approach presented so far has been validated both numerically and experimentally, with its application to a number of single and multi-contact assemblies having been assessed. In its current form, the full interface approach, as presented in Equation 3.14, requires both source and receiver contact interfaces to be excited, whilst the partial interface approach, as presented in Equation 3.11, requires only a single interface to be excited. With either approach, the excitation of a contact interface may prove to be problematic, particularly in a practical scenario where access is limited. For example; auto-mobile engine mounts, machinery footing, etc. Whilst in a laboratory setting test rigs may be designed so as to facilitate interface access, this is generally not the case with when it comes to real life structures. More often than not, in cases where access is limited, the practitioner encounters problems whilst trying to *excite* the structure. The principle of reciprocity is largely employed in such cases, allowing for the interchange of excitation and response positions, for easier measurement. However, if both the excitation *and* response originate at a

coupling interface, for example a point mobility, the principle of reciprocity is of no benefit and we must find an alternative method.

The measurement of an interface response is not generally considered a problem as standard measurement accelerometers are relatively compact in size, not to mention the growing availability of MEMS (micro electro-mechanical system) sensors [131]. The application of a force however, whether through an instrumented hammer or an electro-dynamic shake, requires considerable space. In recent work by Moorhouse et al. [44] it was shown that the coupled point mobility at the interface of two arbitrary sub-structures could be determined from a set of measured transfer mobilities, none of which require excitation at the location of interest. Referred to as the ‘round trip’, a number of studies have highlighted its potential as both a theoretical and experimental tool [45, 82, 132]. It is therefore proposed that the round trip be integrated as part the in-situ characterisation approach, thus providing an entirely remote characterisation method, whereby all interface excitations are relocated to accessible measurement positions.

The round trip identity for the point mobility of a coupled structure is given by Moorhouse et al. [44] as,

Single interface round trip identity:

$$\mathbf{Y}_{C_{cc}} = \mathbf{Y}_{C_{cb}} \mathbf{Y}_{C_{ab}}^{-1} \mathbf{Y}_{C_{ca}}^T \quad (4.11)$$

or by reciprocity,

$$\mathbf{Y}_{C_{cc}} = \mathbf{Y}_{C_{cc}}^T = \mathbf{Y}_{C_{ca}} \mathbf{Y}_{C_{ba}}^{-1} \mathbf{Y}_{C_{cb}}^T. \quad (4.12)$$

where c represents the single coupling interface between a source and receiver sub-structure, a corresponds to some set of remote DoFs on the source, and b a similar set on the receiver.

From inspection of the partial interface relation,

$$\mathbf{Z}_{I_{c2c1}} = [\mathbf{Y}_{C_{c1a}} \mathbf{Y}_{C_{ba}}^{-1} \mathbf{Y}_{C_{c2b}}^T - \mathbf{Y}_{C_{c1c2}}]^{-1}$$

it is clear that the only mobility requiring an interface excitation is that of the transfer mobility $\mathbf{Y}_{C_{c1c2}}$. Likewise, from inspection of the full interface relation,

$$\begin{bmatrix} \mathbf{Z}_{C_{c1c1}} & \mathbf{Z}_{I_{c1c2}} \\ \mathbf{Z}_{I_{c1c2}} & \mathbf{Z}_{C_{c2c2}} \end{bmatrix} = \begin{bmatrix} \mathbf{Y}_{C_{c1c1}} & \mathbf{Y}_{C_{c1c2}} \\ \mathbf{Y}_{C_{c2c1}} & \mathbf{Y}_{C_{c2c2}} \end{bmatrix}^{-1}$$

it is clear that all elements require some interface excitation. The standard round trip identity, given by Equation 4.11, may be used to remotely determine the point mobilities, $\mathbf{Y}_{C_{c1c1}}$ and $\mathbf{Y}_{C_{c2c2}}$. However, the standard round trip identity does not account for the dual interface nature of either $\mathbf{Y}_{C_{c1c2}}$ or $\mathbf{Y}_{C_{c2c1}}$. In what follows, a simple re-derivation of the round trip is performed so as to provide a suitable dual interface relation.

4.2.1 DUAL INTERFACE ROUND TRIP

Following a similar derivation to that of [44] it is possible to formulate a round trip identity that allows for the transfer mobility, $\mathbf{Y}_{C_{c1c2}}$ (or by reciprocity $\mathbf{Y}_{C_{c2c1}}$), to be determined without the need for excitation at either contact interface.

Let us begin by considering the general **SIR** assembly given in Figure 3.1. The resultant velocities on the coupled assembly at positions a , c_1 , and c_2 , due to an applied force at b are given by,

$$\mathbf{v}_{C_a} = \mathbf{Y}_{C_{ab}} \mathbf{f}_{C_b} \quad (4.13)$$

$$\mathbf{v}_{C_{c1}} = \mathbf{Y}_{C_{c1b}} \mathbf{f}_{C_b} \quad (4.14)$$

$$\mathbf{v}_{C_{c2}} = \mathbf{Y}_{C_{c2b}} \mathbf{f}_{C_b}. \quad (4.15)$$

Employing the equivalent field representation of Bobrovnikii [67], the following may be stated,

$$\mathbf{v}_{C_a} = -\mathbf{Y}_{C_{ac2}} \bar{\mathbf{f}}_{R_{c2}} \quad (4.16)$$

$$\mathbf{v}_{C_{c1}} = -\mathbf{Y}_{C_{c1c2}} \bar{\mathbf{f}}_{R_{c2}} \quad (4.17)$$

$$\mathbf{v}_{C_{c2}} = -\mathbf{Y}_{C_{c2c2}} \bar{\mathbf{f}}_{R_{c2}} \quad (4.18)$$

where $\bar{\mathbf{f}}_{R_{c2}}$ is the blocked force produced at interface c_2 , due to the applied force at b . Equating Equations 4.13 and 4.14, whilst eliminating \mathbf{f}_{C_b} , allows the following equality to be established,

$$\mathbf{Y}_{C_{ab}}^{-1} \mathbf{v}_{C_a} = \mathbf{Y}_{C_{c1b}}^{-1} \mathbf{v}_{C_{c1}}. \quad (4.19)$$

Substitution of Equations 4.16 and 4.17 into 4.19 yields,

$$\mathbf{Y}_{C_{ab}}^{-1} \mathbf{Y}_{C_{ac2}} \bar{\mathbf{f}}_{R_{c2}} = \mathbf{Y}_{C_{c1b}}^{-1} \mathbf{Y}_{C_{c1c2}} \bar{\mathbf{f}}_{R_{c2}}. \quad (4.20)$$

Let us now consider the application of multiple forces at b , $\mathbf{f}_{C_{b_1}}$. Each of these applied forces will result in a blocked force at the interface c_2 , $\bar{\mathbf{f}}_{R_{c_2_1}}$. These blocked forces may be arranged as columns of a blocked force matrix, $\bar{\mathbf{F}}_{R_{c_2}}$. With free reign over the nature of the applied forces, we are able to ensure the invertability of the blocked force matrix. We are therefore able to eliminate the blocked force terms by first constructing the blocked forces matrix, $\bar{\mathbf{f}}_{R_{c_2}} \rightarrow \bar{\mathbf{F}}_{R_{c_2}}$, and subsequently post-multiplying both sides of Equation 4.20 by the inverse blocked force matrix, $\bar{\mathbf{F}}_{R_{c_2}}^{-1}$.

$$\mathbf{Y}_{C_{ab}}^{-1} \mathbf{Y}_{C_{ac_2}} = \mathbf{Y}_{C_{c_1b}}^{-1} \mathbf{Y}_{C_{c_1c_2}} \quad (4.21)$$

The pre-multiplication of Equation 4.21 by $\mathbf{Y}_{C_{c_1b}}$, followed by the reciprocal substitution, $\mathbf{Y}_{C_{ac_2}} = \mathbf{Y}_{C_{c_2a}}^T$, yields the round trip identity for a dual contact interface.

Dual interface round trip identity:

$$\mathbf{Y}_{C_{c_1c_2}} = \mathbf{Y}_{C_{c_1b}} \mathbf{Y}_{C_{ab}}^{-1} \mathbf{Y}_{C_{c_2a}}^T \quad (4.22)$$

or by reciprocity,

$$\mathbf{Y}_{C_{c_2c_1}} = \mathbf{Y}_{C_{c_2a}} \mathbf{Y}_{C_{ba}}^{-1} \mathbf{Y}_{C_{c_1b}}^T \quad (4.23)$$

If one chooses the location of c_1 and c_2 to be collocated, such that $c_1 = c_2 = c$, it can be seen that Equations 4.22 and 4.23 are in agreement with the standard round trip identity for the point mobility, as in Equation 4.11 and 4.12.

4.2.2 REMOTE IN-SITU CHARACTERISATION

Together, the single and dual interface round trip identities allow for both the partial and full interface approaches to be extended for use with remote measurement positions, thus avoiding the need to perform excitations at either contact interface.

4.2.2.1 REMOTE PARTIAL INTERFACE METHOD

Substituting Equation 4.22 into the partial interface relation results in an expression for the transfer impedance in terms of remotely measurable mobilities only, none of which require excitation about the interface.

Remote partial interface relation:

$$\mathbf{Z}_{I_{c2c1}} = [\mathbf{Y}_{C_{c1a}} \mathbf{Y}_{C_{ba}}^{-1} \mathbf{Y}_{C_{c2b}}^T - \mathbf{Y}_{C_{c1b}} \mathbf{Y}_{C_{ab}}^{-1} \mathbf{Y}_{C_{c2a}}^T]^{-1} \quad (4.24)$$

The remote partial interface relation offers two main advantages over its direct counterpart, the most obvious being its application in scenarios where excitation at the interface is not practical. Additionally, the incorporation of the round trip identity offers the ability to further over-determine of the problem.

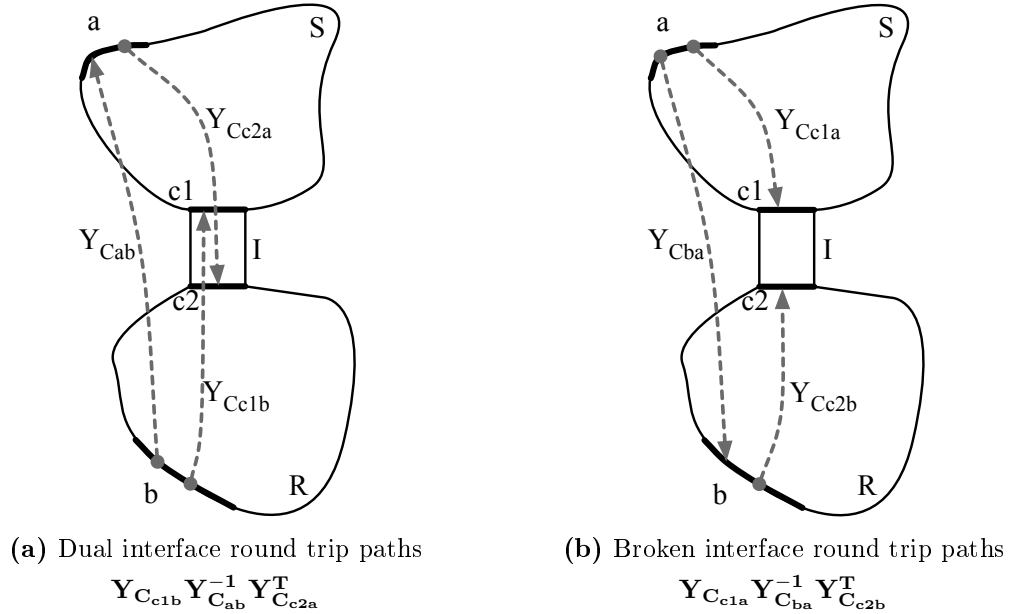


Figure 4.4: Mobility paths for the round trip and ‘broken’ round trip terms of Equation 4.24.

A closer inspection of Equation 4.24 reveals a similarity in form between the right and left hand sides of the difference term. With the right hand side being the round trip, the left hand side could be described as somewhat of a ‘broken’ round trip, as shown in Figure 4.4.

Like this broken round trip term, the number of remote DoFs required to successfully determine the transfer mobility, $\mathbf{Y}_{C_{c1c2}}$, via the round trip will depend upon the number of coupling elements under investigation. For a single element in a single coordinate-DoF, a single remote a and b DoF is sufficient. For each additional element, or coordinate-DoF, included in the characterisation, an additional DoF must be included at either a or b , so as to avoid under-determination.

4.2.2.2 REMOTE FULL INTERFACE METHOD

The remote extension of the full interface approach requires a round trip identity for each element of the coupling interface mobility matrix. Using the single and dual interface round trip identities of Equation 4.11-4.12 and 4.22-4.23, respectively, the following may be established,

$$\mathbf{Y}_{C_{c1c1}} = \mathbf{Y}_{C_{c1b}} \mathbf{Y}_{C_{ab}}^{-1} \mathbf{Y}_{C_{c1a}}^T \quad (4.25)$$

$$\mathbf{Y}_{C_{c1c2}} = \mathbf{Y}_{C_{c1b}} \mathbf{Y}_{C_{ab}}^{-1} \mathbf{Y}_{C_{c2a}}^T \quad (4.26)$$

$$\mathbf{Y}_{C_{c2c1}} = \mathbf{Y}_{C_{c2a}} \mathbf{Y}_{C_{ba}}^{-1} \mathbf{Y}_{C_{c1b}}^T \quad (4.27)$$

$$\mathbf{Y}_{C_{c2c2}} = \mathbf{Y}_{C_{c2a}} \mathbf{Y}_{C_{ba}}^{-1} \mathbf{Y}_{C_{c2b}}^T. \quad (4.28)$$

Together, the above allow for the construction of the coupling interface mobility matrix, whilst requiring excitation only at the remote DoFs, a and b . A more convenient single equation form may be obtained through the factorisation of Equations 4.25-4.28.

Remote full interface relation:

$$\begin{bmatrix} \mathbf{Y}_{C_{c1c1}} & \mathbf{Y}_{C_{c1c2}} \\ \mathbf{Y}_{C_{c2c1}} & \mathbf{Y}_{C_{c2c2}} \end{bmatrix} = \begin{bmatrix} \mathbf{Y}_{C_{c1b}} & 0 \\ 0 & \mathbf{Y}_{C_{c2a}} \end{bmatrix} \begin{bmatrix} \mathbf{Y}_{C_{ab}} & 0 \\ 0 & \mathbf{Y}_{C_{ba}} \end{bmatrix}^{-1} \begin{bmatrix} \mathbf{Y}_{C_{c1a}}^T & \mathbf{Y}_{C_{c2a}}^T \\ \mathbf{Y}_{C_{c1b}}^T & \mathbf{Y}_{C_{c2b}}^T \end{bmatrix} \quad (4.29)$$

As per the direct approach, Equation 4.29 is inverted, and the off-diagonals extracted, in order to obtain the remotely determined transfer impedances.

Like the remote partial interface approach, it is important that a sufficient number of remote DoFs are used so as to avoid under-determination. As each element of the coupled mobility matrix is essentially determined independently, the same remote DoFs may be used for each. As such, the number of remote DoFs required to successfully determine the entire mobility matrix will depend upon the number of elements under investigation. For a single element, in a single coordinate-DoF, a single remote a and b DoF is sufficient. For each additional element, or coordinate-DoF, included in the characterisation, an additional DoF must be included at either a or b , so as to avoid under-determination. Like the remote partial approach, Equation 4.29 also facilitates over-determination through the use of additional remote DoFs.

4.2.3 EXPERIMENTAL VALIDATION

In order to validate the proposed remote extension to the partial and full interface relations, two experimental cases have been investigated. The two cases considered here are the single and multi-contact assemblies, **F (BIP)** and **G (BI(2)P)**, introduced earlier in Chapter 3. In each case the transfer impedance, and subsequently the transfer stiffness, are determined via the remote extensions to the partial and full interface approaches described above.

4.2.3.1 SINGLE CONTACT

BEAM-ISOLATOR-PLATE - The beam-isolator-plate assembly considered here was the same assembly as used in Section 3.4.1, details of which are given in Table 3.4. With the remote partial and full interface approaches requiring the same measured mobilities,

$$\mathbf{Z}_{\mathbf{I}_{c_2c_1}} = [\mathbf{Y}_{\mathbf{C}_{c_1a}} \mathbf{Y}_{\mathbf{C}_{ba}}^{-1} \mathbf{Y}_{\mathbf{C}_{c_2b}}^{\mathbf{T}} - \mathbf{Y}_{\mathbf{C}_{c_1b}} \mathbf{Y}_{\mathbf{C}_{ab}}^{-1} \mathbf{Y}_{\mathbf{C}_{c_2a}}^{\mathbf{T}}]^{-1}$$

$$\begin{bmatrix} \mathbf{Y}_{\mathbf{C}_{c_1c_1}} & \mathbf{Y}_{\mathbf{C}_{c_1c_2}} \\ \mathbf{Y}_{\mathbf{C}_{c_2c_1}} & \mathbf{Y}_{\mathbf{C}_{c_2c_2}} \end{bmatrix} = \begin{bmatrix} \mathbf{Y}_{\mathbf{C}_{c_1b}} & 0 \\ 0 & \mathbf{Y}_{\mathbf{C}_{c_2a}} \end{bmatrix} \begin{bmatrix} \mathbf{Y}_{\mathbf{C}_{ab}} & 0 \\ 0 & \mathbf{Y}_{\mathbf{C}_{ba}} \end{bmatrix}^{-1} \begin{bmatrix} \mathbf{Y}_{\mathbf{C}_{c_1a}}^{\mathbf{T}} & \mathbf{Y}_{\mathbf{C}_{c_2a}}^{\mathbf{T}} \\ \mathbf{Y}_{\mathbf{C}_{c_1b}}^{\mathbf{T}} & \mathbf{Y}_{\mathbf{C}_{c_2b}}^{\mathbf{T}} \end{bmatrix}$$

a single experimental set-up was suitable for both approaches. This set-up is shown diagrammatically in Figure 4.5, where spaced accelerometer pairs are adhered above and below the mount. Also included was an additional remote accelerometer on both the source and receiver sub-structures. Here we will consider only over-determination via forces (at a and b), as such, a single remote accelerometer on each was sufficient. The measurement procedure for the two remote approaches may be outlined as follows:

- 1 Forces are applied at each of the three remote source positions, a , and the transfer mobilities $\mathbf{Y}_{\mathbf{C}_{c_2a}}$, $\mathbf{Y}_{\mathbf{C}_{ba}}$ and $\mathbf{Y}_{\mathbf{C}_{c_1a}}$ are measured.
 - 2 Forces are applied at each of the three remote receiver positions, b , and the transfer mobilities $\mathbf{Y}_{\mathbf{C}_{c_2b}}$, $\mathbf{Y}_{\mathbf{C}_{ab}}$ and $\mathbf{Y}_{\mathbf{C}_{c_1b}}$ are measured.
- * Spaced responses at interfaces c_1 and c_2 are averaged such that they provide the equivalent central responses.

The advantage of the remote extension is evident here in that it requires neither contact interface to be excited, allowing the practitioner carry out measurements more conveniently. Furthermore, the remote approaches may be over-determined through the use of additional excitation and/or response measurements at the remote DoFs a and/or b .

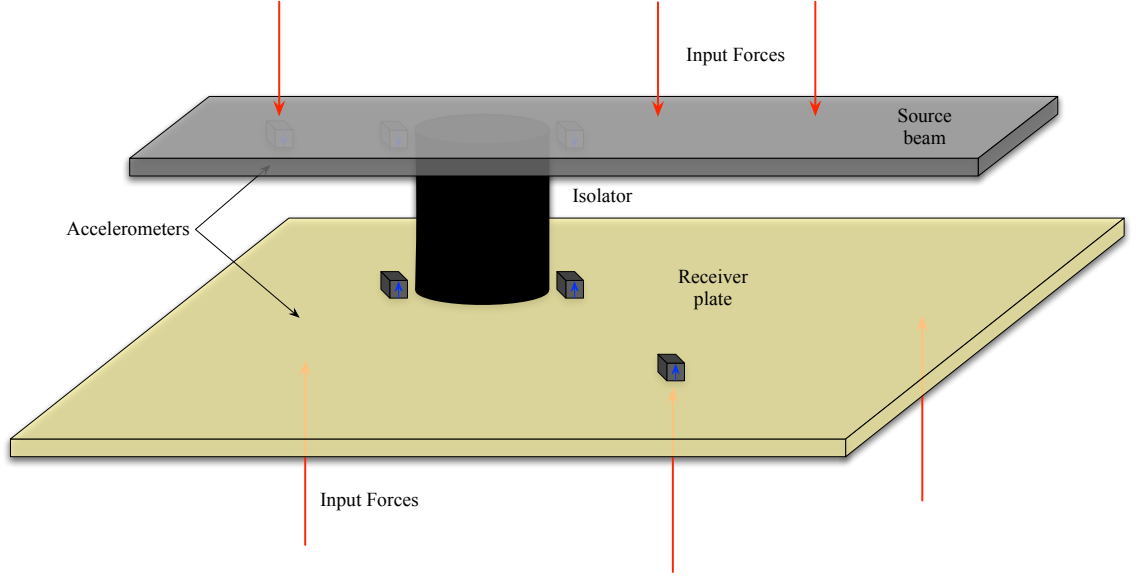


Figure 4.5: Diagrammatic representation of the beam-isolator(2)-plate test rig, **G**. Red arrows correspond to the direction and position of the applied forces, whilst blue arrows indicate the positive direction of the measured accelerations.

Over-determination via forces at a leads to the substitution $\mathbf{Y}_{C_{ab}}^{-1} = \mathbf{Y}_{C_{ba}}^{-T}$ in the second term of Equation 4.24, and in the upper diagonal entry of the inverse matrix of Equation 4.25.

$$\mathbf{Z}_{I_{c2c1}} = [\mathbf{Y}_{C_{c1a}} \mathbf{Y}_{C_{ba}}^{-1} \mathbf{Y}_{C_{c2b}}^T - \mathbf{Y}_{C_{c1b}} \mathbf{Y}_{C_{ba}}^{-T} \mathbf{Y}_{C_{c2a}}^T]^{-1} \quad (4.30)$$

$$\begin{bmatrix} \mathbf{Y}_{C_{c1c1}} & \mathbf{Y}_{C_{c1c2}} \\ \mathbf{Y}_{C_{c2c1}} & \mathbf{Y}_{C_{c2c2}} \end{bmatrix} = \begin{bmatrix} \mathbf{Y}_{C_{c1b}} & 0 \\ 0 & \mathbf{Y}_{C_{c2a}} \end{bmatrix} \begin{bmatrix} \mathbf{Y}_{C_{ba}}^T & 0 \\ 0 & \mathbf{Y}_{C_{ba}} \end{bmatrix}^{-1} \begin{bmatrix} \mathbf{Y}_{C_{c1a}}^T & \mathbf{Y}_{C_{c2a}}^T \\ \mathbf{Y}_{C_{c1b}}^T & \mathbf{Y}_{C_{c2b}}^T \end{bmatrix} \quad (4.31)$$

Similarly, the over-determination at b leads to the substitution $\mathbf{Y}_{C_{ba}}^{-1} = \mathbf{Y}_{C_{ab}}^{-T}$.

Let us first consider the remote full interface approach. Shown in Figure 4.6 are the contact interface mobilities determined via Equation 4.29. Results are presented for both determined (blue) and 3 fold over-determined (orange and yellow) cases. Also shown are the directly measured mobilities (purple) obtained via direct interface

excitations. The results presented in Figure 4.6 show good agreement between each of the remotely determined mobilities and those measured directly, up to approximately 1kHz.

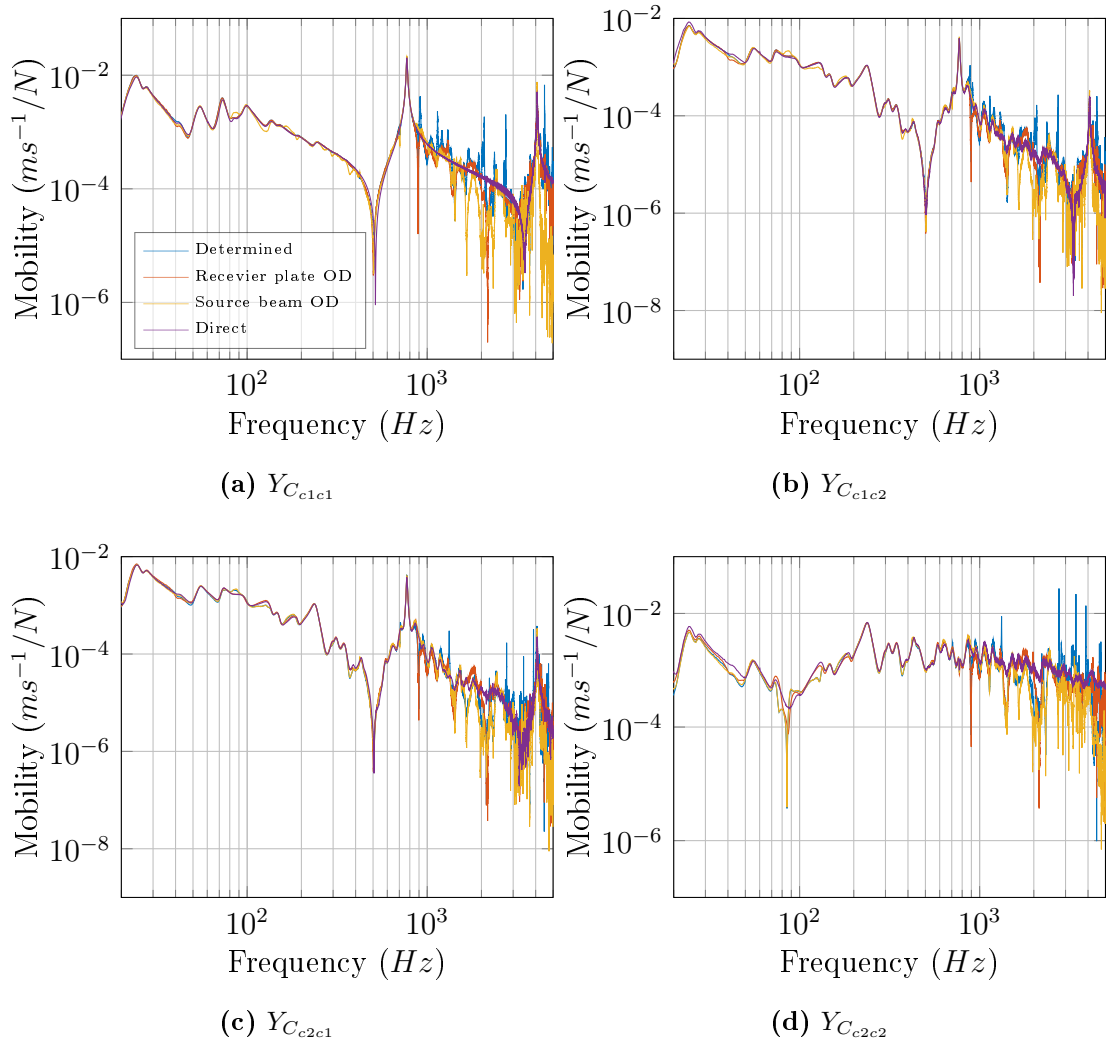


Figure 4.6: Contact interface mobility matrix determined from assembly \mathbf{F} (see tables 3.4) using direct and round trip methods. For the round trip case both determined and over-determined results are presented.

Above this the predictions are contaminated by an increasing amount of noise. This noise is, again, due to the attenuation of the vibration signal through the resilient element causing it to fall below the sensitivity threshold of the measurement equipment.

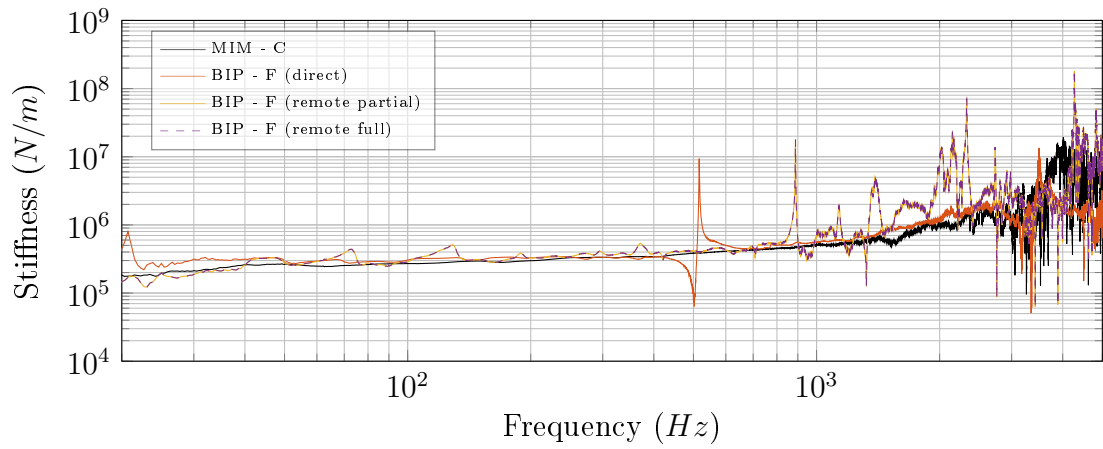
This noise may be avoided in the case of the point mobilities by supposing that both remote DoFs, a and b , exist on the same sub-structure. This may be done by considering the 3 remote DoFs to lie on either side of an imaginary interface

that exists at the mount contact interface. Doing so allows for the point mobilities to be determined without having to measure across the isolator. Unfortunately, however, there is no such option for the transfer mobilities. Instead further over-determination, or additional averaging, may be employed as a method for reducing the high frequency noise. However, with the aim here being simply to demonstrate the application of the remote in-situ approach, the agreement observed in Figure 4.6 is considered acceptable.

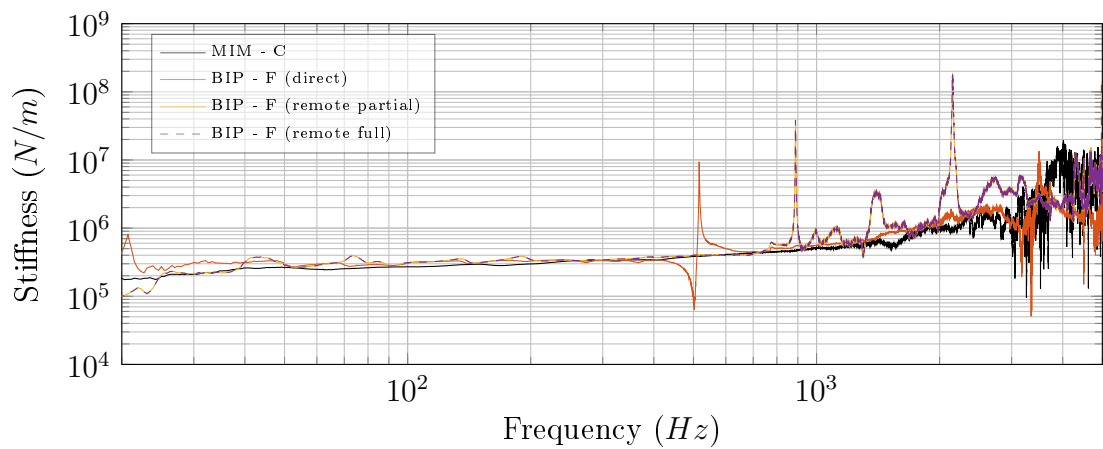
As per the full interface approach, the inversion of this remotely determined mobility matrix yields the dynamic transfer impedance, from which the transfer stiffness is calculated. Shown in Figure 4.7 are the dynamic transfer stiffnesses obtained via the partial (yellow) and full (dashed purple) interface approaches for both determined and over-determined cases. Also shown are the full interface stiffnesses determined directly from assemblies **F** (orange) and **C** (black).

A number of observations can be made from Figure 4.7. Firstly, it can be seen that the remote partial and full interface approaches are in near exact agreement (differences on the level of numerical error), in both determined and over-determined cases. Although, this is not entirely unexpected as the two approaches make use of the same remote DoFs, the same measured mobilities and similar theory. Secondly, like the partial interface results presented in Section 3.4.1, it can be seen that the large anti-resonant artefact present in the directly determined stiffness, occurring at 500hz, has been avoided. Although a strong agreement between the determined and over-determined stiffnesses is observed, a noticeable difference can be seen in the case of Figure 4.7c where a source side over-determination is used. In this case the resonant artefact occurring at 900Hz is avoided. Similarly, over determination on the receiver side results in a reduction in many of the resonant artefacts below this 900Hz artefact.

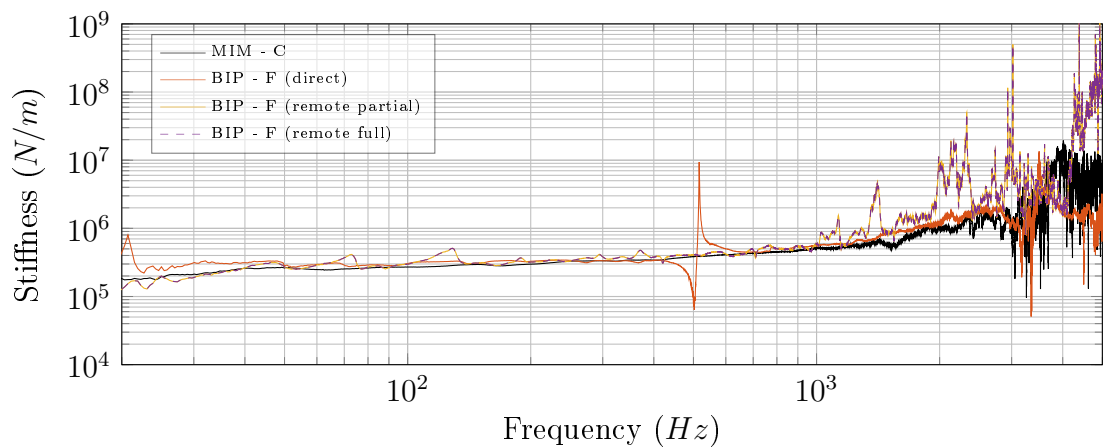
Before moving onto a multi-contact assembly it is perhaps worth noting what has been accomplished here. The dual and single interface round trip identities have been used together in a factorised matrix form to remotely determine the entire contact interface mobility matrix, using remote measurement DoFs. Using these remotely determined mobilities, both the partial and full interface approaches were successfully implemented and used to obtain transfer stiffnesses that were not only in good agreement with those determined from a **MIM** assembly, but in near perfect agreement with one another.



(a) Determined



(b) Over-determined on receiver plate



(c) Over-determined on source beam

Figure 4.7: Dynamic transfer stiffness' $K_{I_{c1c2}}$ determined from assemblies **C** and **F** (see tables 3.2 and 3.4) using direct and remote method (see Sections 3.2 and 4.2.2). For remote cases both determined and over-determined results are presented.

4.2.3.2 MULTIPLE CONTACT

BEAM-ISOLATOR(2)-PLATE - The beam-isolator(2)-plate assembly considered here is the same assembly as used in Section 3.4.2, details of which are given in Table 3.5.

As in the single contact case, the implementation of the remote partial and full interface characterisation was achieved through the same experimental set-up. For the assembly considered here, this set-up is shown diagrammatically in Figure 4.8 where, in addition to the spaced accelerometer pairs, two remote accelerometers were included on the receiver sub-structure. Here we will only consider over-determination via additional forces at a . As such, the reciprocal substitutions presented in Equations 4.30 and 4.31 apply and no remote responses are required at a . The measurement procedure here follows that of the single contact case, whilst accounting for the dual contact responses, and the five remote a DoFs required to facilitates a $2\frac{1}{2}$ fold over-determination.

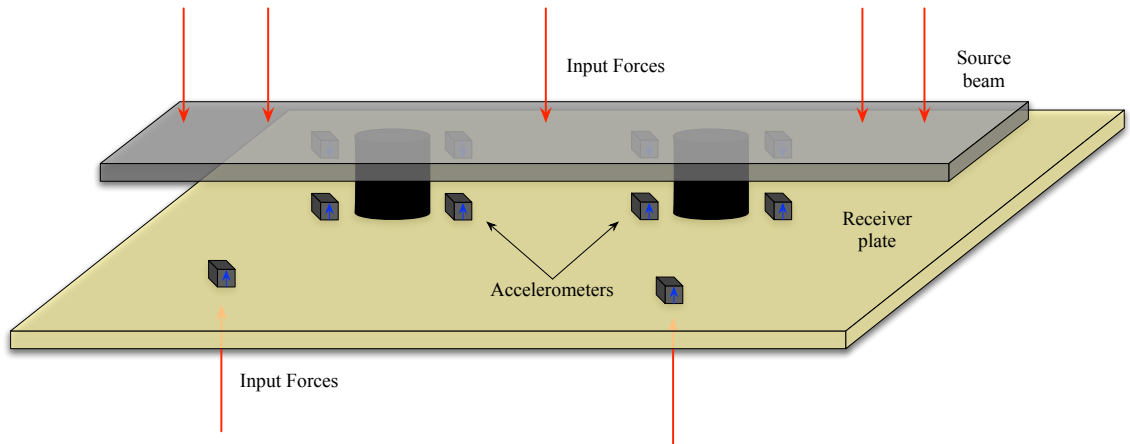


Figure 4.8: Diagrammatic representation of the beam-isolator(2)-plate test rig, **H**. Red arrows correspond to the direction and position of the applied forces, whilst blue arrows indicate the positive direction of the measured accelerations.

Let us first consider the remote full interface approach. Shown in Figure 4.9 are point contact interface mobilities determined remotely via Equation 4.31 (orange and yellow). For clarity, only the point mobilities are presented, the transfer mobilities were, however, in a similar level of agreement to those shown. Results are presented for both determined (orange) and over-determined (yellow) cases. Also shown are the directly measured point mobilities (blue) obtained via direct interface excitations. The remotely determined mobilities presented in Figure 4.9 are in good agreement with those measured directly, up to approximately 1kHz, particularly in

the over-determined case. Over-determination can be seen here to remedy many of the large deviations observed in the determined mobilities, for example the 100Hz anti-resonances in $Y_{C_{c3c3}}$ and $Y_{C_{c4c4}}$.

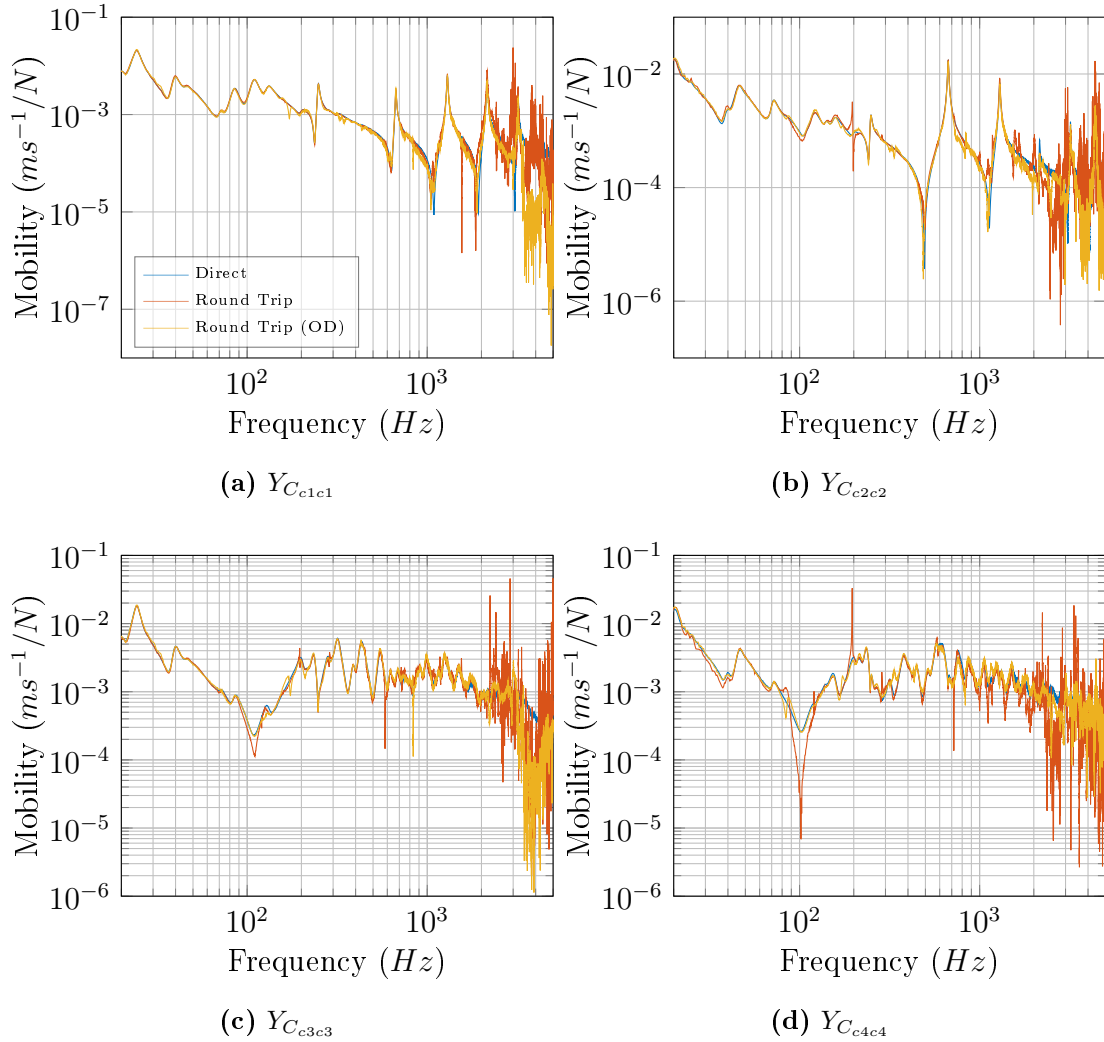
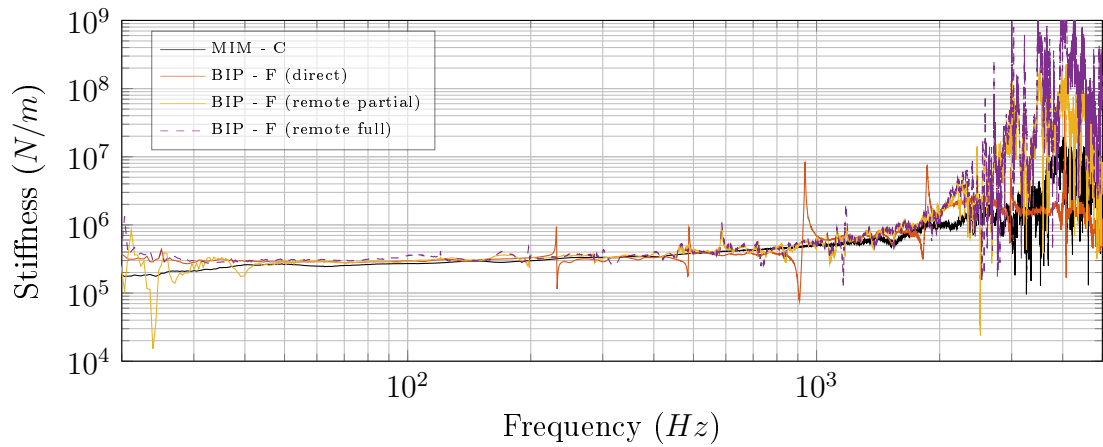
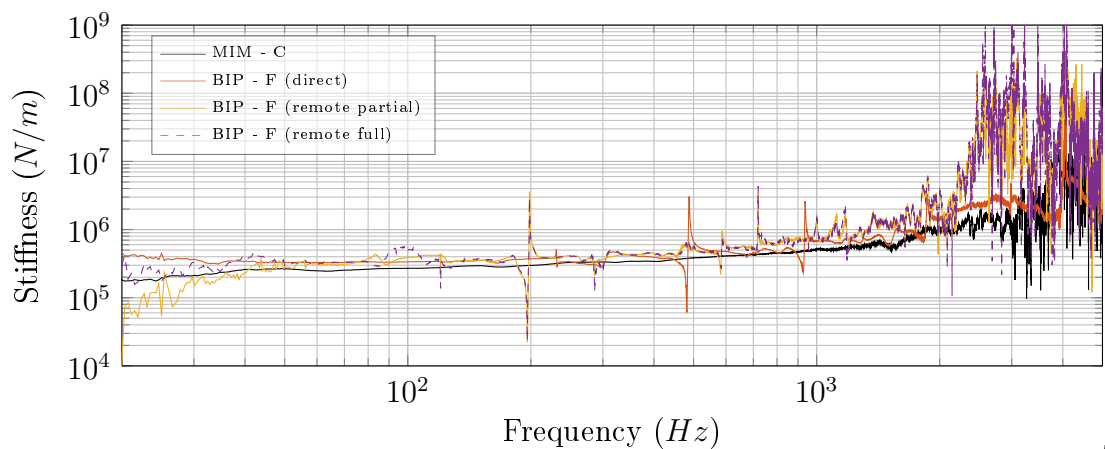


Figure 4.9: Point mobilities from full mobility matrix determine via round trip.

Although used as a means to an end, the multi-contact dual interface implementation of the round trip identities (not to mention the single contact implementation, presented in Figure 4.6) is, in itself, an interesting result. The ability to accurately determine the mobility of a complex interface which is not easily accessible has applications reaching far beyond that of the remote characterisation of resilient elements. Although not investigated further, the impressive success of the round trip identities here must be acknowledged.

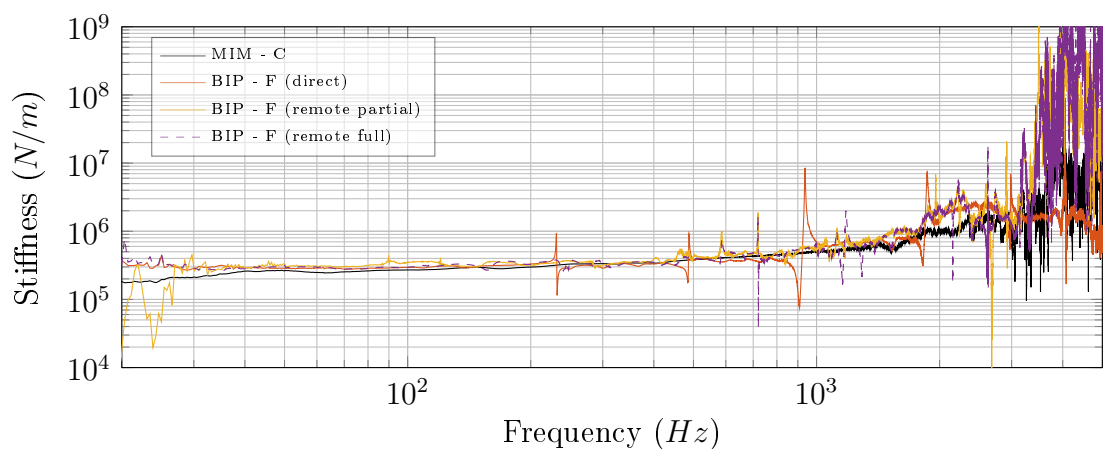


(a) Dynamic transfer stiffness $K_{I_{c11c21}}$ of assembly \mathbf{G} , determined using remote partial and full interface approaches.



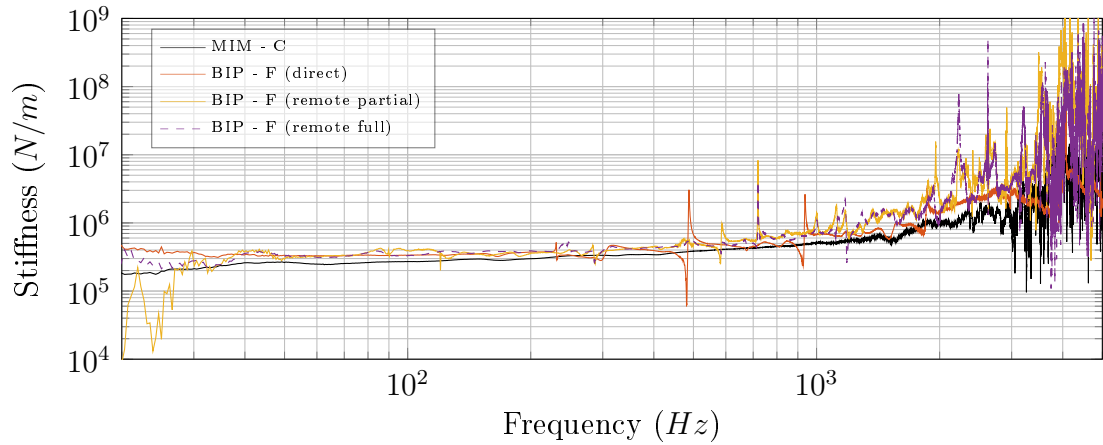
(b) Dynamic transfer stiffness $K_{I_{c12c22}}$ of assembly \mathbf{G} , determined using remote partial and full interface approaches.

ZZ



(c) Dynamic transfer stiffness $K_{I_{c11c21}}$ of assembly \mathbf{G} , determined using over-determined remote partial and full interface approaches.

Figure 4.10: Dynamic transfer stiffnesses $K_{I_{c11c21}}$ and $K_{I_{c12c22}}$ determined from assembly \mathbf{F} using direct and remote methods (see Sections 3.2 and 4.2.2). For remote cases both determined and over-determined results are presented.



(d) Dynamic transfer stiffness $K_{I_{c12c22}}$ of assembly **G**, determined using over-determined remote partial and full interface approaches.

Figure 4.10: (Continued) Dynamic transfer stiffnesses $K_{I_{c11c21}}$ and $K_{I_{c12c22}}$ determined from assembly **F** using direct and remote methods (see Sections 3.2 and 4.2.2). For remote cases both determined and over-determined results are presented.

Having remotely determined the contact interface mobility matrix via Equation 4.31, the dynamic transfer stiffness of each isolator was determined via the full interface approach as per Equation 3.14. Using the same set of measured mobilities, the partial interface approach was also implemented as per Equation 4.30.

Shown in Figure 4.6 are the dynamic transfer stiffnesses obtained via the remote full (dashed purple) and partial (yellow) interface approaches for both determined and over-determined cases. Also shown are the directly measured stiffness values from assemblies **G** (orange) and **C** (black). Figures 4.10c and 4.10d represent the over-determined cases of Figure 4.10a and 4.10b, respectively. It can be seen that in the determined case, both the full and partial approaches avoid the anti-resonant artefacts observed in the direct full interface stiffness. Their agreement with the stiffness obtained from assembly **C** is reasonably good. The full and partial approaches are in considerable agreement across the majority of the frequency range, only deviating significantly below approximately 40Hz. In this region the full interface approach appears to be the more reliable of the two. Although arguably less contaminated than the directly determined stiffness, some additional artefacts are introduced via the remote determination, most notably the 200Hz artefact in Figure 4.10b. The benefit of over-determination is shown in Figures 4.10c and 4.10d where the severity of many of these artefacts is reduced.

4.3 OPERATIONAL CHARACTERISATION VIA THE GENERALISED TRANSMISSIBILITY

As it currently stands, the in-situ approach for the characterisation of a coupling element (via both partial and full interface approaches) requires excitation and response measurements to be made on both source and receiver sub-structures. Whilst the remote extension presented in Section 4.2 allows for the excitations to be relocated to remote DoFs, further simplifications can be made via the application of generalised transmissibilities.

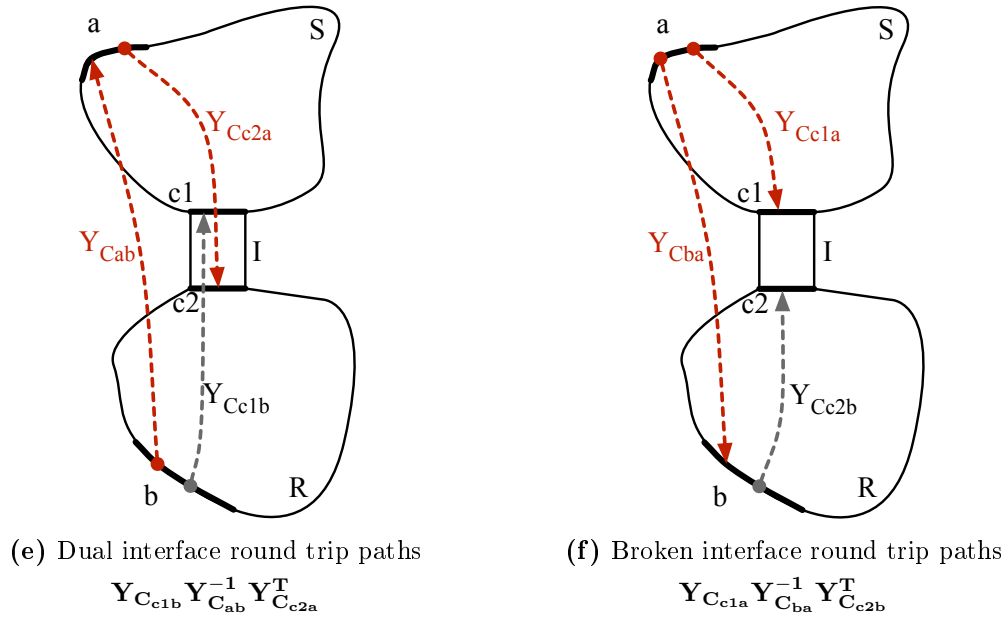


Figure 4.11: Mobility paths for the round trip and ‘broken’ round trip terms of remote partial interface impedance relation of Equation 4.24. Highlighted paths are to be replaced by generalised transmissibility terms.

By considering some set of unknown internal, external, or operational forces, it is proposed that the mobility paths highlighted in Figure 4.11 (as required by the remote partial interface approach), namely those requiring remote source side excitation or response measurement, be replaced by generalised transmissibility terms. Such an extension would be particularly beneficial if access is completely restricted

to the source sub-structure, or in scenarios where the nearest accessible remote measurement position lies far away from the contact interface.²

The replacement of these transfer mobilities with generalised transmissibility terms offers a number of potential advantages. Firstly, its use may further simplify the experimental procedure by removing the need to excite the source sub-structure directly, or at least remove the need for a repeatable coherent excitation. Secondly, by removing the need to excite the source sub-structure, the experimental error associated with excitation inaccuracy is reduced. Thirdly, for assemblies consisting of an active sub-structure, it is proposed that one may use the forces generated via its operation as a means of determining the generalised transmissibilities, thus allowing for part of the data required for characterisation to be obtained under operational conditions. Lastly, depending upon the nature of the active sub-structure, the excitation applied to a resilient mount may exceed the assumption of local linearity. Therefore any non-linearities in the properties of a resilient element whilst under operation may potentially be indicated via the use of a generalised transmissibility.

In this Section we will consider only the case where the unknown internal, external or operational forces are located at fixed positions and provide coherent excitations. Whilst this may place restrictions on the use of operational forces, a further investigation was considered beyond the scope of this work.

The remainder of this Section will focus on the incorporation of the generalised transmissibility concept within the remote in-situ approach.

4.3.1 GENERALISED TRANSMISSIBILITY CONCEPT

The concept of transmissibility is classically defined for a single DoF, for example a mass-spring assembly, as the ratio of input to output velocity (or force). However, with many of the problems faced by engineers being associated with more complicated multi-DoF systems, the classical transmissibility formulation is often only of limited use. Instead, one may consider the generalised transmissibility presented by

²The remote extension implemented via the round trip method relies on a strong phase relationship between the remote DoFs and coupling interfaces. If the coupling interface is sufficiently far away from the nearest accessible remote region, or if the structure under investigation is of a complicated geometry, successful implementation of the round trip may prove difficult. This is due in part to a change in the nature of the wave propagation, i.e. from standing wave type to travelling wave type [133]. In such cases a poor level of coherence is likely to be obtained. This poor coherence would likely go on to have negative effects on the results obtained via the round trip.

Ribeiro et al. [134]. In what follows, the generalised transmissibility for the **SIR** assembly presented in Figure 3.1 will be derived.

With reference to Figure 3.1, consider an unknown excitation force acting within the source sub-structure **S** at some internal positional-DoF i , \mathbf{f}_{C_i} . The resultant assembly velocities due to this unknown excitation may be written as follows:

$$\dot{\mathbf{v}}_{C_a} = \mathbf{Y}_{C_{ai}} \dot{\mathbf{f}}_{C_i} \quad (4.32)$$

$$\dot{\mathbf{v}}_{C_{c1}} = \mathbf{Y}_{C_{c1i}} \dot{\mathbf{f}}_{C_i} \quad (4.33)$$

$$\dot{\mathbf{v}}_{C_{c2}} = \mathbf{Y}_{C_{c2i}} \dot{\mathbf{f}}_{C_i} \quad (4.34)$$

$$\dot{\mathbf{v}}_{C_b} = \mathbf{Y}_{C_{bi}} \dot{\mathbf{f}}_{C_i} \quad (4.35)$$

where $\dot{}$ represents an operational quantity. Pre-multiplication by the appropriate mobility matrix allows any two of the above relations to be equated through the elimination of the force term $\dot{\mathbf{f}}_{C_i}$. For example, Equation 4.32 and 4.33 may be equated to form,

$$\mathbf{Y}_{C_{ai}}^{-1} \dot{\mathbf{v}}_{C_a} = \mathbf{Y}_{C_{c1i}}^{-1} \dot{\mathbf{v}}_{C_{c1}}. \quad (4.36)$$

Pre-multiplication by $\mathbf{Y}_{C_{ai}}$ leads to,

$$\dot{\mathbf{v}}_{C_a} = \mathbf{Y}_{C_{ai}} \mathbf{Y}_{C_{c1i}}^{-1} \dot{\mathbf{v}}_{C_{c1}}. \quad (4.37)$$

Equation 4.37 provides a relationship between the resultant velocity responses at the coupling interface c_1 and the remote DoF a , due to an internal force acting at i . The relating term $\mathbf{Y}_{C_{ai}} \mathbf{Y}_{C_{c1i}}^{-1}$ may be considered a generalised transmissibility matrix and rewritten as $\mathbf{T}_{C_{ac1}}^i$,

$$\dot{\mathbf{v}}_{C_a} = \mathbf{T}_{C_{ac1}}^i \dot{\mathbf{v}}_{C_{c1}}. \quad (4.38)$$

In this vector/matrix form $\mathbf{T}_{C_{ac1}}^i$ is able to relate the velocity between two sets positional-DoFs. Whilst the transmissibility term, $\mathbf{T}_{C_{ac1}}^i$, may clearly be determined from a pair of measured mobilities via,

$$\mathbf{T}_{C_{ac1}}^i = \mathbf{Y}_{C_{ai}} \mathbf{Y}_{C_{c1i}}^{-1}. \quad (4.39)$$

this approach is not of interest to us as we are attempting to use the transmissibility as a means of avoiding the measurement of mobilities. Instead, an alternative

approach may be used whereby only the operational velocities $\dot{\mathbf{v}}_{\mathbf{C}_a}$ and $\dot{\mathbf{v}}_{\mathbf{C}_{c1}}$ are required [135].

Let us consider the case where a number of independent internal forces $\dot{\mathbf{f}}_{\mathbf{C}_{i_i}}$ are applied at the source DoF i . Arranging these force vectors as columns of the force matrix $\dot{\mathbf{F}}_{\mathbf{C}_i} = [\dot{\mathbf{f}}_{\mathbf{C}_{i_1}}, \dot{\mathbf{f}}_{\mathbf{C}_{i_2}} \dots \dot{\mathbf{f}}_{\mathbf{C}_{i_i}}]^T$, the resultant velocities due to each force may be arranged similarly as the columns of a velocity matrix. Following through the derivation of Equation 4.38 accounting for these force and velocity matrices one arrives at the transmissibility relation,

$$\dot{\mathbf{V}}_{\mathbf{C}_a} = \mathbf{T}_{\mathbf{C}_{ac1}}^i \dot{\mathbf{V}}_{\mathbf{C}_{c1}} \quad (4.40)$$

where $\dot{\mathbf{V}}_{\mathbf{C}_a} = [\dot{\mathbf{v}}_{\mathbf{C}_{a_1}}, \dot{\mathbf{v}}_{\mathbf{C}_{a_2}} \dots \dot{\mathbf{v}}_{\mathbf{C}_{a_i}}]$ and $\dot{\mathbf{V}}_{\mathbf{C}_{c1}} = [\dot{\mathbf{v}}_{\mathbf{C}_{c1_1}}, \dot{\mathbf{v}}_{\mathbf{C}_{c1_2}} \dots \dot{\mathbf{v}}_{\mathbf{C}_{c1_i}}]$. Providing that the velocity matrix is non-singular, one may pre-multiply Equation 4.40 by the inverse velocity matrix $\dot{\mathbf{V}}_{\mathbf{C}_{c1}}^{-1}$, thus acquiring a solution to the generalised transmissibility matrix $\mathbf{T}_{\mathbf{C}_{ac1}}^a$ in terms of operation velocities alone.

$$\mathbf{T}_{\mathbf{C}_{ac1}}^a = \dot{\mathbf{V}}_{\mathbf{C}_a} \dot{\mathbf{V}}_{\mathbf{C}_{c1}}^{-1} \quad (4.41)$$

In Equation 4.41, the number of remote DoF at a must be equal to the number of interface DoF at c_1 , else the dimensions of the two velocity matrices will not be compatible. Additionally, in order to form a determined solution, the number of applied forces, i.e. the columns of $\dot{\mathbf{V}}_{\mathbf{C}_a}$ and $\dot{\mathbf{V}}_{\mathbf{C}_{c1}}$, must be equal to the number of interface and remote DoFs used. Furthermore, an essential requirement of Equation 4.41 is that the columns of $\dot{\mathbf{V}}_{\mathbf{C}_{c1}}$ be sufficiently independent from one another, else the resultant velocity matrix will be rank deficient and therefore non-invertable. This may be accomplished by ensuring that the applied forces $\dot{\mathbf{f}}_{\mathbf{C}_{i_i}}$ are sufficiently independent from one another. In practise this may be potentially achieved through operating the active sub-structure at a range of different speeds and/or loads. Lastly, Equation 4.41 also facilitates the over-determination of the problem through the use of additional applied forces. Doing so results in non-square velocity matrices that yield an over-determined transmissibility matrix.

It is important to note that in order to successfully implement Equation 4.41 a reliable phase relationship must be established between the elements of the velocity vector that make up $\dot{\mathbf{V}}_{\mathbf{C}_a}$ and $\dot{\mathbf{V}}_{\mathbf{C}_{c1}}$. As such, auto-spectra data may not be used unless an appropriate phase is applied before hand, for example via the cross-spectrum phase approach as in Section 6.2.3.2.

4.3.2 OPERATIONAL DYNAMIC TRANSFER STIFFNESS

In what follows the concept of generalised transmissibility is applied to the remote partial interface relation, as presented in Equation 4.24. Let us begin by simply considering the remote relation,

$$\mathbf{Z}_{\mathbf{I}_{c_2c_1}} = [\mathbf{Y}_{\mathbf{C}_{c_1a}} \mathbf{Y}_{\mathbf{C}_{ba}}^{-1} \mathbf{Y}_{\mathbf{C}_{c_2b}}^{\mathbf{T}} - \mathbf{Y}_{\mathbf{C}_{c_1b}} \mathbf{Y}_{\mathbf{C}_{ab}}^{-1} \mathbf{Y}_{\mathbf{C}_{c_2a}}^{\mathbf{T}}]^{-1} \quad (4.42)$$

The left hand term within the bracket of Equation 4.42 can be seen to contain the mobility product, $\mathbf{Y}_{\mathbf{C}_{c_1a}} \mathbf{Y}_{\mathbf{C}_{ba}}^{-1}$. If we consider the remote DoF a to lie internally at i , this product takes the same form as that of Equation 4.39, and through a derivation similar to that shown in Section 4.3.1 it may be expressed by the generalised transmissibility matrix $\mathbf{T}_{\mathbf{C}_{c_1b}}^{\mathbf{a}}$. $\mathbf{T}_{\mathbf{C}_{c_1b}}^{\mathbf{a}}$ relates the resultant velocities at the coupling interface c_1 and remote receiver b DoFs due to some applied force at a ,

$$\mathbf{T}_{\mathbf{C}_{c_1b}}^{\mathbf{a}} = \mathbf{Y}_{\mathbf{C}_{c_1a}} \mathbf{Y}_{\mathbf{C}_{ba}}^{-1}. \quad (4.43)$$

Substitution of Equation 4.43 into Equation 4.45 yields,

$$\mathbf{Z}_{\mathbf{I}_{c_2c_1}} = [\mathbf{T}_{\mathbf{C}_{c_1b}}^{\mathbf{a}} \mathbf{Y}_{\mathbf{C}_{c_2b}}^{\mathbf{T}} - \mathbf{Y}_{\mathbf{C}_{c_1b}} \mathbf{Y}_{\mathbf{C}_{ab}}^{-1} \mathbf{Y}_{\mathbf{C}_{c_2a}}^{\mathbf{T}}]^{-1}. \quad (4.44)$$

Turning attention to the round trip relation on the right hand side of Equation 4.45 a mobility product of similar form can be seen; $\mathbf{Y}_{\mathbf{C}_{c_1b}} \mathbf{Y}_{\mathbf{C}_{ab}}^{-1}$. However, having just removed the need for a direct excitation at a from the left hand term, it would be preferable to do the same for the right hand term. Doing so would allow us to eliminate the need for direct excitation at a all together. Let us first call on the reciprocal relation $\mathbf{Y}_{\mathbf{C}_{ab}}^{-1} = \mathbf{Y}_{\mathbf{C}_{ba}}^{-\mathbf{T}}$,

$$\mathbf{Z}_{\mathbf{I}_{c_2c_1}} = [\mathbf{T}_{\mathbf{C}_{c_1b}}^{\mathbf{a}} \mathbf{Y}_{\mathbf{C}_{c_2b}}^{\mathbf{T}} - \mathbf{Y}_{\mathbf{C}_{c_1b}} \mathbf{Y}_{\mathbf{C}_{ba}}^{-\mathbf{T}} \mathbf{Y}_{\mathbf{C}_{c_2a}}^{\mathbf{T}}]^{-1}. \quad (4.45)$$

The transposed mobility product $\mathbf{Y}_{\mathbf{C}_{ba}}^{-\mathbf{T}} \mathbf{Y}_{\mathbf{C}_{c_2a}}^{\mathbf{T}}$ may be rewritten as $(\mathbf{Y}_{\mathbf{C}_{c_2a}} \mathbf{Y}_{\mathbf{C}_{ba}}^{-1})^{\mathbf{T}}$. Making this substitution one arrives at,

$$\mathbf{Z}_{\mathbf{I}_{c_2c_1}} = [\mathbf{T}_{\mathbf{C}_{c_1b}}^{\mathbf{a}} \mathbf{Y}_{\mathbf{C}_{c_2b}}^{\mathbf{T}} - \mathbf{Y}_{\mathbf{C}_{c_1b}} (\mathbf{Y}_{\mathbf{C}_{c_2a}} \mathbf{Y}_{\mathbf{C}_{ba}}^{-1})^{\mathbf{T}}]^{-1}. \quad (4.46)$$

We may now formulate a generalised transmissibility relation for the inner bracketed term,

$$\mathbf{T}_{\mathbf{C}_{c_2b}}^{\mathbf{a}} = \mathbf{Y}_{\mathbf{C}_{c_2a}} \mathbf{Y}_{\mathbf{C}_{ba}}^{-1}. \quad (4.47)$$

Substituting Equation 4.47 into Equation 4.46,

$$\mathbf{Z}_{\mathbf{I}_{c2c1}} = [\mathbf{T}_{\mathbf{C}_{c1b}}^{\mathbf{a}} \mathbf{Y}_{\mathbf{C}_{c2b}}^{\mathbf{T}} - \mathbf{Y}_{\mathbf{C}_{c1b}} (\mathbf{T}_{\mathbf{C}_{c2b}}^{\mathbf{a}})^{\mathbf{T}}]^{-1} \quad (4.48)$$

and rearranging the resulting right hand term yields a transfer impedance formulation that, via the use of generalised transmissibility, does not require any known force excitations at the remote source DoF, a .

Transmissibility based impedance relation:

$$\mathbf{Z}_{\mathbf{I}_{c2c1}} = [\mathbf{T}_{\mathbf{C}_{c1b}}^{\mathbf{a}} \mathbf{Y}_{\mathbf{C}_{c2b}}^{\mathbf{T}} - (\mathbf{T}_{\mathbf{C}_{c2b}}^{\mathbf{a}} \mathbf{Y}_{\mathbf{C}_{c1b}}^{\mathbf{T}})^{\mathbf{T}}]^{-1} \quad (4.49)$$

Equation 4.49 provides an alternative approach for determining the dynamic transfer impedance of a coupling element, utilising the concept of generalised transmissibility. Based on the partial interface relation of Equation 3.11 and its remote extension (see Equation 4.24), the advantage of this approach is that all mobility terms requiring excitation at a are replaced by transmissibility terms. These terms may, in theory, be determined from operational velocities resulting from some unknown source side excitation at a ,

$$\mathbf{T}_{\mathbf{C}_{c1b}}^{\mathbf{a}} = \hat{\mathbf{V}}_{\mathbf{C}_{c1}} \hat{\mathbf{V}}_{\mathbf{C}_b}^{-1} \quad \mathbf{T}_{\mathbf{C}_{c2b}}^{\mathbf{a}} = \hat{\mathbf{V}}_{\mathbf{C}_{c2}} \hat{\mathbf{V}}_{\mathbf{C}_b}^{-1}. \quad (4.50)$$

The nature of this source side excitation is quite general. The DoF a can, in theory, be located anywhere on the source sub-structure and need not be internal. As such, an external excitation, for example via a hammer, may be used to generate the required velocities, as per Equation 4.50. Alternatively, in cases where the source sub-structure is an active component, one may use the ‘internal’ forces generated by its operational activity. Such an approach would be particularly useful in cases where the source sub-structure is completely enclosed and inaccessible.

It is important to reiterate that the velocity based transmissibility approach requires the inversion of a velocity matrix. In order to ensure invertability, it is essential that the sufficient external (or internal) forces are applied and, furthermore, that these forces are linearly independent, else the velocity matrix will be rank deficient and singular. Furthermore, similar to the standard remote approach, the use of additional forces allows for the over-determination of both the transmissibility matrices, and as such may be used as a means of reducing potential error.

4.3.3 EXPERIMENTAL VALIDATION

The use of operational velocities for characterising resilient elements is investigated here for the single and multi-contact assemblies, **F** and **G**, introduced earlier. These studies are brief, with their aim being to simply validate the theoretical developments of Section 4.3.1 and 4.3.2, whilst hopefully highlighting one of many potential applications of the generalised transmissibility concept.

With neither assembly consisting of an active sub-structure, the internal/external forces require, $\hat{\mathbf{f}}_{\mathbf{C}_{i/a}}$, are simulated using remote hammer impacts. In the case of assembly **F** this was done in a trivial manner such that the external forces were the same as those used to remotely determine the isolator stiffness in Section 4.2.3.1. In the case of assembly **G**, operational forces were simulated and used to determine time averaged quantities, from which predictions were made.

4.3.3.1 SINGLE CONTACT

BEAM-ISOLATOR-PLATE - The beam-isolator-plate assembly considered here is the same assembly as used in Section 3.4.1, and later in Section 4.2.3.1, details of which are given in Table 3.4. The measurements used here were carried out simultaneously to the remote characterisation presented in Section 4.2.3.1. The experimental set-up is shown diagrammatically in Figure 4.12 where, in addition to the spaced accelerometer pairs, a single remote accelerometer is adhered to the receiver sub-structure.

The measurement procedure may be outlined as follows:

- 1 A force is applied at the remote receiver position, b , and the transfer mobilities $\mathbf{Y}_{\mathbf{C}_{e2b}}$ and $\mathbf{Y}_{\mathbf{C}_{c1b}}$ are measured.
- 2 Forces are applied at each of the three remote source positions in order to simulate some set of internal operational forces. The resultant velocity auto- and cross-spectra at c_1 , c_2 , and b are measured. An arbitrary accelerometer was chosen as the phase reference for the cross-spectra. (These excitations were the same as those used in Section 4.2.3.1 to measure the transfer mobilities $\mathbf{Y}_{\mathbf{C}_{c2a}}$, $\mathbf{Y}_{\mathbf{C}_{ba}}$ and $\mathbf{Y}_{\mathbf{C}_{c1a}}$)

Following this, the cross-spectra phase was applied to the square-rooted auto-spectra via the cross-spectrum phase approach outlined in Section 6.2.3.2. The resultant

phase referenced velocity vectors were used, as in Equation 4.41, to determine the transmissibilities $\mathbf{T}_{C_{c1b}}$ and $\mathbf{T}_{C_{c2b}}$. It is perhaps worth noting once more that the velocities used by Equation 4.50, and the remaining mobilities required by Equation 4.49, were measured simultaneously to the remote partial interface characterisation presented in Section 4.2.3.1. This was done by storing auto- and cross-spectra data alongside the calculated mobilities.

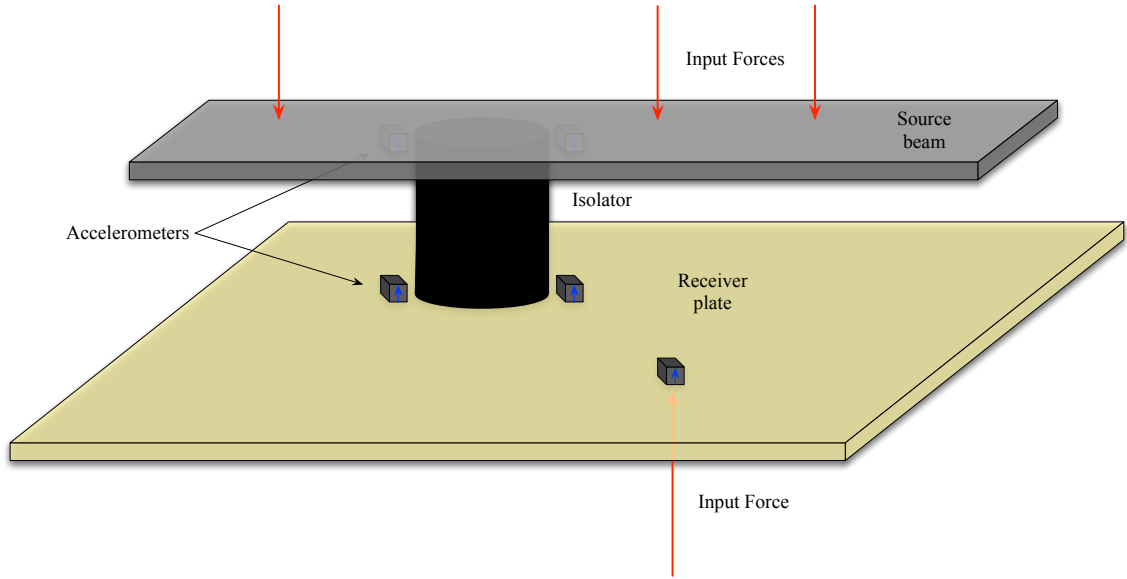
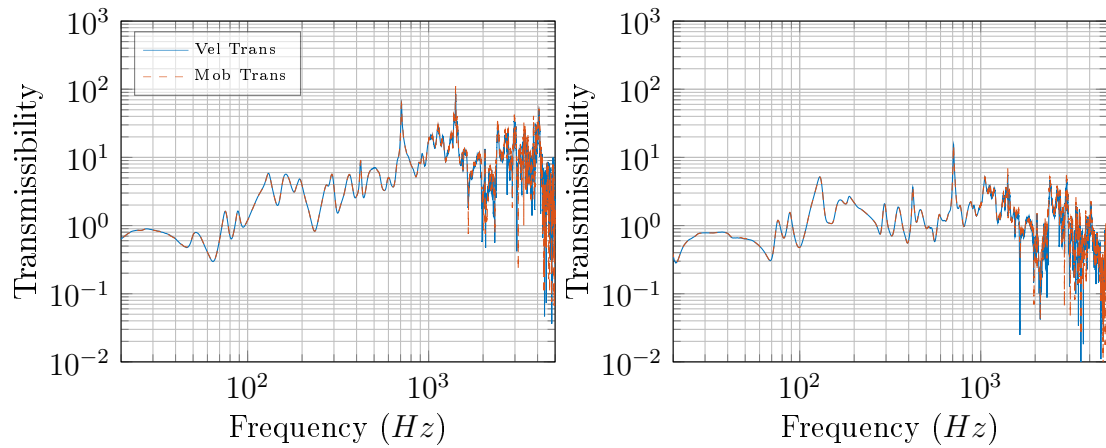
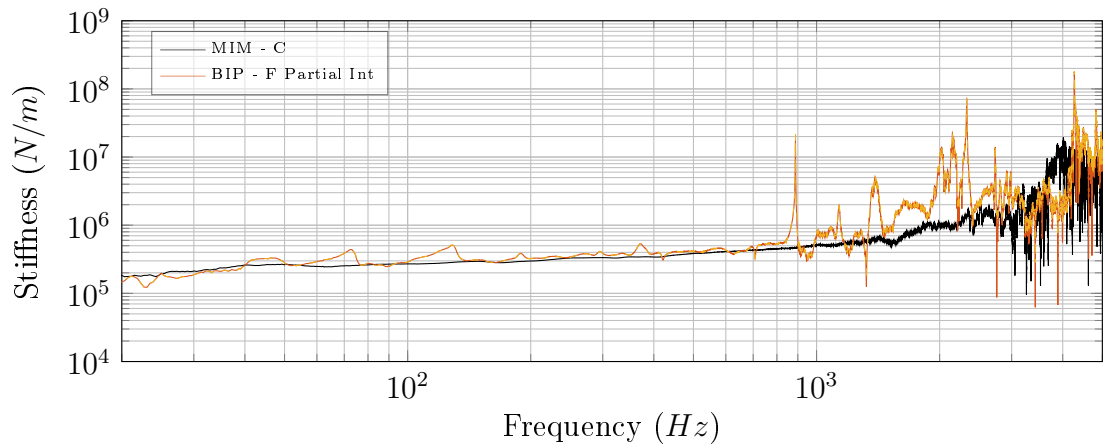


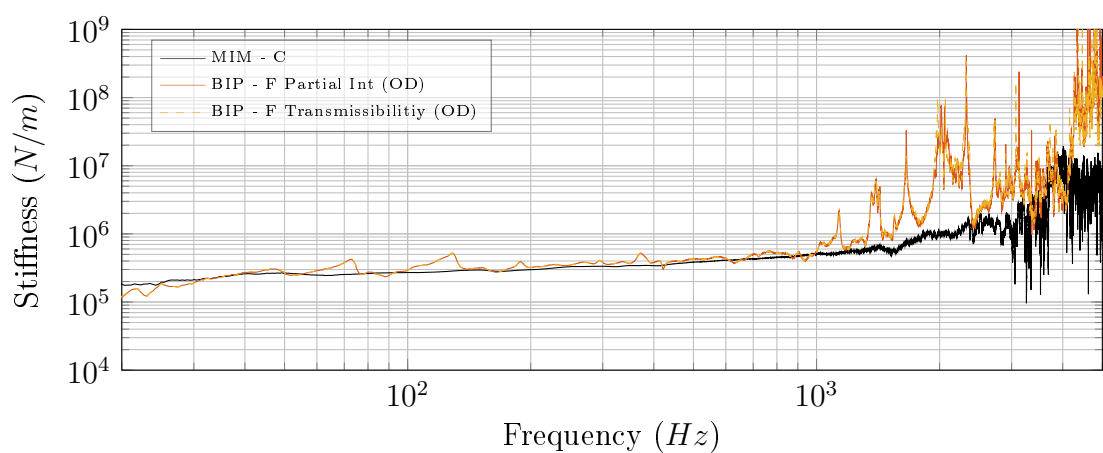
Figure 4.12: Diagrammatic representation of the beam-isolator(2)-plate test rig, **G**. Red arrows correspond to the direction and position of the applied forces, whilst blue arrows indicate the positive direction of the measured accelerations.

Shown in Figures 4.13a and 4.13b are the 3 fold over-determined transmissibilities, $\mathbf{T}_{C_{c2b}}$ and $\mathbf{T}_{C_{c1b}}$, respectively. The transmissibilities were determined via the mobility products $\mathbf{Y}_{C_{c1a}} \mathbf{Y}_{C_{ba}}^{-1}$ and $\mathbf{Y}_{C_{ab}}^{-1} \mathbf{Y}_{C_{c2a}}^T$ (dashed orange), and velocity products $\mathbf{V}_{C_{c1}} \mathbf{V}_{C_b}^{-1}$ and $\mathbf{V}_{C_a} \mathbf{V}_{C_{c2}}^{-1}$ (blue). As one might expect with the velocities having resulted from the same excitations used to determine the mobilities, the two are in near perfect agreement. With these two transmissibility terms in such good agreement, it is no surprise that the dynamic transfer stiffness acquired via the velocity based transmissibility approach is also in near perfect agreement with those determined via the standard remote partial and full interface approaches, as shown in Figure 4.13c and 4.13d.

The results presented in Figure 4.13 are, in a sense, trivial as the same excitation was used in both velocity and mobility based approaches, not to mention that for a single contact point the transmissibility matrices reduce to scalar values. Regardless, Figure 4.13 clearly validates the use of velocity based transmissibilities in the

(a) Transmissibility - $T_{C_{e2b}}$ (b) Transmissibility - $T_{C_{e1b}}$ 

(c) Dynamic transfer stiffness.



(d) Dynamic transfer stiffness (over-determined).

Figure 4.13: Transmissibility based predictions determined from assembly **F** using mobility and velocity based approaches.

determination of dynamic transfer stiffness. In the following Section the velocity based transmissibility approach will be implemented on a multi-contact assembly, with a more realistic excitation type.

4.3.3.2 MULTIPLE CONTACT

BEAM-ISOLATOR(2)-PLATE - The multi-contact assembly considered here is the same **BI(2)P** assembly as used in Section 3.4.2, and later in Section 4.2.3.2, details of which are given in Table 3.5. To avoid the trivial excitation case, the ‘operational’ forces here were simulated using quickly repeated hammer hits in the rough vicinity of the remote source DoFs. These forces were applied over a period of 30 seconds from which the time averaged velocity auto- and cross-spectrum data was calculated.

The experimental set-up used is shown diagrammatically in Figure 4.14, where in addition to the spaced accelerometer pairs, two remote accelerometers are adhered to the receiver sub-structure.

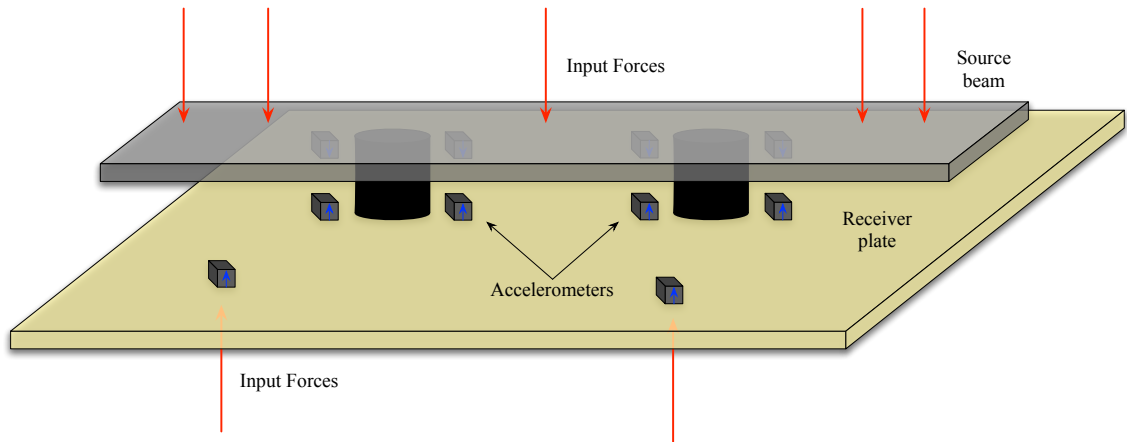


Figure 4.14: Diagrammatic representation of the beam-isolator(2)-plate test rig, **H**. Red arrows correspond to the direction and position of the applied forces, whilst blue arrows indicate the positive direction of the measured accelerations.

The multi-contact nature of assembly **G** has meant that the transmissibility terms, $\mathbf{T}_{C_{e2b}}$ and $\mathbf{T}_{C_{c1b}}$, each take the form of a 2×2 matrix. Shown in Figures 4.15 and 4.16 are the individual entries of each transmissibility matrix, determined via the time averaged velocity (blue) and mobility (dashed orange) based approaches. Good agreement is obtained in all cases, with some slight disagreement occurring in some anti-resonant regions, and at higher frequencies above approximately 2kHz.

Shown in Figure 4.17 are the dynamic transfer stiffnesses acquired using the transmissibility based approach (purple), where the transmissibility terms are determined from the time averaged velocity auto- and cross-spectra. Also shown are the stiffnesses obtained via the standard remote partial interface approach (yellow). In both cases only the over-determined solutions are considered. The stiffness values determined via the transmissibility approach are in good agreement with those measured both directly via the full interface approach (orange), and remotely via the partial interface approach. Like the remote partial interface relation, the transmissibility based approach avoids the large resonant artefacts observed in the directly determined full interface stiffnesses. Unlike the partial interface approach, however, a number of new, arguably less severe, artefacts are introduced, for example those occurring around 100Hz.

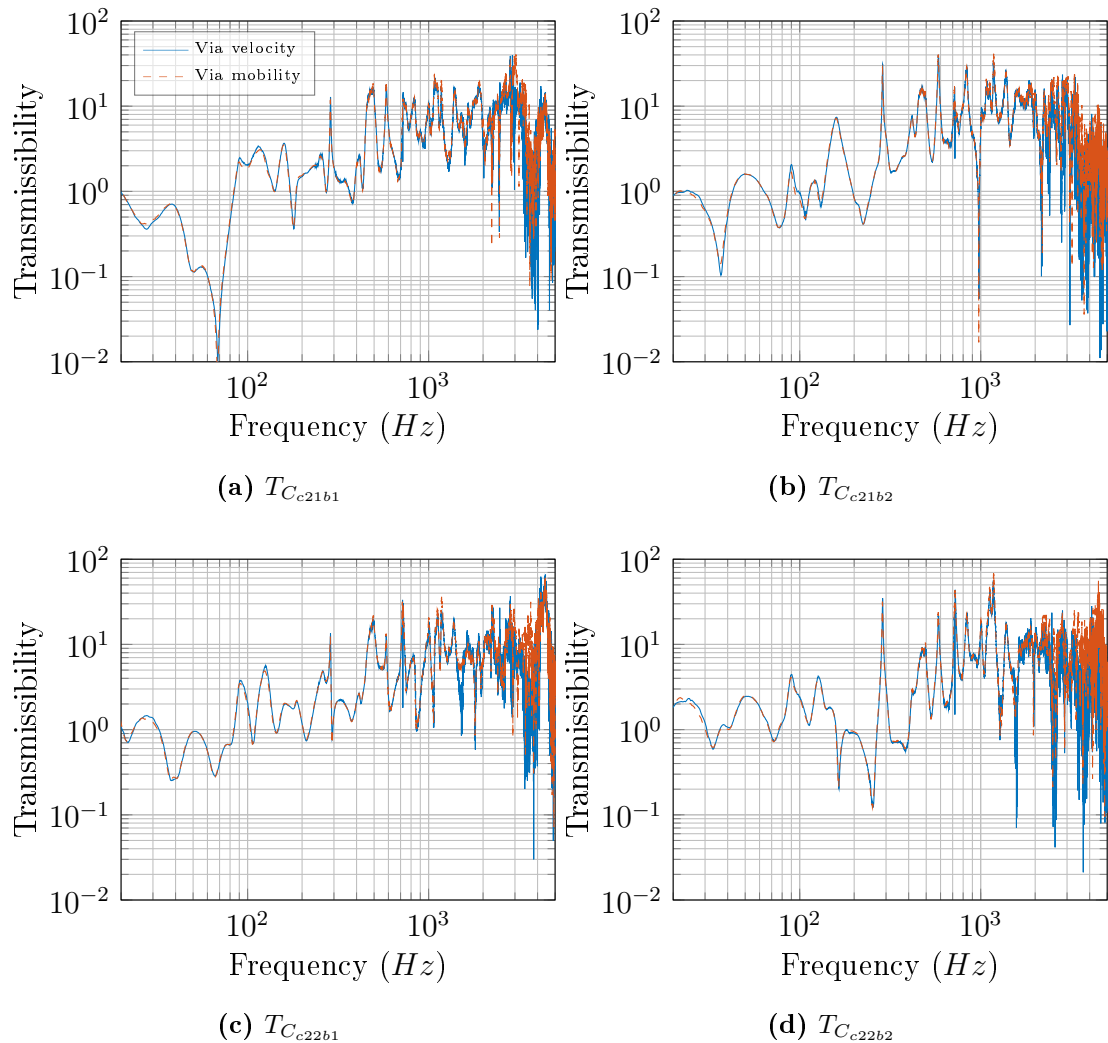


Figure 4.15: Elements of the transmissibility matrix $\mathbf{T}_{C_{c2b}}$ determined via time averaged velocity and standard mobility measurements on assembly \mathbf{G} .

It is interesting to note the improved low frequency response of the transmissibility based approach, over the remote partial interface stiffnesses. This improved response, particularly below 50Hz, likely results from avoiding the source side excitation inaccuracies that would be accompanied by the mobility based approach, and result in poor coherence between the excitation source (i.e. the force hammer) and the resulting responses. Even with very careful excitation it is exceedingly difficult to achieve a mobility with good coherence in this frequency range. The transmissibility based approach, however, requires only a good coherence between the accelerometers across mount, and is therefore far less susceptible to user measurement error.

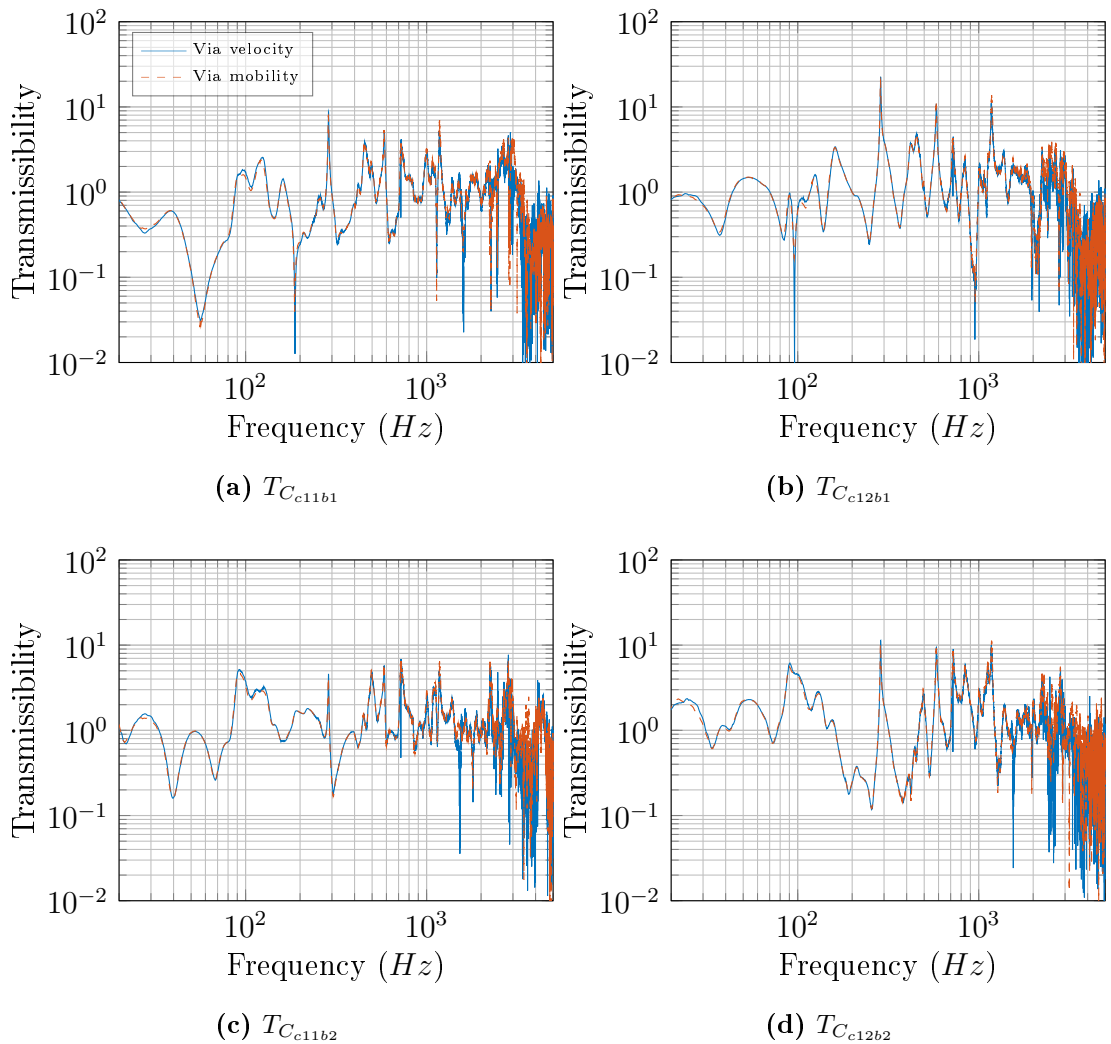
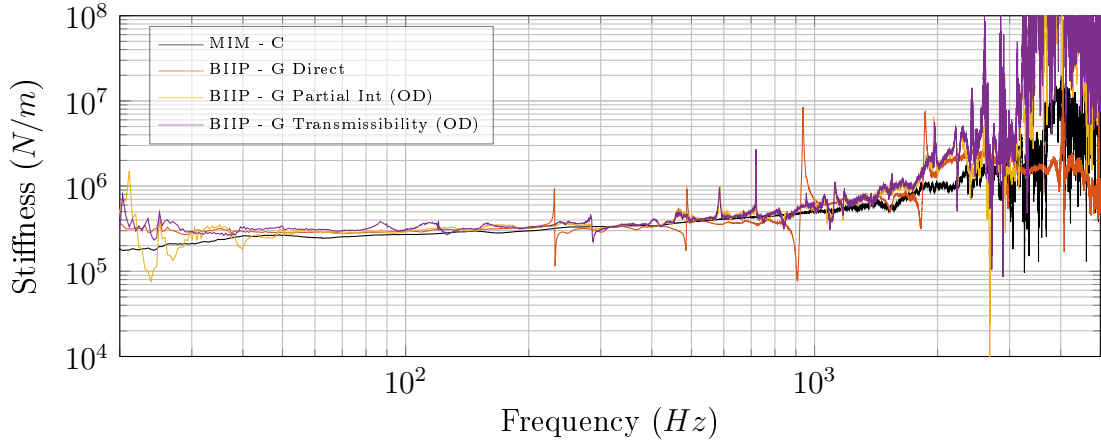


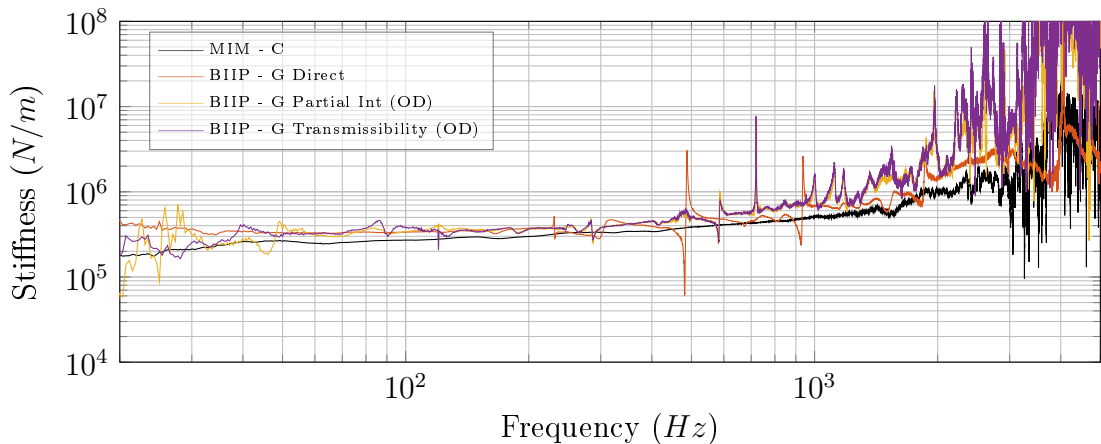
Figure 4.16: Elements of the transmissibility matrix $\mathbf{T}_{C_{1b}}$ determined via time averaged external velocity and standard mobility measurements on assembly \mathbf{G} .

Although only a brief experimental investigation has been carried out, the results

presented here are enough to validate the incorporation of generalised transmissibilities and, furthermore, demonstrate their potential in the determination of dynamic transfer stiffness.



(a) Isolator 1 stiffness



(b) Isolator 2 stiffness

Figure 4.17: Dynamic transfer stiffness predictions for the two resilient elements of assembly \mathbf{G} using the time averaged velocity based transmissibility approach (over-determined).

4.4 CONCLUDING REMARKS

This Chapter has been concerned with the extension of the in-situ approach via state-of-the-art experimental methods. These methods included the finite difference approximation for the inclusion of rotational DoFs, the round trip identity (and its dual interface counterpart) for the extension to remote measurement positions and,

lastly, the concept of generalised transmissibility for the replacement of externally applied forces with operational velocities.

The extensions proposed here have been implemented on numerous assembly types and provided promising results in all cases. Together these extensions offer a characterisation method that is not only applicable in-situ, but flexible enough to be used in practical scenarios.

**PART III. SOURCE AND
RECEIVERS**

IN-SITU SUB-STRUCTURE DECOUPLING

In this Chapter an in-situ approach for the decoupling of resiliently coupled source and receiver sub-structures is proposed. The decoupling procedure makes use of the in-situ characterisation method, as presented in Chapter 3, to determine the free-interface mobility matrices of both source and receiver sub-structures.

CONTENTS

5.1	Sub-structure Decoupling	103
5.2	In-situ Decoupling Theory	106
5.3	Experimental Investigation	112
5.4	Concluding Remarks	125

5.1 SUB-STRUCTURE DECOUPLING

As discussed in Section 2.3, dynamic sub-structuring allows for the behaviour of a coupled assembly to be predicted from the independent properties of its constituent sub-structures. This is achieved through the enforcement of compatibility and equilibrium between appropriate sub-structure frequency response functions. The unique advantages offered by dynamic sub-structuring has seen a large number of published works in the field. A comprehensive overview of these may be found in [136]. However, this Chapter does not concern the coupling of sub-structures, rather the opposite.

In recent years dynamic sub-structuring procedures have been reversed and used instead as a means of de-coupling assemblies. Referred to here as sub-structure decoupling, this approach is used to determine the uncoupled dynamic properties of a particular sub-structure from measurements made on the coupled assembly. The standard decoupling approach requires a residual sub-structure (i.e. the sub-structure from which the target sub-structure is to be decoupled) to be independently characterised beforehand, i.e. the assembly must be *physically* decoupled prior to the sub-structure decoupling. This residual sub-structure is then mathematically decoupled from the assembly, leaving behind the dynamic properties of the target sub-structure. This approach is particularly useful in determining the dynamic properties of a sub-structure that can not be reliably suspended, i.e. for the direct measurement of its free-interface mobility. As an example, consider the experimental characterisation of a train carriage. It is simply impractical to suspend the entire carriage so as to obtain its free-interface mobility. Instead, the mobility of coupled carriage-bogey assembly is measured. The assembly is physically decoupled and the mobility of the bogey (i.e. the residual sub-structure) measured. This residual sub-structure is then mathematically decoupled from the coupled assembly, leaving behind the uncoupled dynamics of the carriage.

Although offering a number of advantages, the standard sub-structure decoupling approach requires the assembly to be *physically* decoupled prior to its implementation. This often defeats the purpose of the approach. If the sub-structures are to be physically decoupled one may as well measure the free-interface mobility directly. That said, this is often impractical. As such, we concern ourselves with an alternative decoupling method where physical decoupling is not required. It will be shown in this Chapter that for resiliently coupled assemblies, the free-interface source and receiver mobilities may be acquired through a de-coupling procedure that requires in-situ measurements only. Such an approach is made possible through the application of the in-situ characterisation method, presented in Chapter 3.

For a sufficiently resilient mounting, source/receiver sub-structures are often considered ‘approximately’ free [29]. However, in the lower frequency region, where the impedance of the resilient mounts become comparable to that of the source/receiver sub-structure, the coupled dynamics differ from that of the true free behaviour. The frequency beyond which a resiliently coupled sub-structure behaves freely will depend on the local impedance of the sub-structure and the stiffness of the resilient element used as a support. Below this frequency, the resilient element will likely

behave as a massless spring, exhibiting no internal resonances. This assumption is key in the development of the proposed in-situ decoupling procedure.

The successful implementation of an in-situ decoupling procedure would, in theory, allow for the source, receiver and coupling elements to be independently characterised, simultaneously, from measurements made in-situ on the coupled assembly. A completely in-situ characterisation procedure would offer a number of unique advantages:

- Only a single test procedure would be required to independently characterise source, isolator and receiver sub-structures.
- Avoids having to ‘freely’ suspend any sub-structures. This would be particularly useful in cases where; the sub-structure of interest is light weight and free suspension would significantly influence its dynamic behaviour, or in cases where the sub-structure is large and free suspension is impractical.
- The free-interface mobility would be determined whilst under of a representative mounting condition, and therefore account for any changes in the physical properties due to its coupled state (i.e. pre-load, additional stresses induced due to coupling, etc.)
- Could be used as a passive counterpart to the in-situ blocked force method (see Section 6), where the independent passive properties of a source sub-structure are also determined in-situ, thus offering a *complete* source/assembly characterisation.

Similar works have been presented in recent years concerning the decoupling of resiliently coupled sub-structures [137–139]. Whilst these approaches differ, their aims remain the same; to independently characterise source/receiver sub-structures from in-situ measurements.

In their two part paper [138, 139] Pavic and Elliot approached the decoupling problem by considering the application of force conservation across the coupling mount. In doing so the authors implicitly make the assumption of a sufficiently resilient coupling element, with a negligible distributed mass. Expressions for the free-interface mobility of both source and receiver sub-structures are presented, requiring only the point and transfer mobilities of the coupled assembly. Numerical validations are presented for both single and multi-contact assemblies, with results compared

against an alternative (benchmark) method where the independent coupling element properties are required to decouple the source and receiver. Whilst numerical simulations were able to validate the method and offer some insight with regards to its sensitivity to noise, the authors fail to provide any experimental results.

An alternative approach, referred to as the link-preserving decoupling (LPD) method, was proposed by Keersmaekers et al. [137]. The authors consider coupling ‘links’ as parallel connections of springs and dampers, operational in only the translational z coordinate-DoFs. Following a lengthy derivation a formula is presented for the decoupled mobility of a receiver sub-structure in terms of coupled assembly mobilities. The LPD approach requires no knowledge of the properties of the coupling elements, as these terms cancel in the derivation. The method is validated via a 6 DoF lumped parameter model. A further numerical study is carried out concerning its application to non-linear coupling elements. It was shown that the LPD method is better suited to dealing with non-linear systems than the standard physical decoupling approach. A brief experimental case study was also presented. Although the LPD method provided a reasonable estimate of the uncoupled mobility, the experimental set-up was simplistic and, furthermore, only concerned frequencies up to 80Hz.

Unlike those discussed above, the proposed in-situ decoupling procedure offers an independent characterisation of the resilient coupling elements alongside the source and receiver sub-structures. Additionally, with the approach being based on the in-situ characterisation presented in Chapter 3, all of its proposed extensions (remote measurement positions, finite difference approximation, and generalized transmissibilities) may, in theory, be utilized. With previous works having focused on numerical validations, this Chapter will consider the experimental implementation of the proposed method.

The remainder of this Chapter will see the development of the in-situ decoupling theory, followed by a series of experimental validations.

5.2 IN-SITU DECOUPLING THEORY

Let us begin by considering an arbitrary multi-contact assembly, as depicted in Figure 5.1. The assembly consists of a source (**S**) and receiver (**R**) sub-structure

coupled together via N resilient supports (\mathbf{I}). Assuming that each positional-DoF is able to move in all 6 coordinate-DoFs, the general coupled impedance matrix is given by,

$$\mathbf{Z}_C = \left[\begin{array}{cccc|cccc} \mathbf{Z}_{C_{c11c11}} & \mathbf{Z}_{S_{c11c12}} & \cdots & \mathbf{Z}_{S_{c11c1N}} & -\mathbf{Z}_{I_{c11c21}} & 0 & 0 & 0 \\ \mathbf{Z}_{S_{c12c11}} & \mathbf{Z}_{C_{c12c12}} & \cdots & \mathbf{Z}_{S_{c12c1N}} & 0 & -\mathbf{Z}_{I_{c12c22}} & 0 & 0 \\ \vdots & \vdots & \ddots & \vdots & 0 & 0 & \ddots & 0 \\ \mathbf{Z}_{S_{c1Nc11}} & \mathbf{Z}_{S_{c1Nc12}} & \cdots & \mathbf{Z}_{C_{c1Nc1N}} & 0 & 0 & 0 & -\mathbf{Z}_{I_{c1Nc2N}} \\ \hline -\mathbf{Z}_{I_{c21c11}} & 0 & 0 & 0 & \mathbf{Z}_{C_{c21c21}} & \mathbf{Z}_{R_{c21c22}} & \cdots & \mathbf{Z}_{R_{c21c2N}} \\ 0 & -\mathbf{Z}_{I_{c22c12}} & 0 & 0 & \mathbf{Z}_{R_{c22c21}} & \mathbf{Z}_{C_{c22c22}} & \cdots & \mathbf{Z}_{R_{c22c2N}} \\ 0 & 0 & \ddots & 0 & \vdots & \vdots & \ddots & \vdots \\ 0 & 0 & 0 & -\mathbf{Z}_{I_{c2Nc1N}} & \mathbf{Z}_{R_{c2Nc21}} & \mathbf{Z}_{R_{c2Nc22}} & \cdots & \mathbf{Z}_{C_{c2Nc2N}} \end{array} \right] \quad (5.1)$$

where, for example, $\mathbf{Z}_{C_{c12c12}}$ is the coupled point impedance matrix at the second contact on the source sub-structure \mathbf{S} , $\mathbf{Z}_{S_{c11c1N}}$ is the coupled transfer impedance matrix between the first and N th contact on the source sub-structure \mathbf{S} , and $\mathbf{Z}_{I_{c11c21}}$ is the coupled transfer impedance matrix across the first resilient mount. In general, each block impedance matrix contains both translational and rotational DoFs, and therefore has the dimensions 6×6 . The density of each block impedance matrix will depend upon the nature of the problem. For example, when the cross coupling between DoFs is minimal, as in many resilient elements, the block impedance matrices will be relatively sparse.

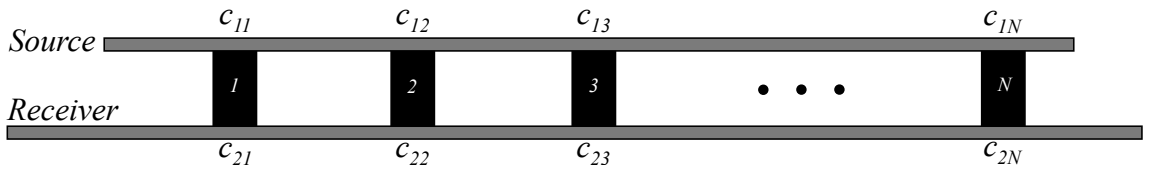


Figure 5.1: Diagrammatic representation of the general multi-contact assembly considered in the in-situ decoupling procedure.

If we consider Equation 5.1 in a further blocked form it is clear that the diagonal elements $\mathbf{Z}_{C_{c1c1}}$ and $\mathbf{Z}_{C_{c2c2}}$ represent properties of the coupled assembly, whilst the off diagonal elements, $\mathbf{Z}_{I_{c1c2}}$ and $\mathbf{Z}_{I_{c2c1}}$, are independent properties of the N coupling elements.

$$\mathbf{Z}_C = \left[\begin{array}{c|c} \mathbf{Z}_{C_{c1c1}} & -\mathbf{Z}_{I_{c1c2}} \\ \hline -\mathbf{Z}_{I_{c2c1}} & \mathbf{Z}_{C_{c2c2}} \end{array} \right] \quad (5.2)$$

Let us now consider the well established relation for the coupled mobility/impedance of two arbitrary sub-structures, referred to here as A and B .

$$Y_{C_{cc}}^{-1} = Y_{A_{cc}}^{-1} + Y_{B_{cc}}^{-1} \quad (5.3)$$

Equation 5.3 states that the coupled point impedance, $Z_{C_{cc}} = Y_{C_{cc}}^{-1}$, at the coupling DoF c , is equal to the sum of the two uncoupled sub-structure point impedances; $Z_{A_{cc}} = Y_{A_{cc}}^{-1}$ and $Z_{B_{cc}} = Y_{B_{cc}}^{-1}$. This relation can be extended to include all 6 coordinate DoFs. For example, in the case of our multi-contact assembly, $\mathbf{Z}_{\mathbf{C}_{c1Nc1N}} = \mathbf{Z}_{\mathbf{S}_{c1Nc1N}} + \mathbf{Z}_{\mathbf{I}_{c1Nc1N}}$, where $\mathbf{Z}_{\mathbf{C}_{c1Nc1N}}$ are the source side coupled point impedances, and $\mathbf{Z}_{\mathbf{S}_{c1Nc1N}}$ and $\mathbf{Z}_{\mathbf{I}_{c1Nc1N}}$ are point impedances of the uncoupled source sub-structure and resilient mounts, respectively.¹ Extended further for each positional-DoF, the impedance of our coupled assembly may be expressed as the sum of the uncoupled sub-structure impedance matrices,

$$\left[\begin{array}{c|c} \mathbf{Z}_{\mathbf{C}_{c1c1}} & -\mathbf{Z}_{\mathbf{I}_{c1c2}} \\ \hline -\mathbf{Z}_{\mathbf{I}_{c2c1}} & \mathbf{Z}_{\mathbf{C}_{c2c2}} \end{array} \right] = \left[\begin{array}{c|c} \mathbf{Z}_{\mathbf{S}_{c1c1}} & 0 \\ \hline 0 & \mathbf{Z}_{\mathbf{R}_{c2c2}} \end{array} \right] + \left[\begin{array}{c|c} \mathbf{Z}_{\mathbf{I}_{c1c1}} & -\mathbf{Z}_{\mathbf{I}_{c1c2}} \\ \hline -\mathbf{Z}_{\mathbf{I}_{c2c1}} & \mathbf{Z}_{\mathbf{I}_{c2c2}} \end{array} \right] \quad (5.4)$$

or in a more condensed form,

$$\mathbf{Z}_{\mathbf{C}} = \mathbf{Z}_{\mathbf{SR}} + \mathbf{Z}_{\mathbf{I}} \quad (5.5)$$

where $\mathbf{Z}_{\mathbf{SR}}$ is a block diagonal matrix containing source and receiver impedance matrices, and $\mathbf{Z}_{\mathbf{I}}$ is a sparse matrix containing the point and transfer impedances of each coupling element.

With the aim of determining the uncoupled source-receiver mobility matrix let us simply rearrange Equation 5.5 such that the source-receiver impedance matrix, $\mathbf{Z}_{\mathbf{SR}}$, is given as the difference between the coupled assembly and coupling element impedance matrices,

$$\mathbf{Z}_{\mathbf{SR}} = \mathbf{Z}_{\mathbf{C}} - \mathbf{Z}_{\mathbf{I}}. \quad (5.6)$$

Similar approaches have, in the past, been used in an attempt to decouple rigidly connected source and receiver sub-structures [82]. However, for the rigid case, one must first separate the source and receiver so as to determine the properties of the ‘residual’ sub-structure, which is then subtracted from the coupled impedance.

¹It is important to note that each block point impedance matrix contains the force/velocity relations between all coordinate-DoFs. All of these, including the cross coupling impedance terms must be accounted for in order to correctly describe the coupling between two sub-structures.

Although used with relative success in the past, this method is not practical in the case of a resiliently mounted assembly, as the residual sub-structure is not directly measurable. Consider the determination of the source sub-structure impedance using a residual sub-structure consisting of the remaining coupled isolator-receiver portion of the assembly. In order to independently characterise this residual sub-structure one would be required to measure the point impedance at the uncoupled end of the isolator. This is clearly impractical as there would likely be no space to perform the required measurements and, furthermore, the isolator would no longer be under a representative mounting condition. It is instead proposed that for a resiliently mounted assembly, we define the residual sub-structure as our isolator impedance matrix, \mathbf{Z}_I , and that the independent properties of this residual sub-structure be determined via the in-situ characterisation approach, presented in Chapter 3. This approach requires only in-situ measurements, and thus avoids the need to dismantle the assembly. Subtraction of this residual sub-structure from the coupled assembly yields the uncoupled and independent source-receiver impedance matrix, \mathbf{Z}_{SR} , from which their corresponding free-interface mobilities may be determined.

In the case of a resiliently coupled assembly, the residual coupling impedance matrix \mathbf{Z}_I is given by,

$$\mathbf{Z}_I = \left[\begin{array}{c|c} \mathbf{Z}_{I_{c1c1}} & -\mathbf{Z}_{I_{c1c2}} \\ \hline -\mathbf{Z}_{I_{c2c1}} & \mathbf{Z}_{I_{c2c2}} \end{array} \right]. \quad (5.7)$$

It was shown in Section 3.2 that the dynamic transfer impedance $\mathbf{Z}_{I_{c1c2}} = \mathbf{Z}_{I_{c2c1}}^T$ could be acquired through the inversion of a coupled interface mobility matrix. Unfortunately, the point impedances cannot be obtained by the same process. However, if we consider the resilient mount as a spring-like element, i.e. with a negligible distributed mass, the force across the mount is conserved and we may assume,

$$\mathbf{Z}_{I_{c1c1}} \approx \mathbf{Z}_{I_{c1c2}} = \mathbf{Z}_{I_{c1c2}}^T \approx \mathbf{Z}_{I_{c2c2}}. \quad (5.8)$$

As such, the entire coupling impedance matrix may be approximated from the in-situ determined transfer impedances.

$$\left[\begin{array}{c|c} \mathbf{Z}_{I_{c1c1}} & -\mathbf{Z}_{I_{c1c2}} \\ \hline -\mathbf{Z}_{I_{c2c1}} & \mathbf{Z}_{I_{c2c2}} \end{array} \right] \approx \left[\begin{array}{c|c} \mathbf{Z}_{I_{c2c1}} & -\mathbf{Z}_{I_{c1c2}} \\ \hline -\mathbf{Z}_{I_{c2c1}} & \mathbf{Z}_{I_{c1c2}} \end{array} \right] \quad (5.9)$$

It is important to reiterate however, that this assumption is only valid whilst the coupling element behaves as a massless spring. This assumption covers a frequency

range up to approximately its first internal resonance, where the distributed mass begins to take effect. Fortunately, for sufficiently resilient elements, the coupling element impedance contributes only at low frequencies, due to the inverse frequency proportionality of spring like elements, $Z_k = \frac{k}{i\omega}$. The dynamics of resiliently coupled source or receiver sub-structures, in the region of an internal mount resonance, are therefore approximately free, regardless. The in-situ decoupling procedure is therefore be given by,

In-situ decoupling procedure:

$$\left[\begin{array}{c|c} \mathbf{Z}_{S_{c1c1}} & 0 \\ \hline 0 & \mathbf{Z}_{R_{c2c2}} \end{array} \right] \approx \left[\begin{array}{c|c} \mathbf{Z}_{C_{c1c1}} & -\mathbf{Z}_{I_{c1c2}} \\ \hline -\mathbf{Z}_{I_{c2c1}} & \mathbf{Z}_{C_{c2c2}} \end{array} \right] - \left[\begin{array}{c|c} \mathbf{Z}_{I_{c1c2}} & -\mathbf{Z}_{I_{c1c2}} \\ \hline -\mathbf{Z}_{I_{c2c1}} & \mathbf{Z}_{I_{c2c1}} \end{array} \right] \quad (5.10)$$

where the entries of the residual isolator impedance matrix are determined via any one of the approaches presented through Chapter 3. Following its acquirement, the source-receiver impedance matrix may be inverted and the uncoupled free-interface matrices attained.

$$\left[\begin{array}{c|c} \mathbf{Y}_{S_{c1c1}} & 0 \\ \hline 0 & \mathbf{Y}_{R_{c2c2}} \end{array} \right] = \left[\begin{array}{c|c} \mathbf{Z}_{S_{c1c1}} & 0 \\ \hline 0 & \mathbf{Z}_{R_{c2c2}} \end{array} \right]^{-1} \quad (5.11)$$

At this point we should note that the above procedure has been presented for the case where all DoFs of interest lie at source/receiver the coupling interface. However, we are often interested in DoFs remote to this interface. It is relatively trivial to extend the approach to include these additional DoFs. If we consider the remote source and receiver DoFs, a and b , as in Figure 3.1, Equation 5.10 may be written more generally as,

$$\begin{aligned} & \left[\begin{array}{cc|cc} \mathbf{Z}_{S_{aa}} & \mathbf{Z}_{S_{ac1}} & 0 & 0 \\ \mathbf{Z}_{S_{c1a}} & \mathbf{Z}_{S_{c1c1}} & 0 & 0 \\ \hline 0 & 0 & \mathbf{Z}_{R_{c2c2}} & \mathbf{Z}_{R_{c2b}} \\ 0 & 0 & \mathbf{Z}_{R_{bc2}} & \mathbf{Z}_{R_{bb}} \end{array} \right] \approx \dots \\ & \dots \approx \left[\begin{array}{cc|cc} \mathbf{Z}_{S_{aa}} & \mathbf{Z}_{S_{ac1}} & 0 & 0 \\ \mathbf{Z}_{S_{c1a}} & \mathbf{Z}_{C_{c1c1}} & -\mathbf{Z}_{I_{c1c2}} & 0 \\ \hline 0 & -\mathbf{Z}_{I_{c2c1}} & \mathbf{Z}_{C_{c2c2}} & \mathbf{Z}_{R_{c2b}} \\ 0 & 0 & \mathbf{Z}_{R_{bc2}} & \mathbf{Z}_{R_{bb}} \end{array} \right] - \left[\begin{array}{cc|cc} 0 & 0 & 0 & 0 \\ 0 & \mathbf{Z}_{I_{c1c2}} & -\mathbf{Z}_{I_{c1c2}} & 0 \\ \hline 0 & -\mathbf{Z}_{I_{c2c1}} & \mathbf{Z}_{I_{c2c1}} & 0 \\ 0 & 0 & 0 & 0 \end{array} \right]. \quad (5.12) \end{aligned}$$

Here the coupling element impedance matrix, $\mathbf{Z}_{\mathbf{I}}$, is located within an otherwise zero block matrix such that the rows and columns it occupies coincide with those of the coupling DoFs. The purpose of this extension is that one may now acquire a free-interface source/receiver mobility matrix that includes the (free-interface) transfer mobilities between coupling interface and remote DoFs.

There are a few important details to note concerning the in-situ decoupling approach. Firstly, the assumption $\mathbf{Z}_{\mathbf{I}_{e1c1}} \approx -\mathbf{Z}_{\mathbf{I}_{e1c2}}$ (and its reciprocal relation) is not limited to coupling elements of a resilient nature; it may also be valid in the case of rigid couplings, provided they too behave as ideal springs (e.g. an elastic rod, below its first internal resonance). As such, Equations 5.9-5.12 are not strictly limited to resiliently coupled sub-structures. However, the ability to determine the independent transfer impedance of the coupling element through the in-situ approach (i.e. the inversion of a contact interface mobility matrix) *is* restricted to resilient elements. In the case of a rigid coupling the velocities above and below the coupling elements are equal and the measured interface mobility matrix becomes singular, and therefore non-invertable. Consequently, the decoupling procedure described above is only applicable to resiliently coupled sub-structures.

Secondly, it is important to consider, when decoupling sub-structures, which DoFs are most important and need to be accounted for. Clearly it is essential that all positional-DoFs be accounted for, else the sub-structures will not be completely decoupled. That said, accounting for all 6 coordinate-DoFs at each positional-DoF would place a high demand on measurement hardware, not to mention experimental effort. Furthermore, it is often far less apparent which coordinate-DoFs are providing a strong coupling between sub-structures, as opposed to positional DoFs which may be clearly identified. It was shown by Elliot [57] that for rigidly coupled sub-structures one often has to consider multiple coordinate-DoFs (i.e rotational and in-plane) in coupling/decoupling procedures. That said, in the case of a resiliently coupled assembly many of these coordinate-DoFs may be considered negligible, and to some extent, ignored. In this work we will consider only the decoupling of sub-structures in the translational z DoF.

Thirdly, with reference to Equation 5.1, we note that $\mathbf{Z}_{\mathbf{I}_{e1c2}}$ is diagonal. This results from the definition of impedance (see Section 2.1.2), i.e. the velocities at all interfaces, other than that being excited by the applied velocity, are constrained. For example, let us consider the transfer impedance $\mathbf{Z}_{\mathbf{I}_{c11c22}}$ from Figure 5.1. As per the definition of impedance, $\mathbf{Z}_{\mathbf{I}_{c11c22}}$ requires the constraint of the interfaces,

$c_{21}, c_{23} \dots c_{2N}$ and $c_{11}, c_{12}, c_{13} \dots c_{1N}$. As such, there is no direct path between c_{11} and c_{22} , and the resulting blocked force $\bar{f}_{c_{11}}$ is 0. This in turn leads to $\mathbf{Z}_{\mathbf{I}_{c_{11}c_{22}}} = 0$. With the above in mind, unless we are able to account for all 6 coordinate-DoFs at each positional-DoF with absolute accuracy, the off-diagonal impedance elements resulting from the full interface approach will be non-zero. This will likely be the case experimentally, where it is difficult to account for all coordinate-DoFs. This matter is further complicated by the fact that coupling interfaces may only be considered point like over a particular frequency range, beyond which they must be treated as continuous interfaces.

Finally, it is interesting to note that further to the decoupling of source and receiver sub-structures, the in-situ approach may be used to mathematically ‘remove’ individual coupling elements from an assembly, whilst leaving the remaining ones installed. Such a use may be of interest when investigating potential structural modifications or whilst trying to assess the contribution of a particular transfer path/mount. Although not investigated further here, such an application may prove an interesting area for further study.

5.3 EXPERIMENTAL INVESTIGATION

In order to validate and assess the implementation of the proposed in-situ decoupling procedure a number of experimental studies have been conducted. In each study the free-interface mobilities of both source and receiver sub-structures are determined via the in-situ decoupling procedure. The assemblies considered are those of **E**, **F** and **G** previously introduced in Chapter 3. These assemblies cover a range of different assembly types, including partly-resonant, resonant, single and multi-contact.

The in-situ decoupling procedure is verified by comparing the resulting free-interface mobilities with those measured directly. That said, source sub-structures must be ‘freely’ suspended in some way so as to measure their free-interface mobilities. With any form of suspension introducing additional impedance, we are unable to determine their true free-interface mobilities for comparison. However, by using simple structures, i.e. masses and beams, whose free-interface dynamic behaviours are well understood, one should be able to verify as to whether the decoupling approach has been at least partly successful without a direct comparison.

5.3.1 SINGLE CONTACT

The two single contact assemblies considered here are the mass-isolator-plate (assembly **E**) and beam-isolator-plate (assembly **F**), previously introduced in Section 3.4.1. Further details of these assemblies may be found in Tables 3.3 and 3.4, with diagrammatic representations presented in Figures 3.11 and 3.13a, respectively.

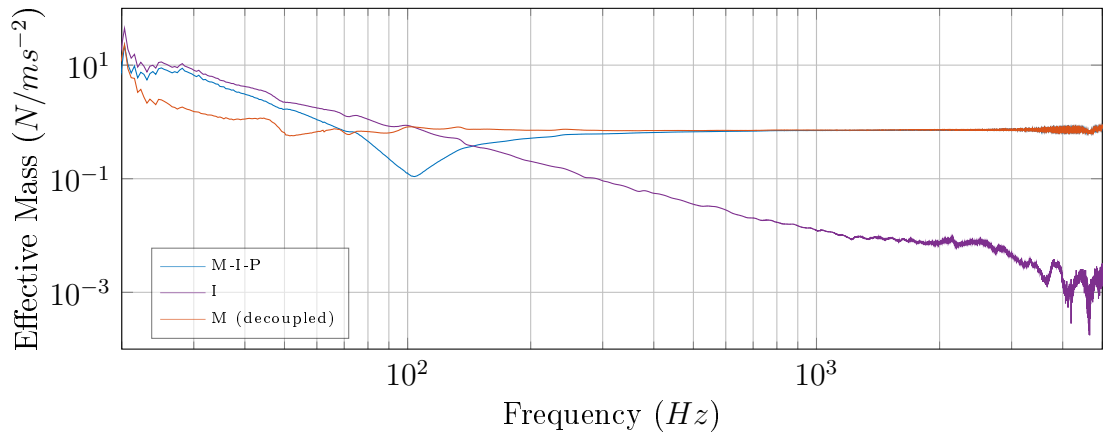
5.3.1.1 MASS-ISOLATOR-PLATE

As per the procedure outlined in Section 5.2, the decoupling of assembly **E** first requires the measurement of its contact interface mobility matrix. As was shown in Section 3.1 this may be done directly, via interface excitations, or remotely via the round trip extension presented in Section 4.2. Here we will consider only the direct implementation, where the coupled assembly contact interface mobility matrix is measured using a spaced accelerometer/force pair, as described in Section 3.4.1. With assembly **E** having already been used in the characterisation of its resilient coupling element, we were able to reuse the measured data from Section 3.4.1 for this study. The experimental set-up for the decoupling procedure may therefore be found in Figure 3.11. Once measured the contact interface mobility matrix was inverted, yielding the coupled assembly impedance matrix, \mathbf{Z}_C . From this we were able to construct the approximate coupling impedance matrix \mathbf{Z}_I , according to Equation 5.9. The block diagonal source-receiver impedance matrix \mathbf{Z}_{SR} was subsequently obtained via Equation 5.10, and the corresponding free-interface mobility matrix via Equation 5.11.

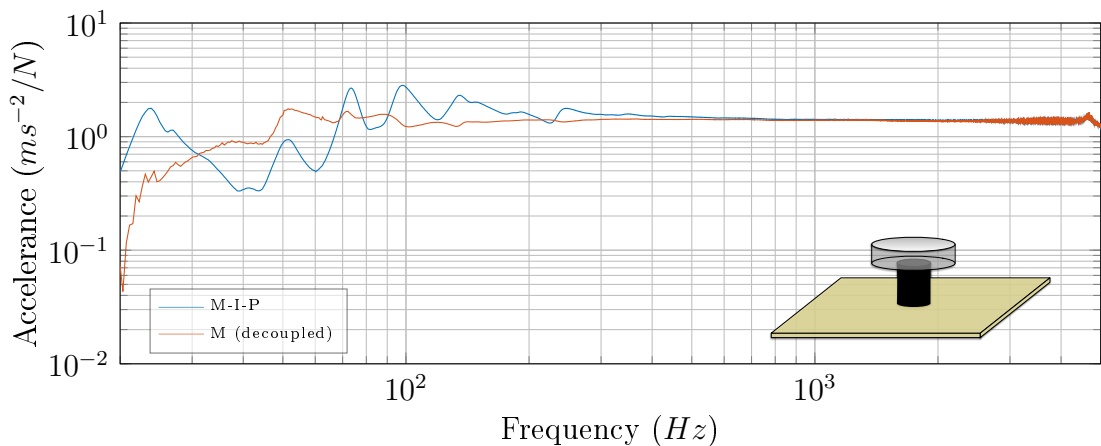
Shown in Figure 5.2 are the in-situ decoupled predictions for assembly **E**. Considering first the source mass. Figure 5.2a shows the effective mass at the source-isolator contact interface of the coupled assembly (blue), the uncoupled isolator (purple, determined from the transfer impedance of the mount) and the in-situ decoupled source mass (orange, determined via the in-situ decoupling procedure).² Results are presented in effective mass form to highlight the expected constant source mass behaviour. A number of observations can be made from Figure 5.2a. Firstly, the inverse frequency proportionality of the isolator's effective mass, $M_{eff} = \frac{k}{-\omega^2}$. Above approximately 300Hz the isolator can be seen to have very little effect on the coupled impedance. Below this, the isolator's contribution becomes increasingly significant

²It is worth noting here the distinction between uncoupled and decoupled structures. Uncoupled structures correspond to those that have been *physically* uncoupled, whilst decoupled structures have been decoupled via the in-situ approach.

until it appears to converge with that of the coupled assembly, suggesting that it has become a dominant contribution of effective mass. A comparison between the coupled assembly and the in-situ decoupled mass reveals that the decoupling procedure has removed almost entirely the 100Hz ‘mass-spring’ anti-resonance observed in the effective mass, further extending the constant behaviour of the source mass. This suggests that the decoupling has been at least partially successful.



(a) Source sub-structure effective mass - also shown, the transfer effective mass of the coupling element.



(b) Source sub-structure accelerance.

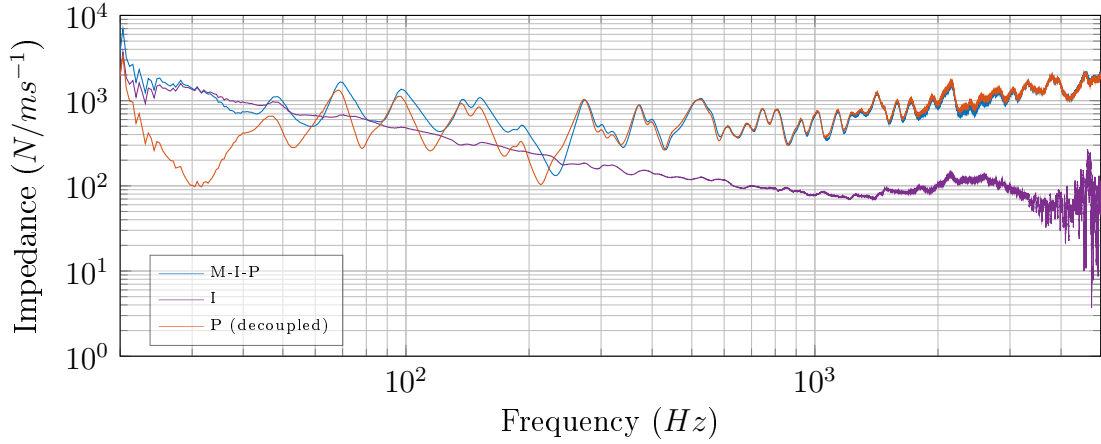
Figure 5.2: Coupled and in-situ decoupled effective mass (a) and accelerance (b) of the source sub-structure of assembly **E**. A diagrammatic representation of the assembly shown in the inset of **b** (a full size diagram can be found in Figure 3.11).

Shown in Figure 5.2b are the free-interface and coupled accelerances of the source mass (orange) and assembly (blue), respectively. Here one can see, as in the effective mass, that the constant accelerance of the source mass has been extended, with a significant reduction in the severity of low frequency resonances, likely resulting

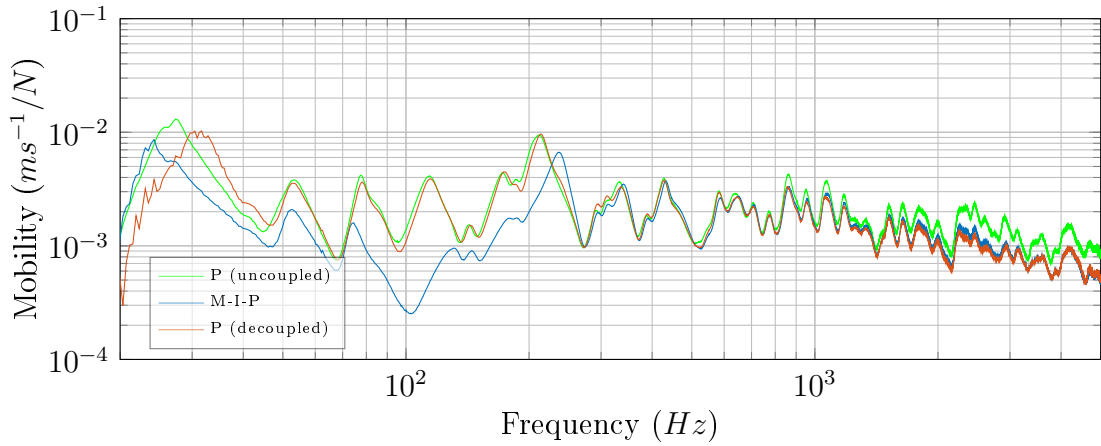
from the coupled receiver plate. Although we do not have a physically uncoupled accelerance for comparison, it is clear that the multiple resonances apparent in the coupled point accelerance do not belong to the source, whose accelerance should in theory be constant. The reduction in resonant behaviour and extension of the constant accelerance therefore suggests that the in-situ decoupling approach has been at least partially successful.

Let us now consider the receiver plate. Shown in Figure 5.2c are the isolator-receiver contact interface impedances for the coupled assembly (blue), the uncoupled isolator (purple) and the in-situ decoupled receiver plate (orange). A number of observations can be made here. Firstly, above approximately 250Hz the impedance of the isolator can be seen to drop continually below the coupled assembly impedance, with the coupled and in-situ decoupled impedances converging. This suggests that the isolator has a negligible effect on the assembly's dynamics above 250Hz. Secondly, at very low frequencies the isolator impedance can be seen to converge with that of the coupled assembly, suggesting that it has become the dominant contribution.

Shown in Figure 5.2d are the contact interface mobilities for the coupled assembly (blue), the in-situ decoupled plate (orange), and the physically uncoupled plate (green). The success of the in-situ decoupling approach is clearly demonstrated here. Below approximately 250Hz the coupled and physically uncoupled mobilities can be seen to differ considerably. This highlights the sort of deviations one might expect by using a resiliently coupled mobility in place of a freely determined one. The in-situ decoupled plate mobility, however, is in excellent agreement with that of the physically uncoupled plate. This agreement extends from 250Hz down to approximately 40Hz. It is suspected that the lack of agreement below this point is due to neglected coordinate-DoFs and/or the error associated with the measurement of low frequency mobilities, and that results may be improved by including additional coordinate DoFs and/or carrying out mobility measurements with a softer hammer tip. It can also be seen from Figure 5.2d that above roughly 300Hz, the in-situ decoupled mobility converges with that of the coupled assembly, whilst diverging slightly from the true uncoupled mobility. This divergence is likely due to a mass loading effect of the isolator. Regardless of this deviation, as we are only interested in the low frequency prediction of uncoupled mobility, since this is where our isolator impedance assumption is valid, Figure 5.2d provides a convincing validation of the in-situ decoupling approach.



(c) Point impedances $\mathbf{Z}_{c_2c_2}$ for isolator, coupled assembly and decoupled receiver.



(d) Point mobility $\mathbf{Y}_{c_2c_2}$ for the coupled assembly, uncoupled receiver and in-situ decoupled receiver.

Figure 5.2: (Continued) Coupled, in-situ decoupled and physically uncoupled impedance (c) and mobility (d) of the receiver sub-structure of assembly \mathbf{E} .

5.3.1.2 BEAM-ISOLATOR-PLATE

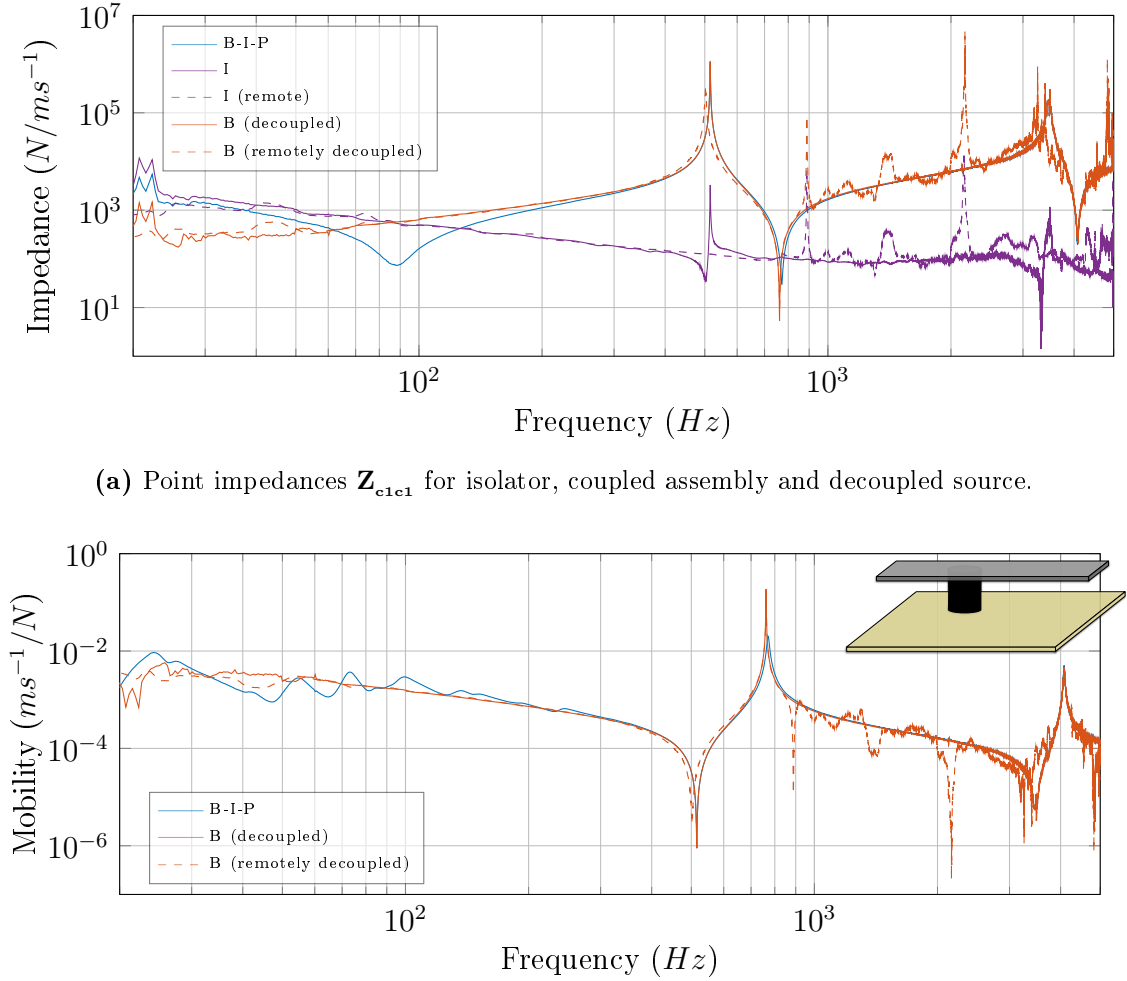
Following the same procedure as above, the decoupling of assembly \mathbf{F} requires first the measurement of its contact interface mobility matrix. This time however, the mobility matrix will be determined both directly and remotely. A remote determination will allow for the potential decoupling of the assembly without requiring excitation access to either contact interface. With the direct approach the assembly's contact interface mobility matrix was measured directly using a spaced accelerometer/force pair, as described in Section 3.4.1. In the remote case, the assembly's contact interface mobility matrix was determined remotely via the single and dual

interface round trip identities, as described in Section 4.2.2.1. In each case the resulting contact interface mobility matrix was inverted and the off-diagonal transfer impedances used to construct the impedance isolator matrix \mathbf{Z}_I .

With assembly \mathbf{F} having already been used in the characterisation of its resilient coupling element, we are once again able to reuse the measured data from Sections 3.4.1 (for direct) and 4.2.3.1 (for remote). The experimental set-up for the two decoupling procedures may therefore be found in Figures 3.13b and 4.5, respectively. Having seen that it provided the best result for the dynamic transfer stiffness, the over-determined plate set-up was used for the remote decoupling.

Shown in Figure 5.3 are the in-situ decoupled impedance and mobility predictions for assembly \mathbf{F} . Considering first the source beam. Shown in Figure 5.3a are the beam-isolator contact interface impedances for the coupled assembly (blue), the uncoupled isolator (purple) and the in-situ decoupled beam (orange). Directly determined impedances are given by solid plots, whilst those determined remotely are given as dashed. It should be noted that once again we are unable to compare the decoupled prediction against a directly measured free-interface response, as this would require the free suspension of the source beam, and this is not possible without the introduction of some additional source of impedance. As in the **MIP** case, a number of interesting phenomena can be observed in Figure 5.3a. Firstly, it can be seen that the decoupling procedure has removed the anti-resonance occurring at approximately 90Hz, yielding a linearly decreasing low frequency impedance, as expected from a free-free beam. This anti-resonance was likely due to the assembly's 'mass-spring' behaviour at low frequencies, and is therefore not a property of the source sub-structure. Secondly, at approximately 750Hz the impedance of the coupled assembly can be seen to drop below that of the isolator. As a result, the decoupling procedure produces a sharper, less damped impedance anti-resonance (or mobility resonance), as one would expect from a freely suspended beam. At higher frequencies a number of artefacts are introduced into the decoupled impedance, particularly in the case of the remote decoupling. However, this is not considered a problem here, as in this region the coupled mobility should converge upon the true free-interface mobility.

Shown in Figure 5.3b are the contact interface mobilities for the coupled assembly (blue) and the in-situ decoupled source beam (orange). Although we have no directly measured free-interface mobility to provide a comparison, a number of promising trends can be observed in the decoupled mobility.



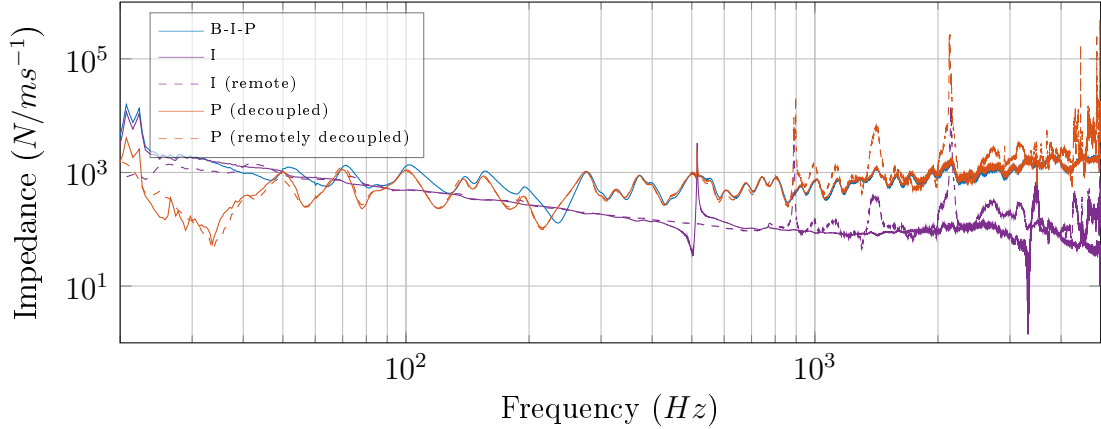
(a) Point impedances \mathbf{Z}_{e1e1} for isolator, coupled assembly and decoupled source.

(b) Point mobility \mathbf{Y}_{e1e1} for the coupled assembly, uncoupled receiver and in-situ decoupled source.

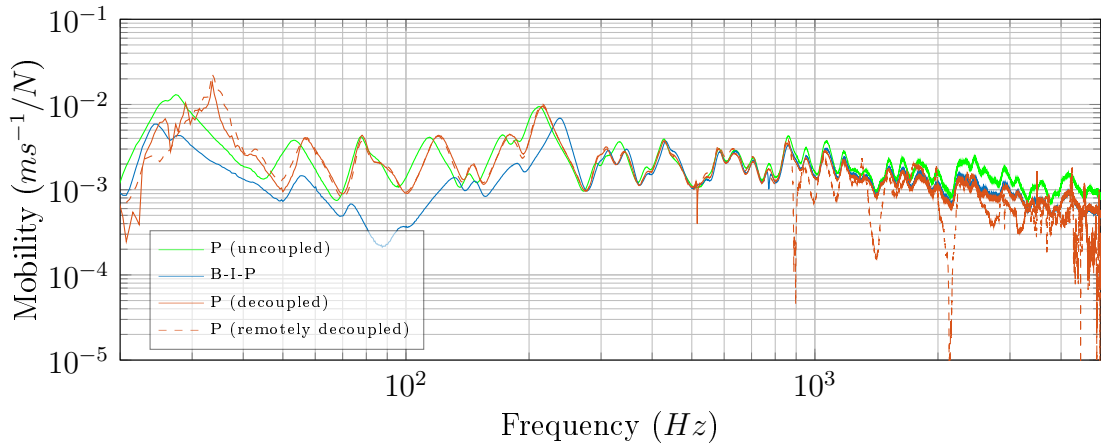
Figure 5.3: Coupled and in-situ decoupled impedance (a) and mobility (b) of the source sub-structure of assembly **F**. A diagrammatic representation of the assembly is shown in the inset of **b** (a full size diagram can be found in Figure 3.13a).

Firstly, it can be seen that below approximately 300Hz the resonant behaviour observed in the coupled mobility is removed almost entirely. The resulting mobility has a near linear low frequency response, akin to what would be expected from a free-free beam. Furthermore, the decoupling procedure can be seen to yield a beam mobility considerably less damped than that of the coupled assembly, suggesting that the decoupling procedure accounts for the damping introduced by the resilient coupling. At high frequencies the error introduced via the remote characterisation can be seen, although this is well beyond our range of interest. The resonant impedance artefact

introduced around 500Hz by the direct approach does not appear to affect the resultant anti-resonance in the predicted mobility. This is likely due to its alignment with impedance resonance which is several order greater in magnitude.



(c) Point impedances \mathbf{Z}_{c2c2} for isolator, coupled assembly and decoupled receiver.



(d) Point mobility \mathbf{Y}_{c2c2} for the coupled assembly, uncoupled receiver and in-situ decoupled receiver.

Figure 5.3: Continued: Coupled, in-situ decoupled and physically uncoupled impedance (d) and mobility (e) of the receiver sub-structure of assembly **F**.

Let us now consider the receiver plate. Shown in Figure 5.3c are the isolator-plate contact interface impedances for the coupled assembly (blue), the uncoupled isolator (purple) and the in-situ decoupled plate (orange). Directly determined impedances are given by solid plots, whilst remotely determined impedances are given as dashed. As with assembly **E**, a number of phenomena can be observed here. Firstly, we can see that at low frequencies, below approximately 300Hz, the impedance of the isolator becomes comparable to that of the coupled assembly, suggesting that it has become a dominant source of impedance. Secondly, the direct and remotely

determined impedances are in good agreement where, as observed in Section 4.2, the remotely determined isolator impedance avoids the sharp 500Hz artefact present in the directly determined impedance (see dashed orange plot in Figure 5.3c). As such, this artefact is avoided in the remote decoupling.

Shown in Figure 5.3d are the contact interface mobilities for the coupled assembly (blue), the in-situ decoupled plate (solid orange) and the physically uncoupled plate (green). Also shown is the remotely decoupled receiver mobility (dashed orange). Although the agreement between the physically uncoupled plate mobility and the in-situ decoupled mobility is not as good as that of the **MIP** case presented in Figure 5.2, Figure 5.3d clearly shows that the in-situ decoupled mobility provides a good prediction of the true uncoupled mobility. Furthermore, Figure 5.3d shows that by utilising the remote extension to the in-situ characterisation approach, decoupling can be achieved without requiring interface access. Moreover, remote decoupling can be seen to avoid the anti-resonance artefact in the free plate mobility, albeit at the expense of the high frequency accuracy.

With the position of the isolator-receiver contact interface left unchanged from that of the **MIP** case, we can confirm that the disagreement between the in-situ decoupled and physically uncoupled mobilities, above approximately 50Hz, is not due to neglected coordinate-DoFs, as in the **MIP** case this range was predicted with considerable accuracy whilst using the same DoFs. This disagreement is likely due to discrepancies in the transfer impedance, and can be seen to result in a slight over prediction of the frequency at which many of the receiver resonances occur. Additionally, a low frequency error, similar to that encountered in the **MIP** case, is observed. This, as before, may be due to neglected coordinate DoFs, or perhaps the unreliability of measured mobilities at low frequencies.

Regardless of the errors encountered, Figure 5.3 clearly demonstrates that the in-situ decoupling procedure may be used to provide an improved estimate of sub-structure free mobility from measurements made in-situ on a coupled assembly and, furthermore, that this may be done without access to the coupling interface by using remote measurement positions.

5.3.2 MULTIPLE CONTACT

So far we have considered the in-situ decoupling of sub-structures that are coupled via a single resilient element. Although promising results were achieved, most assemblies encountered in practice comprise of multiple coupling elements. In the following we will consider the implementation of the in-situ decoupling procedure on a multi-contact assembly.

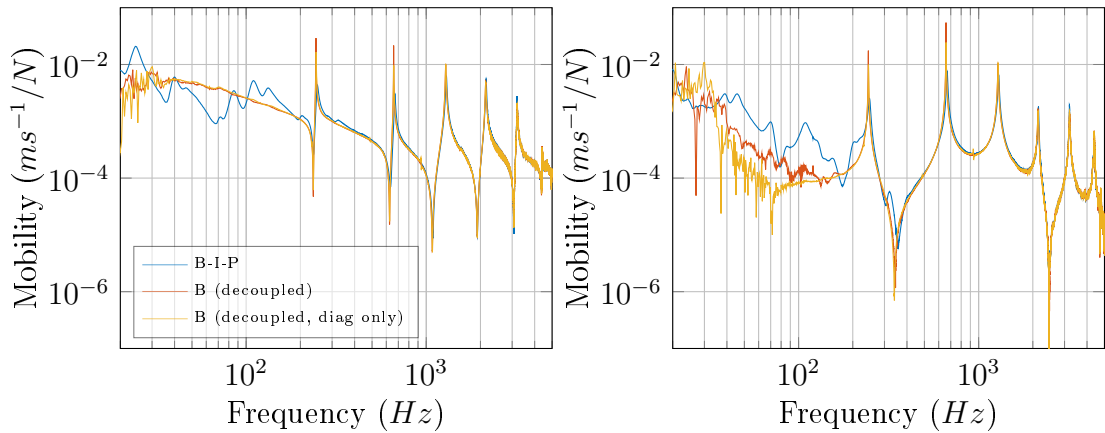
5.3.2.1 BEAM-ISOLATOR(2)-PLATE

The multi-contact assembly considered here is that of the beam-isolator(2)-plate (assembly \mathbf{G}) first introduced in Section 3.4.2, and later in Section 4.2.3.2. Further details on this assembly may be found in Table 3.5, with a diagrammatic representation presented in Figure 3.15a.

Following the same procedure as in the single contact case, the decoupling of assembly \mathbf{G} requires first the measurement of its contact interface mobility matrix, $\mathbf{Y}_{\mathbf{C}}$. Here, for clarity, we will consider only the direct measurement of this mobility matrix. Once measured this matrix was inverted and the resulting coupled impedance matrix, $\mathbf{Z}_{\mathbf{C}}$, used to construct the coupling element impedance matrix, $\mathbf{Z}_{\mathbf{I}}$. The decoupling procedure was then implemented as per Equations 5.10-5.11. With assembly \mathbf{G} composed of two resilient elements, the contact interface mobility matrix, $\mathbf{Y}_{\mathbf{C}}$, has dimensions 4×4 . The block transfer impedance matrix, $\mathbf{Z}_{\mathbf{I}_{\mathbf{c}1\mathbf{c}2}}$, therefore has dimensions 2×2 , with the transfer impedance of each support along its diagonal. It was noted earlier that for a multi-contact assembly the off-diagonal elements of the block transfer impedance matrix should (assuming point like coupling), in theory, be equal to 0. It was further noted that unless all positional- and coordinate-DoFs are accounted for, with absolute accuracy, the off-diagonal transfer impedance elements would be non-zero. With only z coordinate-DoFs considered here, the experimentally determined impedance matrices, $\mathbf{Z}_{\mathbf{I}_{\mathbf{c}1\mathbf{c}2}} = \mathbf{Z}_{\mathbf{I}_{\mathbf{c}2\mathbf{c}1}}^{\mathbf{T}}$, used in the decoupling were not be diagonal. The question then arises as to how we should deal with these off-diagonal elements. In this Section will we consider the in-situ decoupling both with and without these elements, where in the latter they are simply set to 0.

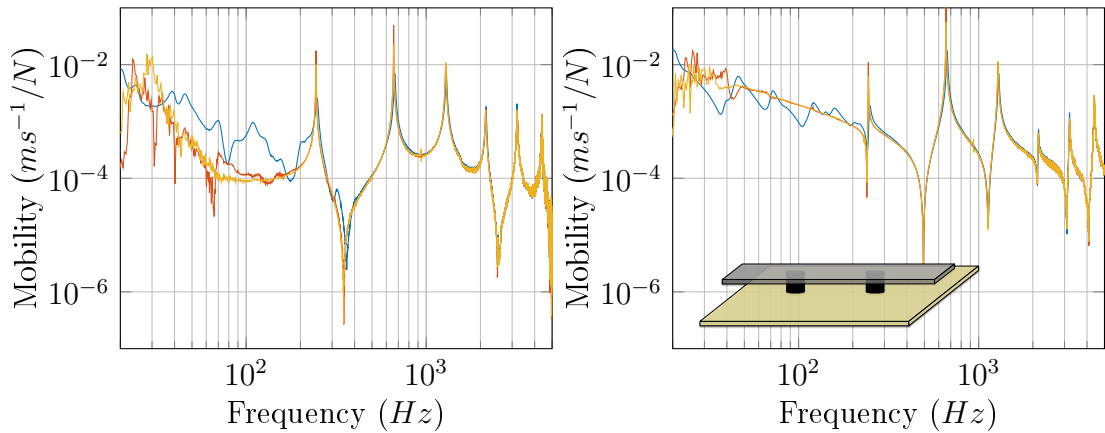
Shown in Figure 5.4 are the in-situ decoupled mobility predictions for assembly \mathbf{G} . Considering first the source beam. Shown in Figures 5.4a-5.4d are the source-isolator contact interface point and transfer mobilities for the coupled assembly (blue), and

the in-situ decoupled source (orange and yellow). It can be seen that a number of promising improvements are achieved through the in-situ decoupling procedure. Firstly, the low frequency resonances occurring below approximately 400Hz , that are likely contributions from the coupled plate, are almost entirely removed in both point and transfer mobilities, leaving a source mobility with the expected low frequency trends.



(a) Point mobility $\mathbf{Y}_{\mathbf{S}_{e11e11}}$ for the coupled and decoupled source beam.

(b) Transfer mobility $\mathbf{Y}_{\mathbf{S}_{e11e12}}$ for the coupled and decoupled source beam.



(c) Transfer mobility $\mathbf{Y}_{\mathbf{S}_{e12e11}}$ for the coupled and decoupled source beam.

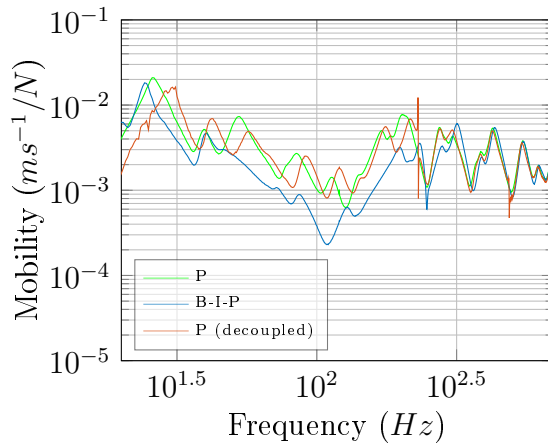
(d) Point mobility $\mathbf{Y}_{\mathbf{S}_{e12e12}}$ for the coupled and decoupled source beam.

Figure 5.4: Coupled and in-situ decoupled mobilities of the source sub-structure of assembly \mathbf{G} . A diagrammatic representation of the assembly is shown in the inset of **d** (a full size diagram can be found in Figure 3.15a).

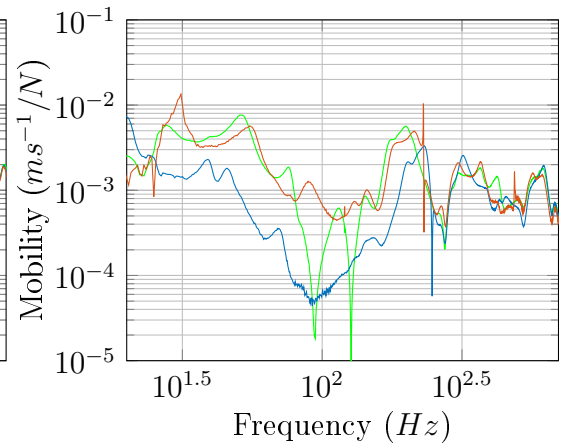
Furthermore, the decoupling procedure can be seen to significantly reduce the damping of the first few resonances. Lastly, as one would expect, the in-situ decoupled mobility converges with that of the coupled mobility with increasing frequency, suggesting that the impedance of the coupling elements becomes less significant. It is

also worth noting the similarity between the decoupled predictions obtained with (orange) and without (yellow) the non-zero off-diagonal transfer impedance elements. This similarity suggests, at least in this particular case, that the assembly interfaces were sufficiently blocked by considering only the translational z coordinate-DoFs.

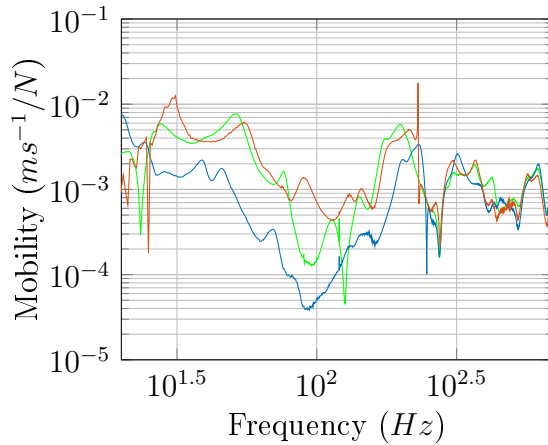
Although we are unable to compare the in-situ decoupled mobility against a physically uncoupled source, the results presented display many of the expected phenomena and therefore suggest that the in-situ decoupling has been at least partly successful.



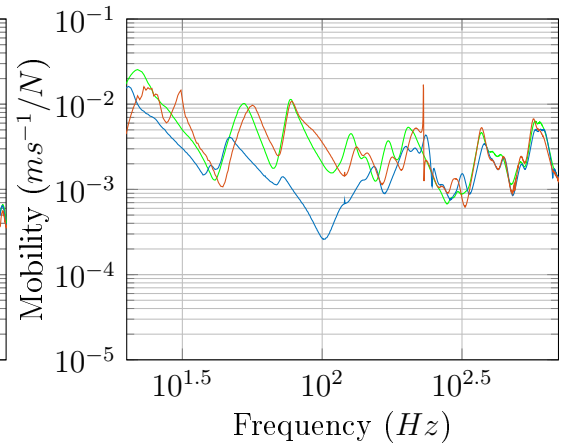
(e) Point mobility $\mathbf{Y}_{\mathbf{R}_{c21c21}}$ for free, coupled, uncoupled and decoupled receiver plate.



(f) Transfer mobility $\mathbf{Y}_{\mathbf{R}_{c21c22}}$ for free, coupled, uncoupled and decoupled receiver plate.



(g) Transfer mobility $\mathbf{Y}_{\mathbf{R}_{c22c21}}$ for free, coupled, uncoupled and decoupled receiver plate.



(h) Point mobility $\mathbf{Y}_{\mathbf{R}_{c22c22}}$ for free, coupled, uncoupled and decoupled receiver plate.

Figure 5.4: Continued: Coupled and in-situ decoupled mobilities of the receiver sub-structure of assembly \mathbf{G} .

Considering now the receiver plate. Shown in figures 5.4e-5.4h are the isolator-receiver contact interface point and transfer mobilities for the coupled assembly (blue), the in-situ decoupled receiver (orange), and the physically uncoupled receiver (green). For clarity we will not consider the removal of \mathbf{Z}_I 's non-zero off-diagonal elements, as it was shown before that their removal made little difference to the decoupled prediction. Results are presented over the frequency range 20-700Hz so as to provide a clearer picture of the region affected by the decoupling procedure. Beyond this range the predicted and measured mobilities (both coupled and uncoupled) tend to converge upon one another.

Although the in-situ decoupled and physically uncoupled mobilities are not in as close agreement as those of the single contact case, Figures 5.4e-5.4h clearly shows that the decoupled prediction offers a better estimate of the free mobility than that of the coupled mobility, which below 300Hz differs significantly. Whilst the in-situ decoupled prediction can be seen to follow the general trend of the uncoupled mobility, there clearly exist a number of errors. The most noticeable of these are located about the 100Hz transfer mobility anti-resonances. As shown in Figures 5.4f and 5.4g the in-situ decoupled mobility fails to accurately predict these anti-resonances. That said, this error is not necessarily the fault of in-situ decoupling procedure. It may result from experimental error whilst measuring the uncoupled receiver mobility, or perhaps from a changes in the properties of the plate due to coupling. Furthermore, it can be seen that the decoupled prediction tends to over estimate the frequency of the free plate resonances, an error similar to that observed in the receiver of the **BIP** case. Also introduced are a number of sharp resonances, most notably at approximately 200Hz. These are due to artefacts resulting from the direct determination of the coupling transfer impedance. However, it is believed that the use of the remote extension would help alleviate this error, as suggested by the results presented earlier in Sections 4.2 and 5.3.1.2.

Regardless of the errors encountered, the predictions presented in Figures 5.4e-5.4h clearly highlight the potential of the in-situ decoupling procedure as a method for determining the free-interface mobility of coupled source and receiver sub-structures. It is believed that many of the errors encountered may be reduce through the use of additional DoFs, or by repeating the measurement procedure with more care. Unfortunately, due to time constraints and contractual arrangements only a single set of measurements were carried out. The author believes that through experimental

optimisation the in-situ decoupling procedure could yield an even greater level of agreement.

5.4 CONCLUDING REMARKS

This Chapter has been concerned with the development of an in-situ sub-structure decoupling procedure suitable for resiliently coupled assemblies. The procedure is able to mathematically decouple the source and receiver sub-structures of both single and multi-contact assemblies. In doing so an independent characterisation is achieved in terms of their free-interface mobilities. The approach may therefore, in theory, be used to provide suitable source and receiver data for use with dynamic sub-structuring. Unlike standard sub-structure decoupling procedures, the in-situ approach does not require the assembly to be dismantled, as it relies upon in-situ measurements only.

The decoupling procedure was shown to correctly predict the low frequency free-interface mobility of both source and receiver sub-structures. Validations were performed on three different assembly types, with a good level of agreement obtained in all cases.

With the in-situ characterisation method forming the basis of the in-situ decoupling procedure, its associated experimental extensions are also applicable. This was shown explicitly for remote measurement extension by decoupling a **BIP** assembly without ever exciting the coupling interfaces. The finite difference and transmissibility extensions were, however, considered beyond the scope of this work.

Having shown the in-situ decoupling procedure to be a practical method for determining the independent passive properties of a source sub-structure, the following Chapter will consider the acquisition of its independent active property; namely, the blocked force.

BLOCKED FORCE CHARACTERISATION

In this Chapter the in-situ blocked force method is introduced as an independent characterisation for the active component of a structural source. Two alternate derivations are presented; based on impedance and mobility formulations. Following this, methods for accessing the quality and/or uncertainty of the determined blocked force are discussed. First, the concepts of ‘on-board’ and ‘transferability’ validations are introduced, where determined forces are assessed on their ability to predict a measured response in an assembly. Secondly, a probabilistic approach is proposed, whereby expected value and standard deviations are derived from a sample space of determined blocked forces. Lastly, the above are demonstrated through an experimental study.

CONTENTS

6.1	Independent Source Characterisation	126
6.2	Blocked Force Theory	128
6.3	Accounting for Uncertainty	140
6.4	Experimental Validation	153
6.5	Concluding Remarks	177

6.1 INDEPENDENT SOURCE CHARACTERISATION

As we have come to appreciate, the most fundamental requirement in the construction of a VAP is the independent characterisation of its constituent components. It is only with *independent* sub-structure properties that components can be interchanged

in a physically representative manner. Whilst passive components, i.e. receiver sub-structures, isolators, etc. may be described entirely by their free-interface mobility or transfer impedance, active components, i.e. pumps, motors, etc. require a second quantity in order to describe their operational activity. In the preceding Chapters 3 and 5, experimental methods were presented whereby the independent passive properties of source, receiver and coupling sub-structures are determined through in-situ measurements. In this Chapter we will consider the last piece of the VAP puzzle, namely, the determination of a suitable *active* quantity for the characterisation of source sub-structures. Decades worth of research has been spent in search of such a quantity, an overview of which is presented in Section 2.2. Alongside its free-interface mobility, an independent quantity describing the activity of a source sub-structure would provide a complete source characterisation and, furthermore, meet the requirements set out by the International Organization for Standardization (ISO), Technical Committee on Acoustics TC43, Working Group [24].

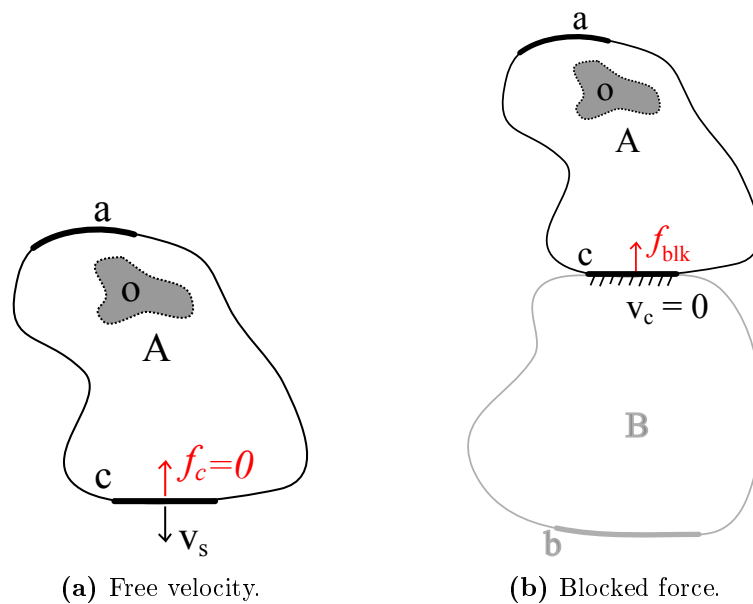


Figure 6.1: Diagrammatic representation of independent source quantities.

There exist two fundamentally independent quantities that describe the operational activity of a given source sub-structure; the free velocity and the blocked force, shown diagrammatically in Figure 6.1. Although standardised measurement procedures exist for the former [29], the shortcomings outlined in Section 2.2 have meant that only the latter is considered here.

Many of the concepts presented in this Section are well established methods and no novelty is claimed, however, in order to provide a complete overview of the virtual assembly and VAP notion, a thorough description is required nonetheless. Further to these concepts, the idea of source uncertainty is introduced with an approach presented for the determination of standard deviations in acquired blocked forces. Although not fully developed, the approach allows for the determination of uncertainty parameters which may subsequently be propagated through an assembly and provide a level of uncertainty in a later prediction.

From a supplier's perspective, the ability to provide a customer with a level of uncertainty in their blocked force is advantageous, as it is stated in the ISO supported document [140] that '*In general, the result of a measurement is only an approximation or estimate of the value of the measurand and thus is complete only when accompanied by a statement of the uncertainty of that estimate*'. Moreover, the ability to carry an uncertainty through a prediction is useful, particularly in the development of VAPs.

The remainder of this Chapter may be outlined as follows; In Section 6.2 we will introduce the in-situ blocked force approach and discuss its experimental implementation. Following this, in Section 6.3 we will cover methods for the assessment of blocked force uncertainty. Lastly, in Section 6.4 an experimental study will be presented in order to illustrate of the above.

6.2 BLOCKED FORCE THEORY

The blocked force offers one of two fundamentally independent source quantities. Defined as the force required to restrain the velocity at a given interface to zero, it may be alternatively thought of as the interface force between an active source sub-structure and an infinitely rigid receiver sub-structure, and may be defined as,

$$\bar{\mathbf{f}}_{\mathbf{S}_c} = \mathbf{f}_{\mathbf{C}_c} \Big|_{\mathbf{v}_{\mathbf{C}_c}=0} \quad (6.1)$$

where $\mathbf{f}_{\mathbf{C}_c}$ is the contact force at a coupling source-receiver interface c , $\mathbf{v}_{\mathbf{C}_c}$ is the velocity at the source-receiver interface, and $\bar{\mathbf{f}}_{\mathbf{S}_c}$ is the blocked force of the source sub-structure. Whilst the concept of the blocked force as an independent source quantity has been around for many decades, only in more recent years has a convenient

method for its determination been developed. Prior to this experimental methods relied on large blocking masses to approximate rigid terminations. Such an approach is clearly inconvenient, not to mention limited to a narrow frequency range.

In 2001 Bobrovnitskii presented his theorem on the representation of fields of forced vibrations in composite elastic systems [67]. In this work the solution to a general forced vibration problem was considered the sum of two simpler ‘auxiliary’ problems. In his first representation, Bobrovnitskii went on to show that an identical velocity field may be produced in a receiver sub-structure through the application of a negative blocked force at the coupling interface. Although not stated explicitly, it may be inferred that this blocked force can be determined from measurements made on an arbitrary coupled assembly, i.e. without the requirement of any large blocking masses. The implications of this were profound, although not realised until several years later, when both Moorhouse et al. [13] and De Klerk [56] independently derived this special case of Bobrovnitskii’s equivalent representation. It was shown explicitly that the blocked force could be determined from measurements made in-situ, via an inverse approach similar to that used in operational force identification, or classical TPA. The in-situ blocked force method has since gone on to form the basis of the in-situ TPA procedure [65] and been used successfully in a number of studies [13, 60, 61, 141]. However, with its relative youth, much work is still ongoing with regards to its application, implementation and limitations.

It is the aim of this Section to outline the concept of the in-situ blocked force, describe its experimental implementation and discuss its limitations. For completeness, the in-situ blocked force relation is derived via two different approaches. In Section 6.2.1 we will work through an impedance based derivation, similar to that of De Klerk [56], whilst in Section 6.2.2 we will follow a mobility based approach similar to that of Moorhouse et al [13]. Section 6.2.3 will provide further details on the experimental determination of the blocked forces using the in-situ approach and its associated considerations.

6.2.1 IMPEDANCE FORMULATION

In what follows, an impedance based derivation of the in-situ blocked force approach is presented.

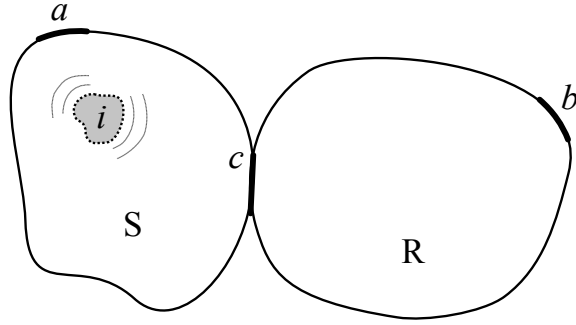


Figure 6.2: General source-receiver system.

Let us begin with the general system of equations that describe the behaviour of the rigidly coupled source-receiver (**SR**) assembly, shown diagrammatically in Figure 6.2. In keeping with the established notation, coupling interface DoFs are denoted c whilst remote receiver DoFs are denoted b . With the source being an active sub-structure, there must exist some internal vibration mechanism. This is represented by the set of unknown excitation forces $\mathbf{f}_{\mathbf{S}i}$, acting at an internal DoF denoted i .

The matrix equations that follow are presented in a general form such that they may be considered partitioned matrices, with individual elements taking either scalar or matrix form.

$$\begin{bmatrix} \mathbf{f}_{\mathbf{S}i} \\ 0 \\ 0 \end{bmatrix} = \begin{bmatrix} \mathbf{Z}_{\mathbf{S}ii} & \mathbf{Z}_{\mathbf{S}ic} & 0 \\ \mathbf{Z}_{\mathbf{S}ci} & \mathbf{Z}_{\mathbf{C}cc} & \mathbf{Z}_{\mathbf{R}cb} \\ 0 & \mathbf{Z}_{\mathbf{R}bc} & \mathbf{Z}_{\mathbf{R}bb} \end{bmatrix} \begin{bmatrix} \mathbf{v}_{\mathbf{C}i} \\ \mathbf{v}_{\mathbf{C}c} \\ \mathbf{v}_{\mathbf{C}b} \end{bmatrix} \quad (6.2)$$

The tri-diagonal nature of the assembly's impedance matrix, i.e. $\mathbf{Z}_{\mathbf{C}ib} = \mathbf{Z}_{\mathbf{C}bi} = 0$, is a consequence of the constrained interface DoF, c , that separates i and b , as per the definition of impedance (see Section 2.1.2).

Equation 6.2 may be written out explicitly and the first two rows equated via the internal velocity $\mathbf{v}_{\mathbf{C}i}$. The remaining two equations may be subsequently recast into matrix form. This reduction process will be referred to hereafter as the 'condensation of rows 1 and 2'. The reduced matrix equation is (see Appendix D for reduction steps),

$$\begin{bmatrix} -\mathbf{Z}_{\mathbf{S}ci} \mathbf{Z}_{\mathbf{S}ii}^{-1} \mathbf{f}_{\mathbf{S}i} \\ 0 \end{bmatrix} = \begin{bmatrix} -\mathbf{Z}_{\mathbf{S}ci} \mathbf{Z}_{\mathbf{S}ii}^{-1} \mathbf{Z}_{\mathbf{S}ic} + \mathbf{Z}_{\mathbf{C}cc} & \mathbf{Z}_{\mathbf{R}cb} \\ \mathbf{Z}_{\mathbf{R}bc} & \mathbf{Z}_{\mathbf{R}bb} \end{bmatrix} \begin{bmatrix} \mathbf{v}_{\mathbf{C}c} \\ \mathbf{v}_{\mathbf{C}b} \end{bmatrix}. \quad (6.3)$$

Whilst Equations 6.2 and 6.3 represent the same assembly, Equation 6.3 does so via some alternate forcing term, $\mathbf{Z}_{\mathbf{S}ci} \mathbf{Z}_{\mathbf{S}ii}^{-1} \mathbf{f}_{\mathbf{S}i}$. This 'equivalent force' (as referred to by De Klerk [56]) is an independent property of the source sub-structure that, when

acting on the interface c , results in the same dynamic behaviour as the internal force $\mathbf{f}_{\mathbf{S}_i}$. It will now be shown that this equivalent force term is in fact the blocked force that results from a constrained coupling interface.

Let us consider the system of equations describing a source sub-structure whose interface DoFs are constrained such that their velocity is 0,

$$\begin{bmatrix} \mathbf{f}_{\mathbf{S}_i} \\ \bar{\mathbf{f}}_{\mathbf{S}_c} \end{bmatrix} = \begin{bmatrix} \mathbf{Z}_{\mathbf{S}_{ii}} & \mathbf{Z}_{\mathbf{S}_{ic}} \\ \mathbf{Z}_{\mathbf{S}_{ci}} & \mathbf{Z}_{\mathbf{C}_{cc}} \end{bmatrix} \begin{bmatrix} \mathbf{v}_{\mathbf{C}_i} \\ 0 \end{bmatrix}. \quad (6.4)$$

For such an assembly the force acting on the interface c is, by definition, the blocked force, $\bar{\mathbf{f}}_{\mathbf{S}_c}$. Condensation of rows 1 and 2 whilst solving for $\bar{\mathbf{f}}_{\mathbf{S}_c}$ yields,

$$\bar{\mathbf{f}}_{\mathbf{S}_c} = \mathbf{Z}_{\mathbf{S}_{ci}} \mathbf{Z}_{\mathbf{S}_{ii}}^{-1} \mathbf{f}_{\mathbf{S}_i}. \quad (6.5)$$

Referring back to Equation 6.3 it can be seen that the equivalent force acting at the interface c is in fact the negative blocked force, $-\bar{\mathbf{f}}_{\mathbf{S}_c}$.

Lastly, it can be shown that the application of the negative blocked force at the coupling interface whilst the internal excitation, $\mathbf{f}_{\mathbf{S}_i}$, is inactive, results in the same system of equations as that of the internally operating force, as in Equations 6.3-6.4.

$$\begin{bmatrix} 0 \\ -\bar{\mathbf{f}}_{\mathbf{S}_c} \\ 0 \end{bmatrix} = \begin{bmatrix} \mathbf{Z}_{\mathbf{S}_{ii}} & \mathbf{Z}_{\mathbf{S}_{ic}} & 0 \\ \mathbf{Z}_{\mathbf{S}_{ci}} & \mathbf{Z}_{\mathbf{C}_{cc}} & \mathbf{Z}_{\mathbf{R}_{cb}} \\ 0 & \mathbf{Z}_{\mathbf{R}_{bc}} & \mathbf{Z}_{\mathbf{R}_{bb}} \end{bmatrix} \begin{bmatrix} \mathbf{v}_{\mathbf{C}_i} \\ \mathbf{v}_{\mathbf{C}_c} \\ \mathbf{v}_{\mathbf{C}_b} \end{bmatrix} \quad (6.6)$$

Let us once again condense rows 1 and 2 of Equation 6.6. The resulting matrix equation,

$$\begin{bmatrix} -\bar{\mathbf{f}}_{\mathbf{S}_c} \\ 0 \end{bmatrix} = \begin{bmatrix} -\mathbf{Z}_{\mathbf{S}_{ci}} \mathbf{Z}_{\mathbf{S}_{ii}}^{-1} \mathbf{Z}_{\mathbf{S}_{ic}} + \mathbf{Z}_{\mathbf{C}_{cc}} & \mathbf{Z}_{\mathbf{R}_{cb}} \\ \mathbf{Z}_{\mathbf{R}_{bc}} & \mathbf{Z}_{\mathbf{R}_{bb}} \end{bmatrix} \begin{bmatrix} \mathbf{v}_{\mathbf{C}_c} \\ \mathbf{v}_{\mathbf{C}_b} \end{bmatrix}, \quad (6.7)$$

can be seen to be in complete agreement with Equation 6.3. This confirms that the application of the negative blocked force at the coupling interface, whilst the internally operating forces are inactive, yields the same dynamic response as the internally operating forces alone.

Let us now consider the inverse of Equation 6.6 where the coupled mobility matrix, \mathbf{Y}_C , is introduced.

$$\begin{bmatrix} \mathbf{v}_{C_i} \\ \mathbf{v}_{C_c} \\ \mathbf{v}_{C_b} \end{bmatrix} = \begin{bmatrix} \mathbf{Y}_{C_{ii}} & \mathbf{Y}_{C_{ic}} & \mathbf{Y}_{C_{ib}} \\ \mathbf{Y}_{C_{ci}} & \mathbf{Y}_{C_{cc}} & \mathbf{Y}_{C_{cb}} \\ \mathbf{Y}_{C_{bi}} & \mathbf{Y}_{C_{bc}} & \mathbf{Y}_{C_{bb}} \end{bmatrix} \begin{bmatrix} 0 \\ -\bar{\mathbf{f}}_{S_c} \\ 0 \end{bmatrix} \quad (6.8)$$

By considering only the responses at the external DoFs, c and b , whilst noting the reciprocal relation, $\mathbf{Y}_{C_{bc}} = \mathbf{Y}_{C_{cb}}^T$, the above mobility formulation may be reduced to,

$$\begin{bmatrix} \mathbf{v}_{C_c} \\ \mathbf{v}_{C_b} \end{bmatrix} = - \begin{bmatrix} \mathbf{Y}_{C_{cc}} \\ \mathbf{Y}_{C_{cb}}^T \end{bmatrix} \begin{bmatrix} \bar{\mathbf{f}}_{S_c} \end{bmatrix}. \quad (6.9)$$

Equation 6.9 states that the velocity of a coupled source-receiver assembly at the coupling interface and remote receiver DoFs, is given by the product of the coupled point and transfer mobility matrices, with the negative blocked force of the source sub-structure.

6.2.2 MOBILITY FORMULATION

In what follows a mobility based derivation of the in-situ blocked force approach is presented.

Considering the same rigidly coupled assembly as in Figure 6.2, let us begin with an expression for the velocities at the coupling interface and remote receiver DoFs, c and b , due to the contact force, \mathbf{f}_{C_c} . This contact force results from some unknown internal force excitation, \mathbf{f}_{S_i} , within the source sub-structure.

$$\begin{bmatrix} \mathbf{v}_{C_c} \\ \mathbf{v}_{C_b} \end{bmatrix} = \begin{bmatrix} \mathbf{Y}_{R_{cc}} \\ \mathbf{Y}_{R_{bc}} \end{bmatrix} \begin{bmatrix} \mathbf{f}_{C_c} \end{bmatrix} \quad (6.10)$$

where \mathbf{f}_{C_c} is the contact force at c , and $\mathbf{Y}_{R_{cc}}$ and $\mathbf{Y}_{R_{bc}}$ are the point and transfer mobility matrices of the uncoupled receiver sub-structure, respectively. The contact force \mathbf{f}_{C_c} may be related to the free-interface velocity, \mathbf{v}_{S_c} , of the source sub-structure via the relation [31],

$$\mathbf{f}_{C_c} = [\mathbf{Y}_{S_{cc}} + \mathbf{Y}_{R_{cc}}]^{-1} \mathbf{v}_{S_c} \quad (6.11)$$

and similarly, the free-interface velocity to the blocked force via [55],

$$\mathbf{v}_{S_c} = -\mathbf{Y}_{S_{cc}} \bar{\mathbf{f}}_{S_c}. \quad (6.12)$$

It is perhaps worth noting that the above Equation is often presented as a positive relation. However, with the blocked force acting in both directions, a negative sign is also correct. For consistency with the impedance based approach the negative relation is used here. Substitution of Equations 6.11 and 6.12 into Equation 6.10, whilst noting the matrix relation B.10, yields,

$$\begin{bmatrix} \mathbf{v}_{C_c} \\ \mathbf{v}_{C_b} \end{bmatrix} = - \begin{bmatrix} (\mathbf{Y}_{S_{cc}}^{-1} + \mathbf{Y}_{R_{cc}}^{-1})^{-1} \\ \mathbf{Y}_{R_{cb}} (\mathbf{Y}_{S_{cc}} + \mathbf{Y}_{R_{cc}})^{-1} \mathbf{Y}_{S_{cc}} \end{bmatrix} \begin{bmatrix} \bar{\mathbf{f}}_{S_c} \end{bmatrix}. \quad (6.13)$$

In keeping with the derivation of Moorhouse et al. [13], it will now be shown that the mobility matrix pertaining to the above Equation is in fact the partitioned point and transfer mobility matrix of the coupled assembly $[\mathbf{Y}_{C_{cc}} | \mathbf{Y}_{C_{bc}}]^T$.

As a thought experiment, let us consider an externally applied force at the coupled assembly interface c , $\hat{\mathbf{f}}_{C_c}$,

$$\begin{bmatrix} \mathbf{v}_{C_c} \\ \mathbf{v}_{C_b} \end{bmatrix} = \begin{bmatrix} \mathbf{Y}_{C_{cc}} \\ \mathbf{Y}_{C_{bc}} \end{bmatrix} \begin{bmatrix} \hat{\mathbf{f}}_{C_c} \end{bmatrix}. \quad (6.14)$$

where here $\hat{\mathbf{f}}$ denotes an externally applied quantity, and $[\mathbf{v}_{C_c} | \mathbf{v}_{C_b}]^T$ are the resultant velocities due to the externally applied force. The velocities at c and b due to the resulting interface force \mathbf{f}_{C_c} may be given by,

$$\mathbf{f}_{C_c} = \mathbf{Y}_{R_{bc}}^{-1} \mathbf{v}_{C_b} = \mathbf{Y}_{R_{cc}}^{-1} \mathbf{v}_{C_c}. \quad (6.15)$$

Pre-multiplication of Equation 6.15 by $\mathbf{Y}_{R_{bc}}$ yields,

$$\mathbf{v}_{C_b} = \mathbf{Y}_{R_{bc}} \mathbf{Y}_{R_{cc}}^{-1} \mathbf{v}_{C_c}. \quad (6.16)$$

By substituting Equation 6.16 into Equation 6.14, whilst noting the coupled impedance relation,

$$\mathbf{Y}_{C_{cc}} = [\mathbf{Y}_{S_{cc}}^{-1} + \mathbf{Y}_{R_{cc}}^{-1}]^{-1} \quad (6.17)$$

one arrives at,

$$\begin{bmatrix} \mathbf{v}_{C_c} \\ \mathbf{v}_{C_b} \end{bmatrix} = \begin{bmatrix} [\mathbf{Y}_{S_{cc}}^{-1} + \mathbf{Y}_{R_{cc}}^{-1}]^{-1} \\ \mathbf{Y}_{R_{bc}} \mathbf{Y}_{R_{cc}}^{-1} [\mathbf{Y}_{S_{cc}}^{-1} + \mathbf{Y}_{R_{cc}}^{-1}]^{-1} \end{bmatrix} \begin{bmatrix} \dot{\mathbf{f}}_{C_c} \end{bmatrix}. \quad (6.18)$$

Making further use of the matrix relation B.10, Equation 6.18 may be rewritten as,

$$\begin{bmatrix} \mathbf{v}_{C_c} \\ \mathbf{v}_{C_b} \end{bmatrix} = \begin{bmatrix} [\mathbf{Y}_{S_{cc}}^{-1} + \mathbf{Y}_{R_{cc}}^{-1}]^{-1} \\ \mathbf{Y}_{R_{bc}} (\mathbf{Y}_{S_{cc}} + \mathbf{Y}_{R_{cc}})^{-1} \mathbf{Y}_{S_{cc}} \end{bmatrix} \begin{bmatrix} \dot{\mathbf{f}}_{C_c} \end{bmatrix}. \quad (6.19)$$

Equation 6.19 relates an externally applied force at the coupling interface DoFs c to the resultant velocities at c and b on the coupled assembly. The corresponding matrix therefore represents the coupled point and transfer mobility matrix $[\mathbf{Y}_{C_{cc}} | \mathbf{Y}_{C_{bc}}]^T$.

$$\begin{bmatrix} [\mathbf{Y}_{S_{cc}}^{-1} + \mathbf{Y}_{R_{cc}}^{-1}]^{-1} \\ \mathbf{Y}_{R_{bc}} (\mathbf{Y}_{S_{cc}} + \mathbf{Y}_{R_{cc}})^{-1} \mathbf{Y}_{S_{cc}} \end{bmatrix} = \begin{bmatrix} \mathbf{Y}_{C_{cc}} \\ \mathbf{Y}_{C_{bc}} \end{bmatrix} \quad (6.20)$$

With this matrix being identical in form to that in Equation 6.13, we arrive at the blocked force identity (again noting the reciprocal relation, $\mathbf{Y}_{C_{bc}} = \mathbf{Y}_{C_{cb}}^T$),

$$\begin{bmatrix} \mathbf{v}_{C_c} \\ \mathbf{v}_{C_b} \end{bmatrix} = - \begin{bmatrix} \mathbf{Y}_{C_{cc}} \\ \mathbf{Y}_{C_{cb}}^T \end{bmatrix} \begin{bmatrix} \bar{\mathbf{f}}_{S_c} \end{bmatrix} \quad (6.21)$$

which can be seen to be in exact agreement with Equation 6.9.

In addition to the blocked force relation of Equation 6.21, the mobility derivation leads to an alternate formulation for the dynamic sub-structuring problem, where in addition to the well established coupled point mobility relations $\mathbf{Y}_{C_{cc}} = (\mathbf{Y}_{S_{cc}}^{-1} + \mathbf{Y}_{R_{cc}}^{-1})^{-1}$, we arrive at the coupled transfer mobility relation, $\mathbf{Y}_{C_{cb}} = \mathbf{Y}_{R_{bc}} (\mathbf{Y}_{S_{cc}} + \mathbf{Y}_{R_{cc}})^{-1} \mathbf{Y}_{S_{cc}}$. This formulation may be used later (see Section 7.2) as an alternative approach for predicting the mobility of a coupled assembly from its constituent sub-structures.

6.2.3 BLOCKED FORCE DETERMINATION

As stated in Section 2.2, an *acoustic* source may often be considered air-borne or structure-borne, depending upon the level at which the practitioner considers the problem. This concept may be further extended in the case of a structural source. Before experimentally determining a set of blocked forces, one must first define what

they wish to consider their source, that is, the location of the source-receiver interface. The location of this interface may vary depending on the level of complexity the practitioner wishes to engage. It is more or less standard practice to define the source-receiver interface as the one that separates the physical source and receiver sub-structures. However, one may instead define the source and, with it, the source-receiver interface, at some internal location nearer the noise generating mechanisms, e.g. bearing shells, gears boxes, etc. Such an approach may, in theory, allow for the independent characterisation of each of the noise generating mechanisms within a structural source. Although such a level of complexity would provide far greater flexibility in any eventual VAP, it is considered beyond the scope of this Thesis. The remainder of this work will consider the source-receiver interface, c , to lie between the physical source and receiver sub-structures, although many of the concepts introduced here are done so generally and are therefore not limited to this definition.

In the experimental determination of blocked forces one may only have access to either c or b DoFs. In such a case Equation 6.21 (also 6.9) may be rewritten, thus providing separate in-situ blocked force relations for the coupling interface and remote receiver DoFs. Considering first the coupling interface DoFs c , we have

Interface blocked force relation:

$$\mathbf{v}_{C_c} = -\mathbf{Y}_{C_{cc}} \bar{\mathbf{f}}_{S_c} \quad (6.22)$$

where for an n DoF system, $\bar{\mathbf{f}}_{S_c} \in \mathbb{C}^n$ is the blocked force vector of the source sub-structure at contact interface c , $\mathbf{Y}_{C_{cc}} \in \mathbb{C}^{n \times n}$ is the coupled mobility matrix measured at the contact interface, and $\mathbf{v}_{C_c} \in \mathbb{C}^n$ is an operational velocity vector of the coupled assembly at the contact interface. The blocked force $\bar{\mathbf{f}}_{S_c}$ may be considered the solution to the above and solved for via the inverse mobility matrix $\mathbf{Y}_{C_{cc}}^{-1}$. The determination of $\bar{\mathbf{f}}_{S_c}$ therefore requires a two part, passive and active measurement for $\mathbf{Y}_{C_{cc}}$ and \mathbf{v}_{C_c} , respectively. $\mathbf{Y}_{C_{cc}}$ is a symmetric matrix ($\mathbf{Y}_{C_{cc}} = \mathbf{Y}_{C_{cc}}^T$), measured whilst the source is not in operation. The source is then operated and the velocity vector \mathbf{v}_{C_c} is measured. The nature of this active measurement is discussed further in Section 6.2.3.2.

Often when dealing with real structures access is limited and the contact interface can not be excited adequately. In such a case we may consider the remote in-situ blocked force relation,

Remote blocked force relation:

$$\mathbf{v}_{\mathbf{C}_b} = -\mathbf{Y}_{\mathbf{C}_{cb}}^T \bar{\mathbf{f}}_{\mathbf{S}_c} \quad (6.23)$$

where $\mathbf{Y}_{\mathbf{C}_{cb}}^T = \mathbf{Y}_{\mathbf{C}_{bc}} \in \mathbb{C}^{m \times n}$ is the coupled transfer mobility matrix between some arbitrary set of remote receiver DoFs b , and the contact interface DoFs c , and $\mathbf{v}_{\mathbf{C}_b} \in \mathbb{C}^m$ is an operational velocity vector of the coupled assembly at the remote DoFs b . The same two part measurement procedure is required as above. This time however, operational responses are measured away from the contact interface. This in turn facilitates the over-determination of Equation 6.23. In order to acquire a determined solution the number of DoFs at b , m , must be equal to the n DoFs being solved for, $m = n$. That said, it is often desirable to solve the over-determined problem ($m > n$) as this provides a least squares solution, which has been shown to lead to a reduction in error when implemented successfully. In such a case the standard matrix inverse may be replaced by the Moore-Penrose pseudo inverse [142].

When access to the contact interface is unrestricted, Equations 6.22 and 6.23 may be used together, as shown in Equations 6.21 and 6.9, to provide an over-determined solution,

General blocked force relation:

$$\begin{bmatrix} \mathbf{v}_{\mathbf{C}_c} \\ \mathbf{v}_{\mathbf{C}_b} \end{bmatrix} = - \begin{bmatrix} \mathbf{Y}_{\mathbf{C}_{cc}} \\ \mathbf{Y}_{\mathbf{C}_{cb}}^T \end{bmatrix} \begin{bmatrix} \bar{\mathbf{f}}_{\mathbf{S}_c} \end{bmatrix} \quad (6.24)$$

where the partitioned matrix formed from $\mathbf{Y}_{\mathbf{C}_{cc}}$ and $\mathbf{Y}_{\mathbf{C}_{cb}}^T$ is $\in \mathbb{C}^{(n+m) \times n}$ and the partitioned vector formed from $\mathbf{v}_{\mathbf{C}_c}$ and $\mathbf{v}_{\mathbf{C}_b}$ is $\in \mathbb{C}^{(n+m)}$.

6.2.3.1 EXPERIMENTAL CONSIDERATIONS

There are a number experimental considerations that must be acknowledged prior to the implementation of the in-situ blocked force approach outlined above.

To begin with, the idea that the blocked force represents an independent source quantity is based on the assumption that the fundamental noise generating mechanisms (or the forces, $\mathbf{f}_{\mathbf{s}_i}$, that they generate) are unaffected by the coupling of source and receiver sub-structures. Although this assumption is often met, there may well

exist scenarios where it does not. It is therefore important to have some physical understanding of the noise generating mechanism when considering the in-situ blocked force approach.

Secondly, with the in-situ blocked force being based on an inverse procedure it is susceptible to ill conditioning. It is important that measures are taken to avoid this, preferably in the experimental phase, to avoid post processing ‘fixes’ if possible. Although approaches have been developed to aid in the reduction of noise resulting from ill conditioning (see Appendix A), these are often employed with little physical rationale. Based on experience it is the author’s opinion that it is better to carry out reliable and well executed measurements, as opposed to relying on regularisation techniques to recover poorly measured data.

Another important consideration is that of which DoFs should be accounted for, whether it be mathematically, or physically. For the true blocked force to be determined one must account for all 6 coordinate-DoFs at each of the coupling interface’s positional-DoFs. Neglecting any DoFs in the inverse procedure will result in those DoFs not being mathematically blocked. This is particularly important as, although these neglected DoFs may not contribute largely to the coupled response of the assembly, their blocking may significantly affect the determined blocked force in the remaining DoFs. The significance of this alteration will be dependent upon the physical constraints on the assembly’s coupling interface. For example, let us consider the same source, both rigidly and resiliently mounted, on a receiver sub-structure of relatively high impedance. Say we determine the blocked force of the source in only the translational z DoFs, for both assemblies. These blocked forces will almost certainly differ. This is because the rigidly coupled source is partially blocked in the translation in-plane x and y DoFs by the physical assembly, whilst the resiliently coupled source is not. In order to determine a blocked force in agreement with that of the rigidly coupled assembly one must also include the in-plane x and y DoFs, such that they are mathematically blocked. This amounts to saying that unless all DoFs are accounted for, the blocked forces should only be transferred between assemblies of similar mounting conditions, i.e. resilient to resilient or rigid to rigid. Avoiding the discrepancy between physically and mathematically blocked DoFs is perhaps the main advantage of the free velocity approach, where the sought after quantity is simply measured directly.

Lastly, the way in which the active measurement procedure is carried out and how the resulting data is processed can have significant effect on the quality of predictions.

This is particularly important with the construction of VAPs in mind, as one would be aiming to reproduce the assembly response in the most realistic way possible. This will be further discussed in the following Section.

6.2.3.2 POST PROCESSING FOR AURALISATION

A fundamental requirement of the inverse approach used in the determination of the blocked force is the existence of a reliable phase relationship between the elements of the operational velocity vector, $[\mathbf{v}_{\mathbf{C}_c} | \mathbf{v}_{\mathbf{C}_b}]^T$. Classically, in both acoustic and vibro-acoustic applications, this type of operational vector is determined from measured auto- and cross-spectra, whereby the cross-spectrum angle between each signal and a reference is assigned to the phase of an appropriate auto-spectrum [51], as in Equation 6.25,

$$\begin{bmatrix} \hat{v}_1 \\ \hat{v}_2 \\ \vdots \\ \hat{v}_n \end{bmatrix} = \begin{bmatrix} \sqrt{\hat{S}_{11}} \\ \sqrt{\hat{S}_{22}} \\ \vdots \\ \sqrt{\hat{S}_{nn}} \end{bmatrix} \odot \begin{bmatrix} e^{i0} \\ e^{i\angle \hat{S}_{12}} \\ \vdots \\ e^{i\angle \hat{S}_{1n}} \end{bmatrix} \quad (6.25)$$

where \odot and $\hat{\cdot}$ represent the Hadamard (element-wise) product and time averaged quantities, respectively.

Although a well established method, this cross-spectrum phase approach not only relies upon constant phase relationships, but assumes a steady state source behaviour. Although a fair assumption in most cases, with the aim of an eventual VAP auralisation in mind such a method is unlikely to be suitable. This is due to the sophistication of the human ear, particularly in detecting small temporal signal variations. As an alternative it is suggested that a sequential Fourier spectrum approach be employed. Such an approach makes no assumptions on the operational behaviour of the source in question, and provides a time dependent blocked force, from which realistic auralisations may be produced. The sequential Fourier spectrum (SFS) approach may be formulated as in Equation 6.26, where $\mathcal{F}\{V_n(\Delta t_m)\}$ represents the Fourier transform of the n th time domain velocity signal (V) over the m th time window (Δt). For a given time window, Δt , the n Fourier spectra are phase referenced to the beginning of that window, and therefore a meaningful phase

relationship is established between signals.

$$\begin{bmatrix} v_1 \\ v_2 \\ \vdots \\ v_n \end{bmatrix}_m = \begin{bmatrix} \mathcal{F}\{V_1(\Delta t_m)\} \\ \mathcal{F}\{V_2(\Delta t_m)\} \\ \vdots \\ \mathcal{F}\{V_n(\Delta t_m)\} \end{bmatrix} \quad (6.26)$$

The operational velocity vector of Equations 6.22-6.24 are thus replaced by $\mathbf{v}_m = [v_1, v_2, \dots, v_n]^T_m$ and the inverse procedure repeated for $m \rightarrow M$, where M is the total number of time windows used.

The SFS approach retains the time structure of the blocked force, and thus provides, in essence, a time domain source characterisation. With that in mind, it may readily be applied to the characterisation of ‘random’ sources. Although, it is important to note that this characterisation is not independent of source operation, i.e. a re-run of the source would not produce an identical operational response. If a source is considered random, then each time history recorded whilst in operation represents a particular set of circumstances which are unlikely to be repeated in any future measurements [143]. Consequently, each measurement may be considered a sample of a population of possible measurements. A full characterisation would require an infinite number of sample measurements to be made. Alternatively one may consider the problem in probabilistic terms.

In the frequency domain this is achieved by considering the blocked force in terms of its cross-spectral matrix, $\mathbf{\Gamma}_{\bar{\mathbf{f}}_{\text{sc}}}$, where auto-spectra are found along the main diagonal, and cross-spectra along the off diagonals. For a stationary stochastic process represented in the frequency domain the cross-spectral matrix form is the correct representation.

For the interface blocked force relation the cross-spectral form may be acquired simply by post multiplying Equation 6.22 by its conjugate transpose,

$$\mathbf{\Gamma}_{\bar{\mathbf{f}}_{\text{sc}}} = \mathbf{Y}_{\text{Ccc}} \mathbf{\Gamma}_{\mathbf{v}_{\text{Cc}}} \mathbf{Y}_{\text{Ccc}}^H \quad (6.27)$$

where $\mathbf{\Gamma}_{\mathbf{v}_{\text{Cc}}}$ is the cross-spectral operational velocity matrix and H represents the Hermitian (conjugate transpose).

6.3 ACCOUNTING FOR UNCERTAINTY

As with any experimental procedure, an element of uncertainty lies with the in-situ blocked force approach. With most standardised test methods it is possible to express such an uncertainty in some definitive way. This is not the case with the in-situ blocked force. The sensitivity of inverse methods to small experimental error makes it very difficult to assign a definite uncertainty. As such, alternative approaches are required.

In the determination of blocked forces it is useful to consider the errors contributing towards an overall uncertainty as either human, assembly or systematic. Human errors are introduced by the user and cover, for example, the incorrect placement of sensors, inconsistent force excitations, insufficient DoFs, incorrect hardware set-up, etc. Assembly errors are a result of the assembly itself and cover, for example, a lack of repeatability of the source, non-linearities introduced by operational conditions, etc. Lastly, systematic errors are introduced by the measurement system and any associated hardware and include, for example, equipment noise floor, cable interferences, AD conversion, numerical error due to finite precision, etc.

In the author's experience it is the human error introduced via poor experimental practice that plays the largest role in successful determination of blocked forces. Fortunately, the severity of this error may be reduced through practise and careful experimental design. However some element of error is unavoidable. This Section will introduce three experimental methods for assessing the remaining uncertainties.

6.3.1 ON-BOARD AND TRANSFERABILITY VALIDATION

Perhaps the simplest method for assessing the quality of experimentally determined blocked forces is to use them in the prediction of some known quantity. One example of this, commonly referred to as an 'on-board validation', involves the prediction of an operational response using blocked forces obtained from the same assembly for which the prediction is carried out. The on-board validation concept may be defined as in Equation 6.28, where the blocked force $\bar{\mathbf{f}}_{\mathbf{s}_c}$ is determined in-situ via the coupling interface and remote receiver DoFs c and b . This blocked force is subsequently used to predict the velocity at an addition remote receiver DoF, \tilde{b} , via the measured transfer mobility matrix, $\mathbf{Y}_{\mathbf{C}_{cb}}^{\mathbf{T}}$. It is important to note that the additional remote receiver DoF \tilde{b} is not used in the determination of the blocked force, that is $\tilde{b} \notin b$.

In Equation 6.28 the subscript, A , correspond to the assembly in which the marked quantity was measured. The on-board validation can therefore be seen to make a prediction for assembly A using blocked forces obtained from assembly A .

On-board validation procedure:

$$\begin{bmatrix} \bar{\mathbf{f}}_{\mathbf{S}_c} \end{bmatrix}_A = - \begin{bmatrix} \mathbf{Y}_{\mathbf{C}_{cc}} \\ \mathbf{Y}_{\mathbf{C}_{cb}}^T \end{bmatrix}_A^+ \begin{bmatrix} \mathbf{v}_{\mathbf{C}_c} \\ \mathbf{v}_{\mathbf{C}_b} \end{bmatrix}_A \quad (6.28a)$$

$$\begin{bmatrix} \mathbf{v}_{\mathbf{C}_b} \end{bmatrix}_A = - \begin{bmatrix} \mathbf{Y}_{\mathbf{C}_{cb}}^T \end{bmatrix}_A \begin{bmatrix} \bar{\mathbf{f}}_{\mathbf{S}_c} \end{bmatrix}_A \quad (6.28b)$$

The reference velocity $[\mathbf{v}_{\mathbf{C}_b}]_A$ and its associated transfer mobility matrix $[\mathbf{Y}_{\mathbf{C}_{cb}}^T]_A$ are measured alongside the DoFs used in the determination of the blocked force, thus allowing for a prediction to be made under identical operational conditions. The on-board validation procedure offers a convenient assessment of the blocked forces as it requires little additional experimental or computational effort. However, it does not account for any variability in the coupling between source and receiver that may occur on installation, or how well the blocked force transfers between assemblies. For this a procedure similar in concept to that of the on-board validation may be used. A transferability validation involves the prediction of an operational response using blocked forces obtained from a different assembly than the one being predicted for, as shown by Equation 6.29.

Transferability validation procedure:

$$\begin{bmatrix} \bar{\mathbf{f}}_{\mathbf{S}_c} \end{bmatrix}_A = - \begin{bmatrix} \mathbf{Y}_{\mathbf{C}_{cc}} \\ \mathbf{Y}_{\mathbf{C}_{cb}}^T \end{bmatrix}_A^+ \begin{bmatrix} \mathbf{v}_{\mathbf{C}_c} \\ \mathbf{v}_{\mathbf{C}_b} \end{bmatrix}_A \quad (6.29a)$$

$$\begin{bmatrix} \mathbf{v}_{\mathbf{C}_b} \end{bmatrix}_B = - \begin{bmatrix} \mathbf{Y}_{\mathbf{C}_{cb}}^T \end{bmatrix}_B \begin{bmatrix} \bar{\mathbf{f}}_{\mathbf{S}_c} \end{bmatrix}_A \quad (6.29b)$$

A transferability validation therefore requires the source to be removed from its original assembly and transferred to another, where the remote receiver velocity $[\mathbf{v}_{\mathbf{C}_b}]_B$ and transfer mobility matrix $[\mathbf{Y}_{\mathbf{C}_{cb}}^T]_B$ are measured.

6.3.1.1 ARTIFICIAL EXCITATION

An alternative method that may be used in conjunction with the on-board validation utilises an artificial impact excitation to simulate the operational behaviour of the source sub-structure. For such an excitation the source is turned off and excited externally via some impact source, i.e. a hammer. For investigative purposes this excitation may be considered a real one and the resulting responses measured. Unlike the true operational response of the source, which may consist of multiple sharp tonal components (due to any rotational or periodic mechanisms), the artificial impact excitation provides a broadband excitation free from such tones, and as such may be used to greater assess the uncertainties associated with the mobility matrix inversion.

Additionally, artificial excitations may be used to excite the source in different coordinate-DoFs, allowing the practitioner to investigate the potential contribution of operational forces acting in other DoFs.

6.3.2 SAMPLE SPACE APPROACH - EXPECTED VALUE AND STANDARD DEVIATION

Although offering a convenient picture of the uncertainties, neither the on-board nor the transferability validation provide a definite blocked force uncertainty, at least not one that may be used to estimate the uncertainty in a future prediction. It is proposed that a more suitable uncertainty assessment be provided via a ‘large sample space’ approach, whereby an over-determined problem is instead considered as multiple *determined* problems, the solutions of which together form a sample space of blocked forces from which one may extract some statistical information.

In theory, the number of response DoFs required to solve for N interface DoFs is simply N . This provides a determined solution resulting from the inversion of an $N \times N$ square matrix. However, often additional response DoFs are included so as to over-determine the problem, resulting in the inversion of a non-square matrix. In such a case the Moore-Penrose pseudo inverse is used to determine the least squares solution. Although often considered beneficial, the over-determination yields only a single blocked force vector from which minimal information, with regards its associated uncertainty, may be extracted. It is instead proposed that the additional response DoFs be used to construct a *set* consisting of multiple *determined* problems. The solutions to this set form a sample space which may be used to extract some probabilistic information with regards to the uncertainty of the determined blocked

forces, i.e. expected values and standard deviations. Here, the expected value is the numerical average of the set consisting of all the determined blocked force vectors. It is believed that, similar to an over-determination, the expected value will lead to a reduction in error and therefore provide an optimal blocked force. Furthermore, with the standard deviation of a quantity possessing the same units, it may be carried through future predictions and used to provide an estimate of the uncertainties in a response, an advantage neither the on-board or transferability validations offer.

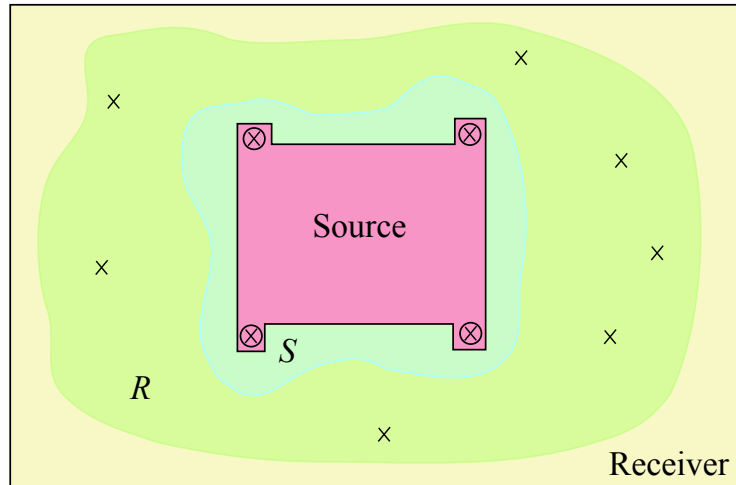


Figure 6.3: Source-receiver assembly highlighting the DoF subsets S and R . Symbols \times represent response DoFs, whilst \otimes represent solution DoFs at the source-receiver interface. In this rigid case $S \subset R$.

Let us now formulate the above approach. Consider an arbitrary assembly consisting of rigid or resiliently coupled source and receiver sub-structures. As in previous Chapters, the source-receiver interface DoFs are denoted c , whilst remote receiver DoFs are denoted b . Let us define a *set* of solution DoFs, S , such that $c \in S$. These are the DoFs we are trying to determine blocked forces at. Let us also define a set of response DoFs, R , such that $b \in R$. These are the DoFs we measure the operational velocity vector at. S may be considered a subset of R if measurements are permitted at the source-receiver interface, $S \subset R$, else $S \not\subset R$. The k -combination of set R is a subset of k distinct elements of R , i.e. the different combinations of k elements where repetitions are not allowed, and order does not matter. For a set that has n elements the number of k -combinations is given generally by the binomial coefficient formula,

$$C(n, k) = \binom{n}{k} = \frac{n!}{k!(n-k)!} \quad (6.30)$$

The binomial coefficient therefore details the number of determined problems one can formulate from a single over-determined system. Considering the determination of blocked forces, $n = |R|$ (where $|R|$ is the cardinality of the set R , that is, how many elements are contained within it, i.e. the number of response DoFs), and $k = |S|$ (i.e. the number of solution DoFs). Therefore, disregarding any repetitions and with no preference of order, the number of subsets r_i of R with cardinality equal to $|S|$ is $C(|R|, |S|)$. For example, if we are aiming to determine 4 blocked forces and we measure 10 response DoFs, the number of determined solutions one can construct is $C(10, 4) = 210$. That is, there are 210 independent combinations of response DoFs that may be used to determine the blocked forces.

From the $C(|R|, |S|)$ determined solutions, the expected value and standard deviations may be calculated. The expected value of the blocked force $E[\bar{\mathbf{f}}_{\mathbf{S}}]$ is given by the linear average of the individual blocked force vectors,

Expected blocked force:

$$E[\bar{\mathbf{f}}_{\mathbf{S}}] = \frac{1}{C(|R|, |S|)} \sum_{i=1}^{C(|R|, |S|)} \mathbf{Y}_{\mathbf{C}_{S r_i}} \mathbf{v}_{\mathbf{C}_{r_i}} \quad (6.31)$$

where $\mathbf{Y}_{\mathbf{C}_{S r_i}}$ is the coupled mobility matrix relating the subset of response DoFs r_i to the solution set DoFs S , $\mathbf{v}_{\mathbf{C}_{r_i}}$ is the operational velocity vector pertaining to the same response DoFs subset, and $E[\bar{\mathbf{f}}_{\mathbf{S}}]$ is the vector of expected blocked force values.

The standard deviation is subsequently given by,

Blocked force standard deviation:

$$\sigma[\bar{\mathbf{f}}_{\mathbf{S}}] = \sqrt{E[\bar{\mathbf{f}}_{\mathbf{S}}^2] - (E[\bar{\mathbf{f}}_{\mathbf{S}}])^2}. \quad (6.32)$$

When dealing with multi-contact assemblies one may be more interested in the variance-covariance matrix, which may be defined generally as,

Blocked force variance-covariance matrix:

$$\Sigma_{\bar{\mathbf{f}}} = E[(\bar{\mathbf{f}}_{\mathbf{S}} - E[\bar{\mathbf{f}}_{\mathbf{S}}])(\bar{\mathbf{f}}_{\mathbf{S}} - E[\bar{\mathbf{f}}_{\mathbf{S}}])^T] \quad (6.33)$$

where the squared standard deviations for each blocked force are found along the main diagonal. Having determined the standard deviation (or variance-covariance matrix) one may use it to derive a number of uncertainty parameters. A popular choice is that of the 95% confidence interval which, assuming the determined blocked forces are normally distributed, is given by $\pm 1.96 \times \sigma[\bar{\mathbf{f}}_{\mathbf{S}}]$. Another commonly used parameter is the standard error of the mean (SEM) which describes the deviation of the sample mean over all possible samples (of a given size), and is given by

Standard error of the mean:

$$\text{SEM}[\bar{\mathbf{f}}_{\mathbf{S}}] = \frac{\sigma[\bar{\mathbf{f}}_{\mathbf{S}}]}{\sqrt{C(|R|, |S|)}}. \quad (6.34)$$

Lastly, the coefficient of variation (\mathbf{C}_v) may be used. Defined as,

$$\mathbf{C}_v = \frac{\sigma[\bar{\mathbf{f}}_{\mathbf{S}}]}{E[\bar{\mathbf{f}}_{\mathbf{S}}]} \quad (6.35)$$

where $\sigma[\bar{\mathbf{f}}_{\mathbf{S}}]$ is the standard deviation and $E[\bar{\mathbf{f}}_{\mathbf{S}}]$ is the expected value, the \mathbf{C}_v describes the standard deviation relative to the mean value. It is a dimensionless parameter and therefore has the advantage that it may be used to compare the uncertainties between quantities of different units.

6.3.2.1 NATURE OF THE SAMPLE SPACE UNCERTAINTY

At this point it is worth considering the nature of the uncertainties acquired via the sample space approach outlined above.

We will begin by considering the forward problem in the absence of noise,

$$\mathbf{v}_{\mathbf{C}_b} = \mathbf{Y}_{\mathbf{C}_{bc}} \bar{\mathbf{f}}_{\mathbf{S}_c} \quad (6.36)$$

where it is assumed that mobility matrix $\mathbf{Y}_{\mathbf{C}_{bc}}$ may be measured with absolute precision. Here $\bar{\mathbf{f}}_{\mathbf{S}_c}$ is the blocked force vector containing all of the forces we *choose* to define the source by. In reality there may exist additional forces arising from DoFs that were not included in the definition of $\bar{\mathbf{f}}_{\mathbf{S}_c}$. Let us denote these forces by $\bar{\mathbf{f}}_{\mathbf{S}_e}$. The forward problem is then given by,

$$\mathbf{v}_{\mathbf{C}_b} = \mathbf{Y}_{\mathbf{C}_{bc}} \bar{\mathbf{f}}_{\mathbf{S}_c} + \mathbf{Y}_{\mathbf{C}_{be}} \bar{\mathbf{f}}_{\mathbf{S}_e} \quad (6.37)$$

where $\mathbf{Y}_{\mathbf{C}_{b\hat{c}}}$ is the transfer mobility between the remote DoFs b and the unknown blocked force DoFs \hat{c} . Pre multiplication of both sides by $\mathbf{Y}_{\mathbf{C}_{bc}}$ leads to,

$$\bar{\mathbf{f}}_{\mathbf{S}_c} + \mathbf{Y}_{\mathbf{C}_{bc}}^{-1} \mathbf{Y}_{\mathbf{C}_{b\hat{c}}} \bar{\mathbf{f}}_{\mathbf{S}_{\hat{c}}} = \mathbf{Y}_{\mathbf{C}_{bc}}^{-1} \mathbf{v}_{\mathbf{C}_b}. \quad (6.38)$$

Equation 6.38 states that for an incomplete source definition the in-situ blocked forces acquired are the sum of the sought after blocked forces, $\bar{\mathbf{f}}_{\mathbf{S}_c}$, and the additional term, $\mathbf{Y}_{\mathbf{C}_{bc}}^{-1} \mathbf{Y}_{\mathbf{C}_{b\hat{c}}} \bar{\mathbf{f}}_{\mathbf{S}_{\hat{c}}}$. This term may be considered the error arising from an incomplete definition of the source. It can be seen that this error term is dependent upon the position of the remote DoFs b . As such, the contribution of the unknown blocked forces to the observed velocities will vary depending on the position of the remote DoFs b . It is therefore proposed that the variance acquired via the sample space approach will account for an incomplete source definition. However, this uncertainty belongs to the assembly in which the source is characterised, and is *not* an independent property of the source. That said, providing the intended installation is similar to that of the initial assembly, these uncertainties are likely to be transferable.

A second scenario may now be considered, that is, the case where all forces are accounted for, in the presence of noise. In such a scenario the forward problem may be formulated as,

$$\mathbf{v}_{\mathbf{C}_b} = [\mathbf{Y}_{\mathbf{C}_{bc}} + \mathbf{N}_{\mathbf{C}_{bc}}] \bar{\mathbf{f}}_{\mathbf{S}_c} \quad (6.39)$$

where $\mathbf{N}_{\mathbf{C}_{bc}}$ accounts for the noise in the measured mobility, $\mathbf{Y}_{\mathbf{C}_{bc}}$. The blocked forces are thus given by,

$$\bar{\mathbf{f}}_{\mathbf{S}_c} = [\mathbf{Y}_{\mathbf{C}_{bc}} + \mathbf{N}_{\mathbf{C}_{bc}}]^{-1} \mathbf{v}_{\mathbf{C}_b}. \quad (6.40)$$

In the above, each column of $\mathbf{N}_{\mathbf{C}_{bc}}$ corresponds to the noise relating to a given mobility measurement (i.e. excitation at a single point, response measurement at multiple points). Therefore, each realisation of $\mathbf{Y}_{\mathbf{C}_{bc}}$ used in the sample space approach (different combination of remote DoFs b) will be independent of one another. As such, each of the determined blocked force vectors acquired via the sample space approach will be affected by different contributions of noise. It is therefore proposed that the variance determined from the sample space approach includes also the effect of measurement error (assuming that this error may be represented in the form of Equation 6.40).

Often one may wish to account for the uncertainty in the operational behaviour of a source. In the standardised measurement of sound power for household appliances [144] this uncertainty is acquired by repeatedly operating the source and accessing the subsequent variance. Although likely a small uncertainty in comparison to that of neglected DoFs and/or measurement error, it may be accounted for in the sample space approach by carrying out repeated operations and including the resultant sample space solutions in the variance and expected value calculations. An example of this is shown later in Section 6.4.1.2.

6.3.2.2 ALTERNATIVE UNCERTAINTY APPROACH

The proposed sample space approach, whilst thorough, may prove computationally expensive in cases where a large number of DoFs are used. It is therefore of interest to formulate an alternative approach. Such an approach is presented here.

Consider the case whereby the only error encountered is through neglected DoFs,

$$\mathbf{v}_{\mathbf{C}_b} = \mathbf{Y}_{\mathbf{C}_{bc}} \bar{\mathbf{f}}_{\mathbf{S}_c} + \mathbf{Y}_{\mathbf{C}_{bc}} \bar{\mathbf{f}}_{\mathbf{S}_e}. \quad (6.41)$$

By replacing the far right side term with ϵ it can be seen that this error takes the form of the classic least-squares problem.

$$\mathbf{v}_{\mathbf{C}_b} = \mathbf{Y}_{\mathbf{C}_{bc}} \bar{\mathbf{f}}_{\mathbf{S}_c} + \epsilon \quad (6.42)$$

The solution to this form is given by

$$\hat{\mathbf{f}}_{\mathbf{S}_c} = (\mathbf{Y}_{\mathbf{C}_{bc}}^T \mathbf{Y}_{\mathbf{C}_{bc}})^{-1} \mathbf{Y}_{\mathbf{C}_{bc}}^T \mathbf{v}_{\mathbf{C}_b} \quad (6.43)$$

where $(\mathbf{Y}_{\mathbf{C}_{bc}}^T \mathbf{Y}_{\mathbf{C}_{bc}})^{-1} \mathbf{Y}_{\mathbf{C}_{bc}}^T$ represents the pseudo inverse of $\mathbf{Y}_{\mathbf{C}_{bc}}^T$, and $\hat{\mathbf{f}}_{\mathbf{S}_c}$ is the least squares solution, i.e. the solution that minimizes the squared error term, $|\mathbf{v}_{\mathbf{C}_b} - \mathbf{Y}_{\mathbf{C}_{bc}} \bar{\mathbf{f}}_{\mathbf{S}_c}|^2$. It can be shown that for a normally distributed error ϵ with zero mean, the least square solution is equal to the expected value. The least squares solution is used heavily throughout vibro-acoustic inverse methods to alleviate the effect of error introduced experimentally. However, its secondary statistics, i.e the variance/covariance matrix, are often ignored.

Let us assume that the error ϵ has a zero mean, $E[\epsilon] = 0$. Under this assumption the Gauss-Markov Theorem states that the expected value of the least square solution is the blocked force, $E[\hat{\mathbf{f}}_{\mathbf{S}_c}] = \bar{\mathbf{f}}_{\mathbf{S}_c}$ [145]. This can be shown as follows. Beginning

with the least squares solution,

$$\hat{\mathbf{f}}_{\mathbf{S}_c} = (\mathbf{Y}_{\mathbf{C}_{bc}}^T \mathbf{Y}_{\mathbf{C}_{bc}})^{-1} \mathbf{Y}_{\mathbf{C}_{bc}}^T \mathbf{v}_{\mathbf{C}_b} \quad (6.44)$$

substituting in the velocity term,

$$\hat{\mathbf{f}}_{\mathbf{S}_c} = (\mathbf{Y}_{\mathbf{C}_{bc}}^T \mathbf{Y}_{\mathbf{C}_{bc}})^{-1} \mathbf{Y}_{\mathbf{C}_{bc}}^T (\mathbf{Y}_{\mathbf{C}_{bc}} \bar{\mathbf{f}}_{\mathbf{S}_c} + \epsilon) \quad (6.45)$$

and expanding,

$$\hat{\mathbf{f}}_{\mathbf{S}_c} = \bar{\mathbf{f}}_{\mathbf{S}_c} + (\mathbf{Y}_{\mathbf{C}_{bc}}^T \mathbf{Y}_{\mathbf{C}_{bc}})^{-1} \mathbf{Y}_{\mathbf{C}_{bc}}^T \epsilon. \quad (6.46)$$

Now taking the expected value of both sides, whilst noting our assumption of zero mean error,

$$\mathbb{E}[\hat{\mathbf{f}}_{\mathbf{S}_c}] = \mathbb{E}[\bar{\mathbf{f}}_{\mathbf{S}_c}]. \quad (6.47)$$

Here we can note that the true blocked force $\bar{\mathbf{f}}_{\mathbf{S}_c}$ is not a stochastic quantity and therefore its expected value is simply itself. As such,

$$\mathbb{E}[\hat{\mathbf{f}}_{\mathbf{S}_c}] = \bar{\mathbf{f}}_{\mathbf{S}_c} \quad (6.48)$$

the expected least squares solution is equal to the blocked force. Consequently, we may write the covariance of the least-squares blocked force as,

$$\begin{aligned} \text{Cov}[\hat{\mathbf{f}}_{\mathbf{S}_c}] &= \mathbb{E}[\{(\hat{\mathbf{f}}_{\mathbf{S}_c} - \bar{\mathbf{f}}_{\mathbf{S}_c})\{\hat{\mathbf{f}}_{\mathbf{S}_c} - \bar{\mathbf{f}}_{\mathbf{S}_c}\}^T] = \dots \\ &\mathbb{E}[\{(\mathbf{Y}_{\mathbf{C}_{bc}}^T \mathbf{Y}_{\mathbf{C}_{bc}})^{-1} \mathbf{Y}_{\mathbf{C}_{bc}}^T (\mathbf{Y}_{\mathbf{C}_{bc}} \bar{\mathbf{f}}_{\mathbf{S}_c} + \epsilon) - \bar{\mathbf{f}}_{\mathbf{S}_c}\} \{(\mathbf{Y}_{\mathbf{C}_{bc}}^T \mathbf{Y}_{\mathbf{C}_{bc}})^{-1} \mathbf{Y}_{\mathbf{C}_{bc}}^T (\mathbf{Y}_{\mathbf{C}_{bc}} \bar{\mathbf{f}}_{\mathbf{S}_c} + \epsilon) - \bar{\mathbf{f}}_{\mathbf{S}_c}\}^T] \end{aligned} \quad (6.49)$$

Expanding the bracketed terms yields,

$$\begin{aligned} \text{Cov}[\hat{\mathbf{f}}_{\mathbf{S}_c}] &= \mathbb{E}[\{(\mathbf{Y}_{\mathbf{C}_{bc}}^T \mathbf{Y}_{\mathbf{C}_{bc}})^{-1} \mathbf{Y}_{\mathbf{C}_{bc}}^T \mathbf{Y}_{\mathbf{C}_{bc}} \bar{\mathbf{f}}_{\mathbf{S}_c} + (\mathbf{Y}_{\mathbf{C}_{bc}}^T \mathbf{Y}_{\mathbf{C}_{bc}})^{-1} \mathbf{Y}_{\mathbf{C}_{bc}}^T \epsilon - \bar{\mathbf{f}}_{\mathbf{S}_c}\} \dots \\ &\quad \{(\mathbf{Y}_{\mathbf{C}_{bc}}^T \mathbf{Y}_{\mathbf{C}_{bc}})^{-1} \mathbf{Y}_{\mathbf{C}_{bc}}^T \mathbf{Y}_{\mathbf{C}_{bc}} \bar{\mathbf{f}}_{\mathbf{S}_c} + (\mathbf{Y}_{\mathbf{C}_{bc}}^T \mathbf{Y}_{\mathbf{C}_{bc}})^{-1} \mathbf{Y}_{\mathbf{C}_{bc}}^T \epsilon - \bar{\mathbf{f}}_{\mathbf{S}_c}\}^T]. \end{aligned} \quad (6.50)$$

Noting that $(\mathbf{Y}_{\mathbf{C}_{bc}}^T \mathbf{Y}_{\mathbf{C}_{bc}})^{-1} \mathbf{Y}_{\mathbf{C}_{bc}}^T \mathbf{Y}_{\mathbf{C}_{bc}} = \mathbf{I}$,

$$\text{Cov}[\hat{\mathbf{f}}_{\mathbf{S}_c}] = \mathbb{E}[\{\bar{\mathbf{f}}_{\mathbf{S}_c} + (\mathbf{Y}_{\mathbf{C}_{bc}}^T \mathbf{Y}_{\mathbf{C}_{bc}})^{-1} \mathbf{Y}_{\mathbf{C}_{bc}}^T \epsilon - \bar{\mathbf{f}}_{\mathbf{S}_c}\} \{\bar{\mathbf{f}}_{\mathbf{S}_c} + (\mathbf{Y}_{\mathbf{C}_{bc}}^T \mathbf{Y}_{\mathbf{C}_{bc}})^{-1} \mathbf{Y}_{\mathbf{C}_{bc}}^T \epsilon - \bar{\mathbf{f}}_{\mathbf{S}_c}\}^T] \quad (6.51)$$

which leads to,

$$\text{Cov}[\hat{\mathbf{f}}_{\mathbf{S}_c}] = E[(\mathbf{Y}_{\mathbf{C}_{bc}}^T \mathbf{Y}_{\mathbf{C}_{bc}})^{-1} \mathbf{Y}_{\mathbf{C}_{bc}}^T \epsilon] ((\mathbf{Y}_{\mathbf{C}_{bc}}^T \mathbf{Y}_{\mathbf{C}_{bc}})^{-1} \mathbf{Y}_{\mathbf{C}_{bc}}^T \epsilon)^T]. \quad (6.52)$$

Making use of the transpose identity $(AB)^T = B^T A^T$, whilst assuming that the mobility matrix $\mathbf{Y}_{\mathbf{C}_{bc}}$ is *not* a random variable, we may reformulate this as,

$$\text{Cov}[\hat{\mathbf{f}}_{\mathbf{S}_c}] = (\mathbf{Y}_{\mathbf{C}_{bc}}^T \mathbf{Y}_{\mathbf{C}_{bc}})^{-1} \mathbf{Y}_{\mathbf{C}_{bc}}^T E[\epsilon \epsilon^T] \mathbf{Y}_{\mathbf{C}_{bc}} (\mathbf{Y}_{\mathbf{C}_{bc}}^T \mathbf{Y}_{\mathbf{C}_{bc}})^{-1}. \quad (6.53)$$

The above equation describes the covariance of the over-determined blocked force in terms of the measured mobility $\mathbf{Y}_{\mathbf{C}_{bc}}$ and an expected value term associated with the unknown error. Noting our zero error mean assumption, this expected value term may be considered the covariance matrix associated with the unknown error.

A further simplification can be made under the assumption of homoskedasticity (i.e. random variables have the same finite variance) and uncorrelated errors, that is, $E[\epsilon \epsilon^T] = \sigma^2 \mathbf{I}$. Making this substitution and simplifying leads to,

$$\text{Cov}[\hat{\mathbf{f}}_{\mathbf{S}_c}] = \sigma^2 \mathbf{I} (\mathbf{Y}_{\mathbf{C}_{bc}}^T \mathbf{Y}_{\mathbf{C}_{bc}})^{-1}. \quad (6.54)$$

However, the above assumes that there exists no correlation between the unknown errors in the blocked forces. If we consider these errors as a result of neglected DoFs it is not unreasonable to expect a degree of correlation to exist. As such this assumption is likely only applicable in cases where source contacts are largely separated, even then, under the assumptions that the neglected DoFs at each foot are uncorrelated.

Turning attention back to the previous covariance form,

$$\text{Cov}[\hat{\mathbf{f}}_{\mathbf{S}_c}] = (\mathbf{Y}_{\mathbf{C}_{bc}}^T \mathbf{Y}_{\mathbf{C}_{bc}})^{-1} \mathbf{Y}_{\mathbf{C}_{bc}}^T E[\epsilon \epsilon^T] \mathbf{Y}_{\mathbf{C}_{bc}} (\mathbf{Y}_{\mathbf{C}_{bc}}^T \mathbf{Y}_{\mathbf{C}_{bc}})^{-1}. \quad (6.55)$$

our task is now to estimate the unknown error covariance matrix $E[\epsilon \epsilon^T]$. At this point we must make one further assumption, that is, there exists no correlation between the errors. This assumption, also referred to as heteroscedasticity, leads to a diagonal error covariance, $E[\epsilon \epsilon^T]$. If the errors are heteroscedastic the least squares covariance matrix is biased, leading to inconsistent statistical properties. The aim is therefore to acquire a heteroscedasticity corrected covariance matrix (HCCM). The

HCCM is based on the estimation of the unknown error ϵ via the residual e .

$$\epsilon_i \approx e_i = |\mathbf{v}_{\mathbf{C}_b} - \mathbf{Y}_{\mathbf{C}_{bc}}^T \hat{\mathbf{f}}_{\mathbf{S}_c}| \quad (6.56)$$

In White's classic paper an asymptotic HCCM was presented [146]. White's particular form of HCCM simply replaces the unknown error covariance matrix $E[\epsilon\epsilon^T]$ with the diagonal residual matrix $\text{diag}(e_1^2, e_2^2, \dots, e_n^2)$, leading to the expression,

$$\text{Cov}[\hat{\mathbf{f}}_{\mathbf{S}_c}] = (\mathbf{Y}_{\mathbf{C}_{bc}}^T \mathbf{Y}_{\mathbf{C}_{bc}})^{-1} \mathbf{Y}_{\mathbf{C}_{bc}}^T \text{diag}[e_i^2] \mathbf{Y}_{\mathbf{C}_{bc}} (\mathbf{Y}_{\mathbf{C}_{bc}}^T \mathbf{Y}_{\mathbf{C}_{bc}})^{-1}. \quad (6.57)$$

where $\mathbf{Y}_{\mathbf{C}_{bc}}^T \hat{\mathbf{f}}_{\mathbf{S}_c} = \hat{\mathbf{v}}_{\mathbf{C}_b}$ is the velocity prediction based on the least squares solution $\hat{\mathbf{f}}_{\mathbf{S}_c}$. Although the residuals themselves may not provide the best estimation of the unknown error, for large sample sizes (largely over-determined problems) it was shown that $\mathbf{Y}_{\mathbf{C}_{bc}}^T \mathbf{e} \mathbf{e}^T \mathbf{Y}_{\mathbf{C}_{bc}}$ is a consistent (but not unbiased) estimator of $\mathbf{Y}_{\mathbf{C}_{bc}}^T E[\epsilon\epsilon^T] \mathbf{Y}_{\mathbf{C}_{bc}}$ [146]. Various authors have since raised concern with regards to the above HCCM's application on small sample sizes, and have since proposed a number of other HCCM's with the aim of improving their small sample size behaviour [147].

Whilst Equation 6.57 in theory provides an estimate of the uncertainties, the implications of the assumptions required in its derivation are currently unknown. Further investigation was considered beyond the scope of this work and the alternative uncertainty approach is not considered any further in this Thesis.

6.3.2.3 PROPAGATION OF UNCERTAINTY

In this Section we will briefly consider the propagation of blocked force uncertainty in the forward prediction of an operational response.

Although providing a rough idea of the uncertainties in the blocked force, the on-board and transferability validations do not facilitate the propagation of uncertainty, and are therefore of limited use. It is proposed that by using the sample space approach presented above uncertainties, in the form of the blocked force variance-covariance matrix, may be propagated through a forward prediction and provide a measure of uncertainty in a predicted operational response. In what follows the *law of error propagation* is introduced and applied to the forward problem under consideration.

The law of error propagation is given, in its most general form, as,

$$\sigma_{x_i x_j} = \mathbf{J}_i \boldsymbol{\Sigma}_y \mathbf{J}_j^T \quad (6.58)$$

where $\sigma_{x_i x_j}$ is the covariance between any two elements of the vector output variable \mathbf{x} , $\boldsymbol{\Sigma}_y$ is the covariance matrix of the vector input variable \mathbf{y} , and \mathbf{J} is the Jacobian associated with the propagating function/model. The propagation model considered here is that of the forward prediction, given for a single response variable as,

$$v_{C_i} = \sum_n^N Y_{C_{in}} \bar{f}_{S_n} \quad (6.59)$$

where subscripts i and n correspond to the elements of the force and velocity response vectors, respectively.

Any two elements of the response vector \mathbf{v}_C may be considered, generally, as outputs of the multi-variable function, $G()$, where input variables correspond to that of mobility and blocked force. For two arbitrary response positions i and j , Equation 6.59 may be written as,

$$v_{C_i} = G(Y_{C_{i1}}, Y_{C_{i2}}, \dots, Y_{C_{iN}}, \bar{f}_{S_1}, \bar{f}_{S_2}, \dots, \bar{f}_{S_N}) = G(\eta_i) \quad (6.60)$$

$$v_{C_j} = G(Y_{C_{j1}}, Y_{C_{j2}}, \dots, Y_{C_{jN}}, \bar{f}_{S_1}, \bar{f}_{S_2}, \dots, \bar{f}_{S_N}) = G(\eta_j) \quad (6.61)$$

where η_i and η_j simply represent the input variable vectors. According to the law of error propagation the covariance between any two elements of the response vector is given by,

$$\sigma_{v_i v_j} = \mathbf{J}_{\eta_i} \boldsymbol{\Sigma}_{\eta_i \eta_j} \mathbf{J}_{\eta_j}^T \quad (6.62)$$

where the Jacobian of the functions $v_{C_i} = G(\eta_i)$ and $v_{C_j} = G(\eta_j)$ are given by,

$$\mathbf{J}_{\eta_i} = \left[\begin{array}{ccccccc} \frac{\partial G(\eta_i)}{\partial Y_{C_{i1}}} & \frac{\partial G(\eta_i)}{\partial Y_{C_{i2}}} & \dots & \frac{\partial G(\eta_i)}{\partial Y_{C_{iN}}} & \frac{\partial G(\eta_i)}{\partial \bar{f}_{S_1}} & \frac{\partial G(\eta_i)}{\partial \bar{f}_{S_2}} & \dots & \frac{\partial G(\eta_i)}{\partial \bar{f}_{S_N}} \end{array} \right] \quad (6.63)$$

and

$$\mathbf{J}_{\eta_j} = \left[\begin{array}{ccccccc} \frac{\partial G(\eta_j)}{\partial Y_{C_{j1}}} & \frac{\partial G(\eta_j)}{\partial Y_{C_{j2}}} & \dots & \frac{\partial G(\eta_j)}{\partial Y_{C_{jN}}} & \frac{\partial G(\eta_j)}{\partial \bar{f}_{S_1}} & \frac{\partial G(\eta_j)}{\partial \bar{f}_{S_2}} & \dots & \frac{\partial G(\eta_j)}{\partial \bar{f}_{S_N}} \end{array} \right] \quad (6.64)$$

respectively, and the input variable covariance matrix by,

$$\Sigma_{\eta_i \eta_j} = \left[\begin{array}{cccc|cccc} \sigma_{Y_{i1}Y_{j1}} & \sigma_{Y_{i1}Y_{j2}} & \cdots & \sigma_{Y_{i1}Y_{jN}} & \sigma_{Y_{i1}\bar{f}_1} & \sigma_{Y_{i1}\bar{f}_2} & \cdots & \sigma_{Y_{i1}\bar{f}_N} \\ \sigma_{Y_{i2}Y_{j1}} & \sigma_{Y_{i2}Y_{j2}} & \cdots & \sigma_{Y_{i2}Y_{jN}} & \sigma_{Y_{i2}\bar{f}_1} & \sigma_{Y_{i2}\bar{f}_2} & \cdots & \sigma_{Y_{i2}\bar{f}_N} \\ \vdots & \vdots & \ddots & \vdots & \vdots & \vdots & \ddots & \vdots \\ \sigma_{Y_{iN}Y_{j1}} & \sigma_{Y_{iN}Y_{j2}} & \cdots & \sigma_{Y_{iN}Y_{jN}} & \sigma_{Y_{iN}\bar{f}_1} & \sigma_{Y_{iN}\bar{f}_2} & \cdots & \sigma_{Y_{iN}\bar{f}_N} \\ \hline \sigma_{\bar{f}_1 Y_{j1}} & \sigma_{\bar{f}_1 Y_{j2}} & \cdots & \sigma_{\bar{f}_1 Y_{jN}} & \sigma_{\bar{f}_1}^2 & \sigma_{\bar{f}_1 \bar{f}_2} & \cdots & \sigma_{\bar{f}_1 \bar{f}_N} \\ \sigma_{\bar{f}_2 Y_{j1}} & \sigma_{\bar{f}_2 Y_{j2}} & \cdots & \sigma_{\bar{f}_2 Y_{jN}} & \sigma_{\bar{f}_2 \bar{f}_1} & \sigma_{\bar{f}_2}^2 & \cdots & \sigma_{\bar{f}_2 \bar{f}_N} \\ \vdots & \vdots & \ddots & \vdots & \vdots & \vdots & \ddots & \vdots \\ \sigma_{\bar{f}_N Y_{j1}} & \sigma_{\bar{f}_N Y_{j2}} & \cdots & \sigma_{\bar{f}_N Y_{jN}} & \sigma_{\bar{f}_N \bar{f}_1} & \sigma_{\bar{f}_N \bar{f}_2} & \cdots & \sigma_{\bar{f}_N}^2 \end{array} \right]. \quad (6.65)$$

Here we are considering the case where it is assumed that the mobility used in the forward prediction, \mathbf{Y}_C , is known exactly. As such the input variable covariance matrix is reduced to the blocked force covariance matrix alone,

$$\Sigma_{\eta_i \eta_j} = \left[\begin{array}{c|c} \mathbf{0} & \mathbf{0} \\ \hline \mathbf{0} & \Sigma_{\bar{\mathbf{f}}} \end{array} \right]. \quad (6.66)$$

Consequently, we need only evaluate the corresponding elements of the Jacobians,

$$\mathbf{J}_{\eta_i} = \left[\begin{array}{cccc} \frac{\partial G(\eta_i)}{\partial f_{S_1}} & \frac{\partial G(\eta_i)}{\partial f_{S_2}} & \cdots & \frac{\partial G(\eta_i)}{\partial f_{S_N}} \end{array} \right] = \left[\begin{array}{cccc} Y_{C_{i1}} & Y_{C_{i2}} & \cdots & Y_{C_{iN}} \end{array} \right] = \mathbf{Y}_{C_{i:}} \quad (6.67)$$

and

$$\mathbf{J}_{\eta_j} = \left[\begin{array}{cccc} \frac{\partial G(\eta_j)}{\partial \bar{f}_{S_1}} & \frac{\partial G(\eta_j)}{\partial \bar{f}_{S_2}} & \cdots & \frac{\partial G(\eta_j)}{\partial \bar{f}_{S_N}} \end{array} \right] = \left[\begin{array}{cccc} Y_{C_{j1}} & Y_{C_{j2}} & \cdots & Y_{C_{jN}} \end{array} \right] = \mathbf{Y}_{C_{j:}}. \quad (6.68)$$

Substitution of the above into Equation 6.62 gives the covariance between any two elements of the response vector as,

$$\sigma_{v_{ij}} = \mathbf{Y}_{C_{i:}} \Sigma_{\bar{\mathbf{f}}} \mathbf{Y}_{C_{j:}}^T. \quad (6.69)$$

The above relation may readily be extended to yield the full variance-covariance matrix between an arbitrary number of responses,

$$\left[\begin{array}{cccc} \sigma_{v_1}^2 & \sigma_{v_1 v_2} & \cdots & \sigma_{v_1 v_N} \\ \sigma_{v_2 v_1} & \sigma_{v_2}^2 & \cdots & \sigma_{v_2 v_N} \\ \vdots & \vdots & \ddots & \vdots \\ \sigma_{v_N v_1} & \sigma_{v_N v_2} & \cdots & \sigma_{v_N}^2 \end{array} \right] = \left[\begin{array}{c} Y_{C_{1:}} \\ Y_{C_{2:}} \\ \vdots \\ Y_{C_{N:}} \end{array} \right] \Sigma_{\bar{\mathbf{f}}} \left[\begin{array}{cccc} Y_{C_{1:}}^T & Y_{C_{2:}}^T & \cdots & Y_{C_{N:}}^T \end{array} \right] \quad (6.70)$$

or more compactly as,

$$\Sigma_{\mathbf{v}} = \mathbf{Y}_{\mathbf{C}} \Sigma_{\bar{\mathbf{f}}} \mathbf{Y}_{\mathbf{C}}^{\mathbf{T}}. \quad (6.71)$$

Equation 6.71 states that the uncertainty in the blocked force is propagated through a forward prediction and onto the response by pre- and post-multiplying the blocked force variance-covariance matrix with the appropriate mobility matrix, and its transpose.

It is important here to acknowledge that the mobility and blocked force are complex quantities. Whilst the concepts of uncertainty may readily be extended to complex variables there does not appear to be an agreed upon approach to dealing with them. Voormeeren et al.[148] dealt with the propagation of complex uncertainty through a dynamic sub-structuring procedure by separating the real and imaginary components using the matrix notation for a complex variables and propagating each separately. Others have considered the separation of real and imaginary components in such a way that the uncertainty of a complex variable is represented in terms of a real/imaginary variance-covariance matrix [149–151]. Perhaps the simplest approach is to simply follow the conventional definition of the covariance matrix of a complex random vector as,

$$\Sigma_{\bar{\mathbf{f}}} = E[(\bar{\mathbf{f}}_{\mathbf{S}} - E[\bar{\mathbf{f}}_{\mathbf{S}}])(\bar{\mathbf{f}}_{\mathbf{S}} - E[\bar{\mathbf{f}}_{\mathbf{S}}])^{\dagger}] \quad (6.72)$$

where \dagger represents the conjugate transpose. Such a definition yields a complex variance-covariance matrix which can subsequently be propagated without the need to separate the real and imaginary components.

6.4 EXPERIMENTAL VALIDATION

In what follows, the in-situ blocked force method outlined in Section 6.2 is used to independently characterise the four footed electric pump shown Figure 6.4a. This pump represents a realistic source that might be encountered in a practical scenario, and will be used later as part of the experimental case studies presented in Chapter 7 and Appendix E. Alongside its characterisation, the methods introduced through Section 6.3 will be employed in order to access the uncertainties involved in the acquired blocked forces. It is worth reminding the reader, however, that this Chapter is not concerned with a detailed analysis of the source in question. Instead, the aim is to demonstrate the *application* of the proposed methods.

Tag	Type	Assembly Details
K	EpI(4)P	Electric pump, perspex plate ($34.5\text{cm} \times 50\text{cm} \times 1\text{cm}$), resilient element model number: Fibet 1413vv10 60 IRHD
L	EpI(4)P	Electric pump, perspex plate ($50\text{cm} \times 75\text{cm} \times 0.7\text{cm}$), resilient element model number: Fibet 1413vv10 45 IRHD

Table 6.1: Details on the construction of experimental assemblies.

Here we will consider only resiliently mounted assemblies. Such assembly types are largely encountered in practise and are in keeping with the work presented through Chapters 3 and 5. Details of the assemblies used in this Chapter are presented in Table 6.1.

In what follows, assembly **K** will be used to characterise the electric pump and illustrate the implementation of the on-board validation and artificial excitation techniques. Assembly **L** will subsequently be used as part of a transferability validation.

6.4.1 RESILIENTLY COUPLED SOURCE AND RECEIVER

The resiliently coupled assemblies considered here consist of a source pump coupled to a receiver plate via 4 small rubber isolators. Two coupled assemblies are considered, **K** and **L**. Each was constructed using different resilient couplings and receiver sub-structures, details of which are presented in Table 6.1. Prior to construction the source was instrumented with 4 single axis accelerometers (B&K Type 4507 B 004), one at each coupling contact, as demonstrated in Figure 6.4b. The source, receiver and coupling elements were adhered together using an industrial strength glue. Due to spatial and instrumental limitations, only out-of-plane z coordinate DoFs were considered. The source accelerometers were kept on throughout the testing of each assembly to avoid error in sensor replacement.

Let us first consider assembly **K**. As per Section 6.2.3, the first step in determining the blocked force is the measurement of the assembly's passive properties, i.e. its mobility. The resilient nature of the assembly considered meant that access to the source-isolator interface was limited. It was therefore not possible to apply a direct excitation at the source-mount interface. As such, the remote blocked force relation of Equation 6.23 was used. In order to provide a sufficient over-determination,

12 remote accelerometers were adhered to the receiver sub-structure. Four of these were mounted directly below the mount-receiver interface, i.e. as close to the source-isolator interface as possible. The remaining 8 were spaced randomly (whilst allowing easy access) across the receiver plate. The importance of correct positioning with regards to the remote measurement DoFs cannot be understated.

The ability to provide a reliable excitation, i.e. without restricted access, is crucial in the minimisation of error and the successful determination of blocked forces, as is choosing locations where a good coherence is achieved. Failure to do so may see the measured mobility matrix populated with poor data, leading to ill-conditioning and the introduction of unwanted inversion error.

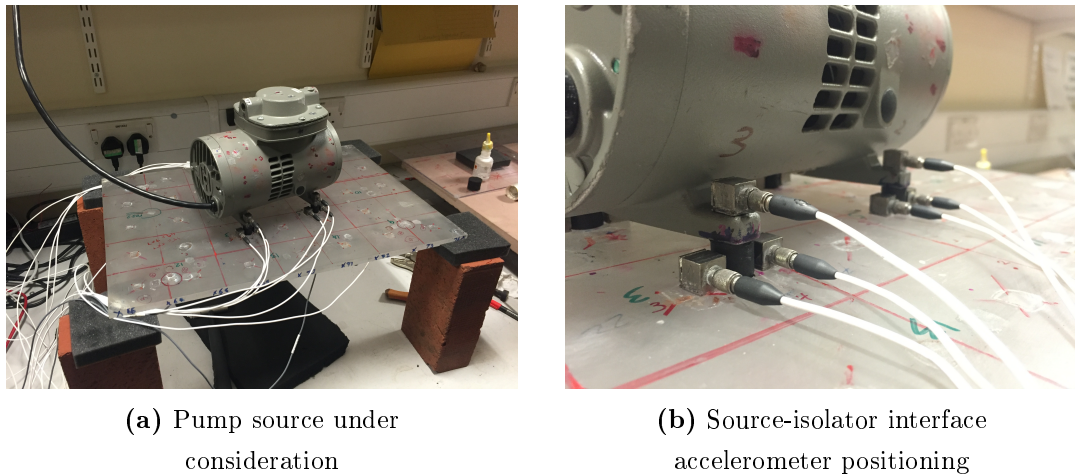


Figure 6.4: Photos of source and sensor positioning used throughout Chapter 6.

Together, the 12 remote DoFs allowed for an almost 3 fold over-determination of the blocked forces, whilst also providing the opportunity to carry out an on-board validation (the 12th accelerometer is not included in the determination of the blocked forces, and instead used as a remote reference). Using the sample space approach, we were able to acquire 330 determined solutions, from which the expected blocked force vector and its associated variance-covariance matrix were computed.

6.4.1.1 ARTIFICIAL EXCITATION

We will begin by considering the artificial excitation of assembly \mathbf{K} , as discussed in Section 6.3.1.1. Here, the measurement procedure may be outlined as follows. The transfer mobility matrix, $\mathbf{Y}_{\mathbf{C}_{1b}}$, was measured by exciting each remote receiver DoF, b_i , with an instrumented force hammer whilst simultaneously measuring the

resultant velocity response at the source-isolator contact interface, c_1 . This constitutes the passive part of the procedure. Following this, the source sub-structure was impacted with a hammer in the vertical z DoF, somewhere relatively central on the structure. This impact acts as an artificial excitation. The resultant velocities at b , \mathbf{v}_{C_b} , were measured. This constitutes the active portion of the procedure. It should be noted that the measurement procedure was carried out across all 12 remote DoFs, that is, including the remote reference. This allows us to later perform an on-board validation.

When dealing with an artificial excitation, as opposed to an operation excitation, only a single time window is needed to capture the required velocities. As such, the phase referenced velocity vector may be constructed via the cross-spectrum phase approach (see in Section 6.2.3.2) with no loss of information.

BLOCKED FORCES AND STANDARD DEVIATIONS - Once measured, the transfer mobility matrix and the corresponding operational velocity vector were used to calculate the blocked forces via the approaches presented above, that is; through a determined, over-determined, or sample space approach. In the determined approach, the 4 remote DoFs located at the isolator-receiver contact interface were used. These DoFs were the closest to the source-isolator interface and provided the best level of coherence. The over-determined and sample space approaches used 11 of the 12 remote DoFs, leaving one for the on-board validation.

Shown in Figure 6.5 are the contact interface blocked forces measured on assembly **K**, and determined via each of the above approaches. Although not particularly useful when displayed on their own, a number of observations can be made. Firstly, it can be seen that the expected blocked forces determined via the sample space approach are in excellent agreement with those acquired via the over-determined inverse. This in-itself shows that the sample space approach is capable of providing a suitable blocked force and, furthermore, suggests that its associated variance-covariance matrix will likely be representative of uncertainties associated with the correct blocked force. The blocked forces obtained via the determined approach are in reasonable agreement with those described above, although a number of large deviations can be observed, particularly between 90-250Hz. At this point, however, we are unable to state which approach provides the most representative blocked force (without some form of validation). That said, their agreement does suggest that the expected and over-determined blocked forces are likely to be the most representative.

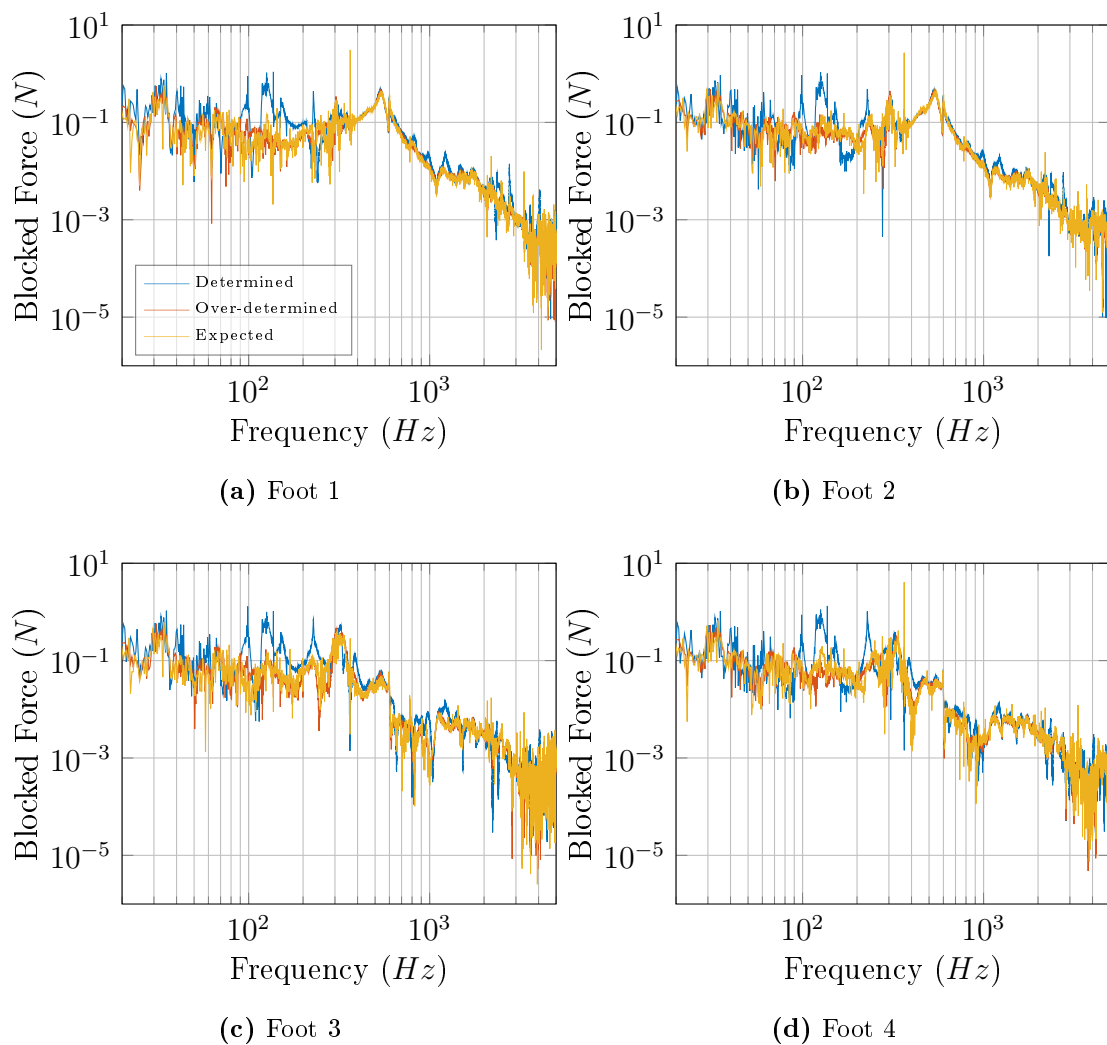
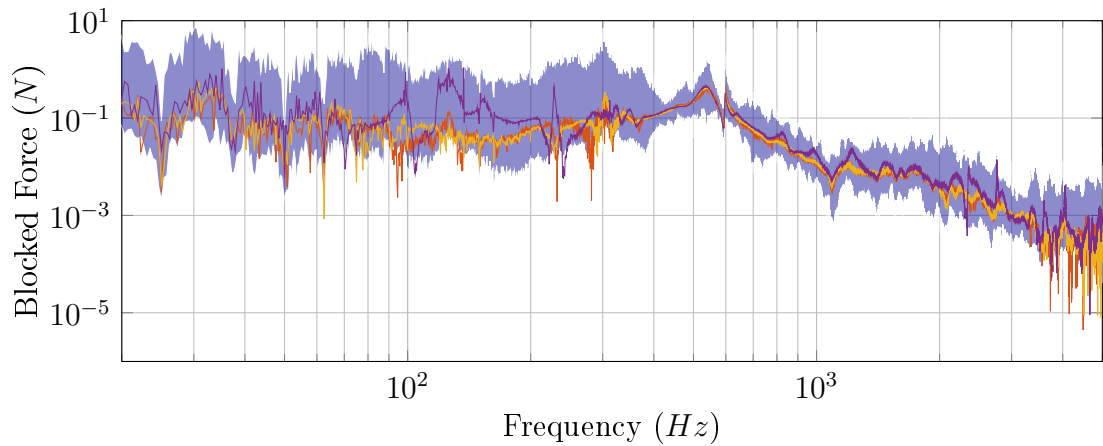


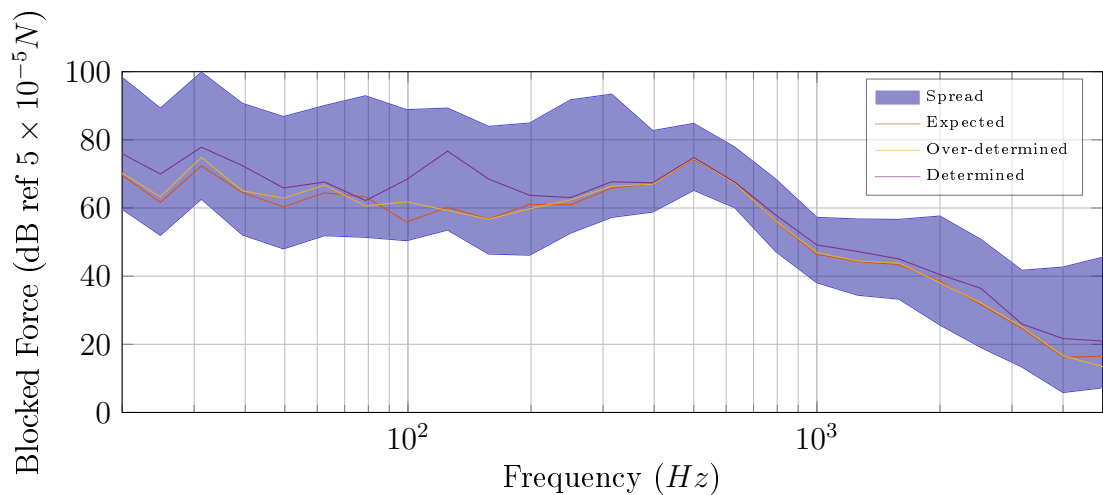
Figure 6.5: Determined, over-determined and expected blocked forces for feet 1-4 of assembly **K**.

Shown in Figure 6.6 is an expected blocked force determined via the sample space approach for a single foot of the pump, alongside the spread of blocked forces used in its calculation. This spread illustrates the variation one may expect by using different remote DoFs in the determination of blocked forces. Also shown is the blocked force acquired via a single over-determined and determined solution. The agreement between the expected and over-determined blocked force is illustrated further here. This suggests that the spread of blocked force sample space has some statistical relevance. It is argued that this spread is due to the uncertainties arising from neglected DoFs and experimental error, and that a statistical description of it may be used to estimate the uncertainties in the acquired blocked force.

Closer inspection of the expected blocked forces presented in Figure 6.5 reveal a number of spurious peaks that are clearly not properties of the source (or the artificial excitation), for example in Figures 6.5a, 6.5b and 6.5d at approximately 350Hz. This error is likely the result of a determined solution being ill-conditioned, and therefore severely affected by inversion error. These ill-conditioned solutions may be easily identified by looking at the distribution of blocked forces determined via each DoF combination at the problem frequency.



(a) Narrow band



(b) 3rd octave band

Figure 6.6: Spread in blocked force sample space for one foot of the pump using artificial excitation. Also shown, the expected, over-determined and determined blocked force.

Shown in Figure 6.7 are the determined blocked forces for each combination of remote DoFs. Blocked forces are presented at 3 frequencies where an error can be easily identified; 144Hz, 365Hz, and 2191Hz. One can clearly see that in each case a

particular combination yields an unusually large blocked force. These blocked forces are clearly erroneous and should therefore not be included in any further processing. These outliers may be removed individually by hand or, alternatively, by using the trimmed mean as opposed to the standard expected value. The trimmed mean yields the expected value of a given central portion of a distribution and may be used to effectively remove outliers.

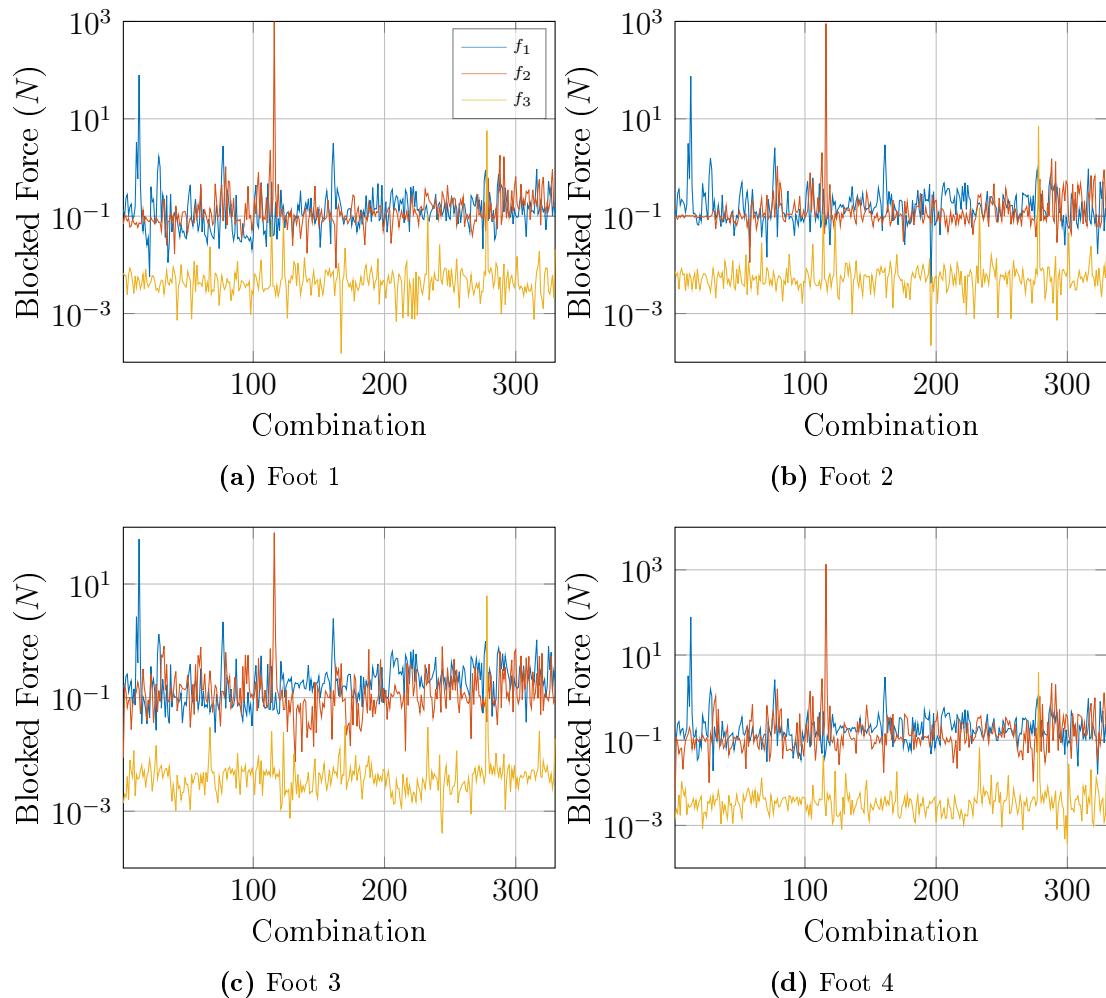


Figure 6.7: Determined forces from assembly **H** for each DoF combination used in the sample space approach, where the frequencies shown are $f_1 \approx 144\text{Hz}$, $f_2 \approx 365\text{Hz}$, and $f_3 \approx 2191\text{Hz}$.

Doing so for the central 99.4% of the blocked force distribution at each foot (for the 330 combinations used this amounts to the removal of the largest single outlier at any given frequency) yields the expected blocked forces presented in Figure 6.8. Inspection of Figure 6.8 clearly shows that the spurious peaks observed in Figure 6.5 have been successfully removed with no worsening of the overall agreement.

Using the trimmed distribution we compute the corresponding variance-covariance matrix from which we are able to calculate a number of different uncertainty parameters. Here, in addition to the standard deviation, we will also consider the standard error of the mean (SEM) and the coefficient of variation (C_v). The SEM, also known as the standard error, describes the variation of the expected value when determined from different portions of a sample space and gives an idea of its reliability. The C_v , also known as the relative standard deviation, describes the dispersion of a distribution relative to its mean value. Together the SEM and C_v can be used to provide a clearer picture of the uncertainties involved.

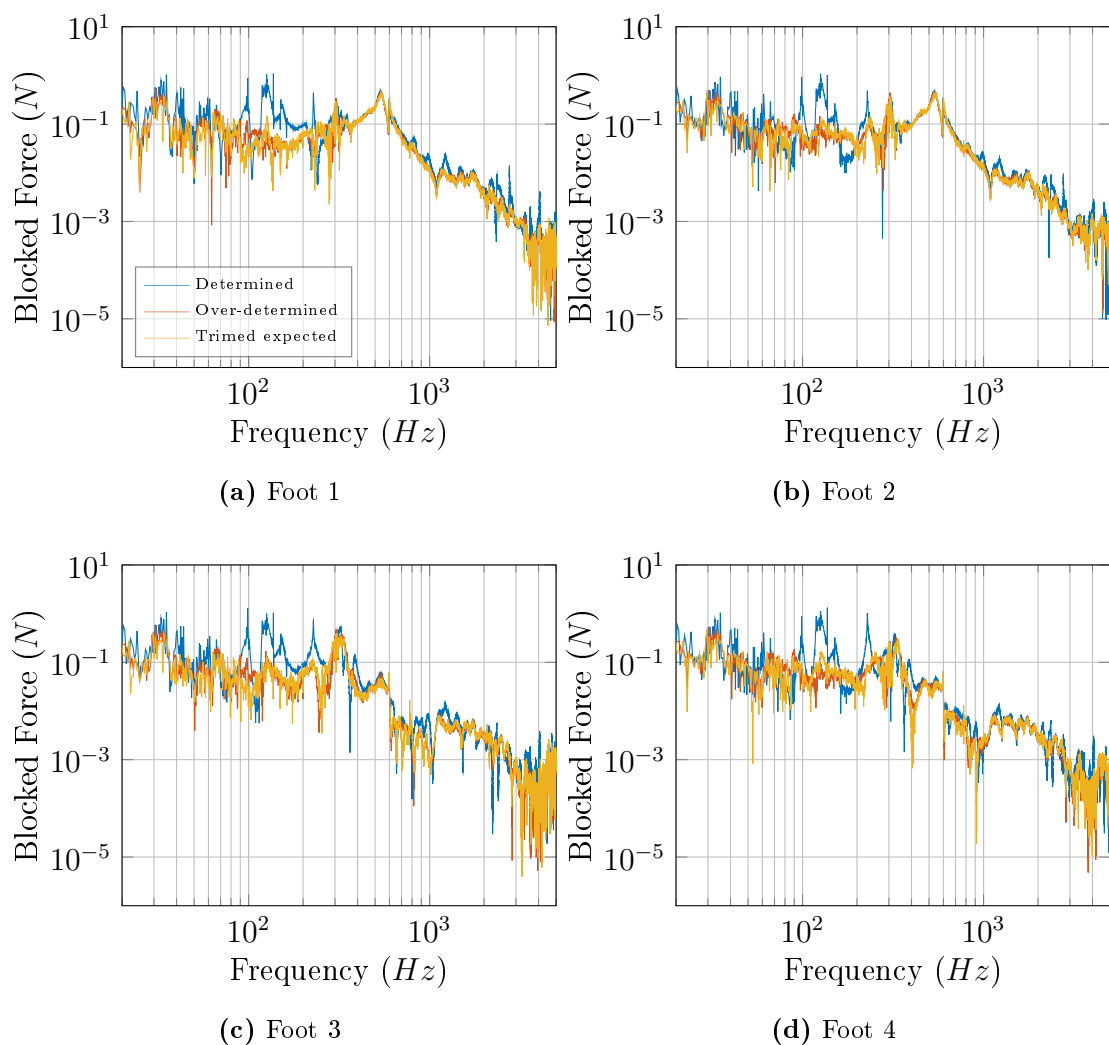


Figure 6.8: Determined, over-determined and trimmed expected blocked forces for feet 1-4 of assembly **H**.

Shown in Figure 6.9 is the expected blocked force at foot 1 determined from the trimmed distribution. Also shown are the \pm trimmed SEM and standard deviation.

As we are not interested in a detailed analysis of the source in question, for clarity we will consider only the results obtained at one foot.

Figure 6.9 illustrates a problem that often occurs when attempting to present the uncertainties of narrow band data in natural units on a loglog scale. When subtracting a particular measure of uncertainty from the mean value (for example standard deviation) one finds themselves computing negative values. Such values can not be represented on a loglog scale, and therefore lead to dropouts in the uncertainty plots, as demonstrated by the lower bound of the standard deviation. It is for this reason that we are interested in an alternative approach for presenting and analysing uncertainties in narrow band data.

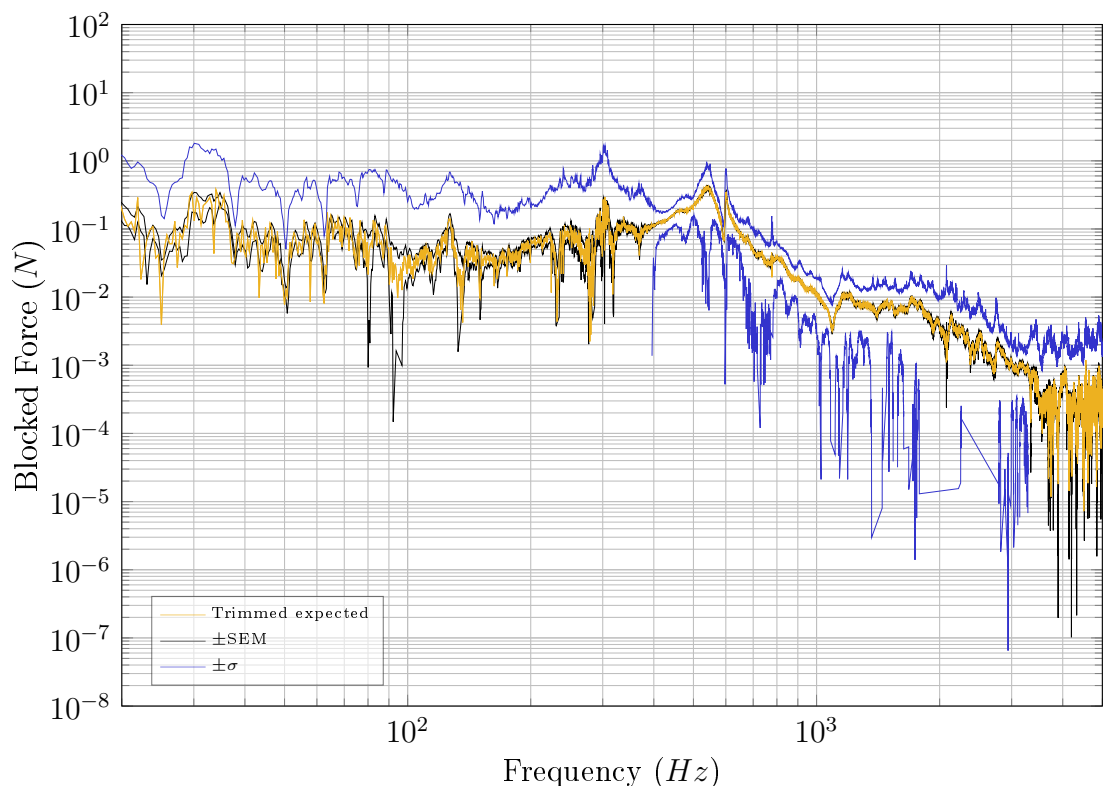


Figure 6.9: Trimmed expected blocked force at foot 1 with \pm the trimmed standard error of the mean. The \pm SEM plot has been passed through a 3 point moving average filter so as to improve clarity.

When considering the standard deviation, what we are really concerned with is its value relative to that of the mean. As such, it would make little sense to present the standard deviation alone. Instead we may use the coefficient of variation (C_v), where a relative measure of the standard deviation is acquired. Shown in Figure 6.10 are the C_v s of each blocked force acquired from the trimmed distribution.

The advantage of each presentation is hopefully illustrated here. The \pm standard deviation allows for the relative importance of uncertainties with regards to frequency to be identified. For example, a large standard deviation about a small expected value is not as much of a concern as a large standard deviation about a large expected value. The standard deviation, however, does suffer from dropouts in the lower bound, making it hard to interpret the general trend of the uncertainties. The C_v provides a clearer picture of the error relative to the mean, albeit with the loss of some information. Together, however, the standard deviation and the C_v offer a relatively complete picture of the uncertainties associated with the blocked forces.

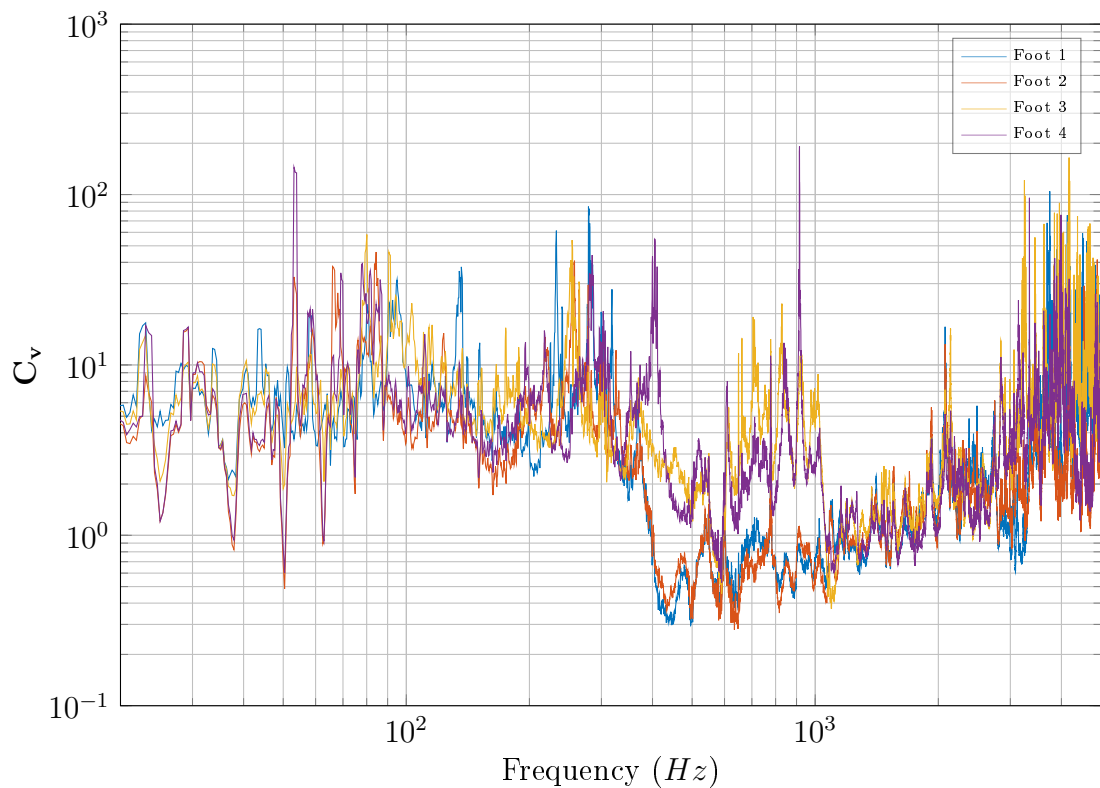


Figure 6.10: Coefficient of variation for the blocked force at foot 1 determined using the trimmed standard deviation and mean.

Let us now consider the uncertainties determined from the source in question. Firstly, from Figure 6.9 it can be seen that the expected value is bounded by a narrow SEM across the majority of the frequency range. This suggests that we have a reasonable degree of confidence in the value of the expected blocked force. Secondly, it can be seen from the upper bound of the standard deviation that the level of uncertainty at high frequencies is less of a concern than in the mid to low frequency range where the expected value is orders of magnitude higher. However,

the way in which this uncertainty propagates has not yet been investigated. The C_v s shown in Figure 6.10 clearly highlight the dependence of uncertainty upon both frequency and position. It can be seen that foot 1 and 2 exhibit a large drop in the C_v about 400Hz, beyond which it gradually begins to increase again. Foot 3 and 4 however remain large until approximately 1kHz, where they subsequently fall into agreement with that of foot 1 and 2. This suggests a greater level of mid-frequency uncertainty in the blocked forces associated with foot 3 and 4, than 1 and 2.

Again, it is important to note that the aim here was not to preform a detailed analysis of the source, but instead, to provide an example of the uncertainty parameters we are able to determine via the sample space approach.

ON-BOARD VALIDATION - Having determined the blocked force resulting from an artificial excitation, let us now consider its on-board validation.

Shown in Figure 6.11 are the results obtained from the on-board validation of assembly **K**. A prediction was made using each of the blocked force approaches presented in Figure 6.8. Although a reasonable agreement is achieved, the determined prediction (orange) is clearly contaminated by the deviations previously observed in the blocked forces. The over-determined (yellow) and expected (purple) predictions avoid these artefacts and provide a good level of agreement with the directly measured velocity response (blue). However, some disagreement can be observed, particularly at the anti-resonant region around approximately 600Hz, and at higher frequencies above approximately 2-3kHz.

Beyond 2-3kHz agreement between the predicted and measured responses, although following the general trend, can be seen to worsen. A likely cause of this error lies in the transfer mobilities used in the prediction of the blocked forces which, from Figure 6.12a, can be seen to deteriorate at high frequencies. This deterioration is further illustrated by a poor level of coherence, as shown in Figure 6.12b. This is likely due to the deterioration of the input force when propagated through the resilient mounts, similar to the high frequency error encountered in the characterisation of resilient elements (see Chapter 3). That said, with the velocity's relatively low level this error may be considered less of a problem.

In the region of 600Hz the on-board validation can be seen to over-predict the measured response. This suggests that the error is unlikely a result of neglected DoFs, as this often manifests itself as an under-prediction. This would suggest that

the cause of error likely lies within the propagating transfer mobility, or the blocked forces themselves.

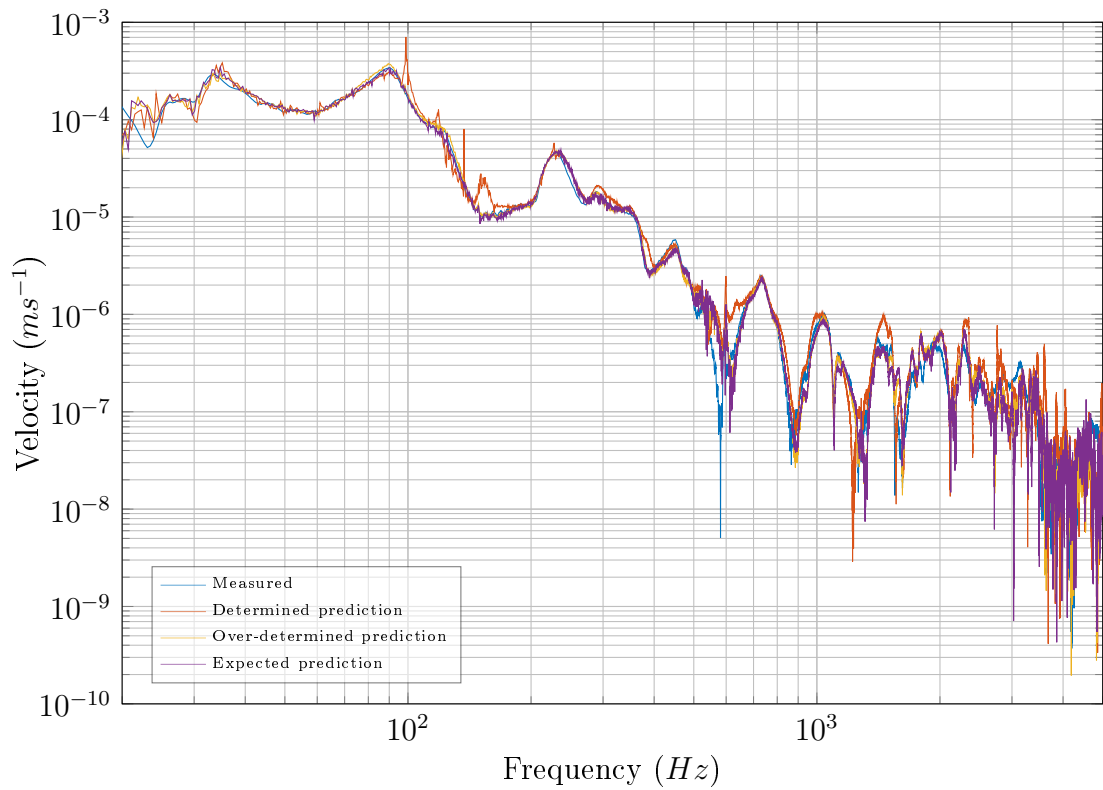


Figure 6.11: On-board validation on assembly **H** using an artificial excitation, using over-determined and expected blocked forces.

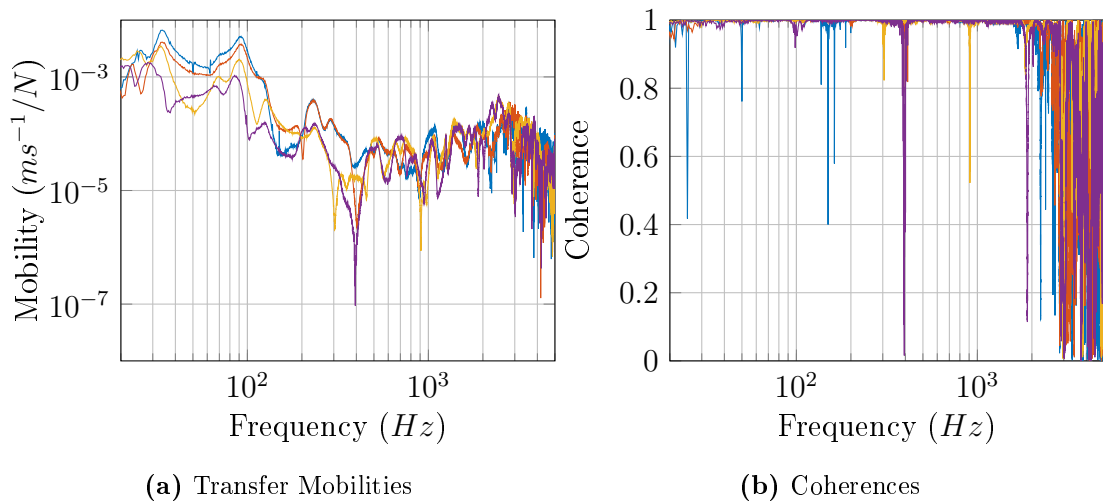


Figure 6.12: Transfer mobilities and corresponding coherences between the remote reference point and each foot of the source.

From Figure 6.12 it can be seen that the mobility appears well defined in the region of the error, with a coherence value of approximately 1. This suggests that the error is unlikely a result of the mobilities used in the prediction, and rather due to the blocked forces themselves. Referring back to Figure 6.8 it can be seen that the blocked force obtained in this frequency region also appears well defined, with a narrow SEM and low \mathbf{C}_v (see Figure 6.10). This suggests that the blocked forces have been determined with reasonable confidence.

In an attempt to further understand the cause of this disagreement, let us consider the propagation of uncertainties from the blocked forces to the velocity response. Pre- and post-multiplication of the covariance matrix by the propagating transfer mobility and its transpose yields the standard deviation in the predicted response.

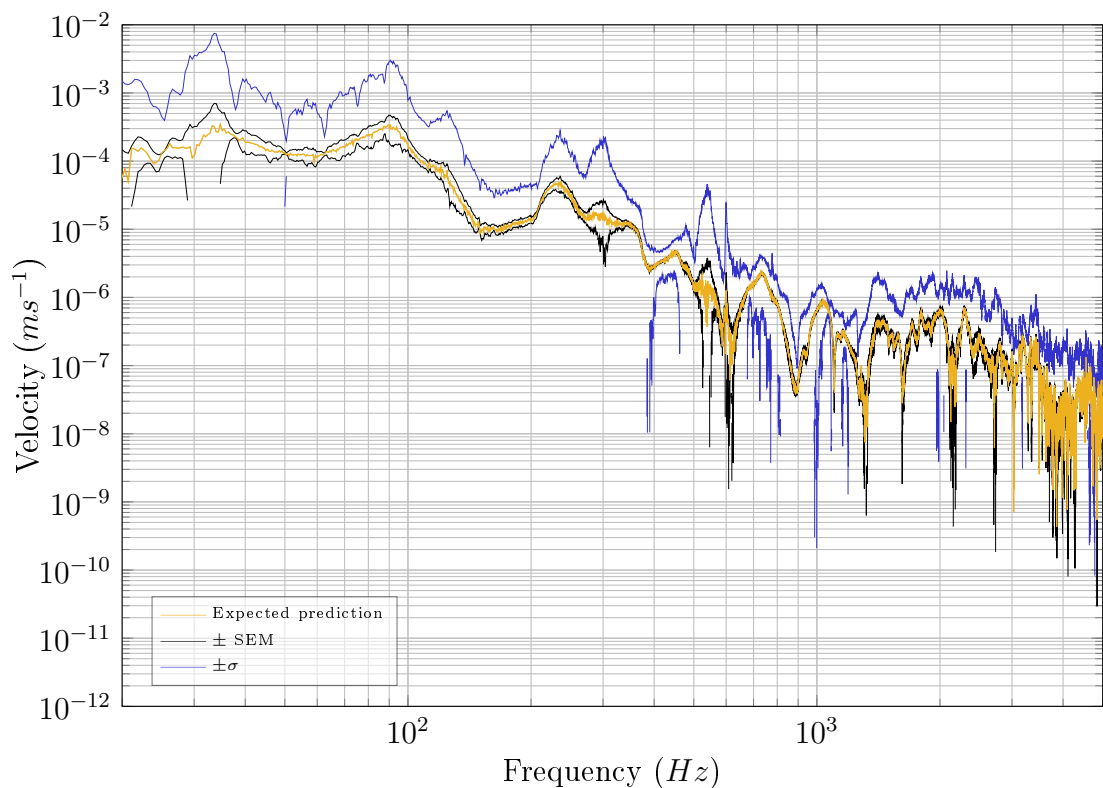


Figure 6.13: On-board validation using expected blocked force with propagated SEM. The \pm SEM plot has been passed through a 5 point moving average filter so as to improve clarity.

Shown in Figure 6.13 are the propagated \pm standard deviations and SEM for the on-board validation. As in Figure 6.9, we can see that the lower bound of the standard deviation suffers from severe dropouts, limiting its use. The upper bound, however, does appear to follow the trend of the expected value, suggesting that it has

been correctly propagated. Unlike the upper bound in Figure 6.9, the propagated standard deviation here appears further spread in the region of 600Hz. This spread is more clearly observed in the propagated \mathbf{C}_v , shown in Figure 6.14. A comparison of the blocked force \mathbf{C}_{vs} to that of the predicted response \mathbf{C}_v (we are able to do this as they are dimensionless quantities) shows that the propagation of uncertainties has negatively affected particular frequency regions more severely.

Below 400Hz the \mathbf{C}_{vs} are in reasonable agreement where, if anything, the \mathbf{C}_v has been decreased marginally. Above this, however, large deviations are observed. These deviations represent regions where propagation has had an adverse effect on the uncertainties. Comparison against Figure 6.9 shows that these deviations coincide with the anti-resonant regions of the predicted response, that is, where a poor prediction is obtained.

Figure 6.14 clearly demonstrates the advantage of the \mathbf{C}_v as an uncertainty parameter over the standard deviation as it allows us to directly compare the relative errors before and after propagation, owing to its dimensionless units.

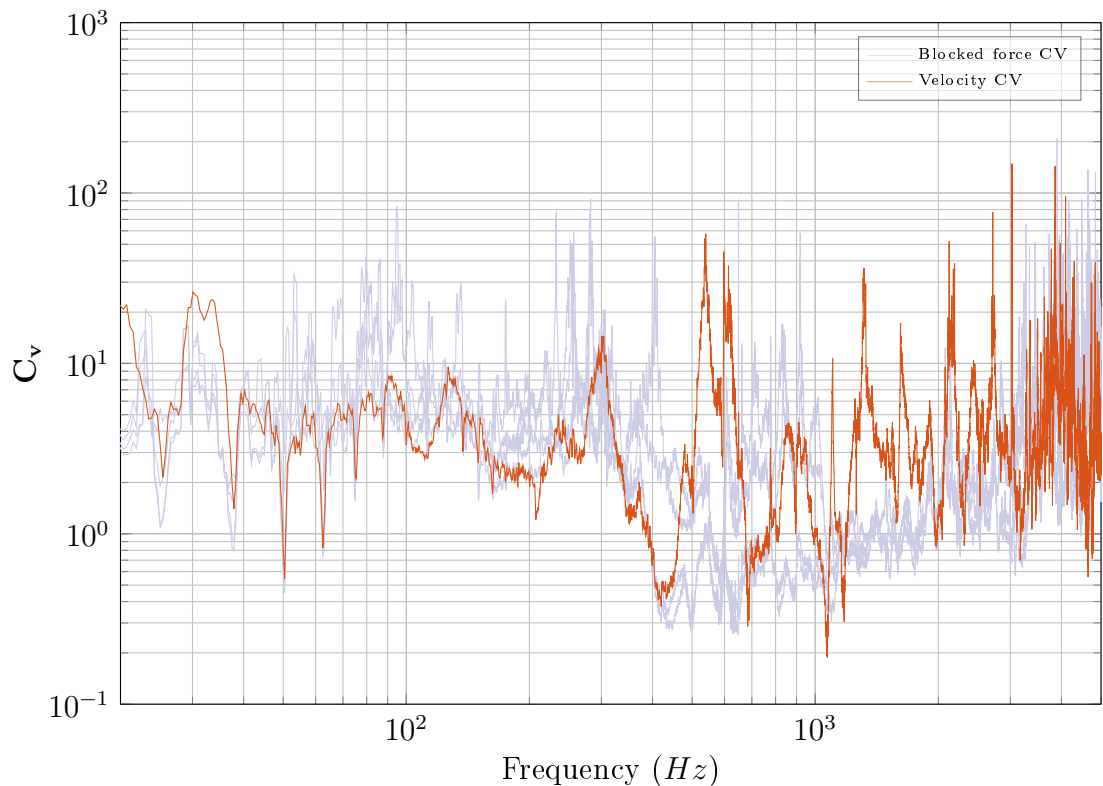


Figure 6.14: Coefficient of variation for each blocked force (grey) used in the on-board validation, and the predicted operational velocity of assembly \mathbf{K} (orange).

6.4.1.2 OPERATIONAL EXCITATION

Let us now consider the operational characterisation of the source. Having already preformed the passive part of the measurement procedure, i.e the measurement of the transfer mobility $\mathbf{Y}_{\mathbf{C}_{cb}}$, the operational velocity vector, $\mathbf{v}_{\mathbf{C}_b}$, was measured. Classically, operational measurements of this sort are done so using time averaged auto- and cross-spectra, as discussed in Section 6.2.3.2. However, to avoid the shortcomings of this approach, particularly those relevant to VAPs and auralisation, the operational velocity vector was constructed using the SFS approach, also outlined in Section 6.2.3.2. Doing so allows for the time domain reconstruction and subsequent auralisation of predictions to be performed at a later stage.

Operational velocities were recorded over a period of 30 seconds at a sample rate of 51200Hz. Using a 0% window overlap, with a 0.390625Hz frequency resolution, 30 individual time windows were acquired. Each time window was used to determine a separate blocked force vector. The SFS approach, whilst crucial in the successful reconstruction of time domain responses, complicates the presentation of data. A suitable presentation is obtained by taking the mean absolute value across all time windows, as opposed to presenting the blocked force for each time window independently. All results presented hereafter will be done so in this form, unless otherwise specified. Additionally, due to the tonal nature of the operational source, results will also be presented in 3rd octave-band dB form. However, it should be noted that the conversion to 3rd octave-bands is always performed at the latest possible stage prior to plotting, and that all calculations and predictions are performed using the complex narrow band Fourier spectra.

BLOCKED FORCES AND STANDARD DEVIATIONS - It was shown in the case of an artificial excitation that the over-determined and trimmed expected blocked forces provided the best on-board validation. As such, we have not considered the determined solution to the operational blocked forces here. In the case of the expected blocked force, the same trimmed distribution is used as in the artificial excitation, thus avoiding outliers in the blocked force distribution.

Presented in Figure 6.15 are the blocked forces determined from assembly \mathbf{K} , via the over-determined and sample space approaches, for an operational source. Shown in Figure 6.17, for clarity, are the blocked forces in 3rd octave-band form. It can be seen from both narrow band and 3rd octave-band results that the over-determined (blue) and expected (orange) blocked forces are in good agreement with one another,

further validating the sample space approach. Some differences in the level of the tonal peaks can be observed. These differences are also found in the 3rd octave band plots. Which of the two is likely to provide the best prediction is not clear and will require an on-board validation to be performed.

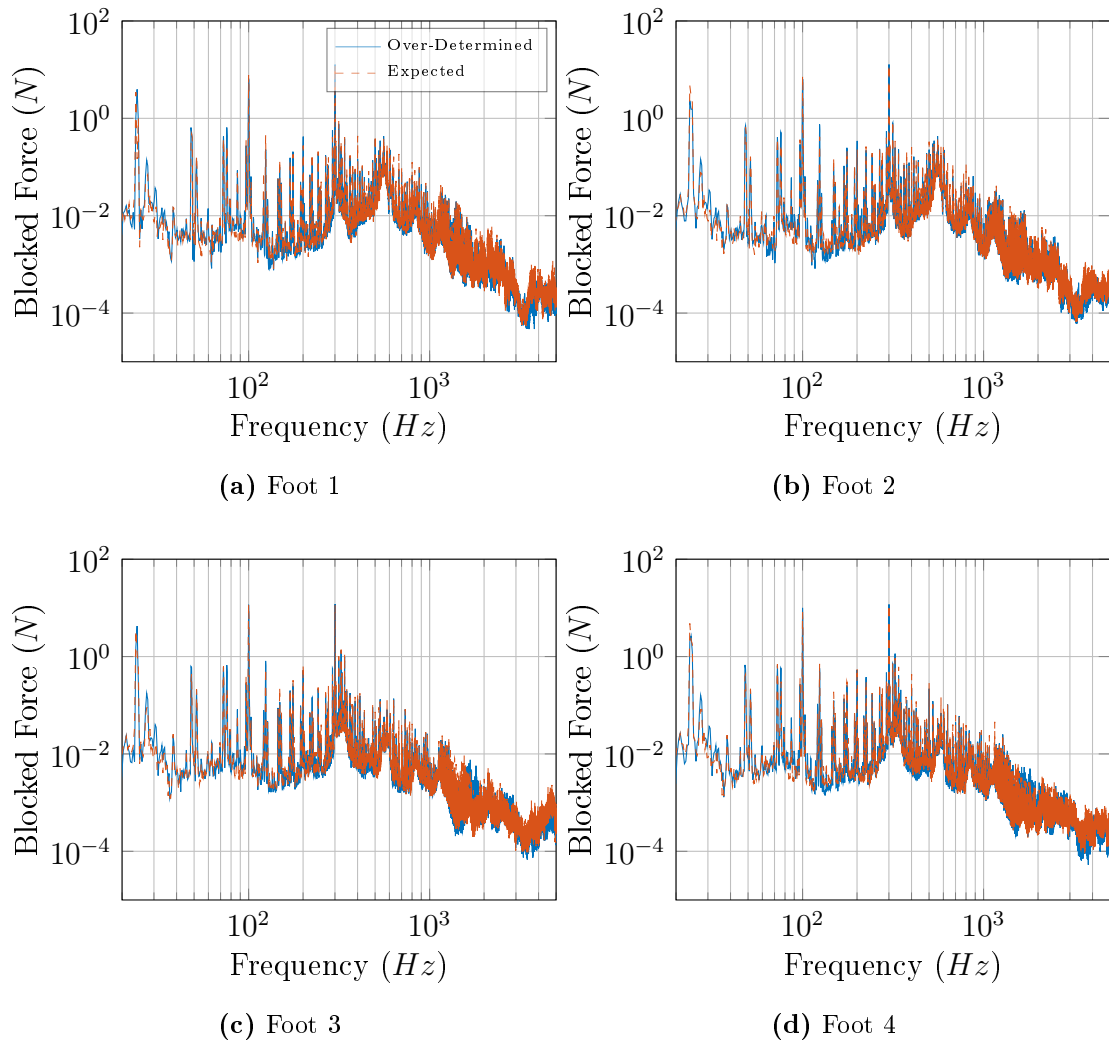
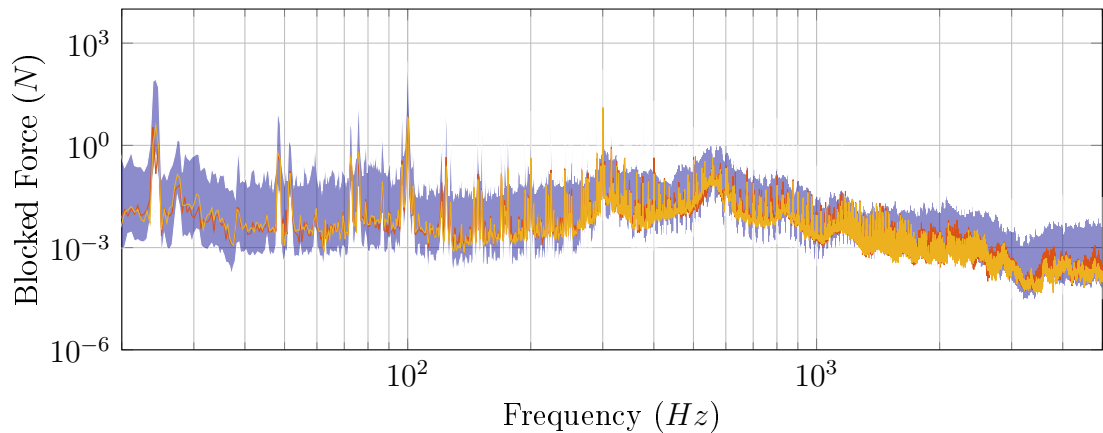


Figure 6.15: Over-determined and trimmed expected operational blocked forces for feet 1-4 of assembly **K**.

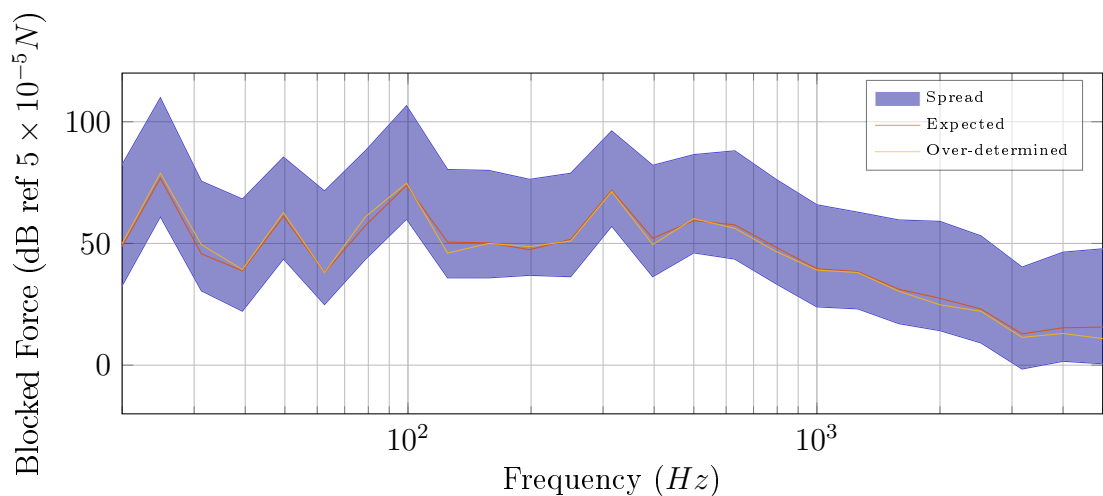
Like the artificial excitation, it is interesting to observe the spread of the determined blocked forces obtained via the sample space approach. This spread is shown in Figure 6.16 alongside the expected and over-determined blocked force for a single foot of the pump. Again, the agreement between the two approaches further suggests that the distribution of determined blocked force is likely of some statistical interest.

Like the artificial excitation, we are able to determine a number of uncertainty parameters from the blocked force distribution acquired via the sample space approach.

Unlike the artificial excitation, however, we now determine a blocked force distribution at each time window. It is therefore proposed, rather than consider each window independently and determine an uncertainty parameter for each, we instead include the distribution of each window in the estimation of a single variance-covariance matrix.



(a) Narrow band



(b) 3rd octave band

Figure 6.16: Spread in blocked force sample space for one foot of the pump using operational excitation. Also shown, the expected, over-determined and determined blocked force.

It is proposed that this variance-covariance matrix will, as a result, account for the uncertainties associated with any temporal variation that the source exhibits over the measurement period. For the case presented here, where 329 DoF combinations are used (accounting for the trimmed distribution), the total number of samples available over the 30 time windows is 9870. This approach not only has the advantage

that it includes temporal fluctuations in the uncertainty, but also provides a larger sample set and, with it, a more reliable variance-covariance matrix estimation. The expected blocked force, however, is determined separately for each window, thus retaining the ability to reconstruct the time domain response at a later stage.

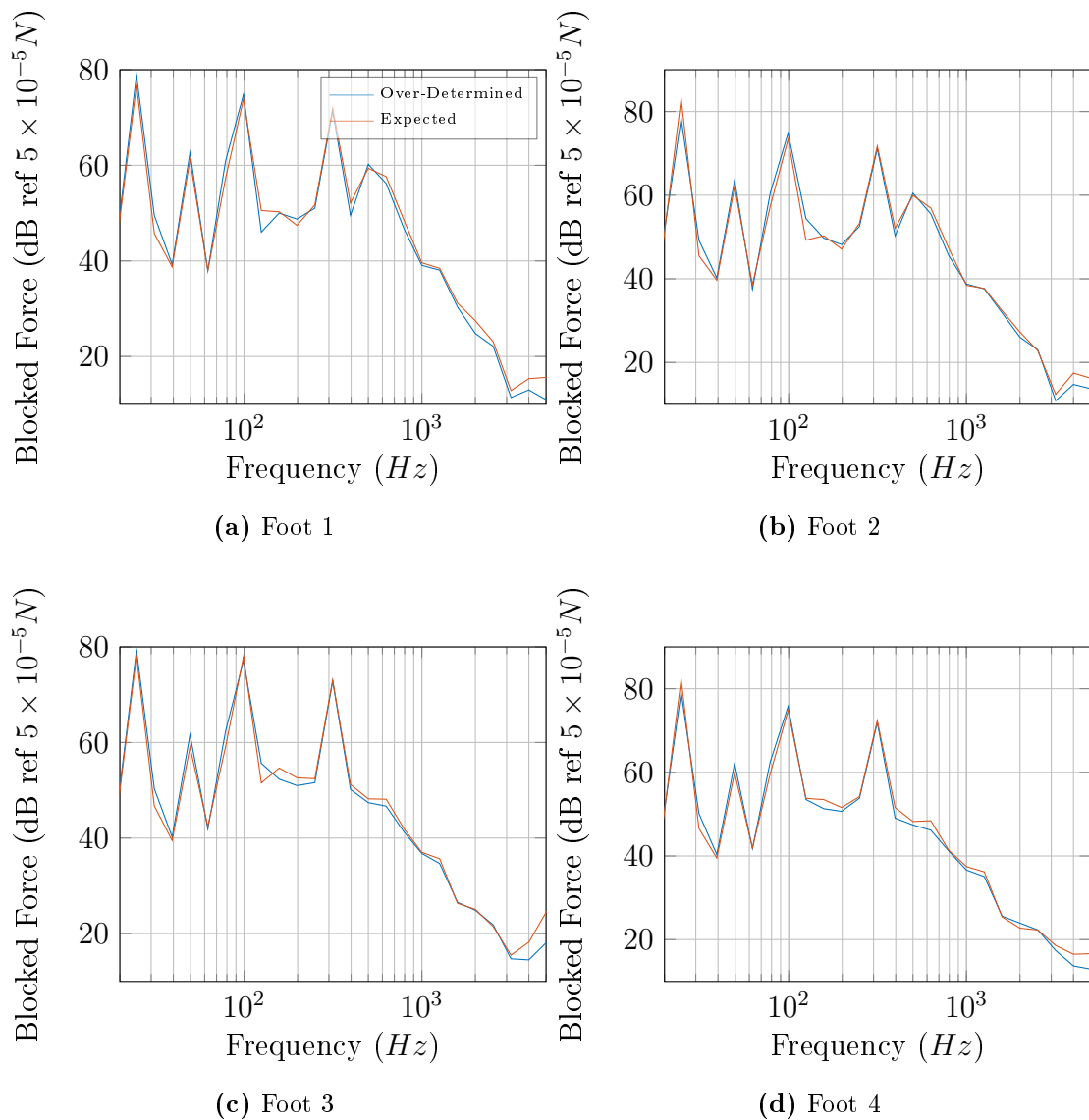


Figure 6.17: Over-determined and trimmed expected operational blocked forces for feet 1-4 of assembly **H** in 3rd octave-bands.

The uncertainties associated with the operational blocked forces are not presented. They will, however, be propagated and used to establish the uncertainties in an on-board validation.

ON-BOARD VALIDATION - Having determined the blocked forces we are now able to perform an on-board validation. Shown in Figures 6.18 and 6.19 are the results of the on-board validation results performed on assembly **K**, presented in narrow band and 3rd octave band, respectively. Let us first consider Figure 6.18. It can be seen that both the over-determined (orange) and expected (yellow) blocked force predictions are in good agreement with that of the directly measured response (blue) across the majority of the frequency range. The on-board validation appears to predict all significant peaks with reasonable accuracy, whilst following the general trend up to 5kHz. At high frequencies the tonal nature of the source leads to a very congested frequency response which can be hard to compare visually. This region is more easily assessed in 3rd octave bands, as in Figure 6.19.

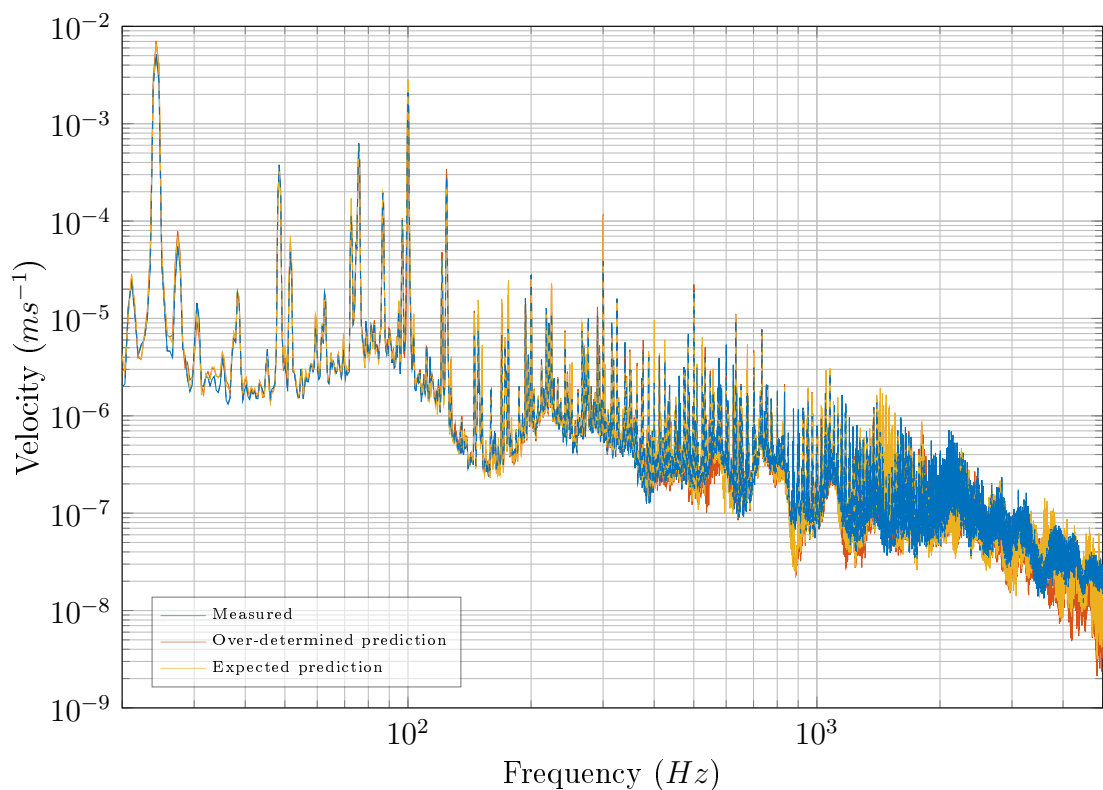


Figure 6.18: On-board validation on assembly **H** for over-determined and expected blocked forces.

Figure 6.19 more clearly displays the agreement between measured and predicted responses, particularly in the mid to high frequency region, where the tonal nature of the source makes narrow band comparisons challenging. Like the narrow band representation, it can be seen that the low frequency response (i.e. below 80Hz) is predicted with reasonable accuracy, deviating no more than 2dB. As the frequency

increases deviations become more apparent. The 3rd octave band peak at 100Hz can be seen to be over- and under-predicted by 4dB for both the expected and over-determined blocked forces, respectively. Above this, the two predictions deviate above and below the measured response by a few dB in roughly equal measures up to 5kHz. Although, it is worth noting that the deviations at high frequencies are less of a concern, as the low frequency response will likely dominate any eventual auralisation. Also shown in Figure 6.19 are the $\pm SEM$ and +95% confidence interval (i.e $\sigma \times 1.96$) for the expected response prediction. These were determined from the propagated blocked force covariance matrix.

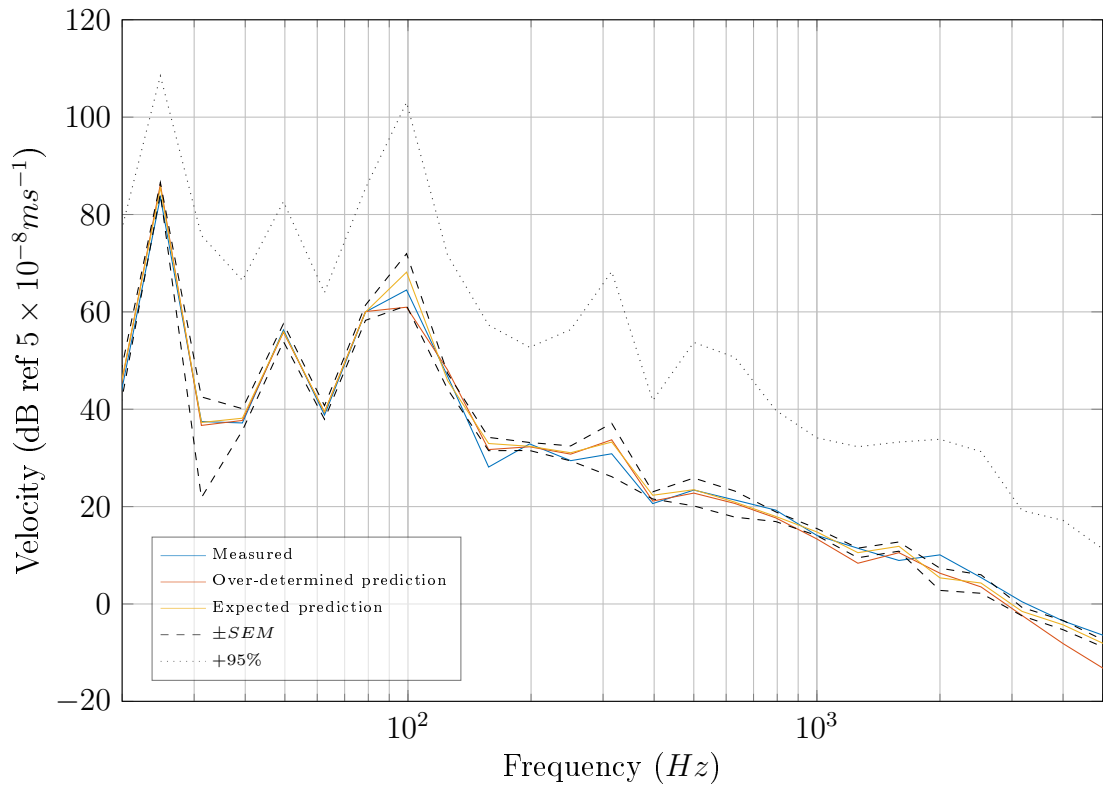


Figure 6.19: On-board validation on assembly **H** for over-determined and expected blocked forces in 3rd octave bands.

The uncertainty parameters can be seen to agree with many of the deviations in the expected prediction, particularly those at 100 and 315Hz. This suggests that the uncertainties acquired via the sample space approach may be used to estimate the uncertainty in a given prediction.

Also shown in Figure 6.20 are the 3rd octave $C_{\mathbf{v}s}$ for the blocked forces (grey) and the predicted response (orange). The $C_{\mathbf{v}s}$ clearly indicate regions where the blocked force uncertainties have been adversely affected by propagation. Many of

these regions can be seen to coincide with areas of disagreement in the on-board validation, for example those at 100, 315 and 2000Hz. Although clearly not an in-depth analysis, the above demonstrates the potential of the sample space approach and the uncertainties it provides.

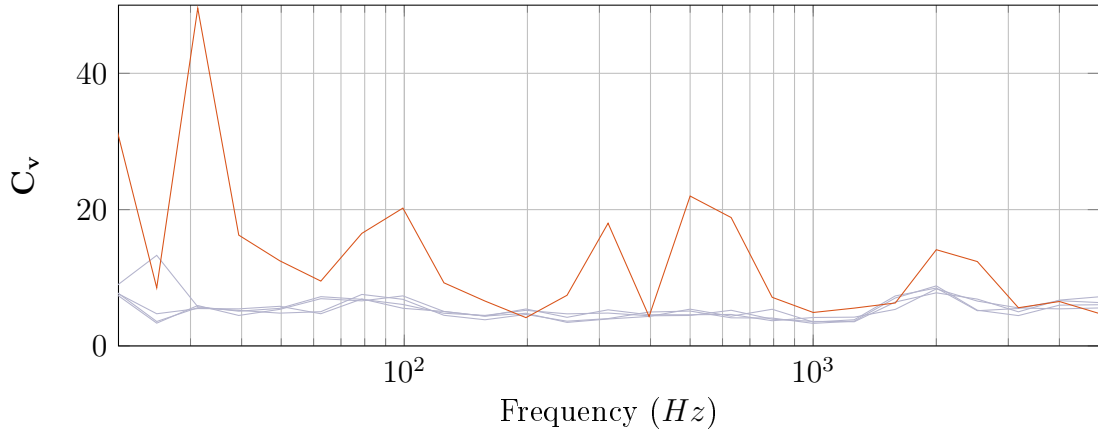


Figure 6.20: Coefficient of variation for each blocked force (grey) and the resultant prediction on assembly **H** (orange), in 3rd octave bands.

TRANSFERABILITY VALIDATION - Having preformed an on-board validation, one may now carry out a transferability validation. This was done by removing the source from its initial assembly (i.e. the one in which it was characterised) and installing it in another. It is important that the assembly to which the source is transferred is representative of the initial assembly and the eventual installation, i.e. resilient to resilient or rigid to rigid. Here, the source was transferred to another resiliently mounted assembly, **L**, details of which are presented in Table 6.1. Once installed, the transfer mobility between a remote reference DoF on the receiver sub-structure and the source-isolator interface was measured. This mobility was multiplied by the blocked force of each time window to yield an operational prediction. The source was then operated and the operation response of the assembly measured at the same remote reference DoF, allowing for a comparison to be made.

Shown in Figures 6.21 and 6.22 are the transferability validation results for narrow band and 3rd octave band, respectively. Let us first consider Figure 6.21. A reasonable agreement is obtained between the two predictions and the directly measured response. Most low frequency tonal peaks are predicted with reasonable accuracy, those at higher frequencies less so. The general trend, however, is predicted in both

over-determined (orange) and expected (yellow) cases. The two predictions themselves are in good agreement with one another across the entire frequency range, making it a challenge to access the superiority of either approach.

Shown in Figure 6.22 are the 3rd octave band transferability validations, alongside the propagated \pm SEM and $+95\%$ confidence interval associated with the expected response prediction. Here the disagreement between the predictions and measured response is more clear. Although there is a strong agreement in the first 3rd octave peak, above this the predictions begin to deviate above and below the measured response by varying amounts up to 5kHz.

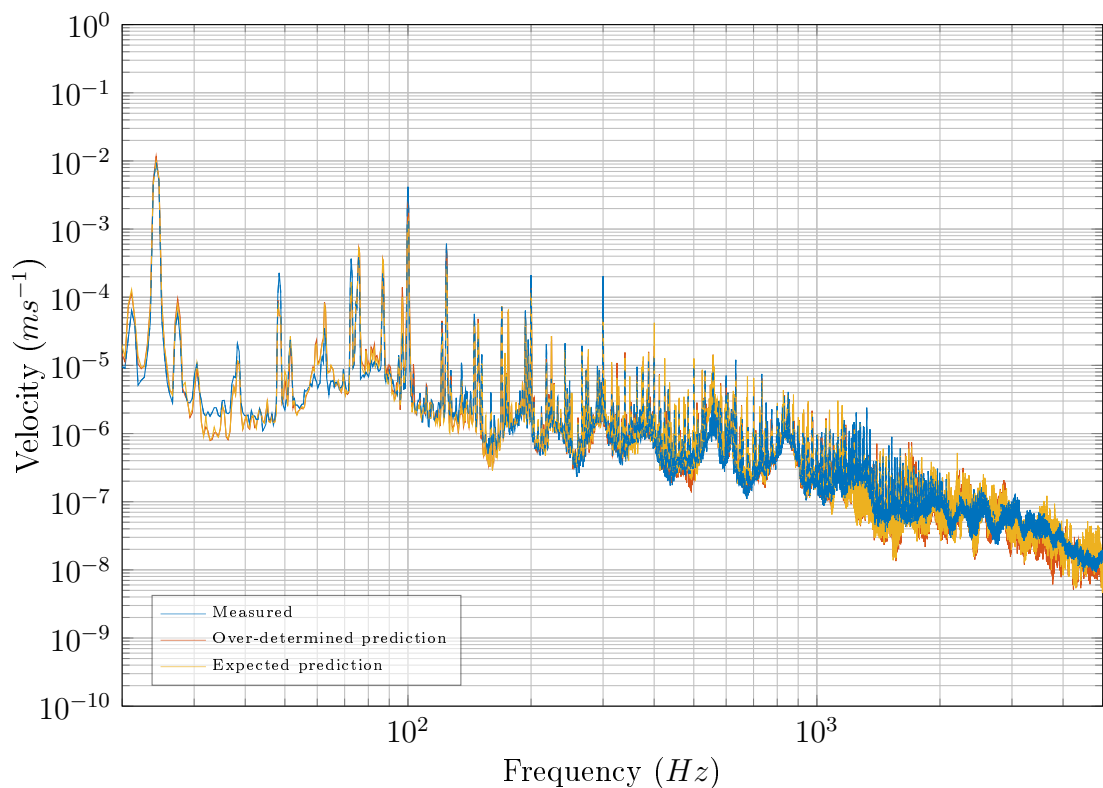


Figure 6.21: Transferability validation using an artificial excitation, using over-determined and expected blocked forces.

With the exception of the 100Hz 3rd octave peak the two predictions are in good agreement. At the 100Hz peak, the over-determined prediction can be seen to under-predict the measured response by 3dB, and the expected prediction by a further 4dB.

Interestingly, as in the on-board validation, areas of significant under-prediction are highlighted by the uncertainty parameters, particularly those at 50, 100 and 315Hz. This suggests that some of the disagreement may be due to the uncertainties

associated with the blocked force. However, these errors may not be entirely due to the acquired blocked forces. Other contributing factors may include differences in the construction (i.e. source-isolator coupling), uncertainty in assembly **L**'s measured transfer mobility, or neglected DoFs having a greater influence on the transferred assembly. These errors are not accounted for by the sample space approach.

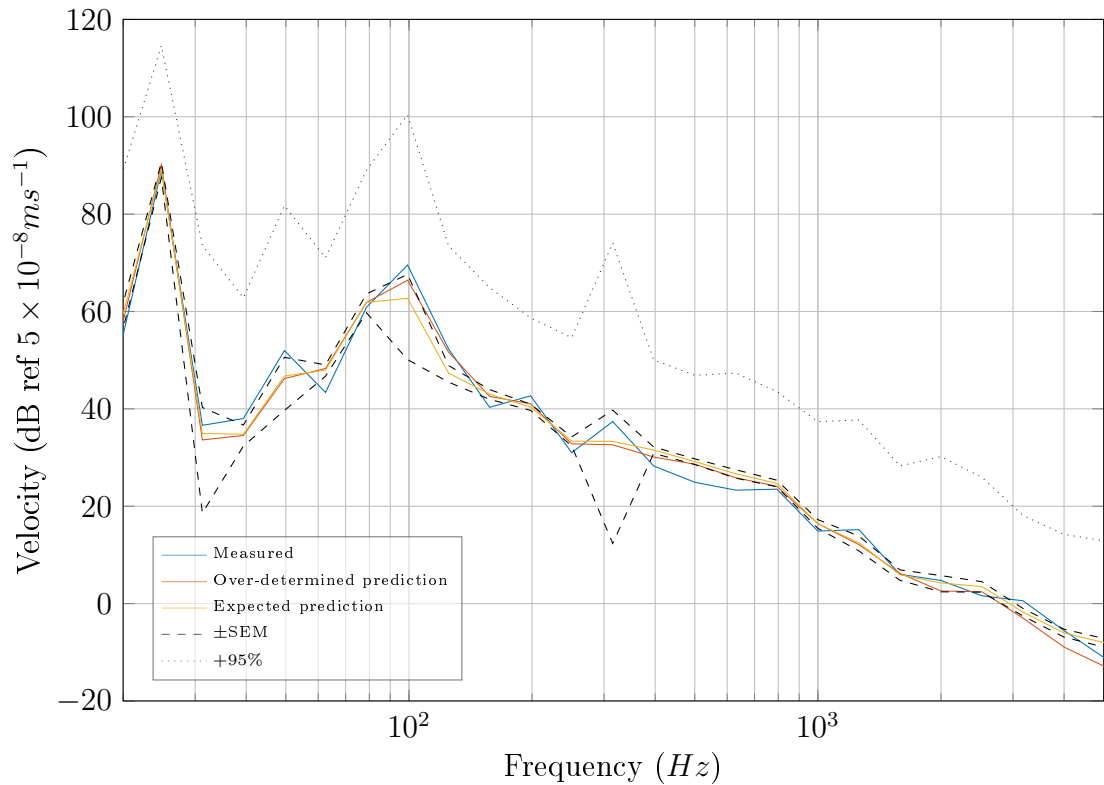


Figure 6.22: Transferability validation using an artificial excitation, using over-determined and expected blocked forces.

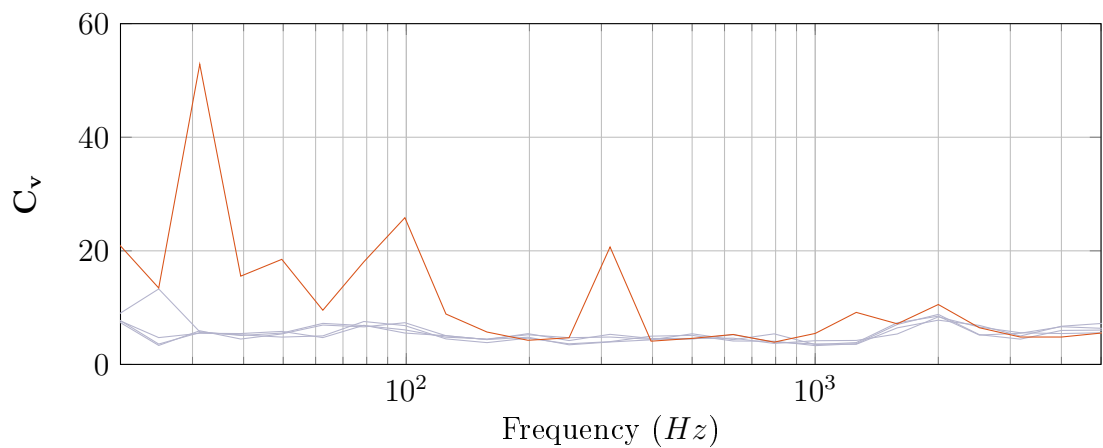


Figure 6.23: Coefficient of variation for each blocked force (grey) and the resultant prediction on assembly **I** (orange), in 3rd octave bands.

Lastly, shown in Figure 6.23 is the \mathbf{C}_v of each blocked force and the predicted response. Here, as in the on-board validation, it can be seen that the regions affected greatest by the propagation of uncertainty coincide with the areas of greatest disagreement in the transferability validation. This result further highlights the potential of the expected blocked force and its associated uncertainties.

6.5 CONCLUDING REMARKS

This Chapter was concerned with the blocked force as an independent characterisation for structural sources. Following its conceptual introduction, two alternative derivations were presented for the in-situ blocked force relation. The experimental implementation of this relation was subsequently discussed alongside some important considerations. Methods for accessing the uncertainty of blocked forces were later discussed and the well-established concepts of on-board and transferability validations introduced. A novel approach was subsequently proposed whereby expected blocked forces are acquired from a sample space of determined solutions. Referred to here as the sample space approach, the method facilitates the estimation of a variance-covariance matrix which is proposed to contain information regarding the uncertainties in the measured blocked force. It was later shown that the expected value obtained through the sample space approach was in excellent agreement with those obtained through an over-determined solution, and that outliers resulting from ill-conditioned solutions may be removed effectively using the trimmed mean. The law of error propagation was derived and subsequently used to propagate blocked force uncertainties through a prediction. These propagated uncertainties, presented in the form of standard errors and coefficients of variation, were shown to coincide with many of the deviations encountered in the on-board and transferability validation, suggesting that they contain statistically relevant information regarding the uncertainties of the blocked forces.

**PART IV. EXPERIMENTAL CASE
STUDY AND
CONCLUSIONS**

CASE STUDY

In this Chapter the methods introduced through Chapters 3 - 6, namely; the in-situ characterisation of resilient elements, the in-situ decoupling of source and receiver sub-structures, and the blocked force characterisation of source sub-structures, will be brought together. These methods will be used in conjunction with a dynamic sub-structuring procedure to build a VAP and predict its operational response.

CONTENTS

7.1	Building Blocks	179
7.2	Dynamic Sub-Structuring	180
7.3	Experimental Case Study	187
7.4	Concluding Remarks	209

7.1 BUILDING BLOCKS

In order to successfully construct a virtual acoustic prototype each assembly component must be independently characterised by some active and/or passive quantity. It is only with independently characterised components that a virtual assembly can be constructed in a physically meaningful way. The independent sub-structure quantities considered in this Thesis are outlined in Table 7.1.

The work presented in this Thesis so far has been focused on the development and implementation of independent characterisation methods for the attainment of the above quantities. In Chapter 3 an in-situ method was presented for the determination of the dynamic transfer impedance of coupling elements. In Chapter 5

an in-situ decoupling procedure was developed to acquire the free-interface mobilities of resiliently coupled source and receiver sub-structures. Lastly, in Chapter 6, the in-situ blocked force relation was introduced as a method for characterising the active properties of a source sub-structure. In this Chapter the above methods will be brought together and used in the construction of a VAP as part of an experimental case study.

Sub-Structure	Active	Passive
Source	Blocked force	Free-interface mobility
Resilient coupling	<i>N/A</i>	Dynamic transfer impedance
Receiver	<i>N/A</i>	Free-interface mobility/vibro-acoustic FRF

Table 7.1: Independent sub-structure quantities used in the construction of a VAP.

First, the concept of dynamic sub-structuring will be introduced and a particular formulation derived. Validation of the approach will be provided through a simple numerical model which will aid in demonstrating the implementation of the chosen procedure. Following this we will consider an experimental case study whereby an electric pump is resiliently coupled to a cavity backed plate.

7.2 DYNAMIC SUB-STRUCTURING

As discussed in Section 2.3, there exist a number of dynamic sub-structuring formulations that have been developed over the years. With advancements in data acquisition and computational power the importance of computationally simplistic algorithms has been reduced. As such, many of the arguments made for alternative formulations are no longer of importance. The approach adopted here is that of the classical impedance method, referred to by some as the primal impedance formulation [75]. In the following a brief summary of its derivation is given, alongside a simple numerical example whereby two free-free beams are rigidly coupled, end to end.

Let us start by considering the general system of equations that govern the motion of n uncoupled sub-structures. Written in block diagonal form we have,

$$[\mathbf{M}]\ddot{\mathbf{x}} + [\mathbf{C}]\dot{\mathbf{x}} + [\mathbf{K}]\mathbf{x} = \mathbf{f} + \mathbf{g} \quad (7.1)$$

where $[\mathbf{M}]$, $[\mathbf{C}]$ and $[\mathbf{K}]$ are block diagonal matrices containing the mass, damping and stiffness matrices of each sub-structure, \mathbf{f} is the block vector (a vector made up of multiple vertically stacked vectors) of externally applied forces, \mathbf{g} is the block vector of coupling forces, and \mathbf{x} is the block vector of displacements.

$$[\mathbf{M}] = \begin{bmatrix} \mathbf{M}_{(1)} & 0 & 0 \\ 0 & \ddots & 0 \\ 0 & 0 & \mathbf{M}_{(n)} \end{bmatrix}, [\mathbf{C}] = \begin{bmatrix} \mathbf{C}_{(1)} & 0 & 0 \\ 0 & \ddots & 0 \\ 0 & 0 & \mathbf{C}_{(n)} \end{bmatrix}, [\mathbf{K}] = \begin{bmatrix} \mathbf{K}_{(1)} & 0 & 0 \\ 0 & \ddots & 0 \\ 0 & 0 & \mathbf{K}_{(n)} \end{bmatrix} \quad (7.2a,b,c)$$

$$\mathbf{f} = [\mathbf{f}_{(1)}, \dots, \mathbf{f}_{(n)}]^T, \quad \mathbf{g} = [\mathbf{g}_{(1)}, \dots, \mathbf{g}_{(n)}]^T, \quad \mathbf{x} = [\mathbf{x}_{(1)}, \dots, \mathbf{x}_{(n)}]^T \quad (7.3a,b,c)$$

Experimentally, we do not have direct access to the mass damping or stiffness matrices from measurement. We instead concern ourselves with the determination of measured frequency response functions, for example, impedance or mobility. It is therefore convenient to express Equation 7.1 in the FRF domain as,

$$[\mathbf{Z}]\mathbf{v} = \mathbf{f} + \mathbf{g} \quad (7.4)$$

where $[\mathbf{Z}]$ is the block diagonal impedance matrix of the n uncoupled sub-structures and \mathbf{v} is the corresponding block vector of velocities.

The rigid coupling of any two neighbouring sub-structures is governed by the conditions of equilibrium and compatibility. The condition of compatibility states that the velocity at any coupling DoFs, v_1 and v_2 , must be equal; $v_1 = v_2$. This condition may be expressed generally using the Boolean localisation matrix, \mathbf{L} , as,

$$\mathbf{v} = \mathbf{L}\tilde{\mathbf{v}} \quad (7.5)$$

where $\tilde{\mathbf{v}}$ is the vector of *coupled* sub-structure velocities (The construction of \mathbf{L} will be discussed shortly in the numerical example.) The condition of equilibrium states that the internal coupling forces at any two coupling DoFs, g_1 and g_2 , must be equal and opposite; $g_1 + g_2 = 0$. This may be conveniently expressed using the transpose of the Boolean coupling matrix, \mathbf{L}^T ,

$$\mathbf{L}^T \mathbf{g} = \tilde{\mathbf{g}} = \mathbf{0} \quad (7.6)$$

where $\tilde{\mathbf{g}}$ is the vector of coupled sub-structure coupling forces, and is equal to the zero vector.

Let us now consider the enforcement of the above conditions on Equation 7.4. Firstly, pre-multiplication of Equation 7.4 by \mathbf{L} can be seen to apply the equilibrium condition,

$$\mathbf{L}^T \mathbf{Z} \mathbf{v} = \tilde{\mathbf{f}} \quad (7.7)$$

where we note that $\mathbf{L}^T \mathbf{g} = \tilde{\mathbf{g}} = \mathbf{0}$ and that $\mathbf{L}^T \mathbf{f}$ corresponds to the externally applied force vector of the coupled assembly, $\tilde{\mathbf{f}}$. Substitution of Equation 7.5 for the uncoupled velocity subsequently applies the condition of compatibility.

$$\mathbf{L}^T \mathbf{Z} \mathbf{L} \tilde{\mathbf{v}} = \tilde{\mathbf{f}} \quad (7.8)$$

Equation 7.8 can be seen to relate the coupled velocity, $\tilde{\mathbf{v}}$, to the coupled force, $\tilde{\mathbf{f}}$. The matrix product $\mathbf{L}^T \mathbf{Z} \mathbf{L}$ must therefore represent the impedance of the *coupled* assembly.

Classical impedance sub-structuring relation:

$$\mathbf{Z}_C = \mathbf{L}^T \mathbf{Z} \mathbf{L}. \quad (7.9)$$

Expansion of Equation 7.9 reveals that the rigid coupling of sub-structures simply amounts to the summation of coupling DoF impedances, as described in [76]. Having acquired the coupled impedance of an assembly one may determine the coupled mobility through its inversion, $\mathbf{Y}_C = \mathbf{Z}_C^{-1}$.

7.2.1 NUMERICAL EXAMPLE: BEAM-BEAM

Having derived the classical impedance sub-structuring relation it is perhaps useful, for completeness, to consider a simple numerical example before moving onto the more complex case study of Section 7.3.

Beam	$L(m)$	$W(m)$	$H(m)$	$E(N/m^2)$	$\rho(kg/m^3)$	$x_{ij}(m)$
S	0.4	0.1	0.01	200×10^9	7000	{0, 0.4 }
R	0.6	0.1	0.01	200×10^9	7000	{ 0 , 0.6}
C	1	0.1	0.01	200×10^9	7000	{0, 0.4 , 1}

Table 7.2: Geometry, material properties and excitation/response positions for free-free beam simulations, where; L - length, W - width, H - height, E - Young's modulus, ρ - density, and x_{ij} - excitation/response position. Highlighted x_{ij} correspond to those of the coupling interfaces, c_1 and c_2 .

The numerical example considered here concerns the rigid coupling of two free-free beams, **S** and **R**. The steps involved in the coupling of these two beams will be demonstrated, including the construction of the Boolean coupling matrix, **L**. The free-free beams are modelled as in Section 3.3, via Equations 3.16-3.21. The geometric and material properties used in this simulation are given in Table 7.2. Also given are the excitation and response positions used in the simulation (highlighted in red are the coupling DoFs). It should be noted that in order to maintain continuity, **S** and **R** must be of equal width, height and material properties. Their lengths may differ providing that their coupled length is in agreement with that of a third beam, **C**. Beam **C** is modelled with the same material properties, width and height as **S** and **R** such that the successfully coupled **SR** assembly should be identical to that of **C**, as shown in Figure 7.1.

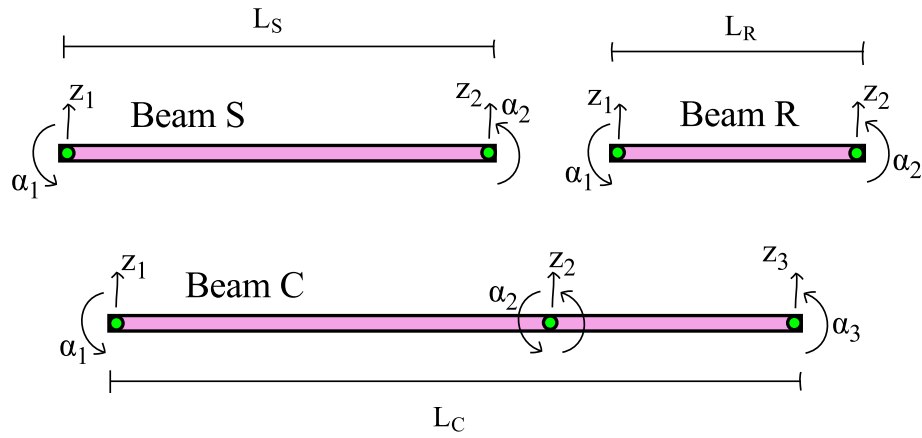


Figure 7.1: Diagrammatic representation of numerical study coupling two beams end-to-end.

Beams **S** and **R** are each characterised by their end-to-end mobility matrices. Since both translational and rotational components are required in the successful coupling of beam elements, the mobility matrices, \mathbf{Y}_S and \mathbf{Y}_R , are of dimension 4×4 ,

$$\mathbf{Y}_S = \begin{bmatrix} Y_{S_{z_1 z_1}} & Y_{S_{z_1 \alpha_1}} & Y_{S_{z_1 z_2}} & Y_{S_{z_1 \alpha_2}} \\ Y_{S_{\alpha_1 z_1}} & Y_{S_{\alpha_1 \alpha_1}} & Y_{S_{\alpha_1 z_2}} & Y_{S_{\alpha_1 \alpha_2}} \\ Y_{S_{z_2 z_1}} & Y_{S_{z_2 \alpha_1}} & Y_{S_{z_2 z_2}} & Y_{S_{z_2 \alpha_2}} \\ Y_{S_{\alpha_2 z_1}} & Y_{S_{\alpha_2 \alpha_1}} & Y_{S_{\alpha_2 z_2}} & Y_{S_{\alpha_2 \alpha_2}} \end{bmatrix}, \quad \mathbf{Y}_R = \begin{bmatrix} Y_{R_{z_1 z_1}} & Y_{R_{z_1 \alpha_1}} & Y_{R_{z_1 z_2}} & Y_{R_{z_1 \alpha_2}} \\ Y_{R_{\alpha_1 z_1}} & Y_{R_{\alpha_1 \alpha_1}} & Y_{R_{\alpha_1 z_2}} & Y_{R_{\alpha_1 \alpha_2}} \\ Y_{R_{z_2 z_1}} & Y_{R_{z_2 \alpha_1}} & Y_{R_{z_2 z_2}} & Y_{R_{z_2 \alpha_2}} \\ Y_{R_{\alpha_2 z_1}} & Y_{R_{\alpha_2 \alpha_1}} & Y_{R_{\alpha_2 z_2}} & Y_{R_{\alpha_2 \alpha_2}} \end{bmatrix} \quad (7.10ab)$$

where, for example, $Y_{N_{z_i \alpha_j}}$ represents the mobility corresponding to a translational response at the i th positional-DoF, due to an applied torque at the j th positional-DoF, on substructure N .

number of system DoFs. This is not the case with all DSS procedures. The dual formulation, for example, yields a coupled mobility matrix with the same number of DoFs as the uncoupled impedance matrix (due to repetitions in the resultant mobility matrix).

Let us now consider now the enforcement of equilibrium. The uncoupled coupling force vector is given by $\mathbf{g} = [0, 0, g_{S_{z2}}, g_{S_{\alpha2}}, g_{R_{z1}}, g_{R_{\alpha1}}, 0, 0]^T$, whilst the coupled coupling force vector is given simply by the zero vector, $\tilde{\mathbf{g}} = \mathbf{0}$. It can be seen quite clearly that the transpose of the Boolean localisation matrix \mathbf{L} enforces the equilibrium condition, as from inspection of Equation 7.13 one may observe that; $g_{S_{z2}} = -g_{R_{z1}}$ and $g_{S_{\alpha2}} = -g_{R_{\alpha1}}$.

$$\begin{bmatrix} 1 & 0 & 0 & 0 & 0 & 0 & 0 & 0 \\ 0 & 1 & 0 & 0 & 0 & 0 & 0 & 0 \\ 0 & 0 & 1 & 0 & 1 & 0 & 0 & 0 \\ 0 & 0 & 0 & 1 & 0 & 1 & 0 & 0 \\ 0 & 0 & 0 & 0 & 0 & 0 & 1 & 0 \\ 0 & 0 & 0 & 0 & 0 & 0 & 0 & 1 \end{bmatrix} \begin{pmatrix} 0 \\ 0 \\ g_{S_{z2}} \\ g_{S_{\alpha2}} \\ g_{R_{z1}} \\ g_{R_{\alpha1}} \\ 0 \\ 0 \end{pmatrix} = \mathbf{0} \quad (7.13)$$

Once the Boolean coupling matrix has been constructed the coupled impedance matrix may be determined as per Equation 7.9.

$$\mathbf{Z}_{\text{SR}} = \mathbf{L}^T \begin{bmatrix} Z_{S_{z1z1}} & Z_{S_{z1\alpha1}} & Z_{S_{z1z2}} & Z_{S_{z1\alpha2}} \\ Z_{S_{\alpha1z1}} & Z_{S_{\alpha1\alpha1}} & Z_{S_{\alpha1z2}} & Z_{S_{\alpha1\alpha2}} \\ Z_{S_{z2z1}} & Z_{S_{z2\alpha1}} & Z_{S_{z2z2}} & Z_{S_{z2\alpha2}} \\ Z_{S_{\alpha2z1}} & Z_{S_{\alpha2\alpha1}} & Z_{S_{\alpha2z2}} & Z_{S_{\alpha2\alpha2}} \\ Z_{R_{z1z1}} & Z_{R_{z1\alpha1}} & Z_{R_{z1z2}} & Z_{R_{z1\alpha2}} \\ Z_{R_{\alpha1z1}} & Z_{R_{\alpha1\alpha1}} & Z_{R_{\alpha1z2}} & Z_{R_{\alpha1\alpha2}} \\ Z_{R_{z2z1}} & Z_{R_{z2\alpha1}} & Z_{R_{z2z2}} & Z_{R_{z2\alpha2}} \\ Z_{R_{\alpha2z1}} & Z_{R_{\alpha2\alpha1}} & Z_{R_{\alpha2z2}} & Z_{R_{\alpha2\alpha2}} \end{bmatrix} \mathbf{L} \quad (7.14)$$

The coupled mobility matrix, \mathbf{Y}_{SR} , is subsequently obtained through the inversion of the coupled impedance matrix,

$$\mathbf{Y}_{\text{SR}} = \mathbf{Z}_{\text{SR}}^{-1}. \quad (7.15)$$

The resulting mobility matrix has dimensions 6×6 and is given by,

$$\mathbf{Y}_{\mathbf{SR}} = \begin{bmatrix} Y_{C_{z_1 z_1}} & Y_{C_{z_1 \alpha_1}} & Y_{C_{z_1 z_2}} & Y_{C_{z_1 \alpha_2}} & Y_{C_{z_1 z_3}} & Y_{C_{z_1 \alpha_3}} \\ Y_{C_{\alpha_1 z_1}} & Y_{C_{\alpha_1 \alpha_1}} & Y_{C_{\alpha_1 z_2}} & Y_{C_{\alpha_1 \alpha_2}} & Y_{C_{\alpha_1 z_3}} & Y_{C_{\alpha_1 \alpha_3}} \\ Y_{C_{z_2 z_1}} & Y_{C_{z_2 \alpha_1}} & Y_{C_{z_2 z_2}} & Y_{C_{z_2 \alpha_2}} & Y_{C_{z_2 z_3}} & Y_{C_{z_2 \alpha_3}} \\ Y_{C_{\alpha_2 z_1}} & Y_{C_{\alpha_2 \alpha_1}} & Y_{C_{\alpha_2 z_2}} & Y_{C_{\alpha_2 \alpha_2}} & Y_{C_{\alpha_2 z_3}} & Y_{C_{\alpha_2 \alpha_3}} \\ Y_{C_{z_3 z_1}} & Y_{C_{z_3 \alpha_1}} & Y_{C_{z_3 z_2}} & Y_{C_{z_3 \alpha_2}} & Y_{C_{z_3 z_3}} & Y_{C_{z_3 \alpha_3}} \\ Y_{C_{\alpha_3 z_1}} & Y_{C_{\alpha_3 \alpha_1}} & Y_{C_{\alpha_3 z_2}} & Y_{C_{\alpha_3 \alpha_2}} & Y_{C_{\alpha_3 z_3}} & Y_{C_{\alpha_3 \alpha_3}} \end{bmatrix}. \quad (7.16)$$

Validation of the above sub-structuring procedure is provided through a comparison of the sub-structured mobility matrix, $\mathbf{Y}_{\mathbf{SR}}$, and the directly simulated mobility matrix, $\mathbf{Y}_{\mathbf{C}}$.

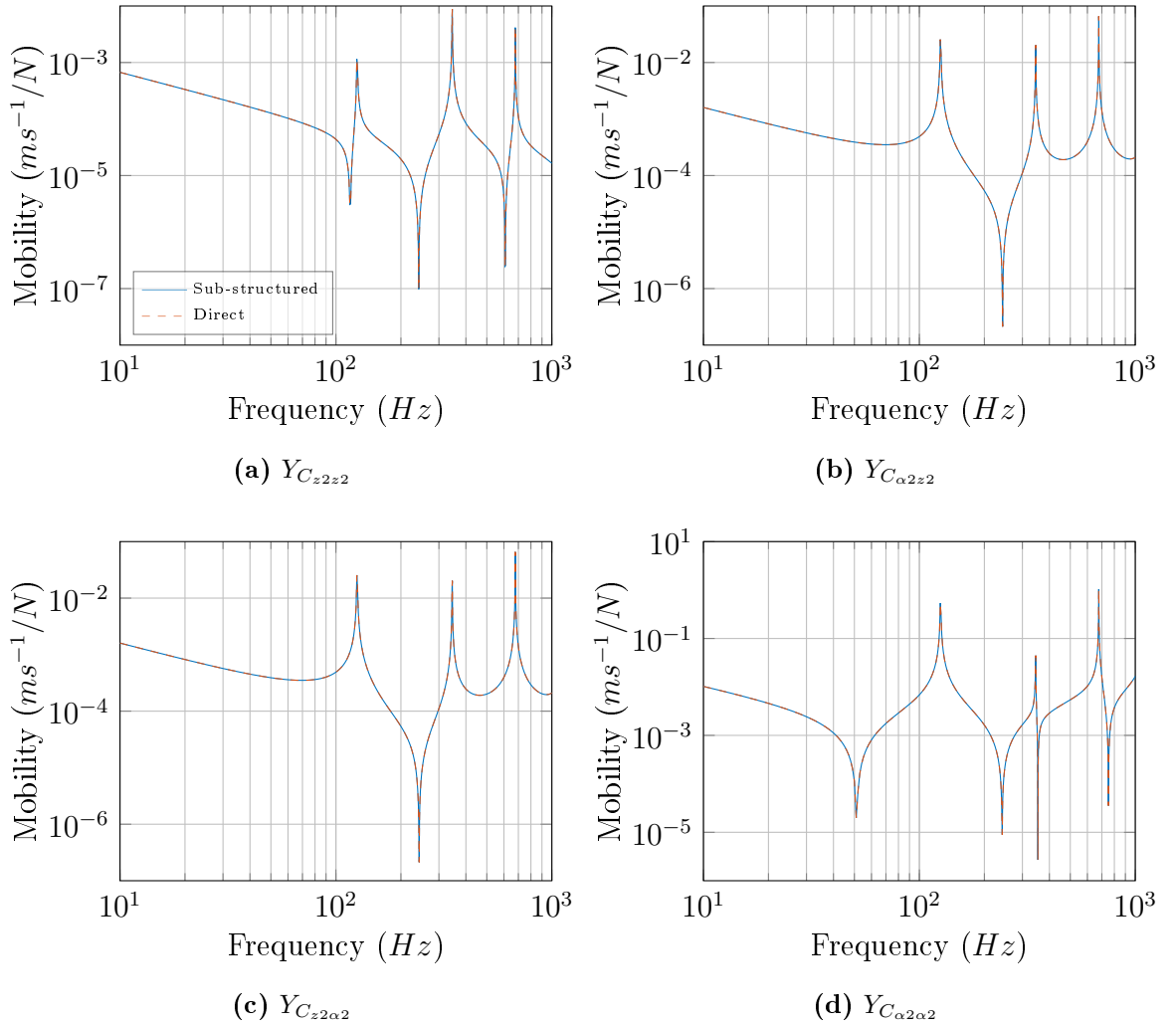


Figure 7.2: Results of a numerically simulated dynamic sub-structuring problem. Point mobility matrix of the sub-structured \mathbf{SR} assembly. Also shown are the mobilities determined directly for assembly \mathbf{C} .

Shown in Figure 7.2 are the translational, rotational and cross mobilities that make up the point mobility matrix at the 2nd positional-DoF of the coupled **SR** assembly. Also shown are the corresponding mobilities obtained from the direct simulation of assembly **C**. It can be seen that the 2 sets of mobilities are in near perfect agreement (within numerical error), confirming the validity of the classical impedance approach as a suitable method for dynamic sub-structuring.

7.3 EXPERIMENTAL CASE STUDY

The experimental case study presented in this Section concerns the construction of the VAP depicted diagrammatically in Figure 7.3, where a 4-footed electric pump is resiliently coupled to a cavity backed plate. The aim is to construct a VAP capable of predicting the operational structural velocity and internal pressure response of the assembly. A similar case study was presented by Meggitt et al. [152]. Although this study consisted of a simpler plate-like receiver it was capable of predicting the structural velocity with promising accuracy. For completeness the manuscript of this conference publication is presented in Appendix E. The cavity backed nature of the assembly considered here is a worthy advancement from this study as it emulates a far greater range of problems one may encounter in practice, and introduces an additional element of complexity.

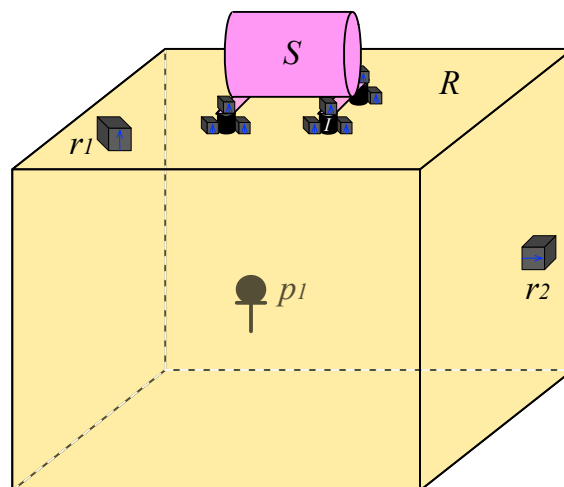


Figure 7.3: Diagrammatic representation of the experimental case study (assembly **N**). Electric pump (S) mounted via 4 resilient elements (I) to a cavity backed plate (R). Two remote sensors (r_1 , r_2) are located on the housing, with a measurement microphone (p_1) in the cavity.

The source sub-structure used in this study was the electric pump previously introduced in Chapter 6. The receiver sub-structure was a wooden box rested on foam pads. The box was constructed out of 18mm chipboard with internal cavity dimensions of $60\text{cm} \times 46\text{cm} \times 48\text{cm}$. The 4 resilient coupling elements used were the same model as one another and identical in geometry to those used in assemblies **K** and **L**, although of a different nominal stiffness.

Tag	Type	Assembly Details
K	EpI(4)P	Electric pump, perspex plate ($34.5\text{cm} \times 50\text{cm} \times 1\text{cm}$), resilient element model number: Fibet 1413vv10 60 IRHD
M	MIM	Source mass 0.678kg, receiver mass 0.858kg, resilient element model number: Fibet 1413vv10 60 IRHD
N	Bx	Chipboard box (cavity: $60\text{cm} \times 46\text{cm} \times 48\text{cm}$, top panel: $46\text{cm} \times 52\text{cm} \times 1.8\text{cm}$)
O	EpI(4)Bx	Electric pump, chipboard box, resilient element model number: Fibet 1413vv10 60 IRHD

Table 7.3: Assembly details for experimental case study.

Details of each component, and the assemblies used in their characterisation are presented in Table 7.3. It should be noted that in this study we considered only translational z DoFs. This choice was made largely due to a shortage of the hardware required for additional DoFs, and was justified largely on the previous success of this assumption.

The steps involved in the construction of the above assembly (virtually) may be outlined as follows:

- 1 Independently characterise the source sub-structure.
 - A** Passive: Free-interface mobility via suspension or in-situ decoupling.
 - B** Active: In-situ blocked force.
- 2 Independently characterise the resilient coupling elements via the in-situ approach.
- 3 Independently characterise the receiver sub-structure via free suspension or in-situ decoupling.

- 4 Couple together passive sub-structure properties using the classical impedance dynamic sub-structuring procedure.
- 5 Inject blocked forces and propagate uncertainties.
- * Reconstruct time domain responses for auralisation.

1A) PASSIVE SOURCE CHARACTERISATION - The source characterisation undertaken here was carried out on assembly **K**. Details of the experimental set-up may be found in Section 6.4. We will begin with the independent characterisation of the source sub-structure's passive properties by attempting to decouple it via the in-situ approach. The free-interface mobility matrix of the 4-footed pump is given by,

$$\mathbf{Y}_{S_{c1c1}} = \begin{bmatrix} Y_{S_{c11c11}} & Y_{S_{c11c12}} & Y_{S_{c11c13}} & Y_{S_{c11c14}} \\ Y_{S_{c12c11}} & Y_{S_{c12c12}} & Y_{S_{c12c13}} & Y_{S_{c12c14}} \\ Y_{S_{c13c11}} & Y_{S_{c13c12}} & Y_{S_{c13c13}} & Y_{S_{c13c14}} \\ Y_{S_{c14c11}} & Y_{S_{c14c12}} & Y_{S_{c14c13}} & Y_{S_{c14c14}} \end{bmatrix}. \quad (7.17)$$

Acquiring the above through the in-situ decoupling first requires the determination of the coupled contact interface mobility matrix. Due to restricted access at the source-isolator interface (see Figure 6.4b) its direct measurement was not possible. It was, however, shown in Section 4.2.3 that it is possible to remotely determine the contact interface mobility matrix of a dual interface assembly using the factorised round trip matrix relation,

$$\begin{bmatrix} \mathbf{Y}_{C_{c1c1}} & \mathbf{Y}_{C_{c1c2}} \\ \mathbf{Y}_{C_{c2c1}} & \mathbf{Y}_{C_{c2c2}} \end{bmatrix} = \begin{bmatrix} \mathbf{Y}_{C_{c1b}} & 0 \\ 0 & \mathbf{Y}_{C_{c2a}} \end{bmatrix} \begin{bmatrix} \mathbf{Y}_{C_{ab}} & 0 \\ 0 & \mathbf{Y}_{C_{ba}} \end{bmatrix}^{-1} \begin{bmatrix} \mathbf{Y}_{C_{c1a}}^T & \mathbf{Y}_{C_{c2a}}^T \\ \mathbf{Y}_{C_{c1b}}^T & \mathbf{Y}_{C_{c2b}}^T \end{bmatrix}.$$

As we have access to the isolator-receiver contact interface we may collocate the remote receiver and interface DoFs, b and c_2 . Additionally, as we would like to avoid remote response measurements on the source sub-structure, we can make the substitution, $\mathbf{Y}_{C_{ab}} = \mathbf{Y}_{C_{ba}}^T$. The resulting matrix relation is given by,

$$\begin{bmatrix} \mathbf{Y}_{C_{c1c1}} & \mathbf{Y}_{C_{c1c2}} \\ \mathbf{Y}_{C_{c2c1}} & \mathbf{Y}_{C_{c2c2}} \end{bmatrix} = \begin{bmatrix} \mathbf{Y}_{C_{c1c2}} & 0 \\ 0 & \mathbf{Y}_{C_{c2a}} \end{bmatrix} \begin{bmatrix} \mathbf{Y}_{C_{c2a}}^T & 0 \\ 0 & \mathbf{Y}_{C_{c2a}} \end{bmatrix}^{-1} \begin{bmatrix} \mathbf{Y}_{C_{c1a}}^T & \mathbf{Y}_{C_{c2a}}^T \\ \mathbf{Y}_{C_{c1c2}}^T & \mathbf{Y}_{C_{c2c2}}^T \end{bmatrix}. \quad (7.18)$$

From expansion of the above one may observe that the receiver side mobility matrix, $\mathbf{Y}_{C_{2c2}}$, is obtained directly, as are the transfer mobility matrices $\mathbf{Y}_{C_{1c2}} = \mathbf{Y}_{C_{2c1}}^T$, where reciprocity is implicitly assumed.

Shown in Figure 7.4 are the remotely determined point mobilities of the coupled source. Results are presented for both the standard and collocated DoF round trip relations of Equations 4.29 and 7.18, respectively. In each case an over-determination was achieved through the use of additional forces applied at a (remote source DoFs). A total of 12 forces were applied, providing in a 3 fold over-determination.

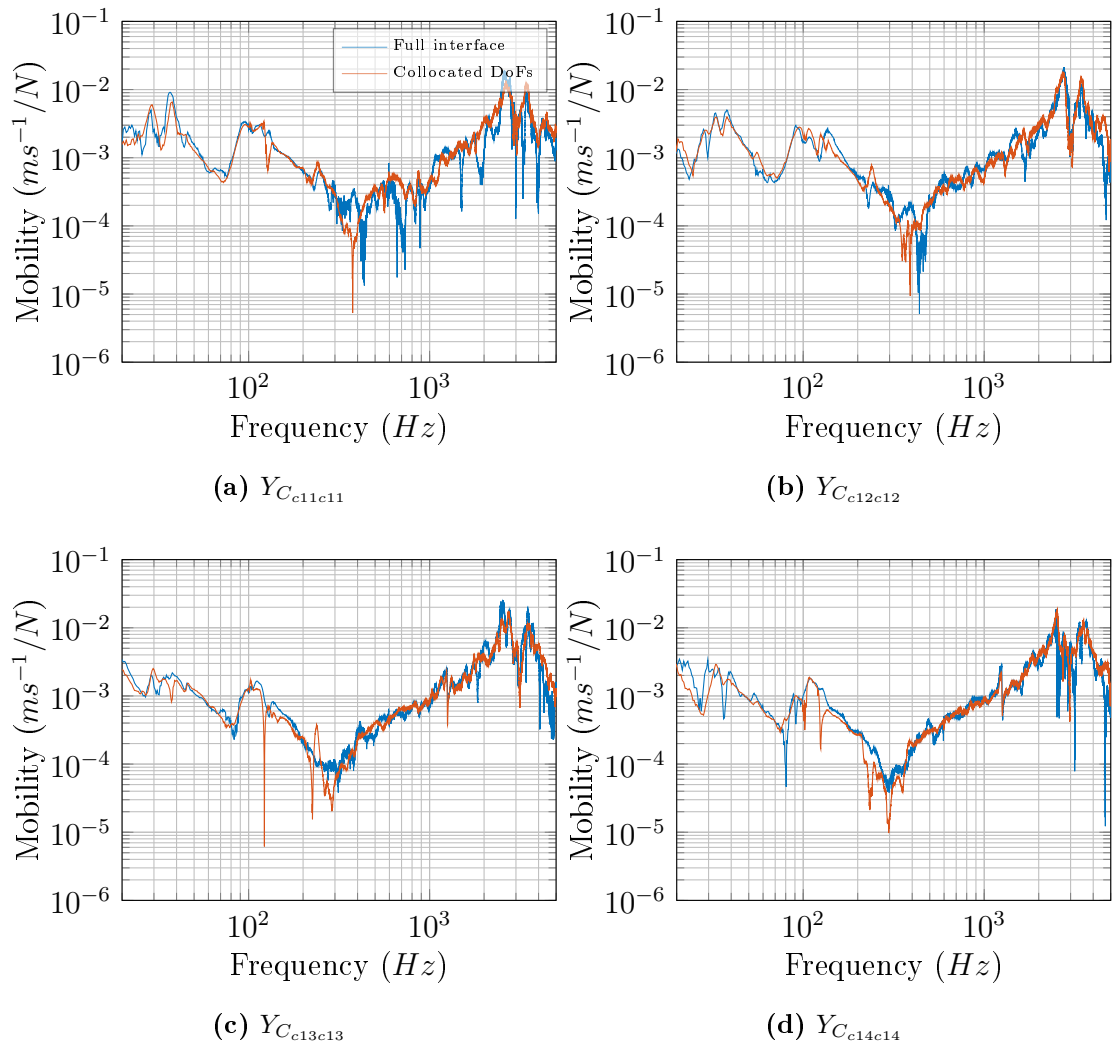


Figure 7.4: Coupled point mobilities of the source sub-structure determined using full remote contact interface relation (see Equation 4.29) and the collocated remote relation (see Equation 7.18).

The full remote and collocated DoF approaches are seen to be in relatively good agreement with one another. Unfortunately, due to the restricted access, we are

unable to measure the coupled mobility directly for comparison.

Having remotely determined the contact interface mobility matrix, carrying out the in-situ decoupling procedure, as per Section 5.2, yields a 4×4 free-interface source mobility matrix, the point mobilities of which are presented in Figure 7.5. Also shown are the free-interface point mobilities obtained whilst the source was ‘freely suspended’ on elastic bungees.

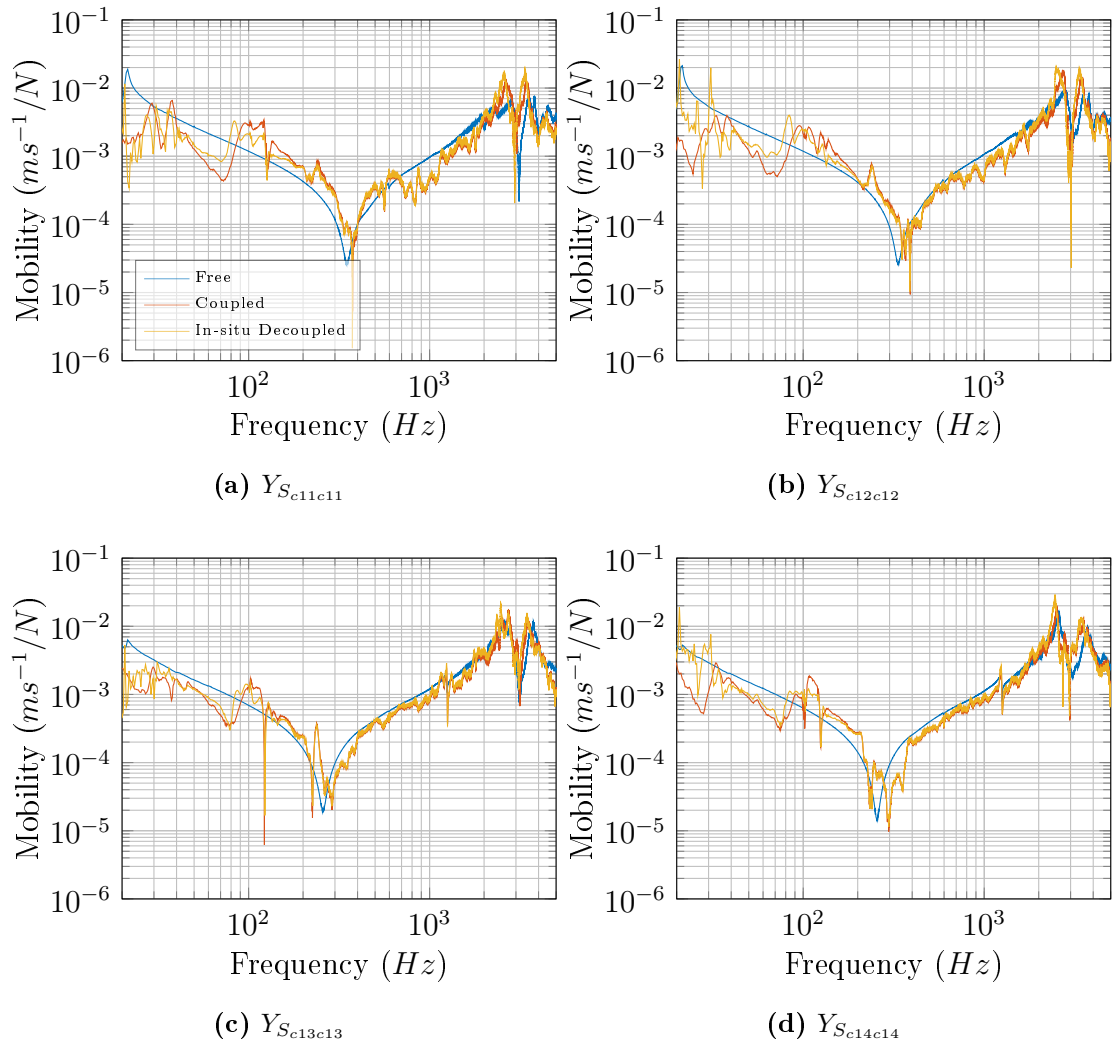


Figure 7.5: Coupled, in-situ decoupled and physically uncoupled point mobilities of the source sub-structure.

From Figure 7.5 it can be seen that the in-situ decoupling approach has clearly been unsuccessful, providing little improvement over the coupled mobility. Although used with promising success in the **MIP**, **BIP** and **BI(2)P** assemblies of Section 5.3, the decoupling of the 4-footed pump perhaps presents too complex a task for the

method at this stage in its development. A number of factors may have contributed to its failure. Firstly, the inversion of a larger 8×8 mobility matrix is likely to have introduced greater error due to ill conditioning, resulting in a less reliable transfer impedance. Secondly, the remote determination of the contact interface mobility may not have provided a sufficiently accurate mobility matrix, particularly for use with an inverse procedure such as the in-situ decoupling. Additionally, we only considered measurement and decoupling in the translational z DoFs. Whilst this appeared sufficient in the previous studies of Section 5.3, the complex nature of the pump considered here may require additional DoFs for a successful decoupling to be achieved.

Although a disappointing result, we may continue with the construction of the VAP by using the mobility acquired from the freely suspended source.

1B) ACTIVE SOURCE CHARACTERISATION - With the same source under consideration, the blocked forces used in this case study are those presented in Section 6.4.1.2, determined from assembly **K**. The reader is referred back for details on the experimental set-up and procedure. We will consider the use of both over-determined and expected blocked forces, as well as the propagation of the associated blocked force variance-covariance matrix.

2) RESILIENT COUPLING ELEMENT CHARACTERISATION - The resilient coupling elements used in the construction of the VAP were geometrically identical to those used in the active and passive characterisation of the source sub-structure, although of different nominal stiffness. These elements were chosen to ensure similar mounting conditions between characterisation and VAP construction, aiding the transferability of the blocked forces.

Due to time constraints only a single resilient element was characterised. It was assumed that the remaining 3 would be similar enough for the purposes of this case study. The element was characterised in the **MIM** assembly **M** (details of which are presented in Table 7.3) following the same procedure used on assemblies **A-D** in Section 3.4.1.

Shown in Figure 7.6 is the dynamic transfer stiffness obtained via the in-situ approach. The stiffness can be seen to exhibit the linear trend expected from a spring-like element. A reasonable prediction appears to have been achieved up to approximately 2-3kHz, beyond which the stiffness is contaminated by an increasing amount of noise.

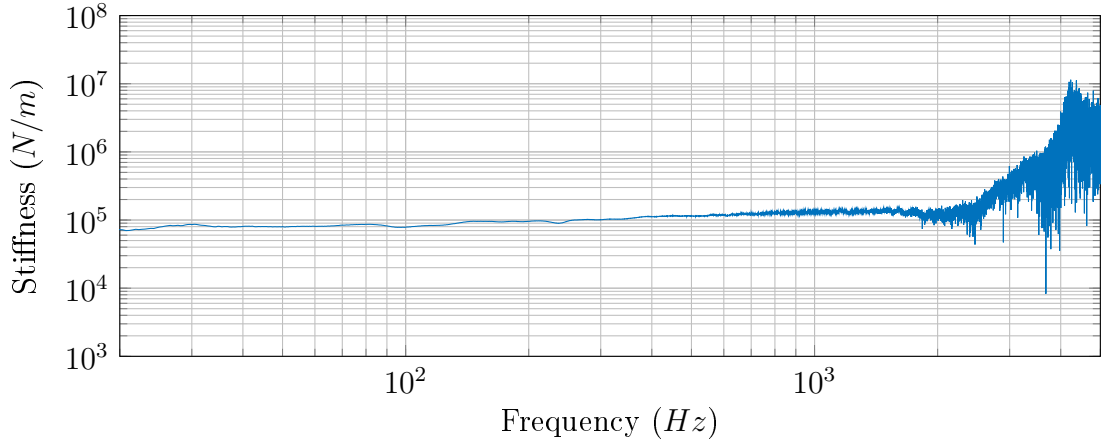


Figure 7.6: Dynamic transfer stiffness obtained from **MIM** assembly for use in experimental case study.

The compact nature of the resilient element meant that the **MIM** assembly was relatively unstable (top mass would wobble largely when excited). Although a convincing stiffness has been determined, this would likely be improved by using a more stable assembly type. Unfortunately, due to time constraints, this was not possible. From the stiffness presented in Figure 7.6 we are able to construct an approximate coupling impedance matrix,

$$\mathbf{Z}_I = \begin{bmatrix} Z_{I_{c1c2}} & -Z_{I_{c1c2}} \\ -Z_{I_{c1c2}} & Z_{I_{c1c2}} \end{bmatrix}. \quad (7.19)$$

This will later be used as part of the dynamic sub-structuring procedure.

3) RECEIVER CHARACTERISATION - With the aim of this study being to construct a VAP capable of predicting the operational response at a number of remote DoFs, the independent characterisation of the receiver sub-structure must include the appropriate transfer functions to these remote DoFs. As such, the cavity backed plate is characterised at both the coupling interface and remote DoFs. The remote DoFs considered here include the normal velocities, v_{Rr1} and v_{Rr2} , on the

where \mathbf{Y}_S , \mathbf{Z}_I and \mathbf{Y}_R are given by Equations 7.17, 7.19 and 7.20, respectively, and $^+$ represents the pseudo inverse. Once constructed the conditions of equilibrium and compatibility are enforced to yield the coupled assembly impedance matrix. This was achieved through pre- and post-multiplication of \mathbf{Z} by the appropriate Boolean coupling matrices.

Unlike the numerical example presented in Section 7.2.1, we were unable to determine the complete receiver mobility matrix \mathbf{Y}_R . This was largely due to the difficulties involved in the reciprocal measurement of the vibro-acoustic transfer function, $\mathbf{H}_{R_{pc2}}$. Additionally, for convenience the remote transfer mobilities $\mathbf{Y}_{R_{r1c2}}$ and $\mathbf{Y}_{R_{r2c2}}$ were measured only directly, neglecting the reciprocal measurement. As such, the receiver mobility matrix \mathbf{Y}_R is non-square (see Equation 7.20), and its inverse is replaced with the pseudo-inverse, denoted by the superscript $^+$. Consequently, we required two Boolean matrices in order to successfully couple the assembly. The pre-multiplicative matrix, now denoted \mathbf{L}_f , enforces equilibrium at the coupling DoFs, and the post-multiplicative matrix, now denoted \mathbf{L}_v , enforces compatibility of the coupling DoFs, whilst also accounting for the remote reference DoFs. The coupled mobility relation for a non-square block diagonal impedance matrix is thus given by,

$$\mathbf{Y}_C = (\mathbf{L}_f^T \mathbf{Z} \mathbf{L}_v)^{-1}. \quad (7.22)$$

For the study considered here, the two Boolean coupling matrices were constructed as in Equation 7.23, with red and blue highlighted values corresponding to the source and receivers coupling DoFs, respectively, and green highlighted values corresponding to the remote receiver DoFs.

$$\mathbf{L}_v = \begin{bmatrix}
1 & 0 & 0 & 0 & 0 & 0 & 0 & 0 & 0 & 0 & 0 \\
0 & 1 & 0 & 0 & 0 & 0 & 0 & 0 & 0 & 0 & 0 \\
0 & 0 & 1 & 0 & 0 & 0 & 0 & 0 & 0 & 0 & 0 \\
0 & 0 & 0 & 1 & 0 & 0 & 0 & 0 & 0 & 0 & 0 \\
1 & 0 & 0 & 0 & 0 & 0 & 0 & 0 & 0 & 0 & 0 \\
0 & 0 & 0 & 0 & 1 & 0 & 0 & 0 & 0 & 0 & 0 \\
0 & 1 & 0 & 0 & 0 & 0 & 0 & 0 & 0 & 0 & 0 \\
0 & 0 & 0 & 0 & 0 & 1 & 0 & 0 & 0 & 0 & 0 \\
0 & 0 & 1 & 0 & 0 & 0 & 0 & 0 & 0 & 0 & 0 \\
0 & 0 & 0 & 0 & 0 & 0 & 1 & 0 & 0 & 0 & 0 \\
0 & 0 & 0 & 1 & 0 & 0 & 0 & 0 & 0 & 0 & 0 \\
0 & 0 & 0 & 0 & 0 & 0 & 0 & 1 & 0 & 0 & 0 \\
0 & 0 & 0 & 0 & 1 & 0 & 0 & 0 & 0 & 0 & 0 \\
0 & 0 & 0 & 0 & 0 & 1 & 0 & 0 & 0 & 0 & 0 \\
0 & 0 & 0 & 0 & 0 & 0 & 1 & 0 & 0 & 0 & 0 \\
0 & 0 & 0 & 0 & 0 & 0 & 0 & 1 & 0 & 0 & 0 \\
0 & 0 & 0 & 0 & 0 & 0 & 0 & 0 & 1 & 0 & 0 \\
0 & 0 & 0 & 0 & 0 & 0 & 0 & 0 & 0 & 1 & 0 \\
0 & 0 & 0 & 0 & 0 & 0 & 0 & 0 & 0 & 0 & 1
\end{bmatrix}, \quad \mathbf{L}_f = \begin{bmatrix}
1 & 0 & 0 & 0 & 0 & 0 & 0 & 0 & 0 \\
0 & 1 & 0 & 0 & 0 & 0 & 0 & 0 & 0 \\
0 & 0 & 1 & 0 & 0 & 0 & 0 & 0 & 0 \\
0 & 0 & 0 & 1 & 0 & 0 & 0 & 0 & 0 \\
1 & 0 & 0 & 0 & 0 & 0 & 0 & 0 & 0 \\
0 & 0 & 0 & 0 & 1 & 0 & 0 & 0 & 0 \\
0 & 1 & 0 & 0 & 0 & 0 & 0 & 0 & 0 \\
0 & 0 & 0 & 0 & 0 & 1 & 0 & 0 & 0 \\
0 & 0 & 1 & 0 & 0 & 0 & 0 & 0 & 0 \\
0 & 0 & 0 & 0 & 0 & 0 & 1 & 0 & 0 \\
0 & 0 & 0 & 1 & 0 & 0 & 0 & 0 & 0 \\
0 & 0 & 0 & 0 & 0 & 0 & 0 & 1 & 0 \\
0 & 0 & 0 & 0 & 0 & 0 & 0 & 0 & 1 \\
0 & 0 & 0 & 0 & 1 & 0 & 0 & 0 & 0 \\
0 & 0 & 0 & 0 & 0 & 1 & 0 & 0 & 0 \\
0 & 0 & 0 & 0 & 0 & 0 & 1 & 0 & 0 \\
0 & 0 & 0 & 0 & 0 & 0 & 0 & 1 & 0 \\
0 & 0 & 0 & 0 & 0 & 0 & 0 & 0 & 1
\end{bmatrix} \tag{7.23}$$

Implementation of Equation 7.22 yields the coupled mobility matrix,

$$\mathbf{Y}_C = \begin{bmatrix}
Y_{C_{c11c11}} & Y_{C_{c11c12}} & Y_{C_{c11c13}} & Y_{C_{c11c14}} & Y_{C_{c11c21}} & Y_{C_{c11c22}} & Y_{C_{c11c23}} & Y_{C_{c11c24}} \\
Y_{C_{c12c11}} & Y_{C_{c12c12}} & Y_{C_{c12c13}} & Y_{C_{c12c14}} & Y_{C_{c12c21}} & Y_{C_{c12c22}} & Y_{C_{c12c23}} & Y_{C_{c12c24}} \\
Y_{C_{c13c11}} & Y_{C_{c13c12}} & Y_{C_{c13c13}} & Y_{C_{c13c14}} & Y_{C_{c13c21}} & Y_{C_{c13c22}} & Y_{C_{c13c23}} & Y_{C_{c13c24}} \\
Y_{C_{c14c11}} & Y_{C_{c14c12}} & Y_{C_{c14c13}} & Y_{C_{c14c14}} & Y_{C_{c14c21}} & Y_{C_{c14c22}} & Y_{C_{c14c23}} & Y_{C_{c14c24}} \\
Y_{C_{c21c11}} & Y_{C_{c21c12}} & Y_{C_{c21c13}} & Y_{C_{c21c14}} & Y_{C_{c21c21}} & Y_{C_{c21c22}} & Y_{C_{c21c23}} & Y_{C_{c21c24}} \\
Y_{C_{c22c11}} & Y_{C_{c22c12}} & Y_{C_{c22c13}} & Y_{C_{c22c14}} & Y_{C_{c22c21}} & Y_{C_{c22c22}} & Y_{C_{c22c23}} & Y_{C_{c22c24}} \\
Y_{C_{c23c11}} & Y_{C_{c23c12}} & Y_{C_{c23c13}} & Y_{C_{c23c14}} & Y_{C_{c23c21}} & Y_{C_{c23c22}} & Y_{C_{c23c23}} & Y_{C_{c23c24}} \\
Y_{C_{c24c11}} & Y_{C_{c24c12}} & Y_{C_{c24c13}} & Y_{C_{c24c14}} & Y_{C_{c24c21}} & Y_{C_{c24c22}} & Y_{C_{c24c23}} & Y_{C_{c24c24}} \\
\hline
Y_{C_{r1c11}} & Y_{C_{r1c12}} & Y_{C_{r1c13}} & Y_{C_{r1c14}} & Y_{C_{r1c21}} & Y_{C_{r1c22}} & Y_{C_{r1c23}} & Y_{C_{r1c24}} \\
Y_{C_{r2c11}} & Y_{C_{r2c12}} & Y_{C_{r2c13}} & Y_{C_{r2c14}} & Y_{C_{r2c21}} & Y_{C_{r2c22}} & Y_{C_{r2c23}} & Y_{C_{r2c24}} \\
H_{C_{p1c11}} & H_{C_{p1c12}} & H_{C_{p1c13}} & H_{C_{p1c14}} & H_{C_{p1c21}} & H_{C_{p1c22}} & H_{C_{p1c23}} & H_{C_{p1c24}}
\end{bmatrix} \tag{7.24}$$

where the last 3 rows contain the transfer mobilities and vibro-acoustic transfer function vectors between the coupling interfaces, c_1 and c_2 , and the remote DoFs r_1 , r_2 and p_1 , respectively.

Shown in Figure 7.7 are the sub-structured transfer mobilities between the source-isolator interface, c_1 , and the remote reference, r_1 , on the top face of the receiver. Also shown are the directly measured transfer mobilities of the physically coupled assembly. With access to the interface c_1 restricted, these were measured reciprocally by exciting the remote reference DoF and measuring the response at the source-isolator interface. It can be seen that a good level of agreement is obtained for each mobility with most major resonances accurately predicted. Some regions do however display a clear disagreement, particularly at low frequencies below approximately 100Hz. In this region the sub-structured mobility can be seen to generally under-predict that of the coupled assembly. It is suspected that this disagreement is likely due to neglected rotational and/or in-plane DoFs which may well be significant in the low frequency coupling of the assembly. Additionally, the inaccuracy in the measurement of low frequency mobilities may well contribute to this disagreement. The use of a softer hammer tip may offer some benefit in this case (albeit at the expense of high frequencies).

A second region of disagreement can be observed at high frequencies, above approximately 3kHz. In this region the noise encountered in the characterisation of the coupling elements becomes dominant, leading to large over predictions in the coupled mobility. However, this region is likely to be at the limit or beyond the assumption of a massless spring used in the construction of the coupling impedance matrix \mathbf{Z}_I , and therefore unreliable regardless of the noise introduced. Some overall level differences can be observed across the mid frequency range, although these are not considered critical, especially as the predictions were made having only characterised a single isolator. In reality the impedance of each coupling element would likely, albeit marginally. Overall, the level of agreement obtained is comparable to that obtained in the case study presented by Meggitt et al. [152], and certainly highlights the potential use of the in-situ characterisation method within a dynamic sub-structuring procedure.

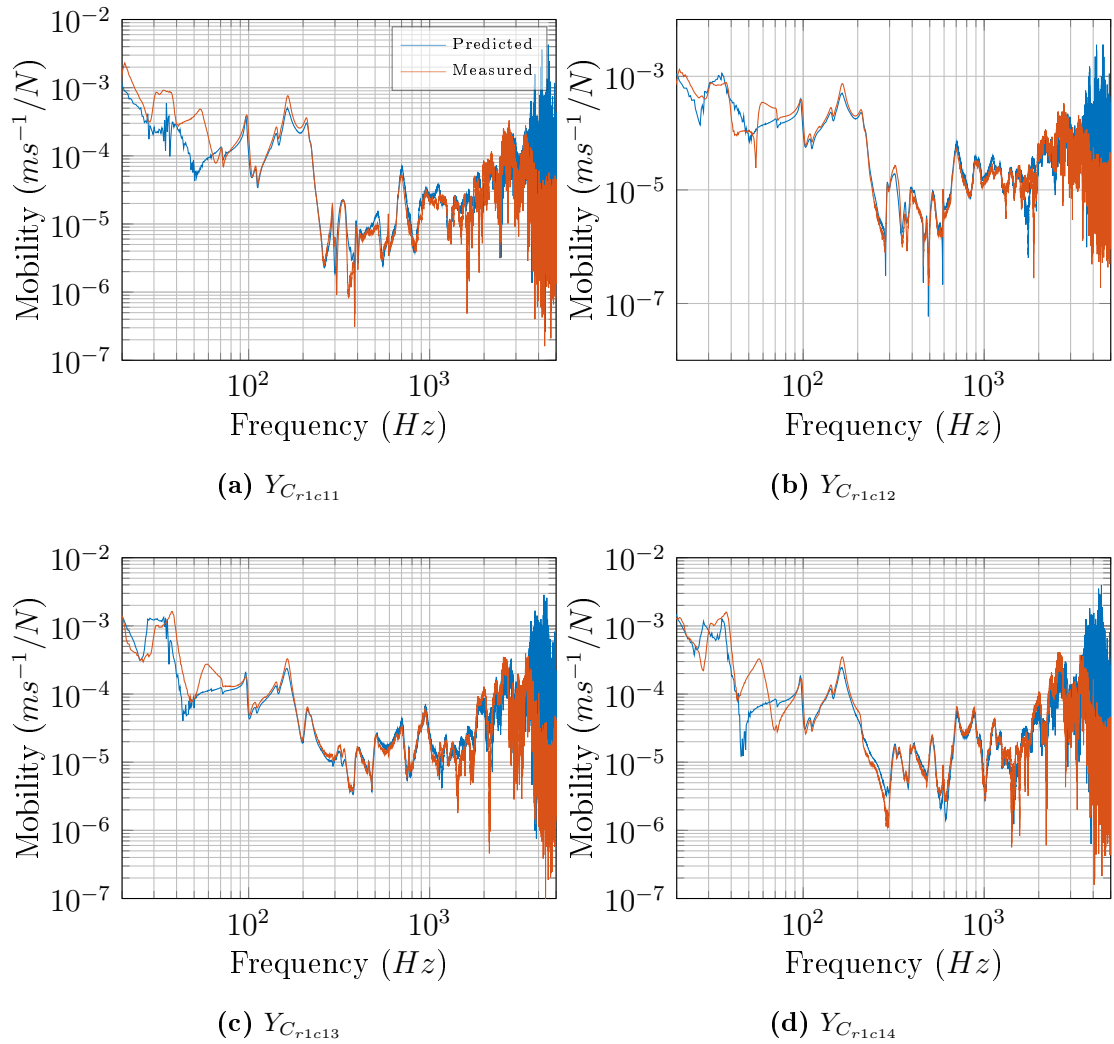


Figure 7.7: Coupled transfer mobilities between the source and the top face determined via dynamic sub-structuring and direct measurement.

Shown in Figure 7.8 are the sub-structured transfer mobilities between interface, c_1 , and the remote reference, r_2 , on the side face of the receiver. Also shown are the directly measured transfer mobilities of the physically coupled assembly, which were again, measured reciprocally. Like those presented in Figure 7.7, the sub-structured mobilities appear in good agreement with those measured directly. In addition to the low and high frequency errors already encountered previously, some discrepancies in the mid frequency prediction can be observed. This additional error is likely due to the more complex transfer path involved. However, regardless of this error, the level of agreement shown in both Figures 7.7 and 7.8 clearly suggests that the independent characterisation and subsequent coupling of the source, isolator and receiver sub-structures has been successful.

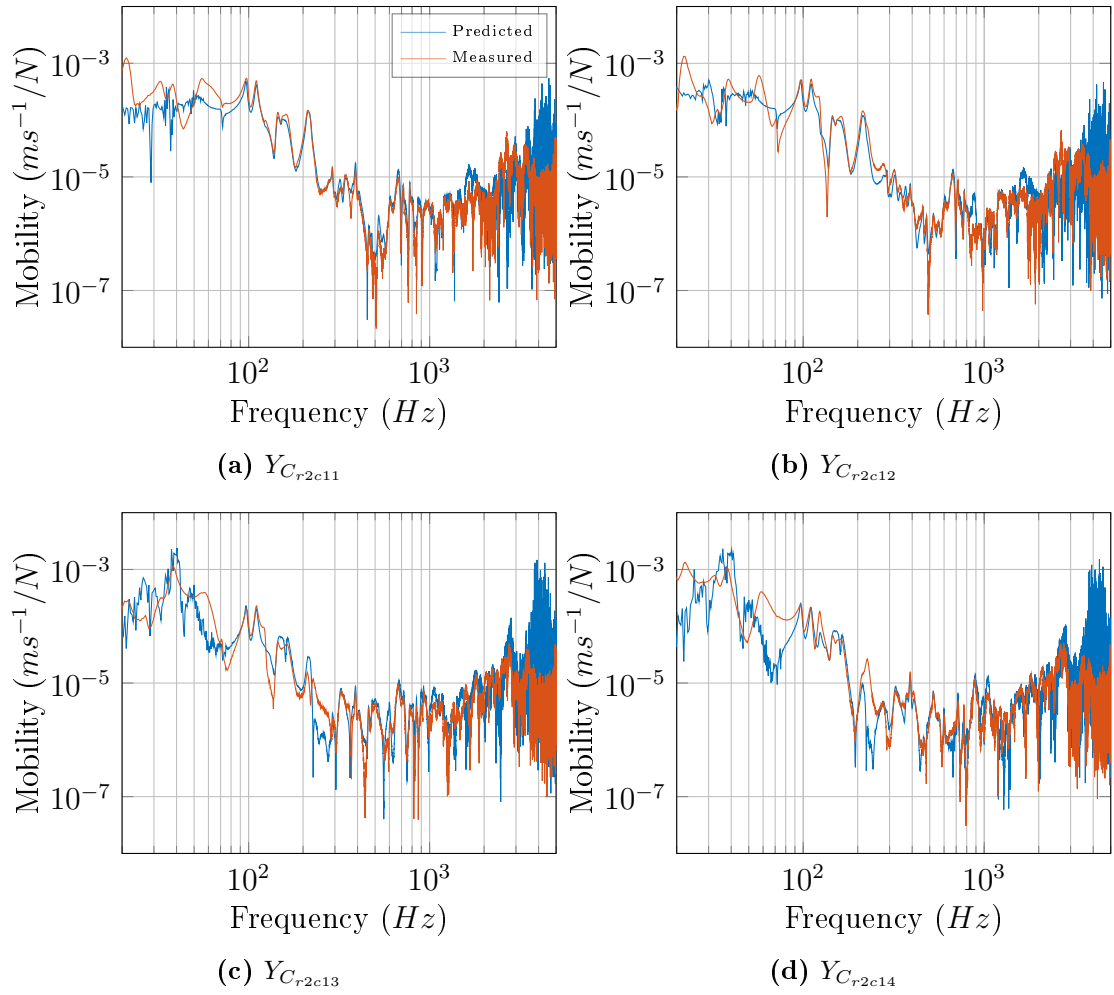


Figure 7.8: Coupled transfer mobilities between the source and side face determined via dynamic sub-structuring and direct measurement.

Shown in Figure 7.9 are the sub-structured vibro-acoustic transfer functions of the coupled assembly. Unlike the structural mobilities, we are unable to directly measure the coupled vibro-acoustic transfer functions between the source-isolator interface, c_1 , and the internal cavity pressure, $p_{C_{p1}}$, making a direct comparison not possible. However, a comparison of the coupled and uncoupled transfer functions between the isolator-receiver interface, c_2 , and cavity pressure, $\mathbf{H}_{C_{p1c2}}$ and $\mathbf{H}_{R_{p1c2}}$, may be presented. Alongside the coupled transfer function from the source-isolator interface c_1 , $\mathbf{H}_{C_{p1c1}}$, these results provide some evidence that the coupling has been successful.

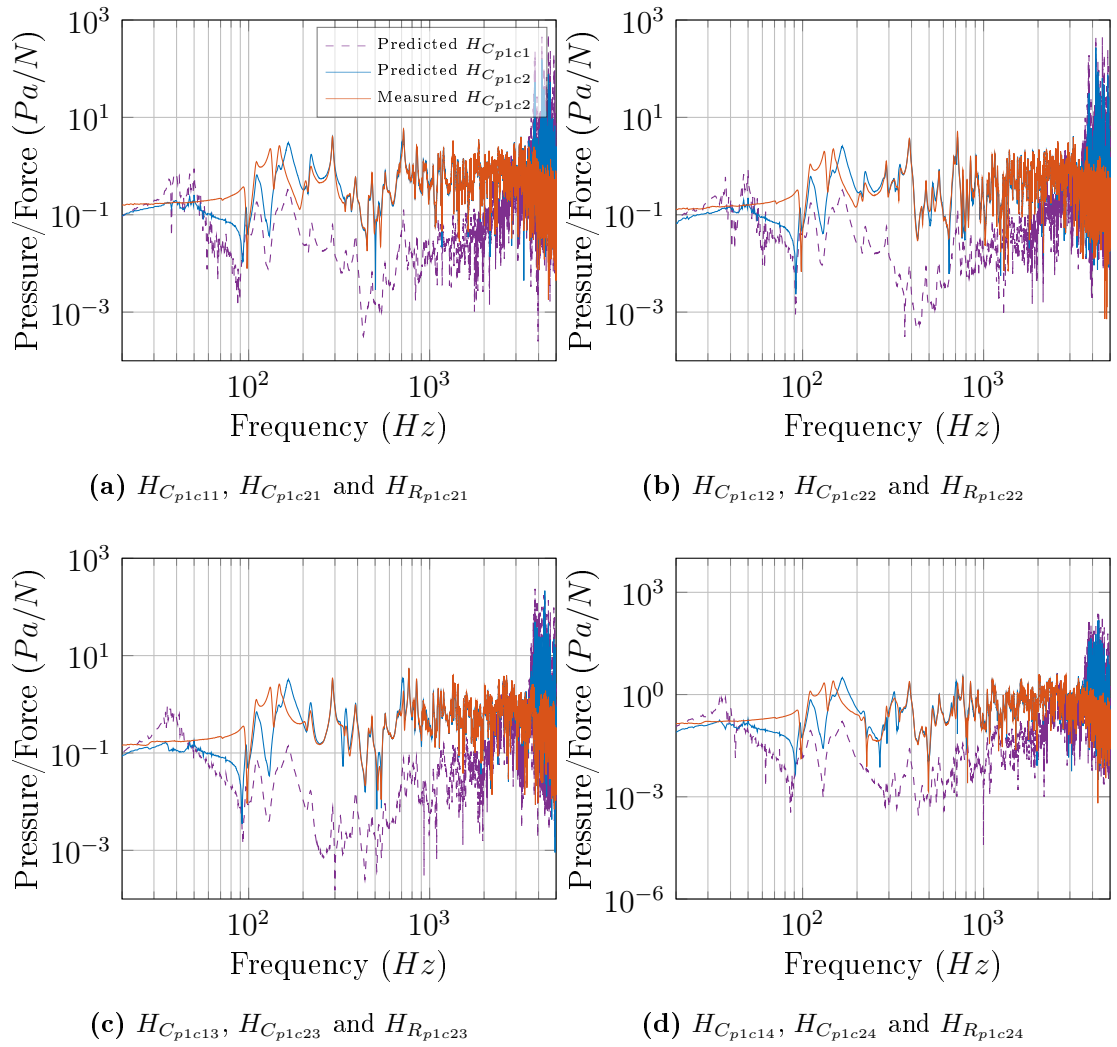


Figure 7.9: Coupled and uncoupled vibro-acoustic transfer functions determined via dynamic sub-structuring and direct measurement.

As shown in Figure 7.9, the uncoupled transfer function, $\mathbf{H}_{R_{p1c2}}$, and the sub-structured prediction, $\mathbf{H}_{C_{p1c2}}$, are in good agreement with one another, deviating only slightly at low frequencies. This suggests that the coupling of the assembly has had a minimal effect on the vibro-acoustic transfer function between the interface c_2 and the internal cavity pressure, $p_{C_{p1}}$, as one might expect. Also shown in Figure 7.9 is the sub-structured transfer function between the source-isolator interface, c_1 , and the internal cavity pressure p_1 , $\mathbf{H}_{C_{p1c1}}$. It can be seen that the sub-structured transfer function $\mathbf{H}_{C_{p1c1}}$ is considerably lower than $\mathbf{H}_{C_{p1c2}}$ across the majority of the frequency range. This is expected as $\mathbf{H}_{C_{p1c1}}$ includes the effect of attenuation across the resilient coupling elements.

Although we are unable to compare $\mathbf{H}_{\mathbf{C}_{p1c1}}$ against a directly measured transfer function, the predicted response appears sensible given the predicted and measured transfer functions $\mathbf{H}_{\mathbf{C}_{p1c2}}$ and $\mathbf{H}_{\mathbf{R}_{p1c2}}$. A more convincing validation of the sub-structured transfer function may be achieved through an operational prediction.

5) OPERATIONAL PREDICTION - Having determined the mobility matrix (including the vibro-acoustic transfer functions) of the coupled assembly, we are able to inject the blocked forces determined earlier in Chapter 6 and make an operational prediction. This may be expressed mathematically in block matrix form as,

$$\begin{pmatrix} \mathbf{v}_{\mathbf{C}_{c1}} \\ \mathbf{v}_{\mathbf{C}_{c2}} \\ \mathbf{v}_{\mathbf{C}_r} \\ \mathbf{p}_{\mathbf{C}_p} \end{pmatrix} = \begin{bmatrix} \mathbf{Y}_{\mathbf{C}_{c1c1}} & \mathbf{Y}_{\mathbf{C}_{c1c2}} \\ \mathbf{Y}_{\mathbf{C}_{c2c1}} & \mathbf{Y}_{\mathbf{C}_{c2c2}} \\ \mathbf{Y}_{\mathbf{C}_{rc1}} & \mathbf{Y}_{\mathbf{C}_{rc2}} \\ \mathbf{H}_{\mathbf{C}_{pc1}} & \mathbf{H}_{\mathbf{C}_{pc2}} \end{bmatrix} \begin{pmatrix} \bar{\mathbf{f}}_{\mathbf{S}_{c1}} \\ \mathbf{0} \end{pmatrix}. \quad (7.25)$$

For brevity we will consider only the operational predictions at the remote reference DoFs, r_1 and p_1 . In the case of r_1 , predictions will be made using both the directly measured and sub-structured mobilities. A comparison of these will enable some indication of the error associated with the transference of the blocked forces. In the case of the remote reference DoF p_1 , only the sub-structured prediction will be considered, as the coupled transfer function could not be measured directly.

Let us consider first the operational velocities obtained from the directly measured transfer mobilities. Shown in Figures 7.10 and 7.11 are the narrow and 3rd octave band predictions for the operation velocity response, respectively. Predictions are made using both the over-determined (blue) and expected (orange) blocked forces. The directly measured velocity response of the physically coupled assembly is also shown (yellow). From the narrow band prediction it can be seen that the general trend of the velocity response has been predicted with reasonable accuracy, with many of the resonances, notably the primary 25Hz resonance, having been predicted with good accuracy. Large deviations may be observed in some regions of the narrow band response however, notably around 50-60Hz and 400Hz. At high frequencies above roughly 1kHz, the ‘hairiness’ of the prediction can be seen to deviate from the measured response, which appears much smoother. Of these deviations it is the low frequency 60Hz error that introduces the largest deviation in the 3rd octave band response.

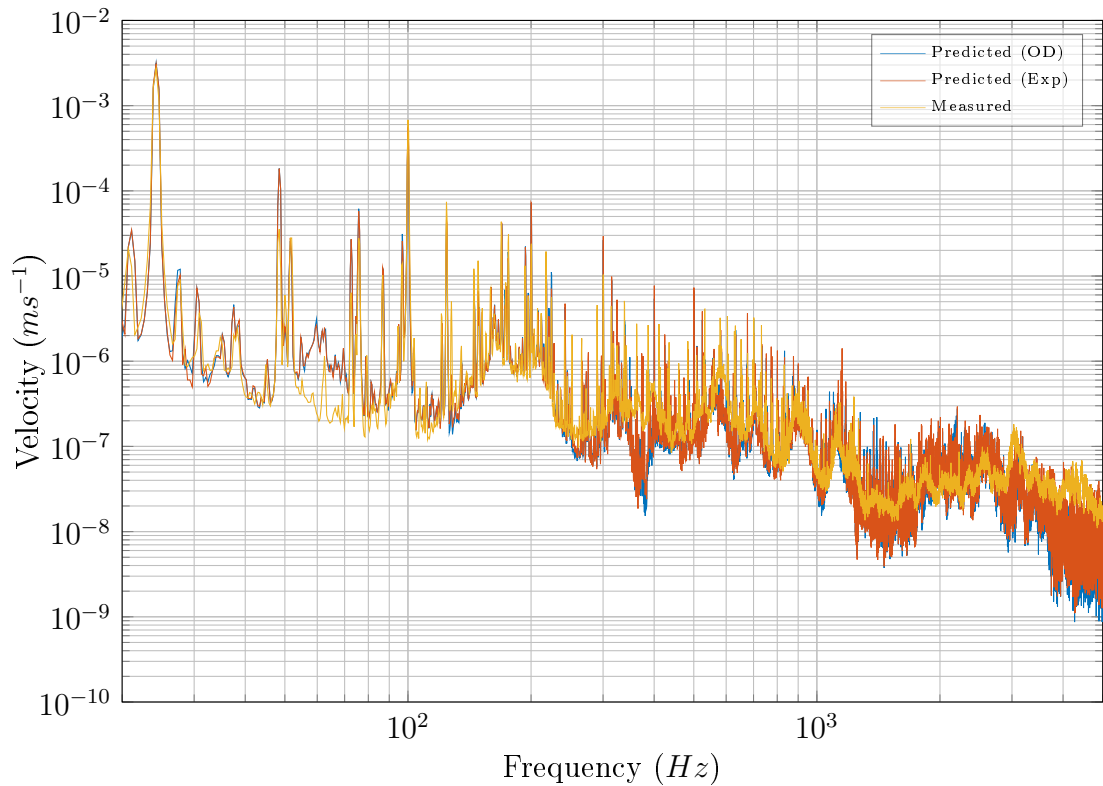


Figure 7.10: Operational velocity prediction at r_1 using transferred blocked forces (over-determined and expected) and directly measured transfer mobilities. Also shown is the directly measured velocity on the coupled assembly.

With predictions being made using the directly measured transfer mobilities, it is likely that the observed deviations are a result of error in the blocked forces and/or in their transference. That is not to say that the directly measured transfer mobilities are free from error, as these were measured reciprocally and may well introduce additional error themselves. Shown in Figure 7.12 are the blocked force and predicted response \mathbf{C}_v s. The response \mathbf{C}_v appears roughly the same magnitude of those of the blocked forces. This along with the narrow SEM suggests that propagation of blocked force uncertainties has retained a high level of confidence in the expected response. This further suggests that the observed deviations may be due to the transferability of the blocked forces.

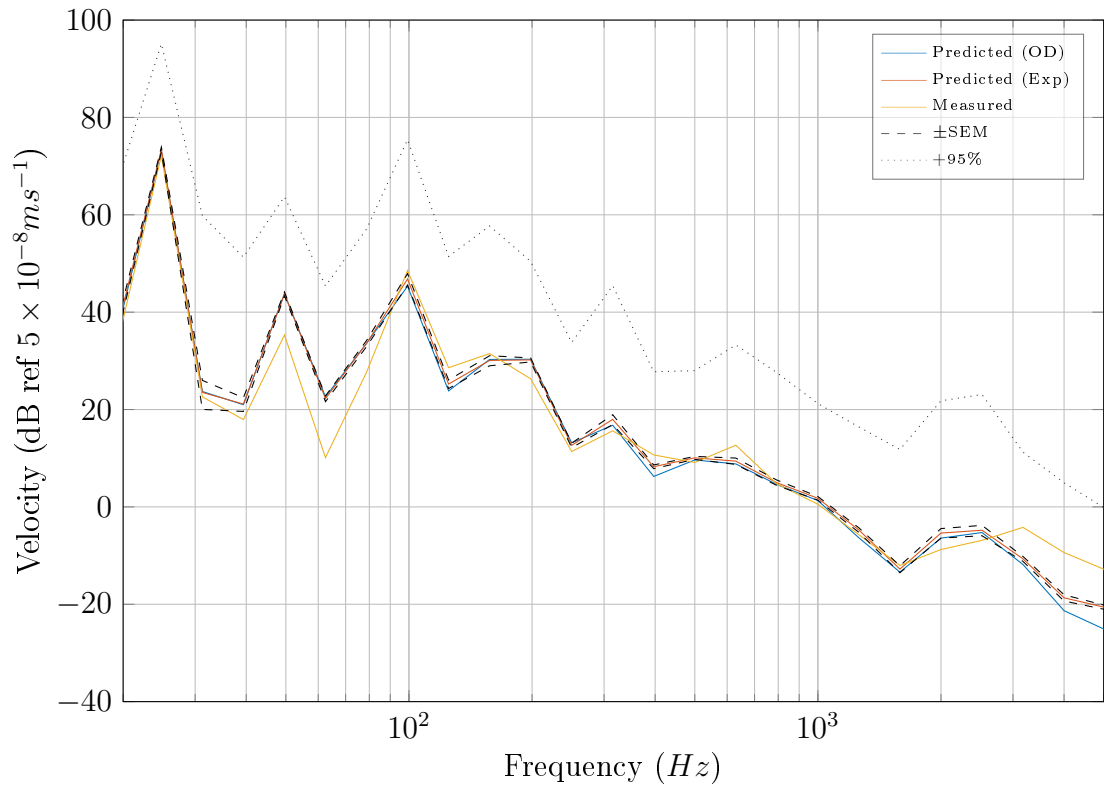


Figure 7.11: Operational velocity prediction at r_1 in 3rd octave bands using transferred blocked forces (over-determined and expected) and directly measured transfer mobilities. Also shown is the directly measured velocity on the coupled assembly and the 95% confidence intervals obtained from the propagated blocked force covariance matrix.

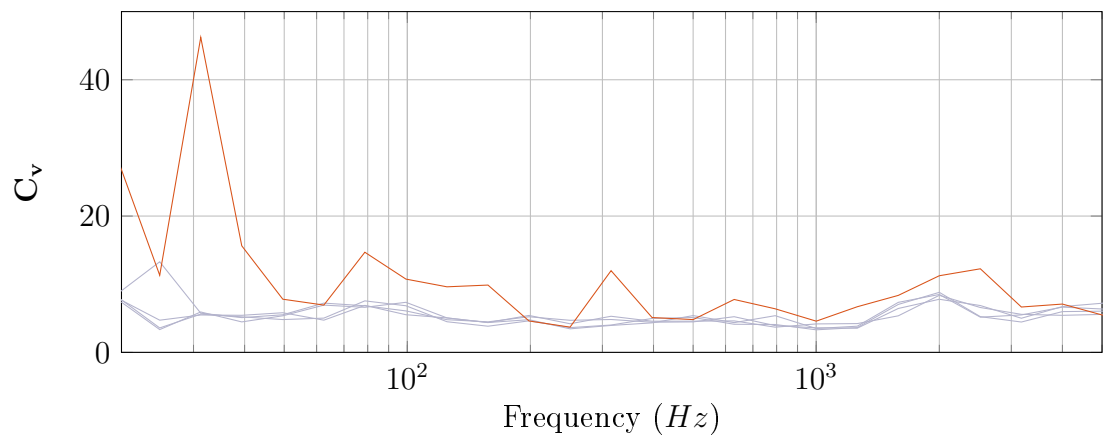


Figure 7.12: Coefficient of variation for each blocked force and the predicted operational velocity (using directly measured transfer mobilities) in 3rd octave bands.

Let us now consider the operational velocities obtained using the sub-structured mobilities. Shown in Figures 7.13 and 7.14 are the narrow and 3rd octave band

predictions for the operation velocity response, respectively. From the narrow band prediction it can be seen that, again, the general trend of the velocity response is predicted to a reasonable accuracy, with the primary 25Hz resonance being predicted to within 1dB.

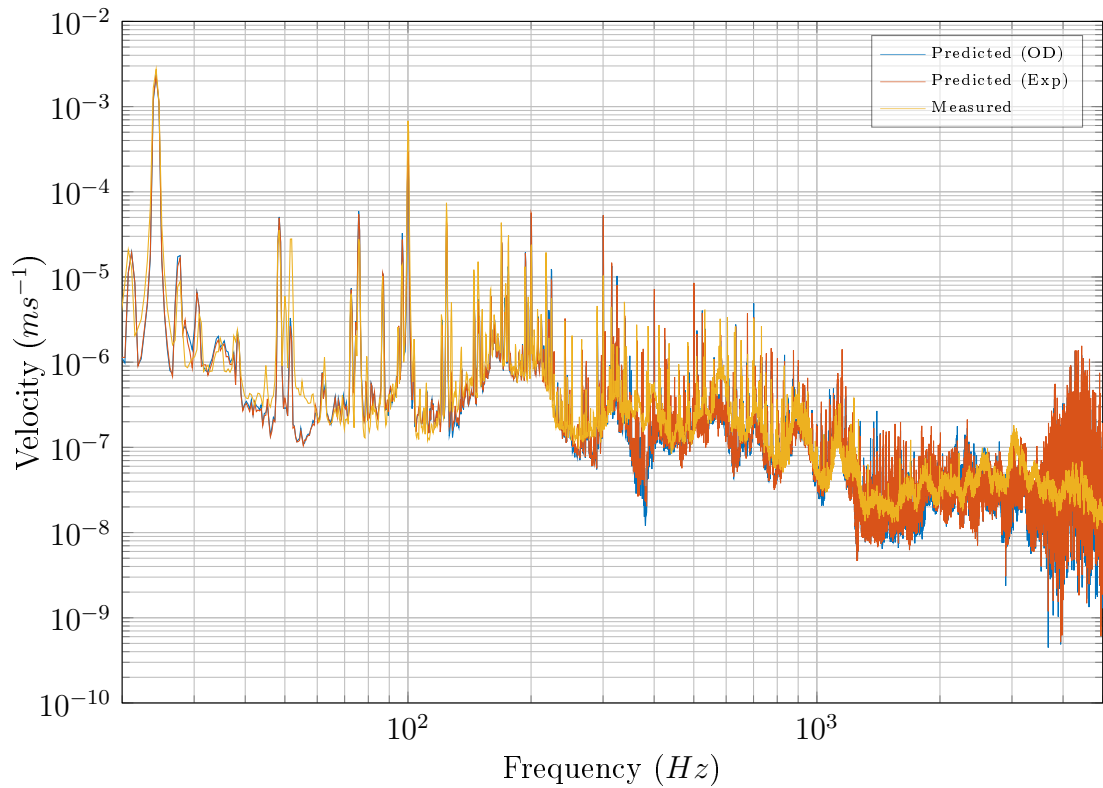


Figure 7.13: Operational velocity prediction at r_1 using transferred blocked forces (over-determined and expected) and sub-structured transfer mobilities. Also shown is the directly measured velocity on the coupled assembly.

Large deviations are observed in some regions of the narrow band response, notably at 50Hz and 400Hz, although these do not appear particularly troublesome when viewed in 3rd octaves. A comparison against Figure 7.10 highlights the influence of the high frequency noise introduced in the isolator characterisation, particularly above 3kHz. Again, however, this error is not considered a problem as it is likely beyond the limit of our approximate coupling impedance matrix assumption. In the region of 50Hz the use of a sub-structured mobility can be seen to benefit the prediction. This is due to the under-prediction of the coupled mobility, as shown in Figure 7.7. However, it should be noted that this is only beneficial as it compensates for the error which is likely to be residing in the transference of the blocked forces, as illustrated in the prediction of Figure 7.10. From Figure 7.14 the main deviations can be seen to occur around 100Hz and 315Hz. The noticeable increase in error at

approximately 100Hz is likely to be due to the under-prediction of the mobility about the 100Hz anti-resonance, as shown in Figure 7.7. Although visually only a small under-prediction, the steep nature of the anti-resonant slope means that a relatively large under-prediction is actually achieved. The over-prediction at 315Hz is likely due, in part, to an over-prediction in the mobilities, notably those of Figure 7.8a and 7.8d. The 100Hz and 315Hz errors can also be seen to coincide with the errors encountered in the transferability validation of the blocked forces (see Figure 6.22). This suggests that the deviations may also, in part, be due to a lack of transferability in the blocked forces.

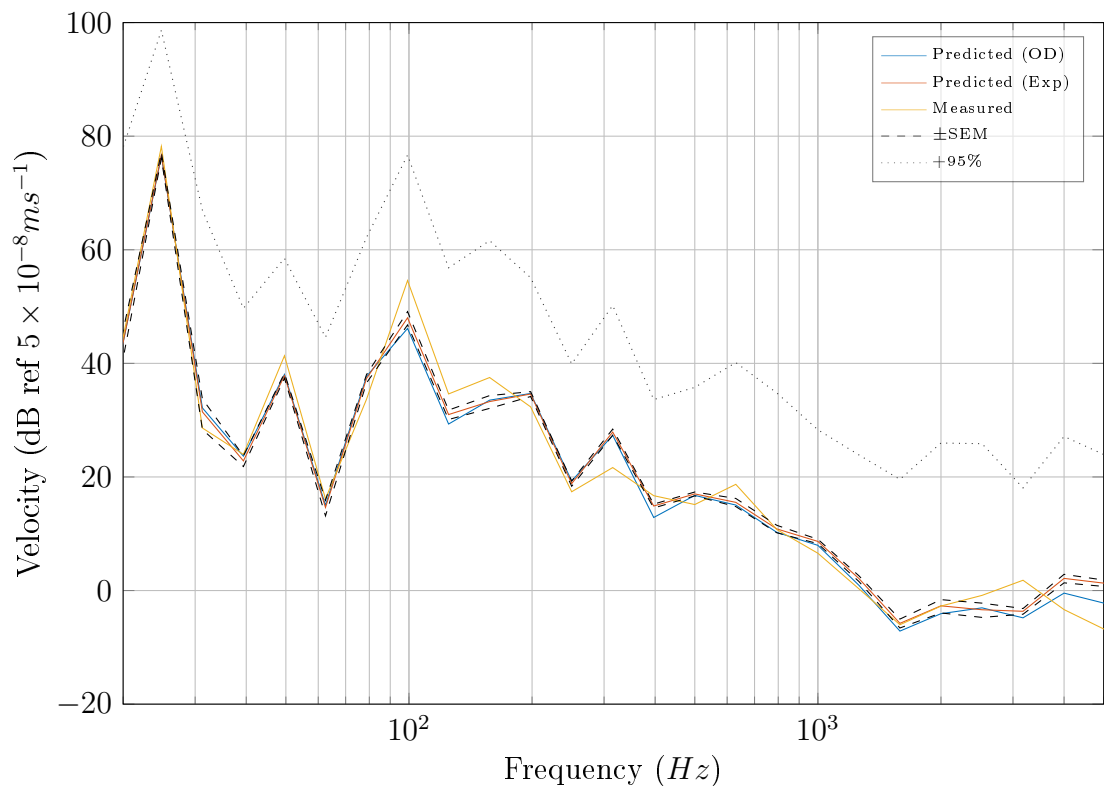


Figure 7.14: Operational velocity prediction at r_1 in 3rd octave bands using transferred blocked forces (over-determined and expected) and sub-structured transfer mobilities. Also shown is the directly measured velocity on the coupled assembly and the 95% confidence intervals obtained from the propagated blocked force covariance matrix.

Shown in Figure 7.15 are the blocked force and predicted response $\mathbf{C}_v \mathbf{s}$. Like the previous prediction, the response \mathbf{C}_v appears roughly the same magnitude as those of the blocked forces. This suggests that deviations are unlikely to be due to uncertainties in the blocked forces.

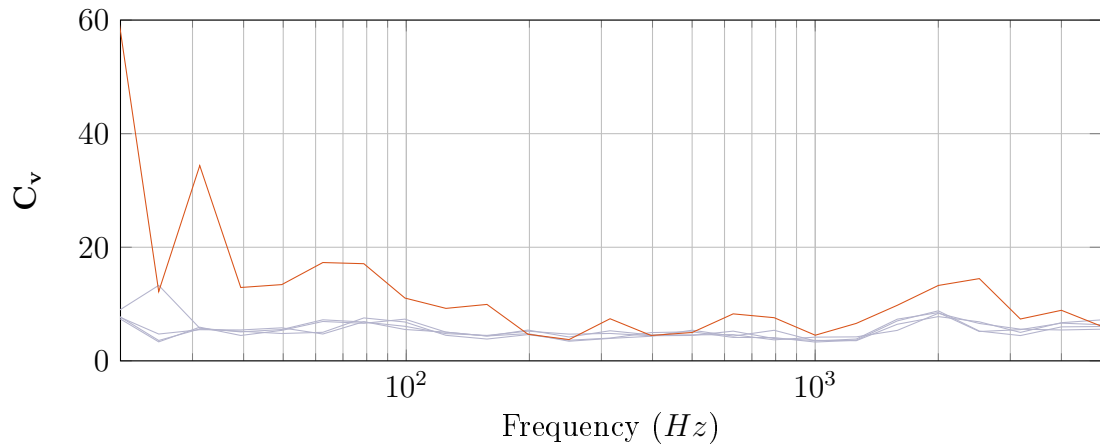


Figure 7.15: Coefficient of variation for each blocked force and the predicted operational velocity (using sub-structured transfer mobilities) in 3rd octave bands.

Regardless of the errors encountered, the predictions shown above clearly demonstrate the potential use of the proposed methods in the construction of virtual assemblies and the prediction of operational responses.

Let us now consider the operational pressures obtained using the sub-structured vibro-acoustic transfer functions. Shown in Figures 7.16 and 7.17 are the narrow and 3rd octave band predictions for the internal cavity pressure, respectively. Also shown in Figure 7.17 are the directly measured pressure responses corresponding to the physically coupled assembly (yellow) and the physically uncoupled receiver (grey), i.e. whilst the source was uncoupled and suspended above the assembly. This can be considered an approximation to the air-borne flanking contribution. From this flanking contribution it can be seen that above 400Hz the measured pressure is dominated by flanking, i.e. the structure-borne contribution is negligible.

From the narrow band prediction it can be seen that below 400Hz the general trend of the pressure response is predicted with reasonable accuracy, with the primary 25Hz resonance being predicted to within 1dB. The largest deviations below 400Hz occur in the region of 40Hz and 100Hz. It can be seen that the propagated confidence interval about the 100Hz deviation is considerably larger than the remainder of the response. This suggests that the uncertainty in the blocked force has been adversely affected by its vibro-acoustic propagation. Unfortunately we are unable to provide an assessment of the error associated with the sub-structured transfer function as no direct comparison is available. The 50Hz disagreement in the directly measured mobility prediction of the structural velocity in Figure 7.10 suggests that the 50Hz error encountered here is also due in part to the transference of the blocked forces.

Although, without a comparison of the directly measured transfer function we can not ascertain to what extent the transference is to blame.

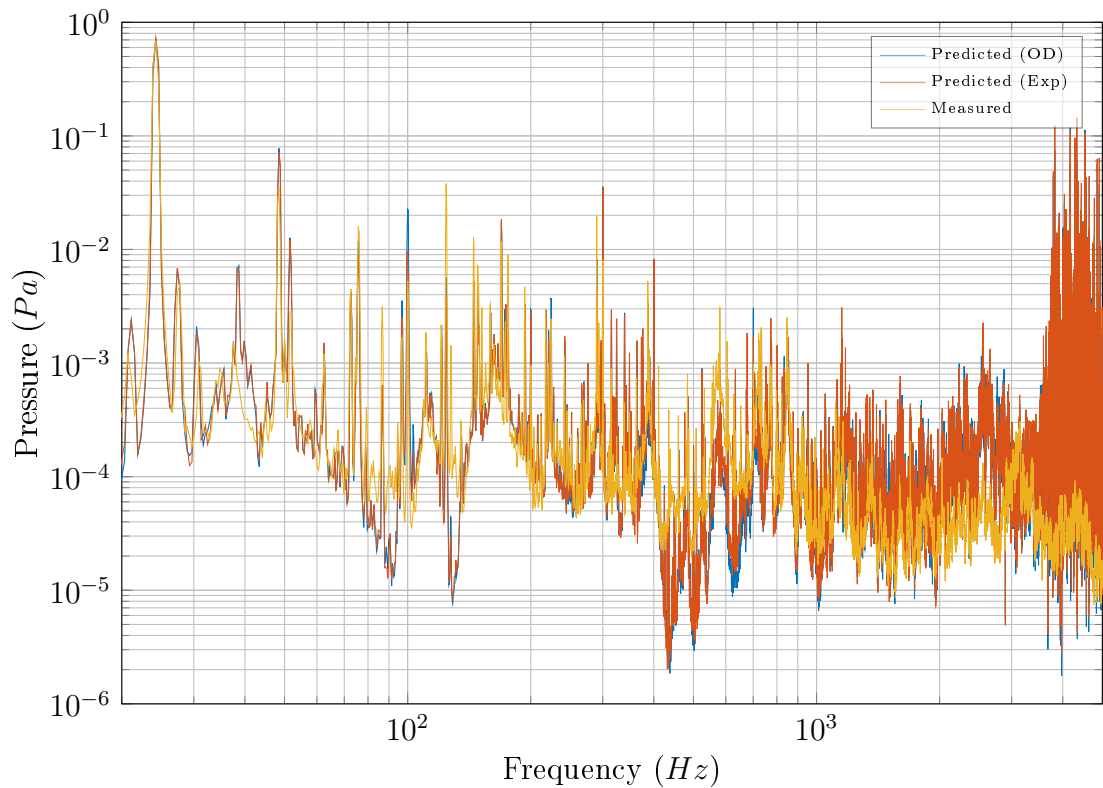


Figure 7.16: Operational cavity pressure prediction at p_1 using transferred blocked forces (over-determined and expected) and sub-structured vibro-acoustic transfer function. Also shown is the directly measured pressure in the coupled assembly.

Regardless of the error encountered, Figures 7.16 and 7.17 clearly demonstrate the potential use of a VAP in the prediction of an operational pressure response. It should be noted however, that due to time constraints imposed on this work the sub-structure characterisation procedures were only carried out only once. The author is confident that given the opportunity to perform these tests again, with some degree of experimental optimisation, better results can be achieved. Furthermore, it is worth again noting that the results presented here are based on the assumption of translation z DoFs only, not to mention the assumption of identical coupling element impedances.

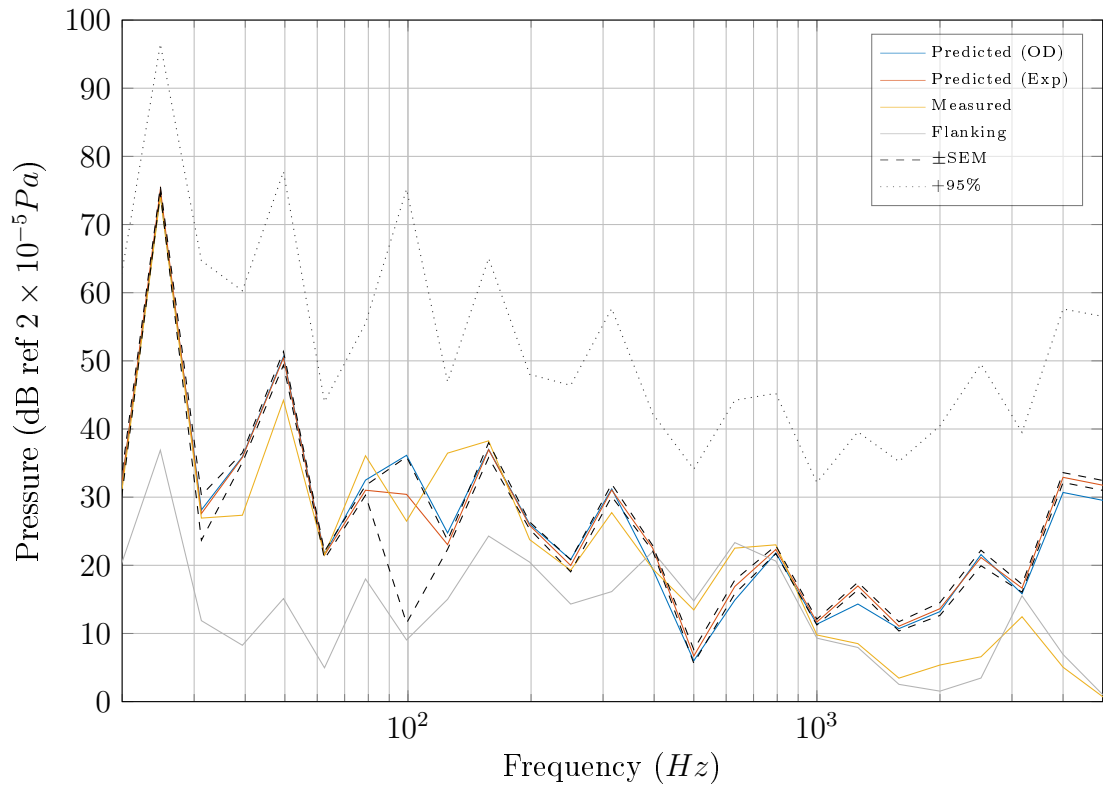


Figure 7.17: Operational cavity pressure prediction at p_1 using transferred blocked forces (over-determined and expected) and sub-structured vibro-acoustic transfer function. Also shown is the directly measured pressure in the coupled assembly and the 95% confidence intervals obtained from the propagated blocked force covariance matrix.

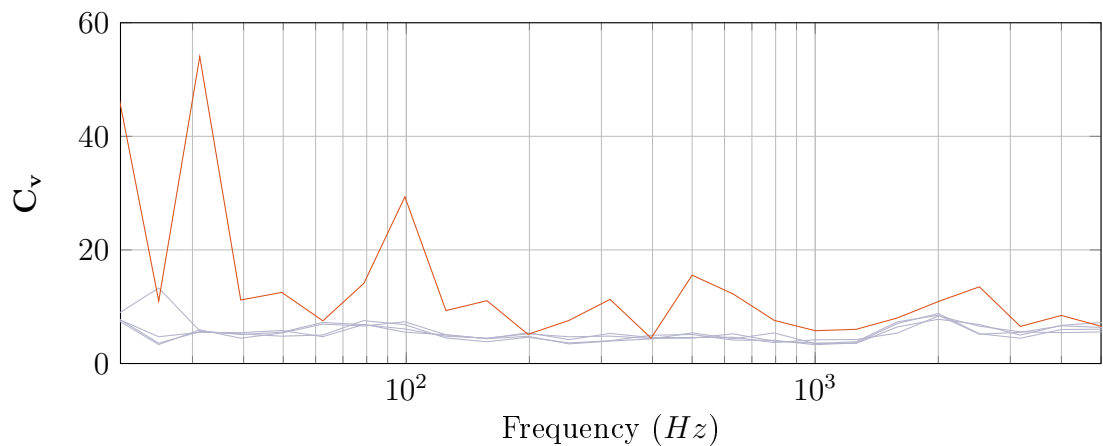


Figure 7.18: Coefficient of variation for each blocked force and the predicted operational cavity pressure in 3rd octave bands.

7.4 CONCLUDING REMARKS

This Chapter was largely concerned with the construction of a virtual acoustic prototype as part of an experimental case study. The assembly considered was a 4-footed pump resiliently coupled to a cavity backed plate. Each component was independently characterised and subsequently coupled using a dynamic sub-structuring procedure. Blocked forces were the injected and the operational velocity and pressure responses predicted.

The source was characterised via its blocked force (determined in Chapter 6) and free mobility. The in-situ decoupling procedure outlined in Chapter 5 was attempted in order to determine the source's free mobility. Unfortunately the resulting mobility did not appear sufficiently independent. Instead, a directly measured free mobility was used. The resilient coupling elements were characterised by their transfer impedance, which was determined via the in-situ approach presented in Chapter 3. Lastly, the receiver was characterised directly via its free mobility/vibro-acoustic transfer function.

The coupled transfer mobilities between the source and remote DoFs were in good agreement with those measured directly, suggesting that the sub-structures' characterisations were sufficiently independent and, furthermore, that the sub-structuring procedure was successful. A direct comparison was not possible in the case of the predicted vibro-acoustic transfer function, although a comparison against other measurable transfer functions suggested that a sensible prediction had been made.

Operational predictions were made using both directly measured and sub-structured mobilities with over-determined and expected blocked forces (determined from a separate assembly). Reasonable levels of agreement were obtained in all cases with the primary resonance largely being predicted to within 1dB. Although some large deviations were encountered (expected considering the underlying assumptions and the lack of experimental optimisation), the results clearly demonstrate the potential application of a proposed methods in the construction of an experimental VAP.

CONCLUSION

This Thesis has been concerned with the development and application of in-situ measurement methods for the independent characterisation of structural assembly components. It was stated in Chapter 1 that the primary aim of this Thesis was to provide a comprehensive set of measurement methods so as to facilitate the construction of a virtual acoustic prototype, and the author believes that this aim has largely been fulfilled.

Following the introductory Chapters of 1 and 2, Chapter 3 introduced perhaps the main contribution of this Thesis, that is, a novel in-situ measurement method for the independent characterisation of coupling elements. Although there exist alternative methods, the general nature of the proposed in-situ approach avoids the limiting assumptions, such as blocking masses and rigid body dynamics, that are often required. As such, the in-situ approach is able to avoid the experimental shortcomings associated with these alternative methods, e.g. large, cumbersome test rigs, unrealistic source and receiver loading, etc. Additionally, this novel approach further benefits from the advantages associated with in-situ methods, that is, the ability to carry out measurements whilst the sub-structure of interest is under a representative mounting condition. The approach was formulated and two alternate relations were presented, requiring either partial or full interface excitations. Validation of the approach was achieved through numerical and experimental studies. These confirmed not only the independent nature of the acquired quantity, but that it was in fact the sought after dynamic transfer impedance/stiffness. Further to these validations a number of additional experimental studies were presented. These included non-resonant, resonant, single contact and multi-contact assemblies and highlighted the methods' application in more complex assemblies. The results obtained were encouraging in all cases, and highlighted the methods' ability to perform a broad frequency characterisation, up to 3kHz in some cases. It was noted, however, that

the inverse approach used in the characterisation appeared particularly sensitive to self consistency issues, for example poor reciprocity. That said, the resultant errors were often clearly identifiable and likely correctable via curve fitting or some alternative approach.

With clear advantages over alternative methods, the in-situ approach was further investigated, particularly with regards to its practical implementation. Consequently, Chapter 4 focused on the further development of the in-situ approach via the novel application of the state-of-the-art experimental methods, namely; the finite difference approximation, round trip identity and generalised transmissibility. These extensions not only illustrated novel applications of the respective methods, but allowed the in-situ approach to; simultaneously determine translational and rotational DoFs, avoid interface excitation through remote measurement positions, and replace source side excitations with operational forces, respectively. It was shown that via its application, the finite difference approximation is able to yield an independent rotational transfer impedance without requiring significant additional hardware. Such an extension is particularly valuable as it avoids the need for multiple test rigs. The dual interface extension to the round trip identity led to the formulation of a remote coupling interface mobility relation. This relation allowed for the coupling interface mobility matrix to be determined without requiring any excitations at the coupling interface, thus allowing for characterisation to be achieved with restricted interface access. Although used as a means to an end, the remotely determined dual interface mobilities may themselves be considered a novel result, which further illustrate the capabilities of the round trip concept. Furthermore, the stiffness results obtained through remote characterisation were in excellent agreement with those determined directly, whilst offering a number of potential advantages, including additional over-determination. The incorporation of generalised transmissibilities not only illustrated a novel application of the concept itself, but meant that 4 of the 6 mobility matrices required by the partial interface relation could be replaced by operationally determinable quantities, thus simplifying the measurement procedure. The results determined via the transmissibility extension were in excellent agreement with those acquired via the standard in-situ approach. The in-situ approach, alongside the above experimental extensions, clearly provides a robust and flexible characterisation method that is capable of avoiding many of the limitations posed by current methods, not to mention the experimental hurdles encountered in practical scenarios.

The in-situ characterisation approach discussed above constitutes only part of a full passive characterisation. The independent passive properties of both source and receiver sub-structures are also required if one is to construct a VAP. Chapter 5 introduced a novel in-situ decoupling procedure, based on the in-situ characterisation approach outlined through Chapters 3-4. Assuming (massless) spring-like coupling elements, the decoupling procedure is capable of determining the independent passive properties of resiliently coupled source and receiver sub-structures. This is achieved by first determining the transfer impedance of the coupling elements, then subsequently subtracting this from the source and receiver impedances. The in-situ decoupling approach was validated experimentally on a number of assembly types, including both single and multi-contact resonant assemblies and was shown to yield mobilities in good agreement with those determined from physically uncoupled sub-structures. This novel decoupling procedure provides an attractive means for acquiring the independent passive properties of source sub-structures, especially those that may not be readily freely suspended. Furthermore, being based on in-situ measurements, the passive properties are acquired whilst under representative mounting conditions, and therefore account for any local non-linearities such as pre-load, etc. Moreover, with the decoupling procedure being based on the in-situ characterisation approach, all of its experimental extensions are also applicable. This was illustrated through the remote extension where it was shown that the decoupling procedure could be carried out with limited access to the coupling interface (i.e. without excitation the coupling interface). Together, the in-situ characterisation and decoupling procedures provide a complete independent passive characterisation of source, receiver and coupling sub-structures, from entirely in-situ measurements.

Following the passive characterisation of an assembly's components one must determine an active quantity that describes the operational activity of the source sub-structure. This was the primary concern of Chapter 6. In keeping with the nature of this Thesis (that is, in-situ measurement methods) the active characterisation considered was that of the in-situ blocked force approach. Following an introduction of necessary theory, the experimental application of the approach was discussed, alongside methods for the assessment of uncertainties. With the concept of source uncertainty under consideration, a novel approach was proposed based on the acquisition of expected blocked forces from a sample space of determined solutions. The 'sample space' approach allowed for associated uncertainties (in the form of a blocked force covariance matrix) to be established. It was shown through a derivation of the 'law of error propagation' that these uncertainties may be propagated

through a prediction, thus providing a measure of uncertainty in the predicted target quantity. An experimental study confirmed the validity of the sample space approach with the expected blocked forces shown to be in excellent agreement with those of a standard over-determined solution. Such a result further suggests that the statistics of the sample space are relevant to the blocked forces and their associated uncertainties. Although far from a complete study, this investigation into source uncertainty may certainly be considered an appropriate starting point to what is clearly an important and largely unexplored research area. As part of the experimental study, on-board and transferability validations were performed, allowing for the propagation and assessment of the acquired source uncertainties. The propagated uncertainties were largely in agreement with the discrepancies between measured and predicted responses, suggesting that they are appropriate for describing some of the uncertainties involved. Although only a brief study, it is clear that the uncertainties associated with inversely determined blocked forces are an essential requirement if the VAP concept is to be used as a industrial design tool, where a level of confidence in a given prediction would generally be of interest.

In order to demonstrate the application of the proposed methods with regards to the construction of a virtual acoustic prototype an experimental case study was presented. The case study, presented in Chapter 7, was chosen such that it would be representative of an assembly that might be encountered in a practical scenario. The assembly under consideration was that of an electric pump resiliently coupled to a cavity backed plate. The aim was to construct a VAP of this assembly that was capable of predicting the operational response (structural velocity and cavity pressure) at a number of remote measurement positions. The sub-structured mobilities were shown to be in good agreement with those measured directly. Likewise, the sub-structured vibro-acoustic transfer functions also appeared sensible. Operational velocity response predictions were in good agreement with those directly measured, as were the internal cavity predictions, with propagated uncertainties highlighting the largest discrepancies. The level of agreement obtained from the case study clearly highlights the potential of the proposed methods and, in a more general sense, the concept of virtual acoustic prototyping as a whole.

Although largely successful, the case study presented in Chapter 7 highlights a number of areas where future work would be best spent. Firstly, with the in-situ decoupling procedure failing to successfully decouple the source pump, further investigation is certainly required. This would likely involve determining the influence

of in-plane and rotational DoFs, whilst carrying out some experimental optimisation. Also highlighted in the case study was the need for a further investigation into the uncertainties associated with the blocked forces *and* sub-structured mobilities. Although some of the operational disagreement was accounted for by the proposed uncertainty approach (an expected blocked force and associated covariance matrix), there remained discrepancies with no clear cause. In order for methods such as those presented in this Thesis to be adopted and used with confidence in an industrial setting one must be able to account for and identify the cause of a greater number of the uncertainties involved. Lastly, key in the success of the methods presented throughout this Thesis is the notion of self consistency. The requirements for self consistency however have not been established here. The author believes that in order for vibro-acoustic inverse methods, such those discussed in this work, to be adopted within industry further investigation is required into the nature of self consistency, and ways in which one may minimise its influence on experimentally determined data.

**PART V. APPENDICES AND
BIBLIOGRAPHY**

APPENDICES

A REGULARISATION

The concept of regularisation, at least in a mathematical sense, refers to a process whereby additional information is introduced so as to solve an ill-posed problem. An ill-posed problem, in the sense of Hadamard, is one that violates one of the following conditions; 1) the existence of a solution, 2) the uniqueness of a solution, or 3) the solution's behaviour changing continuously with initial conditions (stability condition). Inverse problems, such as those encountered within the field of vibro-acoustics, are often ill-conditioned as a result of unwanted measurement noise, neglected degrees of freedom or linear dependence of data.

Although numerous regularisation techniques exist [153], in the realms of experimental vibro-acoustics two particular methods tend to be in favour; Truncated Singular Value Decomposition (TSVD, also referred to as singular value rejection) [154] and Tikhonov regularisation [155]. Crucial in the development of both these is the concept of the Singular Value Decomposition (SVD).

Consider equation A.1 where b is an $n \times 1$ known vector (e.g. an observable response), A is an $m \times n$ known matrix (e.g. a measurable transfer function matrix), x is the $m \times 1$ unknown vector we wish to determine (e.g. operating forces) and e is an associated unknown error vector. This general scenario accounts for many of the inverse problems encountered, particularly within vibro-acoustics.

$$b = \mathbf{A}x + e \tag{A.1}$$

In an experimental setting an exact solution is often unattainable on account of the unknown error vector. However, an optimal solution, \tilde{x} , may be determined through the minimisation of,

$$e = \|b - \mathbf{A}\tilde{x}\|_2 \tag{A.2}$$

where $\|\cdot\|_2$ represents the Euclidean norm. The solution \tilde{x} is referred to as the least squares solution and may be determined through the SVD factorisation of \mathbf{A} . Formally, the SVD of an $m \times n$ real or complex matrix where, $m \geq n$, is given by,

$$\mathbf{A} = \mathbf{U}\mathbf{\Sigma}\mathbf{V}^T \quad (\text{A.3})$$

where $\mathbf{U} = [\mathbf{u}_1, \mathbf{u}_2, \dots, \mathbf{u}_m]$ is an $m \times m$ real or complex unitary matrix (has the property, $\mathbf{U}^H\mathbf{U} = \mathbf{U}\mathbf{U}^H = \mathbf{I}$, where H represents the Hermitian or conjugate transpose) containing what are referred to as the left-singular vectors, $\mathbf{\Sigma} = \text{diag}(\sigma_1, \sigma_2, \dots, \sigma_n)$ is an $m \times n$ rectangular diagonal matrix containing non-negative real numbers along its diagonal, and $\mathbf{V}^T = [\mathbf{v}_1, \mathbf{v}_2, \dots, \mathbf{v}_m]^T$ is an $n \times n$ real or complex unitary matrix containing the right-singular vectors. The diagonal entries of $\mathbf{\Sigma}$, σ_i are referred to as the singular values of \mathbf{A} and convention has them ordered in descending order such that, $(\sigma_1 \geq \sigma_2 \geq \dots \geq \sigma_n \geq 0)$. As σ_i tends to σ_n the associated singular vectors become more oscillatory and therefore tend to be more susceptible to noise induced error. The rank (number of linearly independent rows or columns) of \mathbf{A} is determined by the number of non-zero singular values present in $\mathbf{\Sigma}$. A matrix whose rank is less than its smallest dimension, $< \min\{m, n\}$ is said to be rank deficient, resulting in a violation of Hadamard's 2nd condition of uniqueness. Often linear dependencies in data are masked by measurement error, resulting in rank deficient matrices appearing full rank. Such cases are often highlighted by large condition numbers (defined as the ratio of the largest and smallest singular values, σ_1/σ_n) and are generally prone to numerical inversion errors [51, 52, 156].

It can be shown that from the SVD and, subsequent inverse of \mathbf{A} , the optimum solution \tilde{x} can be obtained,

$$\hat{x} = (\mathbf{U}\mathbf{\Sigma}\mathbf{V}^H)^{-1}b = \mathbf{V}\mathbf{\Sigma}^{-1}\mathbf{U}^Hb = \mathbf{A}^+b \quad (\text{A.4})$$

where the diagonal elements of $\mathbf{\Sigma}$ are replaced by their reciprocals, $1/\sigma_i$. Note that \mathbf{A}^+ is often referred to as the 'Moore-Penrose' pseudo-inverse of \mathbf{A} and corresponds to a least squares solution [142]. The application of the pseudo-inverse does not require a square matrix and thus allows for additional responses (equations) to be introduced, a method referred to as over-determination which, when implemented correctly, has been shown to reduce the severity of numerical inversion error [132]. However, an over-determined matrix can still suffer from large inversion error if ill-conditioned. Written more explicitly it can be seen that the lower order singular

values ($i \rightarrow n$) of \mathbf{A} in fact become the dominant contributions in the computation of its inverse,

$$\hat{x} = \sum_{i=1}^n \frac{\mathbf{u}_i \mathbf{v}}{\sigma_i} b. \quad (\text{A.5})$$

Consequently, in an experimental setting where effective rank deficient matrices may be involved (i.e. the lower order singular values are largely composed of noise and measurement error), there lies the potential for highly erroneous solutions to be formed. It is the aim of both TSVD and Tikhinov regularisation schemes to reduce this error by means of applying an attenuation factor, ϕ_i , to each of the singular values, so as to reduce the contribution of lower order terms.

$$\hat{x} = \sum_{i=1}^n \phi_i \frac{\mathbf{u}_i \mathbf{v}}{\sigma_i} b \quad (\text{A.6})$$

In a TSVD scheme the singular values are attenuated according to equation A.7, where any terms higher than a given rank r are completely rejected.

$$\phi_i = \begin{cases} 1 & i \leq r \\ 0 & i > r \end{cases} \quad (\text{A.7})$$

In a Tikhinov regularisation scheme ϕ_i is determined from the minimisation of the following cost function,

$$J = \min\{(\tilde{e}\tilde{e}^H) + \alpha(F^H F)\}. \quad (\text{A.8})$$

Unlike the least square approach the above cost function introduces a bias into the solution whose influence is determined by the regularisation parameter, α . The resulting value for ϕ_i is given by,

$$\phi_i = \frac{\sigma_i^2}{\sigma_i^2 + \alpha}. \quad (\text{A.9})$$

Essential in the introduction of a minimal bias is the determination of an optimal value of α . Numerous methods exist to aid in this determination, including the L-curve criterion, ordinary cross validation (OCV) and generalised cross validation (GCV) [48, 49].

B MATRIX IDENTITIES

Inversion sum:

$$(A^{-1} + B^{-1})^{-1} = A(A + B)^{-1}B = B(A + B)^{-1}A \quad (\text{B.10})$$

Matrix inversion lemma:

$$(A + BCD)^{-1} = A^{-1}B(C^{-1} + DA^{-1}B)^{-1} \quad (\text{B.11})$$

Pseudo-inverse transpose:

$$(\mathbf{A}^{\mathbf{T}})^+ = (\mathbf{A}^+)^{\mathbf{T}} \quad (\text{B.12})$$

C SUMMARY OF ASSEMBLY DETAILS

Tag	Type	Assembly Details
A	MIM	Source mass 0.86kg, receiver mass 0.68kg, resilient element: Continental CONTITECH 27 796 25-29
B	MIM	Source mass 1.8kg, receiver mass 0.86kg, resilient element: Continental CONTITECH 27 796 25-29
C	MIM	Source mass 0.68kg, receiver mass 0.86kg, resilient element: Fibet 2525vv18 60 IRHD
D	MIM	Source mass 0.68kg, receiver mass 3.25kg, resilient element: Fibet 2525vv18 60 IRHD
E	MIP	Source mass 0.86kg, receiver plate $50\text{cm} \times 75\text{cm} \times 0.7\text{cm}$, resilient element: Fibet 2525vv18 60 IRHD
F	BIP	Source beam ($5\text{cm} \times 25\text{cm} \times 0.9\text{cm}$), receiver plate ($50\text{cm} \times 75\text{cm} \times 0.7\text{cm}$), resilient element: Fibet 2525vv18 60 IRHD
G	BI(2)P	Source beam ($3.7\text{cm} \times 45\text{cm} \times 0.9\text{cm}$), receiver plate ($50\text{cm} \times 75\text{cm} \times 0.7\text{cm}$), resilient element: Fibet 2525vv18 60 IRHD
H	MIM	Source mass 0.86kg, receiver mass 3.2kg, resilient element: Continental CONTITECH 27 796 25-29
I	MIM	Source mass 0.86kg, receiver mass 5.1kg, resilient element: Continental CONTITECH 27 796 25-29
J	MIM	Source mass 0.86kg, receiver mass 18.3kg, resilient element: Continental CONTITECH 27 796 25-29
K	EpI(4)P	Electric pump, perspex plate ($34.5\text{cm} \times 50\text{cm} \times 1\text{cm}$), resilient element model number: Fibet 1413vv10 60 IRHD
L	EpI(4)P	Electric pump, perspex plate ($50\text{cm} \times 75\text{cm} \times 0.7\text{cm}$), resilient element model number: Fibet 1413vv10 45 IRHD
M	MIM	Source mass 0.678kg, receiver mass 0.858kg, resilient element model number: Fibet 1413vv10 60 IRHD
N	Bx	Chipboard box (cavity: $60\text{cm} \times 46\text{cm} \times 48\text{cm}$, top panel: $46\text{cm} \times 52\text{cm} \times 1.8\text{cm}$)
O	EpI(4)Bx	Electric pump, chipboard box, resilient element model number: Fibet 1413vv10 60 IRHD

Table 8.1: Summary of details on the construction of experimental assemblies.

D MATRIX REDUCTION

The reduction process used to arrive at Equation 6.3 is outlined here. We begin with the assembly impedance relation,

$$\begin{bmatrix} \mathbf{f}_{S_i} \\ 0 \\ 0 \end{bmatrix} = \begin{bmatrix} \mathbf{Z}_{S_{ii}} & \mathbf{Z}_{S_{ic}} & 0 \\ \mathbf{Z}_{S_{ci}} & \mathbf{Z}_{C_{cc}} & \mathbf{Z}_{R_{cb}} \\ 0 & \mathbf{Z}_{R_{bc}} & \mathbf{Z}_{R_{bb}} \end{bmatrix} \begin{bmatrix} \mathbf{v}_{C_i} \\ \mathbf{v}_{C_c} \\ \mathbf{v}_{C_b} \end{bmatrix}. \quad (\text{D.13})$$

Writing the top two lines of the above equation out explicitly we have,

$$\mathbf{f}_{S_i} = \mathbf{Z}_{S_{ii}} \mathbf{v}_{C_i} + \mathbf{Z}_{S_{ic}} \mathbf{v}_{C_c} \quad (\text{D.14})$$

$$\mathbf{0} = \mathbf{Z}_{S_{ci}} \mathbf{v}_{C_i} + \mathbf{Z}_{C_{cc}} \mathbf{v}_{C_c} + \mathbf{Z}_{C_{cb}} \mathbf{v}_{C_b} \quad (\text{D.15})$$

We must first rearrange the latter for \mathbf{v}_{C_i} , before substituting it into the former. Subtracting $\mathbf{Z}_{S_{ci}} \mathbf{v}_{C_i}$ from each side of Equation D.15.

$$-\mathbf{Z}_{S_{ci}} \mathbf{v}_{C_i} = \mathbf{Z}_{C_{cc}} \mathbf{v}_{C_c} + \mathbf{Z}_{C_{cb}} \mathbf{v}_{C_b} \quad (\text{D.16})$$

Pre-multiplication of each side by the negative inverse matrix $-\mathbf{Z}_{S_{ci}}^{-1}$,

$$\mathbf{v}_{C_i} = -\mathbf{Z}_{S_{ci}}^{-1} (\mathbf{Z}_{C_{cc}} \mathbf{v}_{C_c} + \mathbf{Z}_{C_{cb}} \mathbf{v}_{C_b}) \quad (\text{D.17})$$

following substitution into Equation D.14 yields,

$$\mathbf{f}_{S_i} = -\mathbf{Z}_{S_{ii}} \mathbf{Z}_{S_{ci}}^{-1} (\mathbf{Z}_{C_{cc}} \mathbf{v}_{C_c} + \mathbf{Z}_{C_{cb}} \mathbf{v}_{C_b}) + \mathbf{Z}_{S_{ic}} \mathbf{v}_{C_c}. \quad (\text{D.18})$$

Pre-multiplication of both sides by $-(\mathbf{Z}_{S_{ii}} \mathbf{Z}_{S_{ci}}^{-1})^{-1} = -\mathbf{Z}_{S_{ci}} \mathbf{Z}_{S_{ii}}^{-1}$,

$$\mathbf{Z}_{S_{ci}} \mathbf{Z}_{S_{ii}}^{-1} \mathbf{f}_{S_i} = -(\mathbf{Z}_{C_{cc}} \mathbf{v}_{C_c} + \mathbf{Z}_{C_{cb}} \mathbf{v}_{C_b}) + \mathbf{Z}_{S_{ci}} \mathbf{Z}_{S_{ii}}^{-1} \mathbf{Z}_{S_{ic}} \mathbf{v}_{C_c}. \quad (\text{D.19})$$

Collecting \mathbf{v}_{C_c} terms we arrive at,

$$-\mathbf{Z}_{S_{ci}} \mathbf{Z}_{S_{ii}}^{-1} \mathbf{f}_{S_i} = (-\mathbf{Z}_{S_{ci}} \mathbf{Z}_{S_{ii}}^{-1} \mathbf{Z}_{S_{ic}} + \mathbf{Z}_{C_{cc}}) \mathbf{v}_{C_c} + \mathbf{Z}_{C_{cb}} \mathbf{v}_{C_b} \quad (\text{D.20})$$

which may be recast into matrix form along with the bottom row of Equation D.13.

$$\begin{bmatrix} -\mathbf{Z}_{S_{ci}}\mathbf{Z}_{S_{ii}}^{-1}\mathbf{f}_{S_i} \\ 0 \end{bmatrix} = \begin{bmatrix} -\mathbf{Z}_{S_{ci}}\mathbf{Z}_{S_{ii}}^{-1}\mathbf{Z}_{S_{ic}} + \mathbf{Z}_{C_{cc}} & \mathbf{Z}_{R_{cb}} \\ \mathbf{Z}_{R_{bc}} & \mathbf{Z}_{R_{bb}} \end{bmatrix} \begin{bmatrix} \mathbf{v}_{C_c} \\ \mathbf{v}_{C_b} \end{bmatrix} \quad (\text{D.21})$$

This is the reduced form of Equation D.13 whereby the internal velocity \mathbf{v}_{C_i} has been cancelled out, yielding the blocked force term $-\mathbf{Z}_{S_{ci}}\mathbf{Z}_{S_{ii}}^{-1}\mathbf{f}_{S_i}$.

E EXPERIMENTAL CASE STUDY - IOA CONFERENCE PROCEEDING MANUSCRIPT

E.1 INTRODUCTION

A drive towards leaner engineering has seen the use of physical prototypes become a limiting factor in the development of new products. Consequently, alternative prototyping methods are of interest. With their ability to reduce cost, time to market and optimise products to higher levels of performance and reliability, virtual methods are generally considered the way forward. Methods for virtual prototyping with respect to visual design and engineering (i.e CAD and CAE) are particularly well developed. Unfortunately, the same cannot be said in the realm of acoustics. Although numerical methods such as FEA and BEM are able to predict, with some accuracy, the passive properties of an assembly, they lack the ability to confidently model the complex behaviour of vibro-acoustic source mechanisms. Consequently, the adoption of any virtual acoustic prototyping (VAP) methodology will require some element of experimental work. While attempts have been made at establishing an experimentally based VAP framework [7], lack of measurement protocols and clear guidelines has seen its adoption within industry hindered. It is therefore the aim of this paper to introduce a set of methodologies that together provide the tools required to construct virtual assemblies for use in the prediction of vibro-acoustic quantities. The aims of this paper may be more specifically stated as:

- 1 Introduce an independent characterisation method for sources of structure-borne sound.
- 2 Recap the classical impedance summation approach for dynamic sub-structuring.

- 3 Introduce a novel method for determining the independent transfer properties of resilient coupling elements.
- 4 Provide an experimental case study utilising the above methodologies.

E.2 SOURCE CHARACTERISATION: BLOCKED FORCE METHOD

The aim of any characterisation method is to determine some quantity that describes both the active and passive behaviour of a source in such a way that it may be used to make forward predictions under operational conditions. Depending on the method used this quantity may or may not be an independent property of the source. In this section the blocked force is introduced as an independent source quantity and an in-situ measurement method outlined.

With the characterisation of structure-borne sources having been a topic of interest for many decades numerous works have been completed in the field. Consequently, numerous methods have been put forward, including free velocity, operational interface force [30], blocked force [13, 56], the source descriptor [31], the characteristic power, mirror power and maximum available power [32] and pseudo forces [33]. Of these, the only standardised method (BS ISO 9611) is currently the free velocity. However, regardless of its standardisation the free velocity approach is seldom used in practise. Its lack of uptake may be put down to the practicality of simulating the required ‘freely suspended’ mounting condition as well as the potential variation in mounting conditions between characterisation and installation. A more common approach is the operational force method, notably within the automotive and aerospace sector [30, 46]. The operational force method, also referred to as inverse force identification, forms the basis of classical TPA (transfer path analysis) and has the advantage that it allows for measurements to be made in-situ, thus avoiding the discrepancy between mounting conditions. However, the operational forces obtained are not independent of the assembly and therefore significantly restrict the transferability of data. The blocked force approach aims to combine the advantages of both the free velocity and operational force methods by providing an independent source quantity from in-situ measurements.

Before considering the blocked force method it is perhaps useful to acknowledge the inverse force identification methodology which has become more or less standard practice. Let us consider two sub-structures, A and B , coupled at one or more

contact points, c , such that they form the assembly C . Sub-structure A may be considered a source when excited by a set of unknown, inaccessible internally operating forces at o , as in Figure 8.1.

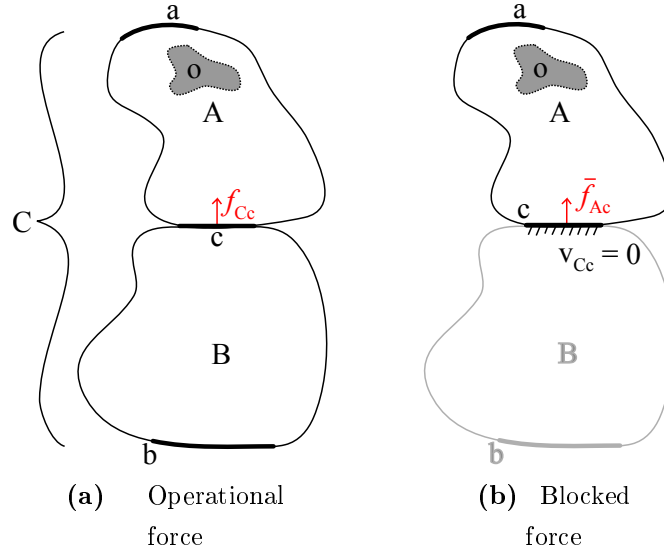


Figure 8.1: Source-receiver diagrams for operational and blocked forces.

Whilst in operation sub-structure B imparts a reaction force upon sub-structure A , $f_{C_c} \in \mathbb{C}^n$. This is a physical force and may be measured directly with the use of a force transducer or determined inversely via,

$$v_{C_c} = \mathbf{Y}_{\mathbf{B}_{cc}} f_{C_c} \implies f_{C_c} = \mathbf{Y}_{\mathbf{B}_{cc}}^{-1} v_{C_c} \quad (\text{E.22})$$

where for an n degree of freedom (DOF) system, $v_{C_c} \in \mathbb{C}^n$ is the operational velocity vector of the coupled assembly at the contact interface c and $\mathbf{Y}_{\mathbf{B}_{cc}} \in \mathbb{C}^{n \times n}$ is the contact interface mobility matrix of the (uncoupled) sub-structure B . This operational force is dependent upon the dynamic behaviour of sub-structure B and is therefore not an independent property of the source.

Suppose the source-receiver interface c were restrained such that $v_{C_c} = \mathbf{0}$, i.e the interface is blocked. With the influence of sub-structure B now removed, whatever force occurs at the interface is a property of sub-structure A and its internal forces only. In order for this restraint to be enforced a particular force must act at the interface, thus restricting its motion. This is the blocked force. It is worth noting that the blocked force is a fictional force and does not exist in reality, for it would

require an infinite impedance to truly restrain the interface. Nonetheless, it was shown by Moorhouse et al. [13] that the blocked force could be measured in-situ, i.e. without having to remove the source from its intended installation, using a similar inverse approach to that of Equation (E.22). The first equation of note is the following,

$$v_{C_c} = \mathbf{Y}_{\mathbf{C}_{cc}} \bar{f}_{A_c}, \quad (\text{E.23})$$

where for an n DOF system, $\bar{f}_{A_c} \in \mathbb{C}^n$ is the blocked force vector of sub-structure A at contact interface c , $\mathbf{Y}_{\mathbf{C}_{cc}} \in \mathbb{C}^{n \times n}$ is the coupled mobility matrix measured at the contact interface and $v_{C_c} \in \mathbb{C}^n$ is the operational velocity of the coupled assembly at the contact interface. The blocked force \bar{f}_{A_c} may be considered the solution to the above and solved for via the inverse mobility matrix $\mathbf{Y}_{\mathbf{C}_{cc}}^{-1}$. The determination of \bar{f}_{A_c} therefore requires a two part, passive and active measurement for $\mathbf{Y}_{\mathbf{C}_{cc}}$ and v_{C_c} respectively. $\mathbf{Y}_{\mathbf{C}_{cc}}$ is a symmetric matrix ($\mathbf{Y}_{\mathbf{C}_{cc}} = \mathbf{Y}_{\mathbf{C}_{cc}}^T$), measured with the source not in operation, whilst the vector v_{C_c} is measured with the source in operation.

Often when dealing with real life structures access is limited and the contact interface cannot be excited adequately. In such a case the response DoF may be relocated to b where forces may be applied with greater ease and following equation used to determine the blocked force vector \bar{f}_{A_c} ,

$$v_{C_b} = \mathbf{Y}_{\mathbf{C}_{cb}}^T \bar{f}_{A_c} \quad (\text{E.24})$$

where $\mathbf{Y}_{\mathbf{C}_{cb}}^T = \mathbf{Y}_{\mathbf{C}_{bc}} \in \mathbb{C}^{m \times n}$ is the coupled transfer mobility matrix between some set of arbitrary remote measurement positions b and the contact interface c , and $v_{C_b} \in \mathbb{C}^m$ is the operational velocity of the coupled assembly at the remote points b . The same two part measurement procedure is required as above, this time however as the operational responses are measured away from the contact interface Equation E.24 facilitates over-determination. In order to form a determined solution the number of remote points b , m , must be equal to the n DoFs being solved for, $m = n$. It is often desirable to solve the over-determined problem ($m > n$) as this provides a least squares solution, and has been shown to lead to reduced inversion error when implemented successfully. In such a case the standard matrix inverse is replaced by the pseudo inverse. When access to the contact interface is unrestricted Eqs E.23 and E.24 may be used in tandem to provide an over-determined solution,

$$\begin{Bmatrix} v_{C_c} \\ v_{C_b} \end{Bmatrix} = \begin{bmatrix} \mathbf{Y}_{C_{cc}} \\ \mathbf{Y}_{C_{cb}}^T \end{bmatrix} \bar{f}_{A_c} \quad (\text{E.25})$$

where the partitioned matrix formed from $\mathbf{Y}_{C_{cc}}$ and $\mathbf{Y}_{C_{cb}}^T$ is $\in \mathbb{C}^{(n+m) \times n}$ and the partitioned vector formed from v_{C_c} and v_{C_b} is $\in \mathbb{C}^{(n+m)}$.

Once blocked forces have been determined they may be transferred between assemblies and used in the forward prediction of vibro-acoustic quantities via a suitable transfer function, $\mathbf{H}_{C_{dc}}$. This transfer function must be for that of the coupled assembly and may be measured directly or predicted using a methodology such as dynamic sub-structuring.

$$v_{C_d} = \mathbf{H}_{C_{dc}} \bar{f}_{A_c} \quad (\text{E.26})$$

E.3 DYNAMIC SUB-STRUCTURING: IMPEDANCE APPROACH

Often when predicting structure-borne sound and vibration it is convenient to model an assembly in such a way that the frequency response functions (FRFs, also referred to as transfer functions) of the individual subsystems are obtained independently, then coupled together mathematically. This method is referred to as ‘dynamic sub-structuring’ (DS). Whilst the concept itself dates back as far as the 1960s, only in more recent years, with advancements in data acquisition has this technique become a useful tool in experimental vibro-acoustics [136]. An important requirement for this sub-structuring methodology is that the FRFs of the individual subsystems are obtained in a transferable manner, i.e. they are solely a property of the subsystem they represent. Since its conception numerous DSS methodologies have been developed. With the physics of the problem remaining unchanged these methods simply go about applying compatibility and equilibrium conditions between neighbouring elements in a different manner. The approach presented below may be referred to as the ‘classical impedance approach’ and is, in the author’s opinion, the most straightforward in terms of its implementation.

It is well understood from electro-mechanical analogues [157], that the coupled point impedance of two sub-structures is equal to the sum of the individual sub-structures impedances. Written simply as,

$$Z_{C_c} = Z_{A_c} + Z_{B_c} \quad (\text{E.27})$$

capitalised subscripts denote the sub-structure, whilst lower case denotes the coupling point. It is the application of this concept that allows us to form the classical impedance approach. Each sub-structure to be coupled must be defined in terms of its mobility matrix, which may be measured or modelled across an arbitrary number of points, providing that it includes those that are to be coupled. As coupling requires the summation of point impedances at connecting nodes, the mobility matrix of each sub-structure is first inverted, and subsequently block diagonalised so as to obtain the block diagonal impedance matrix,

$$\mathbf{Z}_{\text{diag}} = \begin{bmatrix} \mathbf{Y}_1^{-1} & & & \\ & \mathbf{Y}_2^{-1} & & \\ & & \ddots & \\ & & & \mathbf{Y}_N^{-1} \end{bmatrix} \quad (\text{E.28})$$

Each column of \mathbf{Z}_{diag} corresponds to an excitation at a given point on our uncoupled system, whilst each row corresponds to the response at a given point. By summing the rows and columns corresponding to the coupling nodes we obtained the impedance matrix of our coupled system. Such a summation is carried out conveniently by pre and post multiplication of the boolean localisation matrix, \mathbf{L} and its transpose. Details on the construction of \mathbf{L} can be found in the appendix of [136].

$$\mathbf{Z}_{\mathbf{C}} = \mathbf{L}\mathbf{Z}_{\text{diag}}\mathbf{L}^T \quad (\text{E.29})$$

Once the coupled impedance matrix, $\mathbf{Z}_{\mathbf{C}}$, has been determined the coupled mobility matrix, $\mathbf{Y}_{\mathbf{C}}$, may be obtained through inversion.

$$\mathbf{Y}_{\mathbf{C}} = \mathbf{Z}_{\mathbf{C}}^{-1} \quad (\text{E.30})$$

Providing that the source mobility is included as an element in its formulation, $\mathbf{Y}_{\mathbf{C}}$ may be used in conjunction with the blocked force of Equation E.26, allowing for predictions to be made on a ‘virtual’ assembly that may not physically exist. As mentioned previously, the above approach is reliant upon the individual sub-structure mobilities being determined independently. This is generally considered less of a problem for source and receiver sub-structures as their FRFs may be obtained experimentally through an approximated ‘free’ suspension or generated numerically using modelling techniques such as FEA. The problem arises in the case of coupling elements, particularly those that are of a resilient nature. Unlike source and

receiver sub-structures, resilient elements can only be measured whilst installed in some form of assembly, therefore methods for determining a reliable/independent quantity are limited. In the following section a novel in-situ measurement method for determining independent properties of coupling elements will be presented.

E.4 IN-SITU ISOLATOR CHARACTERISATION

Unlike source and receiver mobilities which may be measured directly, the independent property required for the characterisation of a resilient element [114], the dynamic transfer stiffness, is not so easily attained. Current methods [103, 111] including international standard BS ISO 10846 not only require cumbersome test rigs which necessitate that the resilient element be removed from its assembly, but their applications are generally limited to low frequencies. The following approach aims to provide a convenient and flexible method that allows for the dynamic transfer stiffness to be obtained in-situ and over a considerable frequency range.

Consider the SIR (source-isolator-receiver) system shown in Figure 8.2, whereby the sub-structure I may be made up of multiple isolators. If we consider the source inactive, the transfer impedance across I is defined as,

$$\bar{f}_{C_{c2}} = \mathbf{Z}_{\mathbf{I}_{c2c1}} v_{C_{c1}} \quad (\text{E.31})$$

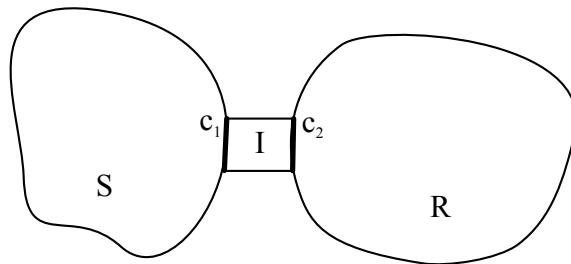


Figure 8.2: General source-isolator-receiver system.

where for an n DOF interface, $\bar{f}_{C_{c2}} \in \mathbb{C}^{\frac{n}{2}}$ is a resultant blocked force vector (with $\bar{\cdot}$ denoting the blocked condition) at interface c_2 due to an applied velocity vector, $v_{C_{c1}} \in \mathbb{C}^{\frac{n}{2}}$, and $\mathbf{Z}_{\mathbf{I}_{c2c1}} \in \mathbb{C}^{\frac{n}{2} \times \frac{n}{2}}$ is the transfer impedance matrix relating the two [14]. The blocked condition at c_2 effectively removes the influence of the receiver structure on the transfer impedance. Similarly, an applied velocity at c_1 is applied irrespective of the source structures passive response. We can therefore assume that the transfer impedance is independent of both the source and receiver and is solely

a property of the isolator. The transfer impedance $\mathbf{Z}_{\mathbf{I}_{c2c1}}$ may be obtained through the inversion of a measured contact interface mobility matrix,

$$\begin{bmatrix} \mathbf{Z}_{\mathbf{C}_{c1c1}} & \mathbf{Z}_{\mathbf{I}_{c1c2}} \\ \mathbf{Z}_{\mathbf{I}_{c2c1}} & \mathbf{Z}_{\mathbf{C}_{c2c2}} \end{bmatrix} = \begin{bmatrix} \mathbf{Y}_{\mathbf{C}_{c1c1}} & \mathbf{Y}_{\mathbf{C}_{c1c2}} \\ \mathbf{Y}_{\mathbf{C}_{c2c1}} & \mathbf{Y}_{\mathbf{C}_{c2c2}} \end{bmatrix}^{-1}. \quad (\text{E.32})$$

The dynamic transfer stiffness, relating force to displacement rather than velocity, may be obtained by multiplying $\mathbf{Z}_{\mathbf{I}_{c2c1}}$ by $i\omega$,

$$i\omega\mathbf{Z}_{\mathbf{I}_{c2c1}} = \mathbf{K}_{\mathbf{I}_{c2c1}}. \quad (\text{E.33})$$

The above method harbours no limitations with regards to the impedance of the coupling element, providing that it is linear and time invariant. Moreover, the method is not restricted to use on resilient elements under linear compression and may be applied to elements under any level of pre-load providing that the applied forces during operation remain locally linear. An experimental validation of the above methodology may be found in [132] along with an extension to cater for rotational degrees of freedom and remote measurement positions.

E.5 CASE-STUDY

The case study presented below involves the construction of virtual assembly, whereby a 4 footed electric pump is resiliently mounted to a perspex plate. The same assembly has been constructed physically for validation purposes. Due to hardware limitations only the out-of-plane z degrees of freedom (DOF) were considered, however the above methodologies may be extended to cater for in-plane and rotational DOF.

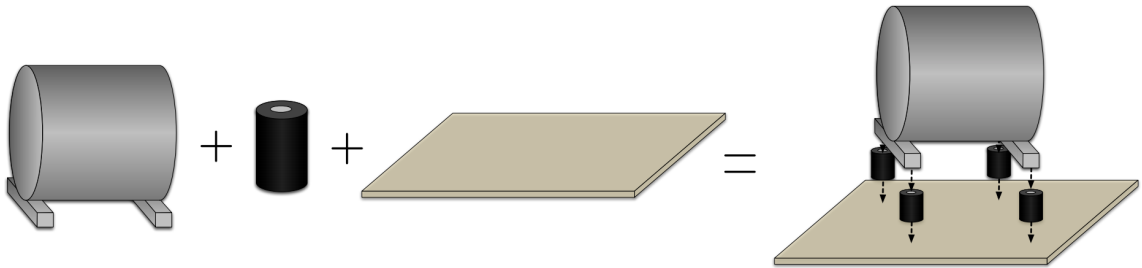


Figure 8.3: Diagrammatic illustration of case study.

The active and passive properties of the electric pump source were first to be determined. For the measurement of free mobility, as required by the dynamic sub-structuring methodology, the source was suspended via elastic bungee cords and the contact interface mobility matrix measured. The source was resiliently mounted to a different assembly and its blocked forces were determined. The two part measurement procedure outlined in Section E.2 was followed. First the coupled contact interface mobility matrix was measured. The pump was then turned on and the operational velocities recorded. Blocked forces were then determined as per Equation E.23. Similarly to the source, the free mobility of the perspex receiver plate was measured by mounting said plate on a set of soft resilient mounts. Whilst measuring the receiver plate's mobility an additional point was included so as to facilitate an operational prediction at a remote location.

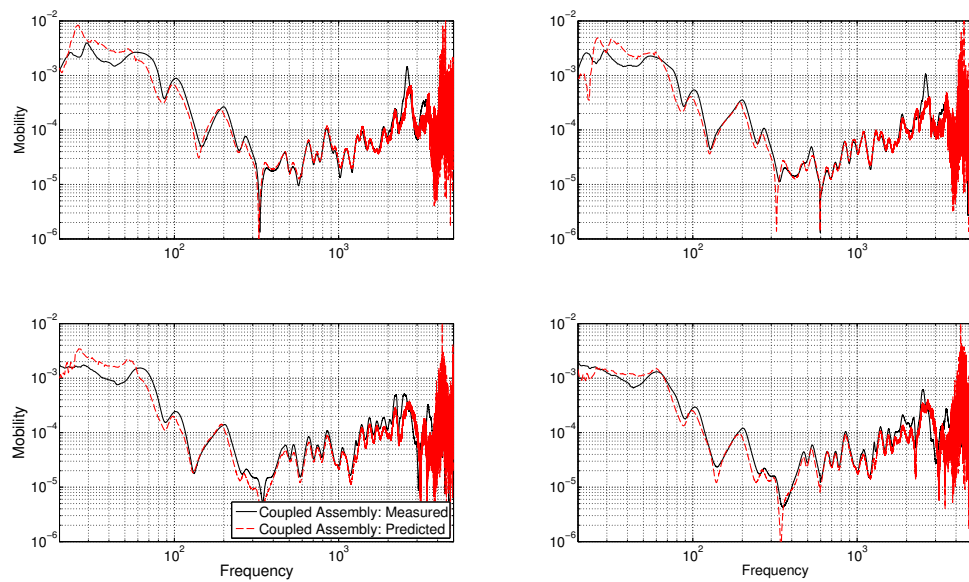


Figure 8.4: Sub-structured and directly measured transfer mobilities between each foot of the source to the remote receiver point.

Lastly, the resilient elements coupling the source and receiver were characterised using the in-situ method presented in Section 3. The same approach was adopted as in [132] where the resilient elements were mounted between two mass like structures. The measurement and subsequent inversion of the contact interface mobility matrix yielded an independent transfer impedance. It is important to note that the method outlined in Section 2 determines an independent *transfer* impedance. The point impedances obtained are still properties of the assembly and therefore not transferable. However, it is well known that below the first internal resonance a resilient mount will behave as a massless spring, corresponding to point and transfer

impedances of equal magnitude. The full impedance matrix of the coupling element may thus be built from the transfer properties alone.

Taking the passive properties of each element and following the method outlined in Section 3 the coupled mobility of the assembly was determined. With 4×4 source and 5×5 receiver mobility matrices, the resultant coupled mobility matrix was 9×9 . Shown in Figure 8.4 are the directly measured (on the physical assembly) and sub-structured transfer mobilities between each foot of the source and the remote receiver point. It can be seen that a reasonable prediction is achieved across the majority of the frequency range, up to approximately 3kHz. Above this noise contaminates the prediction. This noise is a result of the limited dynamic range of the hardware used in the isolator characterisation. Moreover, a slight over prediction can be observed in the low frequency range across all predictions. It is proposed that this is a result of neglected rotational and in-plane DoFs that may contribute to the physical coupling mechanisms at lower frequencies. Regardless of these errors, these results clearly demonstrate the potential of both the in-situ isolator characterisation and dynamic sub-structuring methodologies presented above.

Following the prediction of the assembly's coupled mobility matrix the blocked forces (determined from an alternate assembly) may be applied and an operational prediction made for the remote receiver point.

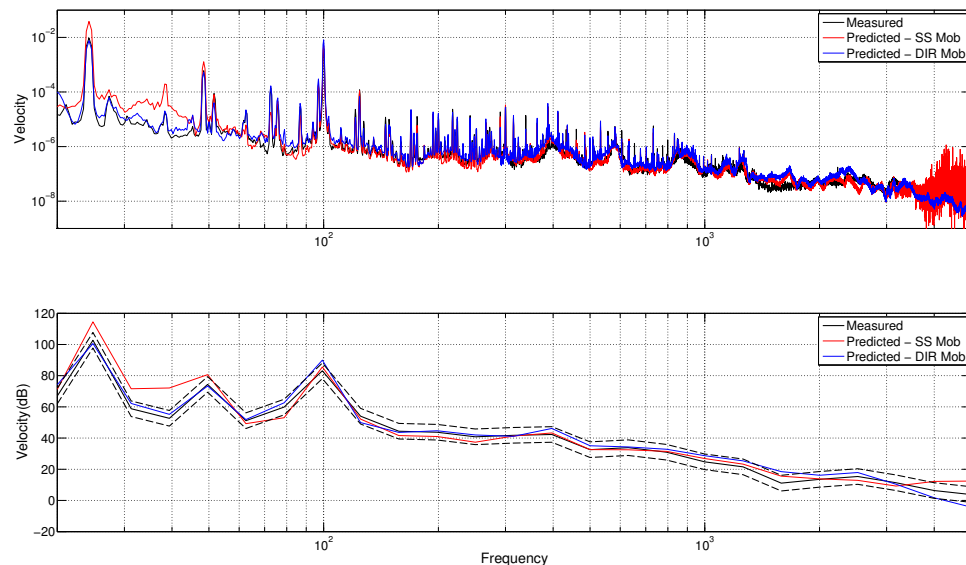


Figure 8.5: Operational response of assembly at remote measurement point. Responses measured directly and predicted (using sub-structured and directly measured transfer mobilities) using blocked forces determined from another assembly. Lower plot shows the above in one third octave bands with ± 5 dB for greater clarity.

Shown in Figure 8.5 are a pair of operational predictions along with a directly measured velocity response. Shown in red is the sub-structured prediction made using the predicted mobility presented in Figure 8.4. In blue is an equivalent prediction made using the directly measured mobility, also shown in Figure 8.4. Lastly, in black is the directly measured velocity response made whilst the physical assembly was in operation. It can be seen that a reasonable prediction is obtained across the majority of the frequency range. At low frequencies the result of the over predicted sub-structured mobilities can be seen to contaminate predictions. Moreover, the effect of the high frequency noise error can also be seen. Regardless of these errors the results provide a promising account of the above methodologies and hopefully highlights their potential applications.

Once the virtual assembly has been constructed elements may be replaced or modified at will, allowing for quick design changes to be assessed quantitatively (or subjectively if the prediction is auralised) i.e. the installation of different isolators or additional damping in receiver structure.

E.6 CONCLUSION

With the aim of providing a set of tools for the construction for virtual assemblies, three experimentally based methodologies have been introduced, namely; in-situ blocked force characterisation, impedance based dynamic sub-structuring and a novel in-situ isolator characterisation method. Through an experimental case-study it has been shown that together these methods allow for the accurate prediction of both passive and active responses across a ‘virtual’ assembly. Some errors were encountered, although it is believed that these are due to neglected DoFs and that additional hardware would counter this.

BIBLIOGRAPHY

- [1] A.B. Garcia, R.P. Gocke Jr, and N.P. Johnson Jr. Virtual prototyping: concept to production. Technical report, DTIC Document, 1994.
- [2] J.C. Schaaf Jr and F.L. Thompson. System concept development with virtual prototyping. In *Proceedings of the 29th conference on Winter simulation*, pages 941–947. IEEE Computer Society, 1997.
- [3] S. Dowlatshahi. Purchasing’s role in a concurrent engineering environment. *International Journal of Purchasing and Materials Management*, 28:21, 1992.
- [4] Y. Asiedy and P. Gu. Product life cycle cost analysis: state of the art review. *International journal of production research*, 36(4):883–908, 1998.
- [5] A.T. Moorhouse. Virtual acoustic prototypes: Listening to machines that don’t exist. *Acoustics Australia*, 33(3):97–105, 2005.
- [6] R. Lyon. *Designing for product sound quality*. CRC Press, 2000.
- [7] G. Pavic. Noise synthesis technology: A tool for virtual noise prototyping. In *19th International Congress on Mechanical Engineering*, 2007.
- [8] K. Janssens, A. Vecchio, P. Mas, H. Van der Auweraer, and P. Van de Ponsele. Sound quality evaluation of structural design changes in a virtual car sound environment. In *Proceedings of the Institute of Acoustic*, volume 26, 2004.
- [9] K. Janssens, A. Vecchio, P. Mas, H. Van der Auweraer, and P. Van de Ponsele. Sound quality evaluation of structural design changes in a virtual car sound environment. In *Proceedings of the Institute of Acoustic*, 2004.
- [10] K. Genuit and R. Bray, W. Prediction of sound and vibration in a virtual automobile. *Sound and Vibration*, 36(7):12–19, 2002.
- [11] H. van der Auweraer and K. Janssens. Virtual prototyping for sound quality design of automobiles. *Sound and Vibration*, 41(4):26, 2007.
- [12] M.V. Van Der Seijs, D. De Klerk, and D.J. Rixen. General framework for transfer path analysis: History, theory and classification of techniques. *Mechanical Systems and Signal Processing*, pages 1–28, 2015.

-
- [13] A.T. Moorhouse, A.S. Elliott, and T.A. Evans. In situ measurement of the blocked force of structure-borne sound sources. *Journal of Sound and Vibration*, 325(4-5):679–685, sep 2009.
- [14] G.J. O’Hara. Mechanical impedance and mobility concepts. *The journal of the Acoustical Society of America*, 41(5):1180–1184, 1967.
- [15] International Organisation for Standardisation. BS ISO 7626-51 2011 Mechanical vibration and shock - Experimental determination of mechanical mobility, Part 1: Basic terms and definitions, and transducer specifications, 2011.
- [16] International Organisation for Standardisation. BS 6897-2 1990, ISO 7626-2 1990 Experimental determination of mechanical mobility - Part 2: Measurement using single-point translation excitation with an attached vibration exciter, 1990.
- [17] International Organisation for Standardisation. BS 6897-5 1995, ISO 7626-5 1994 Experimental determination of mechanical mobility - Part 5: Measurement using impact excitation with an exciter which is not attached to the structure, 1994.
- [18] F.J. Fahy. The vibro-acoustic reciprocity principle and applications to noise control. *Acta Acustica united with Acustica*, 81(6):544–558, 1995.
- [19] The European Parliament and the Council of the European Union. DIRECTIVE 2000/14/EC OF THE EUROPEAN PARLIAMENT AND OF THE COUNCIL of 8 May 2000 - On the approximation of the laws of the Member States relating to the noise emission in the environment by equipment for use outdoors. *Official Journal of the European Communities*, 162:1–78, 2000.
- [20] European Commission. Commission regulation (EU) No 666/2013 of 8th July - Implementing Directive 2009/125/EC of the European Parliament and of the Council with regard to ecodesign requirements for vacuum cleaners. *Official Journal of the European Union*, 285(24):24–34, 2013.
- [21] The European Parliament and the Council of the European Union. Regulation (EU) No 540/2014 of the European Parliament and of the Council of 16 April 2014 - On the sound level of motor vehicles and of replacement silencing systems, and amending Directive 2007/46/EC and repealing Directive 70/157/EEC. *Official Journal of the European Union*, 158:131–195, 2014.
- [22] Statutory Instruments - Health and Safety. The Supply of Machinery (Safety) Regulations, 2008.
- [23] C. Churchill S. Maluski and T.J. Cox. Sound quality testing and labelling of domestic appliances in the UK. In *Proceedings of Internoise*, pages 1–8, 2004.

-
- [24] T.T. Wolde and G.R. Gedefelt. Development of standard measurement methods for structureborne sound emission. *Noise Control Engineering Journal*, 28(1), 1987.
- [25] M.M. Späh and B.M. Gibbs. Reception plate method for characterisation of structure-borne sound sources in buildings: Assumptions and application. *Applied Acoustics*, 70(2):361–368, 2009.
- [26] International Organisation for Standardisation. BS EN ISO 3741 : 2010 Acoustics - Determination of sound power levels and sound energy levels of noise sources using sound pressure - Precision methods for reverberation test rooms (ISO 3741:2010).
- [27] International Organisation for Standardisation. BS EN ISO 3745 : 2010 Acoustics - Determination of sound power levels and sound energy levels of noise sources using sound pressure - Precision methods for anechoic rooms and hemi-anechoic rooms, 2012.
- [28] International Organisation for Standardisation. BE EN ISO 5136 : 2009 Acoustics - Determination of sound power radiated into a duct by fans and other air-moving devices - In-duct method.
- [29] International Organisation for Standardisation. BS ISO 9611:1996 Acoustics - Characterization of sources of structure-borne sound with respect to sound radiation from connected structures - Measurement of velocity at the contact points of machinery when resiliently mounted, 1996.
- [30] B.J. Dobson and E. Rider. A review of the indirect calculation of excitation forces from measured structural response data. In *Proceedings of the Institution of Mechanical Engineers, Part C: Journal of Mechanical Engineering Science*, 1990.
- [31] J.M. Mondot and B. Petersson. Characterization of structure-borne sound sources: the source descriptor and the coupling function. *Journal of Sound and Vibration*, 114(3):507–518, 1987.
- [32] A.T. Moorhouse. On the characteristic power of structure-borne sound sources. *Journal of Sound and Vibration*, 248(3):441–459, 2001.
- [33] M.H.A Janssens and J.W Verheij. A pseudo-forces methodology to be used in characterization of structure-borne sound sources. *Applied Acoustics*, 61(3):285–308, 2000.
- [34] J.M. Mondot. Structure-borne sound source characterization, part 3: multi-point installed source structure. Technical report, Chalmers University of Technology, Department of Building Acoustics, Goteborg, Sweden, 1986.

- [35] B. Petersson and J. Plunt. On effective mobilities in the prediction of structure-borne sound transmission between a source structure and a receiving structure, part I: Theoretical background and basic experimental studies. *Journal of Sound and Vibration*, 82(4):531–540, 1982.
- [36] B. Petersson and J. Plunt. On effective mobilities in the prediction of structure-borne sound transmission between a source structure and a receiving structure, part II: Procedures for the estimation of mobilities. *Journal of Sound and Vibration*, 82(4):531–540, 1982.
- [37] B. Petersson. Structure-borne sound source characterization. In *International Congress on Sound and Vibration*, pages 1751–1765, Stockholm, Sweden, 2003.
- [38] European Standard. EN 12354-5. Building acoustics - Estimation of acoustic performance of buildings from the performance of elements - Part 5: Sounds levels due to the service equipment., 2009.
- [39] M.M. Späh and B.M. Gibbs. Reception plate method for characterisation of structure-borne sound sources in buildings: Installed power and sound pressure from laboratory data. *Applied Acoustics*, 70(11-12):1431–1439, 2009.
- [40] M. Späh, H.M. Fischer, and B. Gibbs. Measurement of structure-borne sound power of mechanical installations. In *DAGA*, pages 173–174, 2004.
- [41] European Standard. EN 15657-1 : 2009 - Acoustic properties of building elements and of buildings. Laboratory measurement of airborne and structure borne sound from building equipment., 2009.
- [42] A.T. Moorhouse and B.M. Gibbs. Prediction of the structure-borne noise emission of machines: development of a methodology. *Journal of Sound and Vibration*, 167(2):223–237, 1993.
- [43] A.T. Moorhouse and B. Gibbs. Measurement of structure-borne sound emission from resiliently mounted machines in situ. *Journal of Sound and Vibration*, 180(1):143–161, 1995.
- [44] A.T. Moorhouse, T.A. Evans, and A.S. Elliott. Some relationships for coupled structures and their application to measurement of structural dynamic properties in situ. *Mechanical Systems and Signal Processing*, 25(5):1574–1584, jul 2011.
- [45] A.T. Moorhouse and A.S. Elliott. The "round trip" theory for reconstruction of Green's functions at passive locations. *The Journal of the Acoustical Society of America*, 134(5):3605–3612, nov 2013.

- [46] J. Plunt. Finding and fixing vehicle NVH problems with transfer path analysis. *Sound and vibration*, 39(11):12–17, 2005.
- [47] H. Lee and Y. Park. Error analysis of indirect force determination and a regularisation method to reduce force determination error. *Mechanical Systems and Signal Processing*, 9(6):615–633, 1995.
- [48] A.N. Thite and D.J. Thompson. The quantification of structure-borne transmission paths by inverse methods. Part 1: Improved singular value rejection methods. *Journal of Sound and Vibration*, 264(2):411–431, jul 2003.
- [49] A.N. Thite and D.J. Thompson. The quantification of structure-borne transmission paths by inverse methods. Part 2: Use of regularization techniques. *Journal of Sound and Vibration*, 264(2):433–451, jul 2003.
- [50] M.H.A. Janssens and J.W. Verheij. Two applications of the pseudo-forces method for characterizing the source strength for structure-borne sound. In *Internoise*, pages 1335–1338, Liverpool, UK, 1996.
- [51] M.H.A. Janssens, J.W. Verheij, and D.J. Thompson. The use of an equivalent forces method for the experimental quantification of structural sound transmission in ships. *Journal of Sound and Vibration*, 226(2):305–328, sep 1999.
- [52] J.W. Verheij. Inverse and reciprocity methods for machinery noise source characterisation and sound path quantification. Part 2: Transmission paths. *International Journal of Acoustics and Vibration*, 2(3):103–112, 1997.
- [53] M. Ohlrich and A. Crone. An equivalent force description of gear-box sources applied in prediction of structural vibrational in wind turbines. *Proceedings of Inter-noise 88*, 1988.
- [54] S. Laugesen and M. Ohlrich. The vibrational source strength descriptor using power input from equivalent forces: a simulation study. *Acta Acustica*, 1994.
- [55] F. Fahy and J. Walker. *Advance applications in acoustics, noise and vibration*. Spoon Press, 2004.
- [56] D. De Klerk. *Dynamic response characterization of complex systems through operational identification and dynamic sub-structuring*. PhD thesis, TU Delft, 2009.
- [57] A.S. Elliott. *Characterisation of structure borne sound sources in-situ*. PhD thesis, University of Salford, 2009.
- [58] A.S. Elliott and A.T. Moorhouse. Characterisation of structure borne sound sources from measurement in-situ. In *Proceedings of Euronoise*, pages 1477–1482, 2008.

- [59] D. De Klerk, D.J. Rixen, and C. Valentin. An experimental gear noise propagation method for a gearbox on a test bench. In *Proceedings of the 25th International Modal Analysis Conference - IMAC*, 2007.
- [60] D. Lennström, M. Olsson, F. Wullens, and A. Nykänen. Validation of the blocked force method for various boundary conditions for automotive source characterization. *Applied Acoustics*, 102(1):108–119, 2016.
- [61] A.S. Elliott, J.W.R. Meggitt, and A.T. Moorhouse. Blocked forces for the characterisation of structure borne noise. In *Proceedings of Internoise 2015*, pages 5798–5805, San Fransisco, 2015.
- [62] H.K. Lai, A.T. Moorhouse, and B. Gibbs. Experimental round-robin evaluation of structure-borne sound source force-power test methods. *Noise Control Engineering Journal*, 64(2):170–180, 2016.
- [63] G. Banwell and R. Faventi. Assessment of experimental techniques to characterise the vibration source strength of a motor radially mounted with resilient elements. In *ISMA*, Leuven, 2016.
- [64] C. Brecher, S. Bäumlner, and M. Daniels. Prediction of dynamics of modified machine tool by experimental sub-structuring. In *Dynamics of Coupled Structures, Volume 1*, pages 297–305, 2014.
- [65] A. S. Elliott, A. T. Moorhouse, T. Huntley, and S. Tate. In-situ source path contribution analysis of structure borne road noise. *Journal of Sound and Vibration*, 332(24):6276–6295, 2013.
- [66] H.K. Lai. Alternative test methods for measuring structure-borne sound power. In *Proceedings of Internoise*, Honolulu, Hawaii, USA, 2006.
- [67] Y.I. Bobrovnitskii. A theorem on the representation of the field of forced vibrations of a composite elastic system. *Acoustical Physics*, 47(5):586–589, 2001.
- [68] W. D’Ambrogio and A. Sestieri. A unified approach to sub-structuring and structural modification problems. *Shock and Vibration*, 11:295–309, 2004.
- [69] B.F. Smith, P.E. Bjorstad, and W.D. Gropp. *Domain decomposition: parallel multi-level methods for elliptic partial differential equations*. Cambridge University Press, Cambridge, 1 edition, 1996.
- [70] H.A. Schwarz. *Gesammelte mathematische abhandlungen*. Springer-Verlag, Berlin, vol 2 edition, 1890.

- [71] W. C. Hurty. Vibrations of structural systems by component mode synthesis. *Journal of Engineering Mechanics*, 86(4):51–69, 1960.
- [72] W.C. Hurty. Dynamic analysis of structural systems using component modes. *AIAA Journal*, 3(4):678–685, 1965.
- [73] J.R. Crowley, A.L. Klosterman, G.T. Rocklin, and H. Vold. Direct structural modification using frequency response functions. In *Proceedings of the Second International Modal Analysis Conference*, pages 58–65, Bethel, 1984.
- [74] B. Jetmundsen, R.L. Bielawa, and W.G. Flannelly. Generalized frequency domain substructure synthesis. *Journal of the American Helicopter Society*, 33(1):55–64, 1988.
- [75] D.J. Rixen, A. Boogaard, M.V. van der Seijs, G. van Schothorst, and T. van der Poel. Vibration source description in substructuring: a theoretical depiction. *Mechanical Systems and Signal Processing*, 60-61:498–511, 2015.
- [76] D.J. Ewins. *Modal testing: theory and practice*, 1984.
- [77] B. Jetmundsen. *On frequency domain methodologies for structural modification and subsystem synthesis*. Phd, Rensselaer Polytechnic Institute, Troy, NY, 1986.
- [78] D. De Klerk, D.J. Rixen, and J. De Jong. The frequency based substructuring (FBS) method reformulated according to the dual domain decomposition method. In *24th International Modal Analysis Conference, St. Louis, MO*, 2006.
- [79] W. D’Ambrogio and A. Fregolent. Promises and pitfalls of decoupling procedures. In *Proceeding of 26th IMAC. Orlando (USA)*, 2008.
- [80] P. Ind and D.J. Ewins. Impedance based decoupling and its application to indirect modal testing and component measurement: a numerical investigation. In *Proceedings of the Twenty First International Modal Analysis Conference, Kissimmee, FL*, 2003.
- [81] S.N. Voormeeren and D.J. Rixen. A family of substructure decoupling techniques based on a dual assembly approach. *Mechanical Systems and Signal Processing*, 27:379–396, feb 2012.
- [82] C. Höller and B.M. Gibbs. Indirect determination of the mobility of structure-borne sound sources. *Journal of Sound and Vibration*, 344:38–58, 2015.
- [83] W. D’Ambrogio and A. Fregolent. Substructure decoupling without using rotational DoFs: Fact or fiction? *Mechanical Systems and Signal Processing*, 72-73:499–512, 2016.

- [84] P. Sjövall and T. Abrahamsson. Substructure system identification from coupled system test data. *Mechanical Systems and Signal Processing*, 22(1):15–33, jan 2008.
- [85] J.W. Verheij. *Multi-path sound transfer from resiliently mounted shipboard machinery: Experimental methods for analyzing and improving noise control*. PhD thesis, TU Delft, Delft University of Technology, 1982.
- [86] K.A. Burgemeister and R.J. Greer. Using insertion gains to evaluate railway vibration isolation systems. In *Proceedings of Acoustics 2004*, pages 427–432, 2004.
- [87] C.M. Mak and K.C.O. George. Development of an insertion loss for vibration isolation of building services equipment. *Architectural Science Review*, 46(2):193–205, 2003.
- [88] R.J. Pinnington and R.G. White. Power flow through machine isolators to resonant and non-resonant beams. *Journal of Sound and Vibration*, 75(2):179–197, 1981.
- [89] H.G.D. Goyder and R.G. White. Vibrational power flow from machines into built-up structures, Part III: Power flow through isolation systems. *Journal of sound and vibration*, 68(1):97–117, 1980.
- [90] M. Harrison, A.O. Sykes, and M. Martin. Wave effects in isolation mounts. *The Journal of the Acoustical Society of America*, 24(1):62–71, 1952.
- [91] C.M. Harris and A.G. Piersol. *Shock and vibration handbook*, volume 5. McGraw-Hill New York, 2002.
- [92] International Organisation for Standardisation. BS ISO 18312-2:2012 Mechanical vibration and shock - Measurement of vibration power flow from machines into connected support structures, Part 2: Indirect method, 2012.
- [93] J.J. de Espindola, J.M. da Silva Neto, and E.M.O. Lopes. A generalised fractional derivative approach to viscoelastic material properties measurement. *Applied Mathematics and Computation*, 164(2):493–506, may 2005.
- [94] N. Gil-Negrete, J. Viñolas, and L. Kari. A simplified methodology to predict the dynamic stiffness of carbon-black filled rubber isolators using a finite element code. *Journal of Sound and Vibration*, 296(4-5):757–776, oct 2006.
- [95] L. Kari. On the dynamic stiffness of preloaded vibration isolators in the audible frequency range: modelling and experiments. *The Journal of the Acoustical Society of America*, 113(4):1909, 2003.
- [96] A. Coronado, M.A. Trindade, and R. Sampaio. Frequency-dependent viscoelastic models for passive vibration isolation systems. *Shock and Vibration*, 9(4-5):253–264, 2002.

- [97] L. Kari. On the waveguide modelling of dynamic stiffness of cylindrical vibration isolators. part II: the dispersion relation solution, convergence analysis and comparison with simple models. *Journal of Sound and Vibration*, 244(2):235–257, jul 2001.
- [98] L. Kari. On the waveguide modelling of dynamic stiffness of cylindrical vibration isolators. part I: the model, solution and experimental comparison. *Journal of Sound and Vibration*, 244(2):211–233, jul 2001.
- [99] J.C. Snowdon. Vibration isolation: use and characterization. *The Journal of the Acoustical Society of America*, 66(5):1245–1274, 1979.
- [100] S. Nadeau and Y. Champoux. Application of the direct complex stiffness method to engine mounts. *Experimental Techniques*, 24(3):21–23, 2000.
- [101] S. Kim and R. Singh. Multi-Dimensional Characterization of Vibration Isolators Over a Wide Range of Frequencies. *Journal of Sound and Vibration*, 245(5):877–913, aug 2001.
- [102] D.J. Thompson and J.W. Verheij. The dynamic behaviour of rail fasteners at high frequencies. *Applied Acoustics*, 52(1):1–17, 1997.
- [103] D.J. Thompson, W.J. Van Vliet, and J.W. Verheij. Developments of the indirect method for measuring the high frequency dynamic stiffness of resilient elements. *Journal of Sound and Vibration*, 213(1):169–188, 1998.
- [104] A. Brekke. Dynamic stiffness and mobility for vibration isolators. In *Proc. Meeting of Scandinavian Acoustical Society*, pages 345–348, 1986.
- [105] S. Lindblad. A simple measuring method for blocked translational and angular transfer stiffness of vibration isolation elements. In *Proceedings of Internoise*, pages 605–608, Poughkeepsie, New York, 1997.
- [106] U.J. Kurze. Laboratory measurements of vibro-acoustical properties of resilient elements, Part I: theoretical basis. *Acta Acustica*, 2:483–490, 1994.
- [107] Å. Fenander. Frequency dependent stiffness and damping of railpads. *Journal of Rail and Rapid Transit*, 211(1):51–62, 1997.
- [108] International Organisation for Standardisation. BS EN ISO 10846-2:2008 Acoustics and vibration - Laboratory measurement of vibro-acoustic transfer properties of resilient elements, Part 2: Direct method for determination of the dynamic stiffness of resilient supports for translatory motion, 2008.

-
- [109] International Organisation for Standardisation. BS EN ISO 10846-3:2002 Acoustics and vibration - Laboratory measurement of vibro-acoustic transfer properties of resilient elements, Part 3: Indirect method for determination of the dynamic stiffness of resilient supports for translatory motion, 2002.
- [110] International Organisation for Standardisation. BS EN ISO 10846-5:2009 Acoustics and vibration - Laboratory measurement of vibro-acoustic transfer properties of resilient elements, Part 5: Driving point method for determination of the low-frequency transfer stiffness of resilient supports for translatory motion, 2009.
- [111] L. Kari. Dynamic transfer stiffness measurements of vibration isolators in the audible frequency range. *Noise Control Engineering Journal*, 49(2):88–102, 2001.
- [112] T.R. Lin, N.H. Farag, and J. Pan. Evaluation of frequency dependent rubber mount stiffness and damping by impact test. *Applied Acoustics*, 66(7):829–844, jul 2005.
- [113] L.E. Ooi and Z.M. Ripin. Dynamic stiffness and loss factor measurement of engine rubber mount by impact test. *Materials & Design*, 32(4):1880–1887, apr 2011.
- [114] International Organisation for Standardisation. BS EN ISO 10846-1:2008 Acoustics and vibration - Laboratory measurement of vibroacoustic transfer properties of resilient elements, Part 1: Principles and guidelines, 2008.
- [115] D.J. Tylavsky and G.R.L. Sohie. Generalization of the matrix inversion lemma. *Proceedings of the IEEE*, 74(7):1050–1052, 1986.
- [116] G. Strang. *Linear algebra and its application*. Brooks/Cole, 4th edition, 2004.
- [117] J.X. Su. *Simplified characterisation of structure-borne sound sources with multi-point connections*. Phd, University of Liverpool, 2003.
- [118] S.Z. Rad. *Methods For updating numerical models In structural dynamics*. Phd, Imperial College, University of London, 1997.
- [119] MATLAB. version 8.5.0, 2015.
- [120] R.B. Randall. *Frequency Analysis*. Bruel & Kjaer, 3rd edition, 1987.
- [121] M.A. Sanderson and C.R. Fredö. Direct measurement of moment mobility: Part I: A theoretical study. *Journal of Sound and Vibration*, 179:669–684, 1995.
- [122] D.J. Ewins and P.T. Gleeson. Experimental determination of multidirectional mobility data for beams. Technical report, 1974.

- [123] J.E. Smith. Measurement of the total structural mobility matrix. Technical report, DTIC Document, 1966.
- [124] J.E. Mottershead, M.G. Tehrani, D. Stancioiu, S. James, and H. Shahverdi. Structural modification of a helicopter tailcone. *Journal of Sound and Vibration*, 298(1):366–384, 2006.
- [125] B. Petersson. On the use of giant magnetostrictive devices for moment excitation. *Journal of Sound and Vibration*, 116(1):191–194, 1987.
- [126] S.U. Jianxin and C.M. Mak. Direct measurement of moment mobility and a moment excitation system. *Applied Acoustics*, 63(2):139–151, 2002.
- [127] Y. Champoux, V. Cotoni, B. Paillard, and O. Beslin. Moment excitation of structures using two synchronised impact hammers. *Journal of Sound and Vibration*, 263(3):515–533, 2003.
- [128] A.S. Elliott, A.T. Moorhouse, and G. Pavić. Moment excitation and the measurement of moment mobilities. *Journal of sound and vibration*, 331(1):2499–2519, 2012.
- [129] S.S. Sattinger. A method for experimentally determining rotational mobilities of structures. *Shock and Vibration Bulletin*, 50:17–27, 1980.
- [130] M. Van Der Seijs, D. Van Den Bosch, and D. De Klerk. An improved methodology for the virtual point transformation of measured frequency response functions in dynamic substructuring. In *4th ECCOMAS Thematic Conference on Computational Methods in Structural Dynamics and Earthquake Engineering*, Kos Island, Greece, 2013.
- [131] A. Albarbar, A. Badri, J.K. Sinha, and A. Starr. Performance evaluation of MEMS accelerometers. *Measurement*, 42(5):790–795, 2009.
- [132] J.W.R. Meggitt, A.S. Elliott, and A.T. Moorhouse. In-situ determination of dynamic stiffness for resilient elements. *Journal of Mechanical Engineering Science*, 230(6):986–993, 2015.
- [133] M.F. Dimentberg and K.V. Frolov. *Vibroacoustical Diagnostics for Machines and Structures*. Research Studies Press LTD, Taunton, 1991.
- [134] A.M.R. Ribeiro, J.M.M. Silva, and N.M.M. Maia. On the generalisation of the transmissibility concept. *Mechanical Systems and Signal Processing*, 14(1):29–35, 1998.

- [135] N.M.M. Mais, J.M.M. Silva, and A.M.R. Ribeiro. The transmissibility concept in multi-degree-of-freedom systems. *Mechanical Systems and Signal Processing*, 15(1):129–137, 2001.
- [136] D. De Klerk, D.J. Rixen, and S.N. Voormeeren. General framework for dynamic substructuring: history, review and classification of techniques. *AIAA Journal*, 46(5):1169–1181, may 2008.
- [137] L. Keersmaekers, L. Mertens, R. Penne, P. Guillaume, and G. Steenackers. Decoupling of mechanical systems based on in-situ frequency response functions: The link-preserving, decoupling method. *Mechanical Systems and Signal Processing*, 58-59:340–354, 2015.
- [138] G. Pavić and A.S. Elliott. Structure-borne sound characterization of coupled structures - part II : feasibility study. *Journal of Vibration and Acoustics*, 132(August):1–13, 2010.
- [139] G. Pavić and A.S. Elliott. Structure-borne sound characterization of coupled structures - part I : simple demonstrator model. *Journal of Vibration and Acoustics*, 132(August):1–7, 2010.
- [140] Joint Committee For Guides In Metrology. Evaluation of measurement data - Guide to the expression of uncertainty in measurement, 2008.
- [141] D. De Klerk and D.J. Rixen. Component transfer path analysis method with compensation for test bench dynamics. *Mechanical Systems and Signal Processing*, 24(6):1693–1710, 2010.
- [142] R. Penrose and J. A. Todd. A generalized inverse for matrices. *Mathematical Proceedings of the Cambridge Philosophical Society*, 51(03):406, 1955.
- [143] J.S. Bendat and A.G. Piersol. *Engineering Applications of Correlation and Spectral Analysis*. John Wiley & Sons, Inc., 2nd edition, 1993.
- [144] International Organization for Standardization. BS EN 60704-1 : Test code for the determination of airborne acoustical noise emitted by household and similar electrical appliances - Part 1. General requirements, 1995.
- [145] W.H. Greene. *Econometric Analysis*, volume 97. Prentice Hall, 2002.
- [146] H. White. A heteroskedasticity-consistent covariance matrix estimator and a direct test for heteroskedasticity. *Econometrica: Journal of the Econometric Society*, pages 817–838, 1980.

-
- [147] J. S. Long and L. H. Ervin. Correcting for heteroscedasticity with heteroscedasticity consistent standard errors in the linear regression model: Small sample considerations, 1998.
- [148] S. N. Voormeeren, D. De Klerk, and D. J. Rixen. Uncertainty quantification in experimental frequency based substructuring. *Mechanical Systems and Signal Processing*, 24(1):106–118, 2010.
- [149] N.M. Ridler and M.J. Slater. An approach to the treatment of uncertainty in complex-parameter measurements. *Metrologia*, 39(3):295–302, 2002.
- [150] B.D. Hall. On the propagation of uncertainty in complex-valued quantities. *Metrologia*, 41(3):173–177, 2004.
- [151] H.S. Kim and T.L. Schmitz. Bivariate uncertainty analysis for impact testing. *Measurement Science and Technology*, 18(11):3565–3571, 2007.
- [152] J.W.R. Meggitt, A.S. Elliott, and A.T. Moorhouse. Virtual assemblies and their use in the prediction of vibro-acoustic responses. In *Proceedings of the Institute of Acoustics*, Warwickshire, 2016.
- [153] H.W. Engl, M. Hanke, and A. Neubauer. *Regularization of inverse problems*. Springer Science & Business Media, 1996.
- [154] A.T. Moorhouse. Compensation for discarded singular values in vibro-acoustic inverse methods. *Journal of Sound and Vibration*, 267(2):245–252, oct 2003.
- [155] A.N. Tikhonov, V.A. Arsenin, and F. John. *Solutions of ill-posed problems*, volume 14. Winston Washington, DC, 1977.
- [156] J.W. Verheij. Inverse and reciprocity methods for machinery noise source characterisation and sound path quantification. Part 1: Sources. *International Journal of Acoustics and Vibration*, 2(1):11–20, 1997.
- [157] P. Gardonio and M.J. Brennan. On the origins and development of mobility and impedance methods in structural dynamics. *Journal of Sound and Vibration*, 249(3):557–573, jan 2002.